APPLICATION OF THE THEORY OF CRITICAL DISTANCE TECHNIQUE TO PREDICT FRACTURE TOUGHNESS IN FRICTION STIR WELDED Ti-6Al-4V SHEET

By

William Henry Rall

A thesis submitted in fulfilment of the requirements for the degree of

Doctor of Philosophiae: Engineering - Mechanical

In the
FACULTY OF ENGINEERING, THE BUILT ENVIRONMENT AND INFORMATION TECHNOLOGY NELSON MANDELA METROPOLITAN UNIVERSITY
PO BOX 77000, Port Elizabeth South Africa

April 2017

Supervisor: Prof DG Hattingh

Declaration

I, William Henry Rall (s9341463), hereby declare that the thesis for Students qualification to be awarded is my own work and that it has not previously been submitted for assessment or completion of any postgraduate qualification to another University or for another qualification.

Author Signature…………………… Date……………………

William Henry Rall

Acknowledgements

When attempting a project such as this, it is inevitable that many people will be required to lend some support.

I would like to thank Professor Danie Hattingh for all his support and advice over the many years. I would like to thank his team at eNTSA. If I had to isolate individuals for special gratitude, it would be Nadine for assisting with administrative support, Riaan Brown for helping after hours on the wire cutter and MTS platform and Stephen Grewar for helping out with some of the fracture testing work. The staff at the metallurgy laboratory need to be commended for always helping under trying times. Thank you Glynne Erasmus, Marlon Koopman, Christiaan du Preez and Kurt Jenniker. Without your dedication it would have been nearly impossible to finish this thesis.

I would like to thank the Dean of my Faculty, Dr Franks; HOD, Gysbert Kleyn; Doctor Lombard and my department for their belief in me and allowing me time to complete this study.

I would like to thank my parents for their support in helping me with picking up children during the day. It saved me so much time and enabled me to complete tests uninterrupted.

Finally, I would like to thank my wife Olga and children (Liam and Willow) for their belief and support. You are the light in my life.

Table of contents

Table of contents

List of figures

List of tables

Nomenclature

a :	Notch depth
B :	Sample thickness
r :	Notch radius (unless stated otherwise)
W :	Sample width
W_o :	Ligament length – this would be the material remaining beyond the notch or crack tip
S :	Distance between centres in three point bend test
σ_n :	Nominal stress i.e. the stress applied across the full section of the structure
σ_u :	Ultimate tensile strength
$\sigma_{0.2}$:	0.2% yield strength
σ_y :	Yield strength
σ_n :	Nominal applied stress (on geometrically non-modified section)
σ_f :	Nominal stress at failure (on geometrically non-modified section)
σ_0 :	Critical stress at failure
K_{Capp} :	Apparent fracture toughness. This would fracture toughness calculated from the peak fracture force
Y =	The form factor which relates σ_n to the stress intensity ahead of the crack tip

Glossary of terms

ASTM E399 - Standard test method for Linear-Elastic Plane-Strain Fracture Toughness K_{IC} of Metallic Materials.

ASTM E561 – Standard test method for testing plane stress fracture toughness.

ASTM1820 – Standard test method for determining parameters J, K and CTOD.

CTOD – Crack tip opening displacement is a method of describing the crack tip condition and can be used as a failure criterion. It essentially measures the blunting of the crack tip due to plastic deformation. This is measured by noting the crack opening displacement before loading and then the resulting displacement at the crack opening due to the plastic deformation at the crack tip. CTOD is part of elastic-plastic fracture mechanics theory which is used in cases when nonlinear deformation ahead of the crack becomes large. This condition holds true for most metals[1].

EPFM – Elastic plastic fracture mechanics

Equiaxed microstructure – This is a microstructure which has very similar dimensions in all directions.

ELI – Extra low interstitial – this refers to a titanium grade has a lower percentage oxygen.

Forge force – The force acting along the tool pin centreline.

FPRI – Friction Processing Research Institute.

FSW – Friction stir welding – Friction stir welding is a welding technique developed in the early nineties by TWI (The Welding Institute) in Britain. It is a solid state joining technique which has many metallurgical benefits (especially when applied to aluminium); the drawback of the technique is setup cost due to tooling.

HAZ – Heat affected zone – this is the zone in which metallurgical changes occur during the welding process.

J Integral – J is the non-linear energy release rate. It can be used as an energy parameter or a stress intensity parameter[1]

K – Stress intensity factor relates the geometry of a specimen and the crack to the stress at the tip of the crack.

K_{IC} – K_{IC} is the critical stress intensity factor of a material. This factor describes the stress condition at the crack tip when the crack becomes unstable and propagates. For brittle materials it is a single value, but for ductile materials it is not a specific value but more an estimated value due to the materials ability to arrest the crack. It is related to the R-curve by $R = (K_I)^2/E'$[1]

LEFM – Linear elastic fracture mechanics – Linear fracture mechanics assumes linear elastic behaviour of the material at the crack tip. This is a simplified version of fracture mechanics and best describes the behaviour of brittle materials or crack tip behaviour at low stress intensities.

Interstitial – This typically occurs when an atom occupies a space in the crystal structure where normally there would be no atom.

R – Curve - The material resistance curve. The R-Curve can indicate a specific point of instability or it can have various permutations depending on the mechanical properties of the material. A flat curve is obtained with a brittle material. A rising R-curve is typical of a ductile material whilst a material that fails by cleavage could typically yield a falling R-curve. Component geometry can play a role in the shape of the R-curve, for example, a thin material may yield a much steeper curve than usual[1]

Solidus temperature – The temperature at which melting occurs during heating

STA – Heat treatment that involves the metal to be solution treated and then annealed

Transus temperature – The temperature beyond which a full phase transformation would occur

TMAZ – Thermo-mechanical affected zone

Abstract

Application of the theory of critical distance technique to predict fracture toughness in friction stir welded Ti-6Al-4V sheet

W. H. Rall
Faculty of Engineering, the Built Environment and Information Technology
Nelson Mandela Metropolitan University
P O BOX 77000, Port Elizabeth, South Africa
Thesis: Doctor of Philosophy: Engineering: Mechanical
January 2017

With modern day socioeconomic pressures to deliver more cost effective, higher performance and energy efficient mechanisms and structures, light weight design is coming more to the forefront of design methodologies. These methodologies need to apply lightweight materials in unison with a defect tolerant design strategy. Titanium is certainly not a new material and was used in large quantities in the 1960's and '70s, but mostly in military applications. The main drawback of this material was cost, however due to current design needs as mentioned the consumption of the material is rising rapidly.

Friction stir welding is by no means a new technique anymore, however, relatively speaking it is still in its infancy when compared to other traditional welding techniques. It has been applied mostly to low melting temperature metals, more specifically aluminium; however, its application to higher melting temperatures has started to enjoy more attention over the last few years. The lower temperatures at which the weld occurs, when compared to conventional processes, is the main reason for applying this technique to materials melting at a higher temperature such as titanium.

Fracture mechanics allows modern-day designers and maintenance engineers to operate structures with an inherent flaw. These flaws may be due to geometric features of the design; fabrication defects or defects such as cracks that have developed over time within an operational structure. Fracture mechanics has evolved significantly since Griffith first proposed it in the early 20th century. The application of the method is often complex and determining the material properties for fracture resistance can be problematic and costly. Many techniques have been proposed over time to simplify the application of this method and one of these techniques would be the theory of critical distance. Since the technique is relatively new and has mostly been applied to more brittle materials, this study aimed not only to apply this technique to a more ductile material but additionally to one that is classified as a sheet material.

The initial tests of this study investigated if a common convergent point could be determined by using three notches varying in size. The technique does not have a standard that governs its application. The initial tests did not yield a common intersecting point thus a second study was applied to see if sample width would influence the results. The results from the study indicated that wider samples seemed to yield similar apparent fracture toughness results, however a common convergence point could still not be established. This prompted a more in-depth study which involved various sample widths coupled with varying notch depths. Sharper notches were also applied and samples with controlled cracks were also tested. The results clearly showed that as the plastic zone size increases in relation to the ligament length of the sample, the critical distance becomes larger. The results also suggested that it would perhaps be best to use sample sizes with notches which allow fracture of the sample before the nett section stress reaches the material's yield strength.

The final tests involved testing the friction stir welded material. Various other studies were also done to corroborate the fracture toughness results. The stress relieved samples showed a reduction in the fracture toughness due to possible precipitation hardening during the stress relieving heat treatment process. The welded material showed an increase in the apparent fracture toughness when compared to the parent plate. The results indicate that residual stresses have an influence on the fracture toughness. In terms of the critical distance, it would appear that the value stays unchanged from the parent plate to the welded material; however, what is significant was that the value seemed to stay more or less constant as long as the nett section stress of the notched samples stayed below the yield stress of the material.

Chapter 1

Research Methodology

1.1 Introduction

Titanium is an abundant mineral in South Africa, yet most of the raw product is exported only to be imported in its reworked state at high cost[2]. The titanium market is growing at a rapid rate owing to lean design methods for products. Due to the drive for lower energy consumption, the aircraft industry has responded by substantially increasing the use of titanium in their designs. Airbus for instance used 12 tons of titanium on their A320 and has increased the titanium application in the A380 to 77 tons[3]. The South African government has recognised that this trend presents many opportunities and has established the Titanium Centre of Competence (TiCoC) as part of the light metals initiative since, not only will the demand for this material grow, but considering its expense, knowledge on lean design and manufacture will become vital[4].

Friction stir welding is a solid state joining technique and much has been published on this technique over the years. Most published work to date pertains to lower melting materials such as aluminium, however, in the last few years some focus has shifted to friction processing of higher melting metals including titanium. Friction stir welding of titanium presents a fair amount of challenges due to its inability to conduct heat very well as well as the temperature needed to be achieved to yield a successful weld. Titanium becomes very reactive at higher temperatures which in itself presents a challenge since the weld needs to be shielded from the surrounding atmosphere to prevent the formation of oxides and nitrides, but it may also react with the tooling required to do the weld and the fixtures required to stabilise the weld samples[5-7].

Most research thus far has focused mainly on process development and the subsequent mechanical properties including fatigue. Only in more recent studies has fracture toughness been investigated using more traditional fracture mechanics techniques. The theory of critical distance is a relatively new technique that could simplify testing and analysis dramatically. In view of the limited experience in the field of fracture mechanics at the NMMU, this work is intended to initiate research in this field at the NMMU.

1.2 Title

Application of the theory of critical distance technique to predict the fracture toughness in friction stir welded Ti-6Al-4V sheet.

1.3 Rationale and motivation

With the increased demand for light weight design the demand for material with a good strength to weight ratio is becoming more popular. The application of light weight design requires joining methods that will be more energy efficient and yield a better joint efficiency. In most instances some flaw will be present within the working structure, either as a geometrical anomaly or in the material itself due to the fabrication process. Friction stir welding has been attracting a lot of attention due to its ability to produce joints that are superior to those made by fusion processes. Most of the studies on this method have been focused on lower melting temperature materials such as aluminium, however, in recent years the focus has shifted to higher melting metals including titanium.

The field of fracture mechanics is significant since it allows for defect tolerant design, meaning structures can be designed to be lighter in weight. The field of fracture mechanics, however, is a complex field. The test methods are often expensive and generally only reveal the fracture technique to follow after numerous tests have been done. The theory of critical distance is not a new technique, but it has been revolutionised by newer technologies and has been championed in recent years by the likes of Professors Taylor and Susmel[8-11]. The method proposes not only a much more simplified method for determining the fracture toughness of the material with a crack, but also techniques to predict the fracture toughness of notches of various radii.

1.4 Delimitations

The study will focus on Ti-6Al-4V 3.2mm sheet in the mill annealed condition. The friction stir welding parameters will be based on the findings published by Mashinini[7]. The fracture study will focus mostly on K_{Capp}, and comparisons of the fracture toughness of the notch and the crack will be based on this parameter. Since the theory of critical distance (TCD) method is largely based on linear elastic fracture mechanics theory, the testing techniques will mainly focus on this area. Since the technique promotes the possibility of utilising much simpler and cheaper samples than traditional fracture mechanics testing techniques, this study will essentially focus on utilizing double edge notch tension (DENT) specimens.

1.5 Problem statement

Most of the research done on fracture toughness of Ti-6Al-4V was done using traditional fracture mechanics techniques. Most of the studies that applied the TCD technique did so on more brittle materials and only a few studies applied it to more ductile metals. Thus the effectiveness of applying this method to titanium sheet needs to be established.

1.6 Sub-problems

Sub-problem 1

Establish suitable manufacturing techniques that will yield an acceptable level of dimensional accuracy of the notch radius.

Sub-problem 2

Determine suitable notch radii that will yield a common critical distance

Sub-problem 3

Determine what effect sample size has on the critical distance

Sub-problem 4

Determine the radius that will yield similar results when compared to a sample containing a crack.

Sub-problem 5

Determine the fracture toughness variation along the weld direction as well as transverse to the weld direction. The use of compact tension (CT) samples will be necessary and moderation will be required between the DENT samples and the CT samples.

1.7 Objective

The main objective of this study will be to develop an understanding of the TCD method in its application to friction stir welded titanium sheet.

1.8 Hypothesis

This study will develop an understanding of the application of the theory of critical distance to Ti-6Al-4V sheet in the mill annealed condition and friction stir welded condition. In doing so, the effect of friction stir welding on the fracture toughness of the material may be determined by the theory of critical distance.

1.9 Research methods

The theory of critical distance is a fairly new method and its application to ductile materials not well investigated. Most research on the topic was undertaken on materials more brittle in behaviour. Studies on more ductile materials did so with test coupons that varied in size. Some of these studies based their methodology on existing testing standards such as the ASTM E399, however, in reality the premise of this method is that it is a more simplistic manner to determine the fracture toughness of a material. Therefore, several tests will have to be done in order to establish the validity of the method.

Since the method is new there is no standard that governs its testing procedures. Therefore, it will be necessary to establish the size notches that can be used to achieve the critical parameters. Tests will have to be done to establish if and how sample size affects the critical parameters. This thesis will mainly focus on using DENT samples, however, the use of CT samples will also be employed to save material when testing fracture toughness for notches transverse to the weld.

Once these parameters have been established testing on the friction stir welded plates will commence. Since variations in these values are expected, analytical work such as hardness tests, microscopy work, study of the fracture surfaces including SEM work and residual stress measurements will be done. The data obtained from these tests could aid in understanding the variation in measured fracture toughness.

1.10 Organization of thesis

This thesis is divided into essentially two sections. The first few chapters will deal with the back-ground theory pertaining to this study, whilst the last few chapters will deal with the research aspect of this study.

Chapter 2 will elaborate on the technical aspects of titanium. Typical microstructures and their mechanical behaviour will be investigated. The formation of these microstructures is of importance since the welding process will cause microstructural changes and subsequently alter the performance of the material.

Chapter 3 will deal with the friction stir welding process. Aspects such as process parameters and their effects on the material performance will be highlighted. This chapter will also discuss research done specifically on friction stir welding of Ti-6Al-4V and the fracture studies done on this topic.

Chapter 4 pertains to fracture mechanics. The field of fracture mechanics is complex and many text books have been published on it. This chapter will only high light some of the pertinent aspects and try to relate linear elastic fracture mechanics to the theory of critical distance.

Chapters 5 and 6 will summate the process of relating the TCD process to Ti-6Al-4V sheet and the friction stir welded sheet.

Chapter 7 will conclude the research study and propose matters for future research.

Chapter 2

Titanium – Metallurgical Aspects

2.1 Introduction

Ti-6Al-4V is a heat treatable titanium alloy. Like most metals its performance can be manipulated by altering the material's microstructure. Since this project will concern itself with the fracture toughness of Ti-6Al-4V sheet that has been friction stir processed, it is the aim of this chapter to investigate the various metallurgical aspects of Ti-6Al-4V and how these typically influence this material's mechanical performance in terms of static strength and fracture toughness.

2.2 Metallurgy of Ti-6Al-4V

Titanium is a fairly abundant metal; however, extracting it from its raw state is an intensive process, which is costly and therefore limits its fabrication to batch processes, further exacerbating the costs of the material[12].

Since titanium as an element can have two phases it is considered to be an allotropic material. At room temperature its crystal structure is that of a hexagonal closed packed form (HCP). This structure, however, transforms to a body centred cubic (BCC) structure at a temperature above 1000°C (for Ti-6Al-4V) [13]. The HCP structure is referred to as the alpha (α) phase, whilst the BCC structure is referred to as the beta (β) phase. Since titanium can be alloyed, the alloy structure for the various alloys can be described as such, alpha, near alpha, alpha-beta or beta. The microstructure as well as the crystal shape are both important in the behaviour of the alloy[13]. An alpha-beta alloy suggests that the alloy would transform readily to a beta phase during heating and may retain some of the beta crystal structures, depending on the cooling rates[13].

Ti-6Al-4V is known as an alpha-beta alloy. When alloying titanium, elements are added which stabilise the alpha-phase, whilst others are added that lower the beta-phase transformation temperature and allow the retention of the beta-phase crystal structure after cooling. There are a number of elements that act as alpha-stabilisers, but in terms of Ti-6Al-4V, aluminium, oxygen, carbon and nitrogen could be considered as the most influential. Likewise, there are a few elements used as beta-stabilisers (there is an isomorphous group and a eutectoid group) but in terms of Ti-6Al-4V, vanadium is added for this purpose (hydrogen is also a beta phase stabiliser but is regarded as a contaminant). The beta transus for Ti-6Al-4V is approximately 980ºC[13].

Secondary phases can form in an α-β alloy in the form of martensitic structures. These phases include α', hexagonal crystal with an acicular appearance, and α'', a supersaturated orthorhombic phase. In formation of these martensitic phases, the cooling rate is of significance[13].

The fact that both phases (α and β) can be present in the material is significant in terms of developing alloys with varied properties. These varied crystal structures influence the material's deformation and fusion rate. The alpha phase

HCP crystal structure is anisotropic in behaviour, specifically, in terms of its elastic response along its various planes[12].

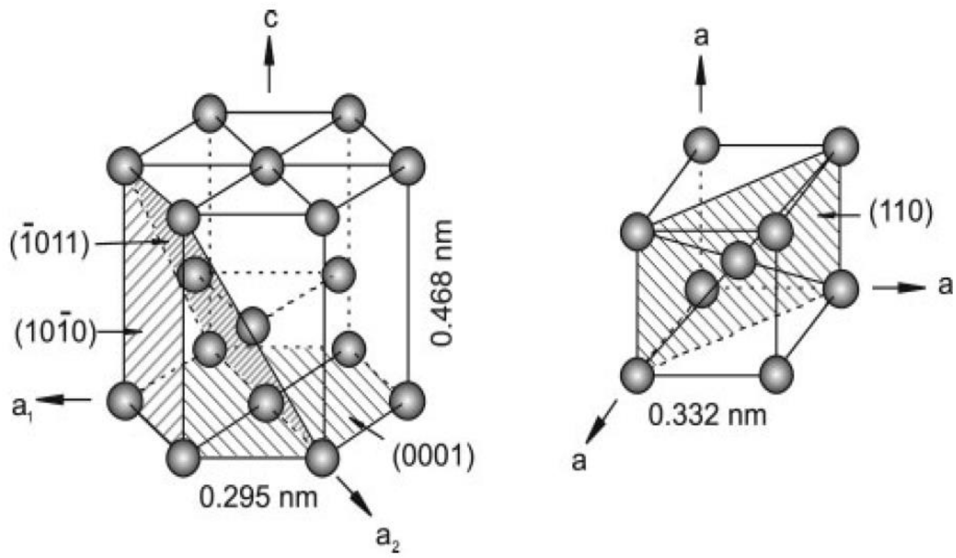

Figure 2-1 - Crystal structures for HCP alpha and BCC beta phase titanium[12]

HCP atom packing density is greater than that of a BCC structure and should favour slip more readily. However, the HCP crystal structure is more resistant to deformation compared to that of the BCC crystal structures. This is due to the fewer slip systems along which slip can occur within the crystal lattice slip systems for the HCP (3) when compared to the BCC crystal (12) and the fact that the minimum slip length for the titanium HCP crystal is larger than the minimum slip length of the BCC crystal structure. Due to its complex structure polycrystalline HCP titanium is difficult to deform and deformation usually occurs by means of twinning or slip along its secondary slip systems[12]. One of the reasons for the complex polycrystalline structure is the fact that the c/a ratio (Figure 2-1) for a titanium HCP crystal is not the same as that of a perfect HCP crystal. This imperfect ratio is a result of cooling from the β phase, where the

HCP crystals start to form on the most densely populated (atom wise) plane of the BCC crystal structure, that being the 110 plane (Figure 2-1). Both these planes contain 5 atoms; however, the atom spacing between the HCP basal plane (0001) and the BCC 110 planes do not match which causes the c/a ratio of the titanium HCP crystal to not conform to the c/a ratio of a perfect HCP crystal. It is due to this distortion that a slight volume increase can be witnessed during cooling from the β–phase to the α–phase.

2.3 Heat treatment of titanium

Ti-6Al-4V is a heat treatable alloy and can be aged. In its annealed condition its microstructure can consist of up to 90% alpha phase. The alpha phase is made up of the aluminium and is its structure is that of a hexagonal close pack form.

There are various heat treating methods for Ti-6Al-4V which can increase the strength of the alloy significantly; however, it is most commonly used in the mill anneal condition. One of the reasons for this, is that the condition offers an overall good performance in terms of mechanical properties and corrosion resistance. Another reason involves the cooling rate required during quenching of thick sections (it is difficult to obtain a constant cooling rate in sections thicker than 25 mm) [13, 14].

Similar to alloyed steels, there are various heat treatment processes that affect the performance of the material significantly (the microstructural changes during these heat treatments will be discussed in later sections). Heat treatment can be useful to reduce residual stress, increase strength or produce a microstructure that behaves optimally in terms of strength and ductility.

Stress relieving for Ti-6Al-4V typically happens at temperatures ranging from 260 – 650ºC. Higher temperatures are more effective at relieving stresses and requires shorter treatment times. When heat treating Ti-6Al-4V at the high end of the temperature scale (which is recommended for weldments) more than 70% of the stress can be relieved within an hour. Cooling from this temperature is usually done evenly by either furnace cooling or air cooling especially in the temperatures ranging between 480 - 315ºC[13, 15]. Water cooling is not allowed for this treatment. There are complications to consider when stress relieving titanium. Low temperatures may require excessive times to remove the stress and even so may not relieve enough of it. At the recommended temperatures ageing may occur by means of the formation of α_2 (Ti_3Al) microstructures. The solvus range for the formation of this detrimental structure is between 550 - 600ºC[14, 16]. When heating the material in an oxygen and nitrogen rich environment, these two elements react with the material causing a hard brittle scale to form referred to as an α-case. Higher temperatures will result in the formation of thicker layers. Some studies indicate that an oxide layer of less than 20 µm will build up when Ti-6Al-4V is kept at a temperature of 595ºC for less than 10 hours[14]. The removal of these α-case layers is difficult since they are very hard and abrasive.

Other annealing processes could involve annealing in the high α-β phase or just above the beta transus temperature. This results in a lamellar or Widmanstatten structure which enhances properties such as fracture toughness, crack resistance, corrosion and creep resistance[14].

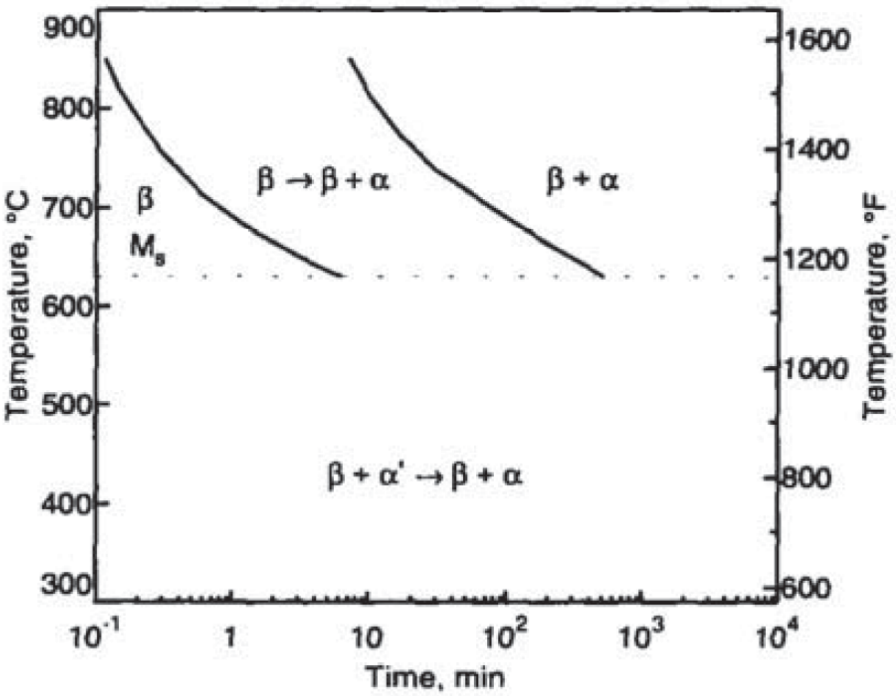

Figure 2-2 - Time temperature diagram of Ti-6Al-4V – Solution annealed at 1020 °C and quenched directly to reaction temperatures[14]

Various solution heat treatment processes result in various crystal structures being formed. For instance, solution heat treating above the β transus and then quenching the material results in the formation of a microstructure consisting of mostly acicular α' martensite microstructures and a small amount of beta, whilst quenching at temperatures ranging between 900°C and a 1000°C results in a mixed α and α' structure. Quenching at a temperature between 800 – 900°C, a mixture of α and α'' structures may be obtained. The α'' structure is a very soft structure. These heat treatments are often coupled with an ageing process which involves re-heating the material to temperatures between 300°C and 600°C[14].

The various heat treatment processes result in a variety of possible crystalline structures. These typically include, lamellar structures, equiaxed, bimodal structures and interface phases.

When cooling an Alpha-Beta alloy, transformation from the β to α range transformation either happens from nucleation from the β grain boundaries, when cooling slowly, or martensitically when quenching[15].

Lamellar structures are typically obtained in Ti-6Al-4V by heating the material beyond its transus temperature followed by cooling. When cooling it slowly α phase crystals nucleate on the densely packed basal plane (refer to section 2.2)of the β crystal (along the grain boundaries). The crystals grow relatively slowly in the direction perpendicular to this plane but faster along the plane thus causing plates to form. The α phase crystals grow perpendicular to this plane and due to the six nonparallel planes within the β phase crystal, the α plane will grow in these directions forming the Widmanstätten structure[13]. When quenching the material rapidly from above the beta transus temperature the β phase is converted into a martensitic structure. This martensitic structure can consist of either α' (alpha prime) or a combination of α' and α'' (alpha double prime). The α' is typically achieved by quenching from a temperature of 900ºC or higher (at a rate faster than 18ºC/sec) whilst α'' forms when quenching from a lower temperature, that typically being from 750ºC to 900ºC[14, 17]. During the quenching process some of the β is not able to transform fully into the martensitic α' or α'' and is thus retained within the structure.

Figure 2-3 shows the constant cooling diagram for Ti-6Al-4V.

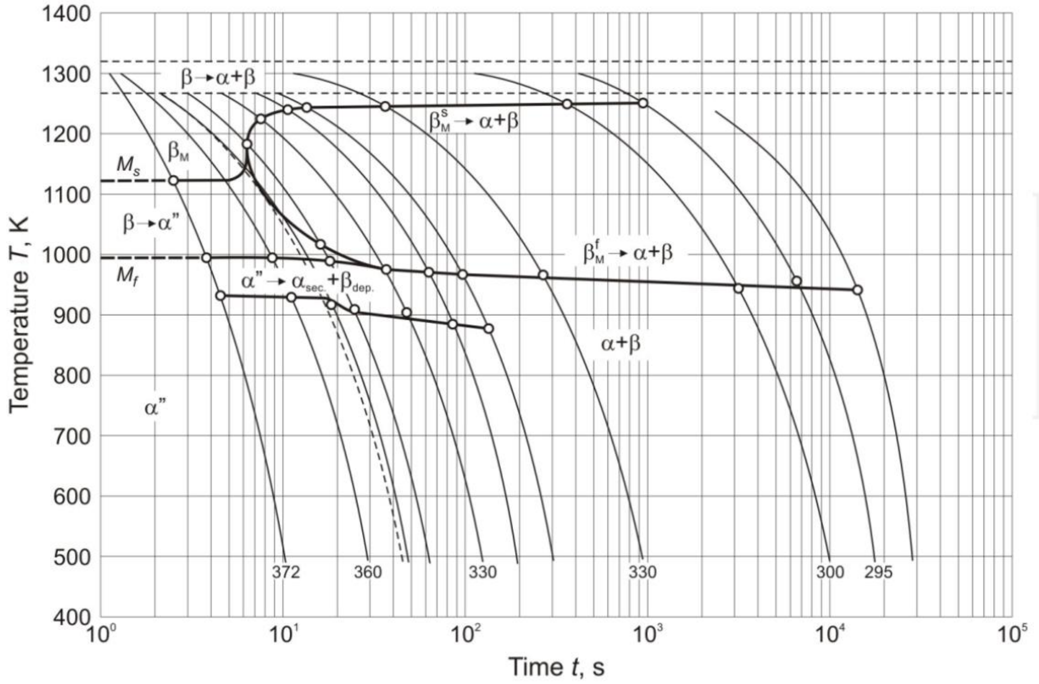

Figure 2-3 - CCT diagram for Ti-6Al-4V[17]

The martensitic phase α' is needle-like in appearance and often similar in appearance to the acicular α structure. It is a non-equilibrium supersaturated α structure and therefore has a HCP form. Alpha double prime, however, is a non-equilibrium supersaturated orthorhombic phase[15].

Non-equilibrium β structures can be retained in Ti-6Al-4V since the end of the martensite transform temperature (M_f) is below 25ºC.

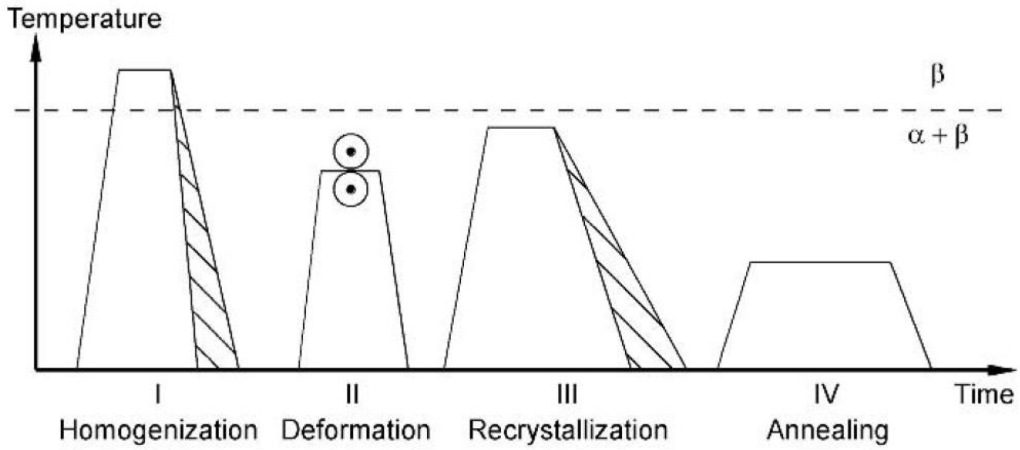

Figure 2-4 - Process whereby equiaxed grains can be obtained[16]

There are two ways in which equiaxed microstructures are created, but this usually involves hot working (enough to break up the recrystallised Ti-6Al-4V) at a temperature below the β transus temperature (in the $\alpha - \beta$ filed). The primary difference between the two methods involves the temperature and the cooling rate during the recrystallisation process (Figure 2-4). In both cases, the cooling rate must be sufficiently low to allow for the growth of primary α grains and for no alpha lamellar grains to form.

The mill anneal process also achieves an equiaxed microstructure, however this method omits the recrystallisation step (step iii - Figure 2-4). The mill anneal process is not a well-defined process and it stands to reason that there could be slight variations in the performance of mill annealed products due to variations during the deformation process and the subsequent heat treatment processes. These variations do not only apply between manufacturers, but also among batches from the same supplier[14, 16]. As an example, mill annealed plates can be shipped from suppliers with a final anneal time that can vary between 1 and 8 hours[16]. Unlike the two other methods (to achieve an equiaxed microstructure) the final annealing process for a mill annealed product does not result in the formation of α_2 (Ti_3Al) structures[16]. Mill annealing typically produces a crystal structure of globular β crystals within the α matrix. It is a general annealing process used by mills and often leaves traces of the deformed microstructure due to the prior forming processes[13, 17].

Bi-modal microstructures are essentially prime α microstructures contained within a transformed beta matrix. The process to obtain these structures is similar to the equiaxed process shown in Figure 2-4, with the primary difference being the cooling rate after the recrystallisation process which controls the size of the lamellar plates formed[16]. Bi-modal structures can be obtained by heating equiaxed material to the $\alpha - \beta$ temperature range followed by a sufficiently high cooling rate[16].

2.4 Microstructure and properties

Advantages of the acicular microstructure typically include better creep properties, increased fracture toughness, increased crack growth resistance and increased resistance to stress corrosion, but these structures may have lower strength. Equiaxed microstructures typically perform better in terms of ductility and formability, have higher strength and also have better low cycle fatigue strength[15].

In terms of lamellar structures, strength and ductility are very much dependent on the grain sizes and the type of structure formed. Research has shown that as the cooling rate is increased the yield strength of the material increases. During this increase in yield strength, the ductility (measured in terms of % elongation) increases initially up to a point thereafter decreasing rapidly with an increase in cooling rate. These fractures occur as a dimpled ductile trans-crystalline fracture (for slow cooling rates) and a ductile inter-crystalline fracture at higher cooling rates. The inter-crystalline fracture typically occurs in the alpha phase layers along the β grains[16].

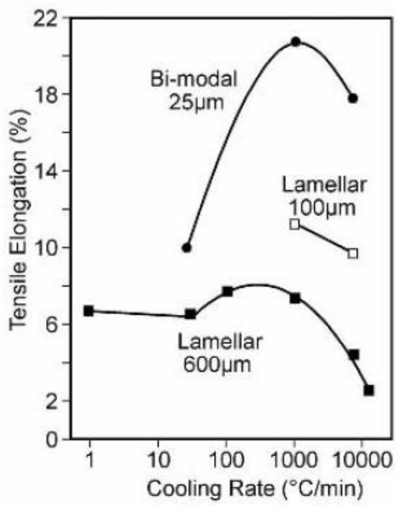

Figure 2-5 - The effect of cooling rates, microstructure size and microstructure type on the ductility of Ti-6Al-4V[16]

Figure 2-5 indicates not only the influence cooling rate has on the ductility of Ti-6Al-4V but also indicates that smaller grain sizes appear to increase the ductility of the metal (for lamellar microstructures). The smaller grain sizes in this case were controlled by reducing the β grain sizes from 600 μm to 100 μm by means of higher heating rates[16]. As the α colony sizes decreased the slip length decreased, hence an increase in the yield strength of the material.

Fracture toughness is dependent on the α colony size and typically increases with an increase in the α colony even though ductility decreases. The reason for this is that the rougher crack front is more dominant than the ductility term. Experiments have shown that for Ti-6Al-4V cooled at 1ºC/min (resulting in a coarse lamellar structure) the fracture toughness was 75 $MPa.m^{1/2}$, whilst for Ti-6Al-4V cooled at 8000ºC/min (resulting in a fine lamellar microstructure) the fracture toughness decreased to 50 $MPa.m^{1/2}$ (both were treated for 24hrs at 500ºC)[16].

In bi-modal structures the relatively small β grain size is the dominant factor on the mechanical properties of this structure type. The β grain size is mainly dependant on the % volume fraction of primary alpha (α_p) structures. In general, the β grain size is in the region of 30-70 µm. The length of slip will once again be the determinant of a range of properties. The smaller grain size results in an increase in yield stress, higher ductility, higher high-cycle fatigue strength, higher resistance to fatigue crack propagation of micro cracks and a higher low cycle fatigue strength as compared to lamellar structures, all compared at similar cooling rates. Fracture toughness for these structures are lower compared to that of the lamellar structures.

A similar analogy can be made for fully equiaxed structures, except in this instance the α grain size mainly determines the slip length and therefore is the biggest determinant influencing the mechanical properties of this structure type. An increase in yield strength and high cycle fatigue strength for this structure type is achieved with smaller grain sizes. In terms of comparison to a bi-modal structure which had a similar heat treatment process, the bi-modal structure yielded slightly higher yield strength and high cycle fatigue strength. In comparison to fully lamellar structures of similar grain size, the equiaxed grain structure shows a superior yield and high cycle fatigue strength. In terms of macro-crack growth rates, larger grain sizes perform slightly better than smaller grain sizes. Bi-modal structures have a similar performance to that of equiaxed structures in terms of macro crack growth rate, but the equiaxed microstructure has a higher micro-crack growth rate. A smaller grain size in the equiaxed structure also yielded a lower fracture toughness (45 $MPa.m^{1/2}$ for a 2 µm grain size and 65 $MPa.m^{1/2}$ for a 12 µm grain size)[16].

The material presented above indicates that the mechanical properties of Ti-6Al-4V can vary significantly by manipulation of the grain size, type and orientation, all of which are dependent on the thermo-mechanical and heat treatment processes applied to the material. The influence of interstitial elements such as oxygen also has a significant effect on the mechanical performance of the material. Young's modulus is also dependent on the heat treatment and the variations in texture. The values for the elastic modulus for Ti-6Al-4V can vary between 100-130 GPa[14].

The variation in fracture toughness within certain titanium alloys can be as much as a factor of 2 to 3. This variation can be explained by the variation in microstructure as described in earlier sections. Another explanation is related to interstitial elements such as oxygen and nitrogen. Oxygen, however, is the element which has the most pronounced effect on fracture toughness. Lower values of oxygen tends to yield lower strength (Table 2-1) but higher fracture strength. Ti-6Al-4V ELI (maximum allowable oxygen content of 0.13%) has a higher fracture toughness than the commercial grade of Ti-6Al-4V (maximum allowable oxygen content of 0.2%) as Table 2-2 would suggest[14, 15]. Since microstructural changes within a welded zone is significant compared to that of the parent material, a variation in the resulting mechanical properties is expected.

Table 2-1. Typical mechanical properties of Ti-6Al-4V (Note: in columns containing a range the lower value indicates the minimum measured and the higher value the mean value. In the instance of columns containing one value only it indicates a mean)

Material	Condition	σ_U (MPa)	σ_Y (MPa)	Elong. %	E (GPa)	ν
Ti-6Al-4V[15]	Annealed	900-993	830-924	14	113.8	0.342
Ti-6Al-4V[15]	STA	1172	1103	10	-	-
Ti-6Al-4V Low O_2[15]	Annealed	830-896	760-827	15	113.8	0.342

Table 2-2. Relation grain structure has on yield stress and pane strain fracture toughness of Ti-6Al-4V

Material	Grain Structure	σ_Y (MPa)	K_{1c} (Plane strain) $MPa.m^{1/2}$
TI-6AL-4V[15]	Equiaxed	910	44-66
TI-6AL-4V[15]	Transformed	875	88-110
TI-6AL-4V Low O_2[15]	α-β rolled + mill annealed	1095	32

Welds typically contain transformed microstructures which generally result in a higher fracture toughness[15]. However, Table 2-3 indicates the fracture toughness of welded Ti-6Al-4V as compared to the fracture toughness of the base metal.

Table 2-3. Fracture toughness of welded Ti-6Al-4V (0.11% O)[13]

	K_{Ic} $(MPa.m^{1/2})$		
Post Stress relief	**Weld**	**HAZ**	**Base Metal**
2hrs at 590ºC, AC	87(b)	81(c)	92
1hr at 590ºC, AC	85(d)	77(d) (e)	92
1hr at 590ºC, AC	-	76(d)	92

AC, air cool (a) Recrystallization anneal at 0.11 wt% O. (b) Based on sample size of 2. (c) Sample size of 20. (d) Sample size of 1. (e) Annealed for 2hrs at 650 ºC

2.5 Summary

Ti-6Al-4V is the work horse of the Titanium industry. It is an alpha-beta alloy and is therefore heat treatable. Heat treatment processes alter metallurgical aspect such as the crystal type, the primary grain size, the colony size of the transformed grains and the transformed grain size itself. Other metallurgical aspects include the formation of precipitates such as $TiAl_3$ and when heat treatment is done in a vacuum furnace interstitial elements may be cooked out.

All these aspects contribute to the mechanical performance of the material. For this study Ti-6Al-4V in the mill anneal condition will be used. The base metal is therefore expected to have an equiaxed microstructure with a yield strength in the region of 900 MPa and an ultimate tensile strength of 950 MPa. The fracture toughness of this material is also very much dependent on the afore mentioned variables, however, variation in the fracture toughness of the material may be significantly more than the variation in static strength, especially when the oxygen content is varied.

Chapter 3

Friction Stir Processing of Ti-6Al-4V

3.1 Introduction

This aim of this chapter is to introduce and briefly explain the solid state friction stir welding process. Joining materials by means of welding often requires very precise procedures to ensure optimum joint integrity. Some of these parameters will be explained and contextualised in terms of friction stir welding of titanium, the metallurgical phenomena and mechanical behaviour.

3.2 The friction stir welding process in brief

Friction stir welding (FSW) is by no means a new or novel process anymore and much has been published on the method since its invention in 1991. This is especially true for its application to aluminium since the welding process has enabled the joining of aluminium alloys which are notoriously hard to join using conventional welding methods[16]. Friction stir welding is a solid-state hot-shearing process. It is part of the friction welding group, but unlike other friction welding processes whereby the materials are rubbed against each other under force, friction stir welding relies on a tool to generate heat to plasticise and forge the material.

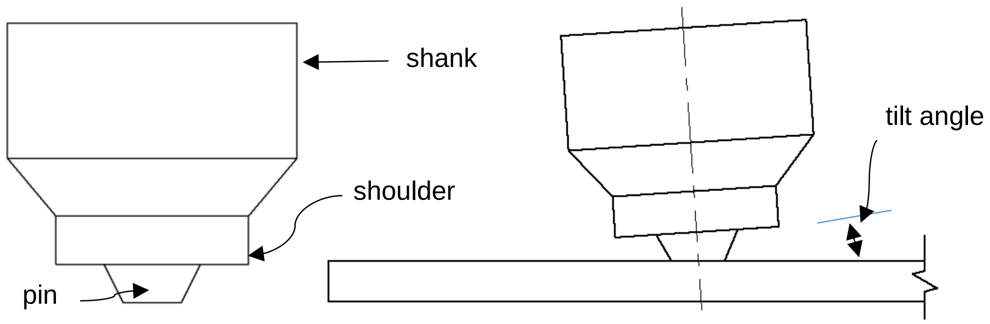

Figure 3-1 - Typical geometry of a friction stir welding tool

The rotating tool typically has a shoulder which aids in heating and creating a forge force on the material directly beneath it (Figure 3-1). From the shoulder the tool diameter reduces to a smaller pin which causes the material deep within the material being processed, to be moved from the front to the trailing edge of the tool[18]. Due to the rotation of the pin, the process is asymmetrical and the two sides on either side of the pin are referred to either as the advancing side or the retreating side (Figure 3-2).

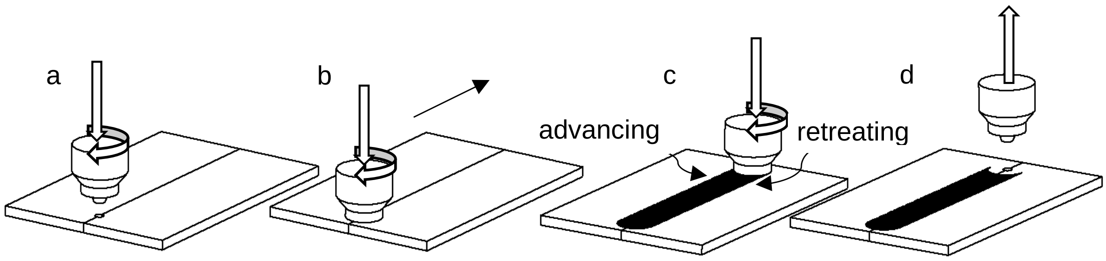

Figure 3-2 - Friction stir welding process (a) initial plunge force and spindle rotation (b) dwell time with forge foce and weld rotation applied (c) welding along the joint line (d) retracting the tool

Figure 3-2 shows the essential steps of the friction stir welding process. The tool is spun up to the speed required for plunging into the material. This plunging process in softer materials is done without a pilot hole; however, in his study

Mashinini found that in welding titanium a pilot hole is required to relieve the tool tip of some of the stresses induced during the plunging process[6, 7].

High forces may develop in the weld direction due to the weld process and the pin itself may cause large forces perpendicular to the weld direction which can cause the plates being joined to separate[19]. It is therefore necessary to clamp the work pieces rigidly onto a backing plate.

The parameters that influence weld integrity can be categorised in terms of tooling and process variables. Tooling parameters typically include tool geometry, backing plate material, weld tool material, cooling methods, clamping methods and machine-related issues such as rigidity and control. Process-related variables may include dwell time, feed rate (either in terms of force or speed), tool rotation speed, tool tilt angle, plunge depth (associated with tool geometry and the ligament length), control type (force control or position control) and shielding requirements.

3.3 Friction stir welding tooling parameters

3.3.1 The weld tool

There are many aspects to consider when selecting a tool for friction stir welding. These can be sub-divided into categories pertaining to the tool type, tool geometry and tool material. The tool type considers tools that weld from one side of the joint only, both sides of the joint (so called bobbin tool) or whether the tool may need to retract.

When welding low melting materials such as aluminium, tool steel such as H13 can be used; however, in terms of high temperature welding, as in the case of titanium, refractory materials are generally used. Typical materials include lanthanated tungsten (W-1%La_2O_3) or tungsten rhenium[7, 20]. The reason for using these materials can be related to titanium's tenacity to become highly reactive to other materials at higher temperatures and these refractory materials being more resistant to reacting with titanium[20]. Traces of tungsten may however still be deposited into the weld[16].

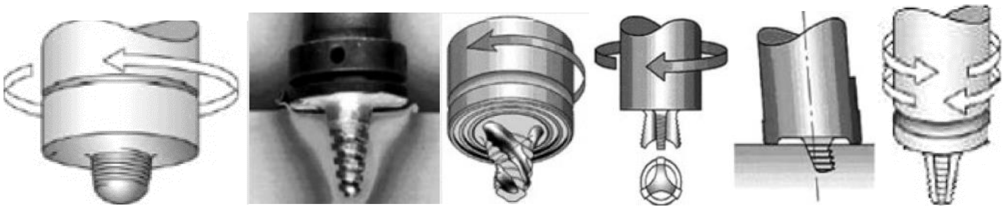

Figure 3-3 - Various FSW tool designs[18]

When welding lower melting point materials there are many possible shapes that are used. Figure 3-3 shows some of the pins shapes developed by TWI[18]. The pin, for instance, often has thread-like features to increase or direct the material flow around the pin. Literature suggests, however, that these features are mainly applicable to low temperature welds as the excessive wear experienced during high temperature welds renders these features impractical[7].

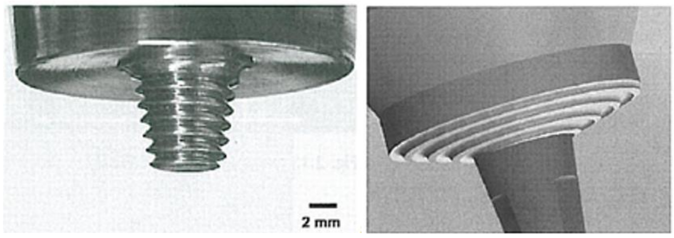

Figure 3-4 - Shoulder geometries of FSW tools[21]

For conventional friction stir welding techniques the shoulder of the tool is for the most part the main source of heat generation during the welding process. Over and above the variations in diameter size, the geometry of the shoulder may vary as well. Flat, convex and concave shoulders have been used (Figure 3-4). The convex shoulders often features spirals which direct the flow of material to the tool pin[6, 19]. Flat shoulders are often used with a slightly tilted tool (Figure 3-1). Titanium is not the best conductor of heat and it has been reported in some literature that the process heat is mostly dependend on the heat from the tool pin and therefore small shoulders or shoulders that do not rotate are often employed[20].

Ding *et al*., for instance, used a shoulder-less tool with a spiral machined on the tool pin. The weld material (grade 2 titanium) immediately ahead of the tool, however, was preheated to 595ºC[5]. There are several studies, however, that have utilised shoulders whilst friction stir welding titanium[7, 22-24]. In his studies, Mashinini developed a tool which yielded a defect-free weld zone. It appears from these studies that a slightly larger tool pin tip results in more heat being generated by the tool. Mashinini also found that the defect-free weld zone was also dependent on a slight tool tilt of 1.5º. This was attributed to the extra forge force generated by the tilt that aided in the consolidation of the plasticised material under the tool shoulder[6, 7].

3.3.2 Welding process parameters

Friction stir welding is usually done on a machine operating with a closed loop control system. Pre-determined parameters can therefore be set and not only controlled, but also monitored. The machines will usually monitor and, or control parameters related to forces, displacements, torque and also the speeds and accelerations of these parameters.

Figure 3-5 shows an example of the measurements recorded during a typical friction stir welding process. The initial sequence which includes the plunging process and dwell time is of great significance. During the plunge the tool has to physically displace material. If the speed is too fast one risks breaking or deforming the tool, damaging the friction welding platform and of course, affecting the weld quality. The plunge depth, which is determined by the tool pin length and the material thickness, is important since it will ensure that the shoulder of the tool stays in contact with the welded plate, and keeps the ligament length (the distance between the tool pin and the backing plate) constant. The ligament length Mashinini used to weld 3.2 mm sheet was 0.1 mm. The control of the plunge depth is also important during welding as it controls not only the pin position from the anvil, but also ensures contact between the tool shoulder and the material being welded. When plunging too deep the tool tip may drag on the anvil, which is detrimental to the tool. An excessive plunge depth can also result in the tool leaving an excessive depression causing the weld area to thin. This in turn may result in excessive friction which in turn results in higher temperatures in the weld zone, so much so that the temperature may reach the solidus temperature of the material which may cause a running pore (worm hole) on the top surface or subsurface[19].

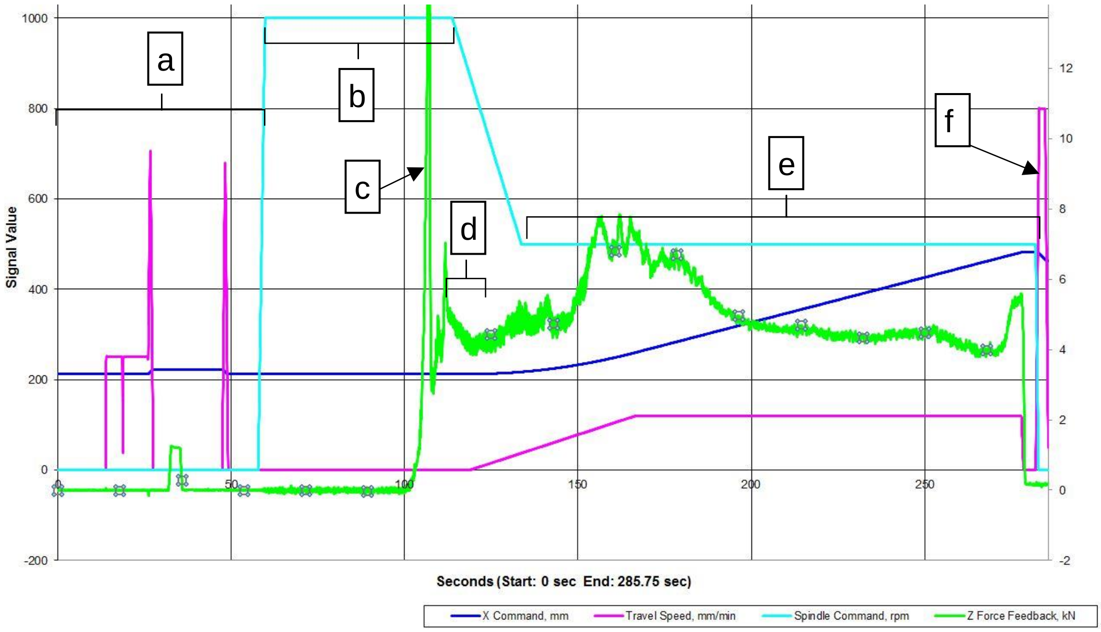

Figure 3-5 - Response feedback of the FSW process: a) Initial positioning of tool; b) Plunge sequence; c) Tool contact with plate; d) Dwell sequence; e) Weld sequence; f) End of welding and tool retract

The dwell time is of importance since it needs to ensure that enough heat has built up to plasticise the material. Too long a dwell time, however, could cause the material to heat up too much resulting in poor flow characteristics[6]. Since titanium becomes very reactive at higher temperatures, which means that it readily reacts with oxygen, nitrogen and take up hydrogen, it is important to shield the weld zone during the entire weld process with an inert gas[19].

The process speeds and feeds will determine how much heat is generated during the weld and also determines the quality of the weld. Mashinini did an extensive survey on past methods used to friction stir weld titanium and based on these he refined the process parameters for 3 mm Ti-6Al-4V sheet for optimal fatigue properties. These parameters are dealt with in section 6.2.

3.3.3 Typical friction stir welding defects

Friction stir welding defects include incomplete penetration, excessive flash, under fill, kissing bond joint, joint line remnant (lazy-s) discontinuity and voids[6].

Figure 3-6 - Joint line remnant [20]

Incomplete penetration and excessive flash are typically attributed to process and procedure parameters. When the forge force is too high or the shoulder plunges too deep, flash typically occurs. Incomplete penetration is typically the result of the use of a pin that is too short or a lack of plunge depth[19].

Kissing bond and “lazy s” defects are metallurgical defects caused by incomplete fusion between the two plates. It can be attributed to oxide layers on the original joint surfaces which are not completely dispersed during welding. Other possible causes for kissing bond defects could be a lack of forge force or tool stiffness[19]. Voids or wormholes are formed due to lack of forge force or incorrect tool geometry.

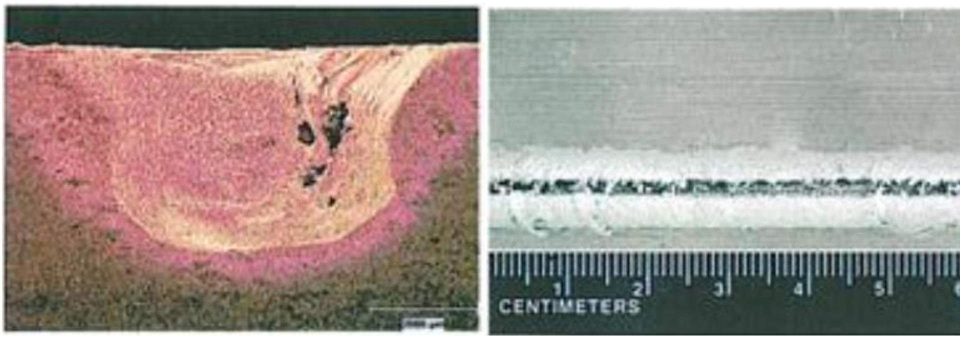

Figure 3-7 - Examples of voids and a wormhole[19]

3.3.4 Mechanical and metallurgical behaviour of friction stir welded Ti-6Al-4V

Figure 3-8 - FSW weld zones: a) parent metal; b) heat-affected zone (HAZ); c) Thermomechanically-affected zone (TMAZ); d) stir zone (SZ)[21]

Liu et al. welded on 2 mm mill annealed plate using a tungsten-rhenium tool with a tilt angle of 2.5º. For their study the rotation speed was kept constant at 400 rpm whilst varying the weld traverse speed. The speeds used were 25, 50 and 100 mm/min. Microstructurally it was noted that the heat affected zone of all three speeds had similar microstructures and it was concluded that in this part of the weld the temperature was under the β transus. It was also reported that no TMAZ was found on either side (that being the advancing side and retreating side of the weld) of the stir zone (Figure 3-8). The stir zone micro structure was of a bi-modal type consisting of equiaxed dislocation free α_p grains with transformed β grains containing lamellar α and β grains. The welds made with the lower traverse speeds had finer grain structures compared to those of the welds made with the 100 mm/min traverse speed and was indeed observed to be finer than that of the parent plate grain structure. The smaller grain sizes were attributed to dynamic recrystallization, whilst at the higher speed the weld was too cold for this to happen. The hardness of the material decreased with the smaller grain size as did the strength of the material. Interestingly the % elongation of the material also decreased with the decrease in strength. Liu et al. explained that this was due to the more randomly orientated grain structure of the finer grains developed at low traverse speeds[25].

Zhou et al. conducted a study using the same tools as Liu mentioned above, except in this case the rotation speed was varied whilst keeping the traversing speed constant at 75 mm/min. The spindle rotation speeds used were 400, 500 and 600 rpm. The results showed the formation of a bi-modal microstructure (finer than the base metal) at the lower spindle speed, whilst more lamellar α and β grains formed on the boundaries of the prior β grains. It was concluded that at the lower spindle speed the temperature did not exceed the β transus and the microstructure was possibly caused by a combination of dynamic recrystallisation at a sufficiently high temperature. The microstructures formed at 500 and 600 rpm suggest that the process developed temperatures exceeding the β transus. The hardness tests indicated that there was a slight decrease in hardness of the samples made using 400 rpm spindle speed compared to the samples made using 500 rpm. There was a marked decrease in hardness of the weld zone material made using 500 rpm compared to the hardness of the weld zone of the 600 rpm samples. The strength also decreased according to the spindle speed from the samples made using 400 rpm samples compared to the samples made using 600 rpm[23].

Another study that investigated the effect variation in spindle rotation has on the microstructure and mechanical performance of friction stir welded Ti-6Al-4V was carried out by Zang et al. A 15 mm diameter shoulder tool with a tool pin that tapered from a diameter of 5 mm to 3 mm was used on 3 mm plate. On a macroscopic level defect free welds were made when using 400 and 500 rpm spindle speeds coupled with a traverse speed of 60 mm/min. The results in terms of microstructure were similar to that of Zhou, however, the study also quantified the grain refinement caused by the friction stir welding process. For all the spindle speeds used the grain size was significantly lower than that of the base metal and it was also shown that the grain size of welded material increased as the spindle speed increased[26].

Pilchak et al. also reported that the microstructure in the stir zone is not so much dependent on the grain structure prior to welding as it is on the process parameters. It was also concluded that the dislocations within microstructure in the stir zone is dependent on the process parameters[27].

In their study, Steuwer et al., found similar results to that of Liu et al. when varying the traverse speed whilst keeping the spindle speed constant at 550 rpm. The welds were performed on 3 mm Ti-6Al-4V sheet whilst the weld was performed using position control. The weld speed range varied between 45 $mm.min^{-1}$ to 165 $mm.min^{-1}$. The Steuwer study showed that the residual stresses longitudinal to the weld direction followed a similar trend to that of the hardness measurements; this being a decrease in measured stress as the weld speed decreased. The transverse stresses were reported to be close to zero for all weld speeds. These stresses were measured at the mid thickness of the plate and spanned across the weld from the advancing side through to the retreating side. The stresses all seemed to plateau in the stir zone with the maximum tensile stress being in the region of 400 MPa and the lowest tensile stress being in the region of 250 MPa (referring to the maximum and minimum stress measured in the stir zone for the 165 $mm.min^{-1}$ and 45 $mm.min^{-1}$ weld results respectively)[22]. Pasta and Reynolds also reported a similar stress distribution in the longitudinal direction to the weld (combining 150 rpm spindle speed with traverse speed of 100 $mm.min^{-1}$ in load control). Their study showed the peak stress varied between 200 and 300 MPa, but this could be attributed to either the methodology of determining the stress (the paper compared two evaluation techniques) or perhaps the experimental technique[28].

In his studies Mashinini comprehensively studied the various parameters that influence the integrity of friction stir welded Ti-6Al-4V sheet. He noted that the root type flaw would be more common when the forge force was below 5 kN[7].

His study quantified the welds in terms of heat input and concluded that for higher heat input weld a basket weave lamellar α/β type microstructure would be prominent in the weld nugget, whilst a lower heat input weld would have a more acicular lamellar α/β lamella colonies[7]. He also reported that there are virtually no β microstructures within the weld nugget and attributed it to the refined microstructure within the weld nugget. In terms of hardness, the softest state was found using a combination of the slowest traverse speed (40mm/min) and slowest spindle rotational speed (350 rpm). This combination yielded a hardness of more or less 330 HV; very similar to that of the parent plate. For most the hardness recorded was approximately 350 HV[7].

Ding et al. studied the fracture toughness of friction stir welded grade 2 titanium and found that there was a decrease in fracture toughness in the stir zone in both the longitudinal and transverse directions to the weld. This decrease was small; however, it coincided with a slight increase in strength of the material in the stir zone[5].

Fracture studies more specifically to Ti-6Al-4V were also done. In all these studies the plate was not thick enough to qualify for plain strain fracture toughness testing and therefore the ASTM E561 standard for plain stress fracture testing was applied. In their study, Edwards et al., used 6 mm thick Ti-6Al-4V plate and tested the toughness of the parent plate and in the weld centre, with the cracks orientated longitudinal to the weld direction and transverse to the weld direction. The welds for fracture toughness testing were heat treated at 760ºC for 30 minutes with weights applied to straighten the plate. This study indicated that the parent plate was tougher than the welded material. In turn the material showed lower fracture toughness with the crack orientated longitudinal to the weld. The study recorded three possible fracture toughness values, that being K_{app}, K_{IC} and K_{PMax}. K_{app} was explained as being the fracture toughness when initial tearing starts, K_{1C} was determined from the R-Curve and K_{PMax} was determined using the peak load at final fracture length. In all three instances the parent plate had a higher fracture toughness than the weld. The apparent fracture toughness values were 90.9 MPa.m$^{0.5}$ (parent plate), 84.9 MPa.m$^{0.5}$ (transverse to weld) and 69.9 MPa.m$^{0.5}$ (longitudinal to weld)[29, 30].

In a repeat of the study Edwards et al. found similar results. This study, however, also examined the hardness variation and residual stress distribution of the welded plate. The study showed tensile stresses in the order of 400 MPa acting along the weld direction with compressive stresses in the order of 60 MPa. In spite of the stresses being relieved it appeared that the fracture toughness decreased. The hardness of the as welded metal was lower than when the stress was relieved[30].

Another study using 2.54 mm sheet indicated that the weld centre of the friction stir welded plate had the lowest fracture toughness compared to other areas of the weld. The material in this study was stress relieved at 774ºC and it indicated that there was an increase in the fracture toughness when stress relieving at this temperature. The as welded fracture toughness was in the region of 75 MPa.m$^{0.5}$ whilst the stress relieved and the machined stressed relieved samples had fracture toughness values in the region of 130 MPa.m$^{0.5}$ and 140 MPa.m$^{0.5}$

respectively. The increase in fracture toughness was attributed to the lowered residual stress as well as lowered stress concentrations in the case of the machined stress relieved samples[31].

3.4 Summary

Friction stir welding is a well-established welding technique for lower melting temperature materials such as aluminium. Research applying this technique to Ti-6Al-4V is not as abundant when compared to aluminium due to the more complex and costly set up required.

There are numerous parameters to consider when applying the friction stir welding technique. The tool geometry, weld tool material, tooling and process parameters are all important factors when using friction stir welding. Titanium becomes highly reactive at temperatures exceeding 600ºC and therefore most tools used in friction stir welding are made from some form of tungsten alloy (most commonly are would lanthanated tungsten and tungsten rhenium). In his study Mashinini focused on optimising parameters such as tool geometry and process parameters for maximum fatigue life using 3.2 mm Ti-6Al-4V sheet. This study will apply these parameters to investigate the fracture toughness of the weld using the theory of critical distance method.

In general, the material undergoes a complex transformation during the welding process. The weld temperature is dependent on the combination of spindle rotation speed and the weld traverse speed. It is suggested that the weld temperature will exceed the β transus temperature when the weld speed is lower whilst higher traverse speeds and lower rotation speeds may result in a cooler weld; possibly lower than the β transus. The microstructure of the weld consists of a bi-modal microstructure which is finer than the equiaxed microstructure of the parent plate. This bi-modal microstructure consists of fine lamellar α platelets contained in a transformed β microstructure.

Not much has been published in terms of fracture toughness of friction stir welded Ti-6Al-4V sheet, but the studies that have been done indicate a lower fracture toughness in the welded material compared to the parent plate. Heat treatment of the welds above 750ºC could increase the fracture toughness of the weld. The increase in the fracture toughness after heat treatment was attributed to the lowered residual stress.

Chapter 4

Linear Elastic Fracture Mechanics and the Theory of Critical Distance

4.1 Introduction

Fracture mechanics is by no means a recent concept, but in terms of other theories of failure it is certainly still new. Predicting failure from inherent flaws in a structure allows designers to design leaner structures as well as to extend the lifetime of current structures which were designed with much more conservative design methodologies. Failure by means of a crack is a complex subject as there are many material and geometrical effects that influence crack behaviour.

This chapter will address some of the basic aspects of traditional fracture mechanics theories and intricacies which will form the basis for explaining the development of the Theory of Critical Distance (hence forth referred to as TCD). The TCD method promises some significant benefits in terms of testing and design as compared to traditional fracture mechanics methods. The established standards require expensive test coupons with size requirements that are often physically not possible in terms of sheer size or practically not possible in terms of extracting them from working structures. The methods of evaluation are often complicated for simple test samples and even more so in the instance of components in service.

4.2 Fracture mechanics techniques

4.2.1 Linear elastic fracture mechanics in brief

Assuming a material is linear elastic and isotropic in behaviour, closed formed solutions for determining the stress field ahead of the crack for certain geometries were formulated by Westergaard, Irwin, Sneddon and Williams[1]. In polar coordinates the stress field in a linear elastic application is as follows:

$$\boldsymbol{\sigma_{ij}} = \left(\frac{\boldsymbol{k}}{\sqrt{\boldsymbol{r}}}\right)\boldsymbol{f_{ij}}(\boldsymbol{\theta}) + \sum_{\boldsymbol{m}=0}^{\infty}\boldsymbol{A_m}\boldsymbol{r}^{\frac{\boldsymbol{m}}{2}}\boldsymbol{g_{ij}^{(m)}}(\boldsymbol{\theta}) \qquad \textbf{Equation 4-1[1]}$$

Where

σ_{ij} = stress tensor

r = the distance from the crack tip at which the stress acts

θ = the angular coordinate determined from the plane in line with the crack plane

f_{ij} = dimensionless function of θ in the leading term

A_m = amplitude (dependent on geometry)

g_{ij} = dimensionless constant for θ for the m^{th} term (dependent on geometry)

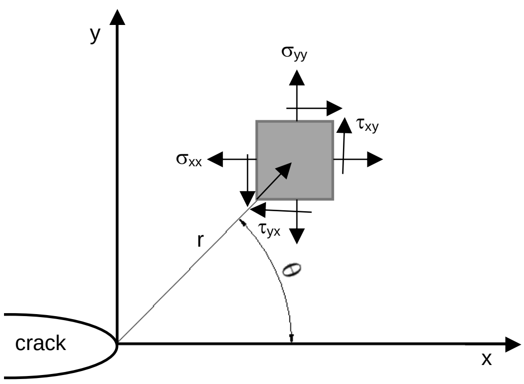

Figure 4-1 – Coordinate system ahead of the crack[1]

The leading term in this equation would be the $\frac{1}{\sqrt{r}}$ term which would lead to a singularity as r approaches 0 since according to the equation stress would be asymptotic at r = 0. Fracture mechanics differentiates among three different modes of loading (see Figure 4-2). Mode I occurs when the loading is perpendicular to the crack plane, whilst Mode II occurs when the load shears the material along the crack plane. Mode III occurs when the applied load creates out of plane shear.

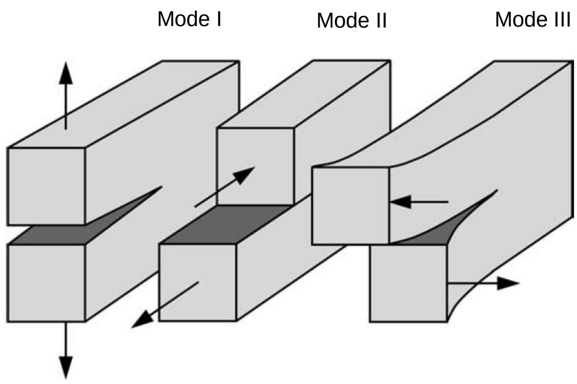

Figure 4-2 – Three loading modes to cause fracture[1]

The loading mode considered for this research study is Mode I type loading, which is applicable when the applied loads are perpendicular to the crack plane. The type of loading will determine the constants k and f_{ij}. The constant k in Equation 4-1 is replaced by the stress intensity factor K (which was proposed by Irwin) where $K = k\sqrt{2\pi}$[1]. For each loading mode there will be a relevant stress intensity factor and these are signified by applying the mode number as a subscript to the symbol K, thus K_I would signify mode I loading. Equation 4-1 thus simplifies to:

$$\lim_{r \to 0} \sigma_{ij}^{(1)} = \frac{K_I}{\sqrt{2\pi r}} f_{ij}^{1}(\theta)$$ **Equation 4-2**[1]

This equation is further simplified if only the stress acting on the crack plane is considered (θ = 0). The formula then reduces further to:

$$\sigma_{xx} = \sigma_{yy} = \frac{K_I}{\sqrt{2\pi r}}$$ **Equation 4-3**[1]

This equation is typically applicable to stress fields close to the crack tip (in linear elastic mode). It has been shown that the predicted stress using this equation tends to become inaccurate at the time that the stress ahead of the crack becomes more stable as shown in Figure 4-3.

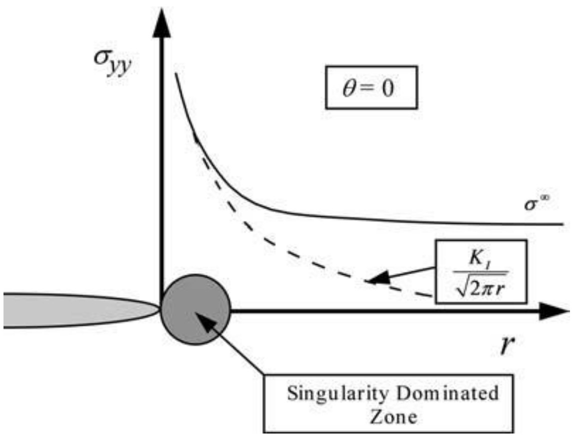

Figure 4-3 - Variation of the predicted stress beyond a singularity zone [1]

The problem in Equation 4-3 is that K needs to be known in order to calculate the stress ahead of the crack tip. The stress intensity value can be determined in terms of the crack geometry and the behaviour of the structural loads by means of the following formula:

$$K_{(I,II,III)} = Y\sigma_n\sqrt{\pi a}$$ **Equation 4-4**

The constant Y in Equation 4-4 is the form factor which takes the various geometrical aspects into consideration and σ_n is the nominal stress acting on the defect free section. For a plate of infinite width with a central crack through its thickness the form factor Y would be equal to unity. There are various texts available that offer some equations to determine Y for some common shapes. For this research study three shapes were considered, these being the double edge notched type (DENT), compact tension (CT) type and the three-point bend type (TPB).

For a double edge notched plate, Equation 4-4 can be used with the form factor described as per Equation 4-5 below.

$$Y = \frac{1.122 - 1.122\left(\frac{a}{W}\right) - 0.820\left(\frac{a}{W}\right)^2 + 3.768\left(\frac{a}{W}\right)^3 - 3.040\left(\frac{a}{W}\right)^4}{\sqrt{1 - \frac{2a}{W}}}$$ **Equation 4-5[32]**

Where *a* would be the notch depth and *W* the sample width.

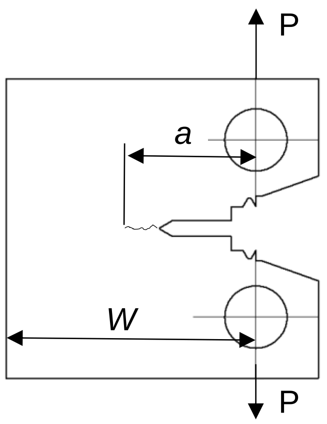

Figure 4-4 - Compact tension (CT) specimen diagram

The stress in the compact tension type specimen can be calculated using the following formula (Figure 4-4):

$$K_I = \frac{P}{BW^{\frac{1}{2}}} . f\left(\frac{a}{W}\right)$$ **Equation 4-6[32]**

where $f(\frac{a}{W}) = \frac{\left(2+\frac{a}{W}\right)\left\{0.886+4.64\left(\frac{a}{W}\right)-13.32\left(\frac{a}{W}\right)^2+14.72\left(\frac{a}{W}\right)^3-5.6\left(\frac{a}{W}\right)^4\right\}}{\left(1-\frac{a}{W}\right)^{\frac{3}{2}}}$ **Equation 4-7**

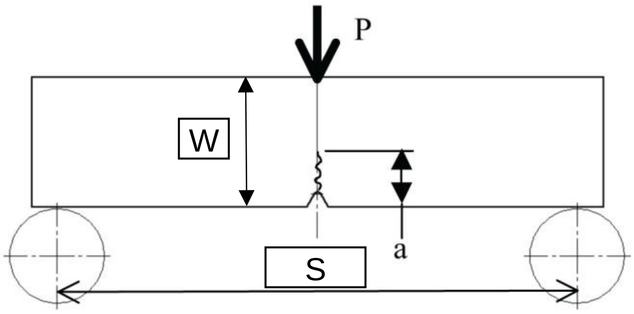

Figure 4-5 - Three-point bend diagram

For a three-point bend specimen the stress intensity factor is calculated using the following formula (see Figure 4-5):

$$K_I = \frac{P.S}{BW^{\frac{3}{2}}} . f(\frac{a}{W})$$ **Equation 4-8[32]**

Where $f(\frac{a}{W}) = \frac{3\left(\frac{a}{W}\right)^{\frac{1}{2}}\left[1.99-\frac{a}{W}\left(1-\frac{a}{W}\right)\left\{2.15-3.93\left(\frac{a}{W}\right)+2.7\left(\frac{a}{W}\right)^2\right\}\right]}{2\left(1+2(\frac{a}{W})\right)\left(1-(\frac{a}{W})\right)^{\frac{3}{2}}}$ **Equation 4-9**

It is clear from Equation 4-4 that the stress intensity is reliant on change in crack length (*a*) and the nominal stress (σ_n) and it would therefore suggest that *K* would increase as these factors increase and at some stage some form of failure should occur. At this stage the stress intensity has reached a critical value commonly referred to as K_C, the critical stress intensity factor. This critical value is dependent on the mode of loading and as stated previously this study will focus on Mode I type loading thus the critical stress intensity factor is denoted as K_{IC}.

K_{IC} is considered to be a material constant, however, the matter is somewhat complicated, since, as stated above, all the mathematical solutions up to this stage have assumed linear elastic behaviour at crack as well as a constant stress distribution throughout the thickness of the material. These assumptions stem back to when Griffith started the field of fracture mechanics and based his original ideas on very brittle materials such as glass. These arguments are flawed since most engineering materials, especially metals, will behave in a non-linear manner when stressed to failure. Additionally, when the material becomes thick enough boundary effects from the free surfaces and edges adjacent to the crack tip (or notch for that matter) create a tri-axial stress state at the crack tip. In essence, the materials ability to deform plastically and the geometry of the structure, specifically thickness "B". are important factors in determining how and when fracture will occur.

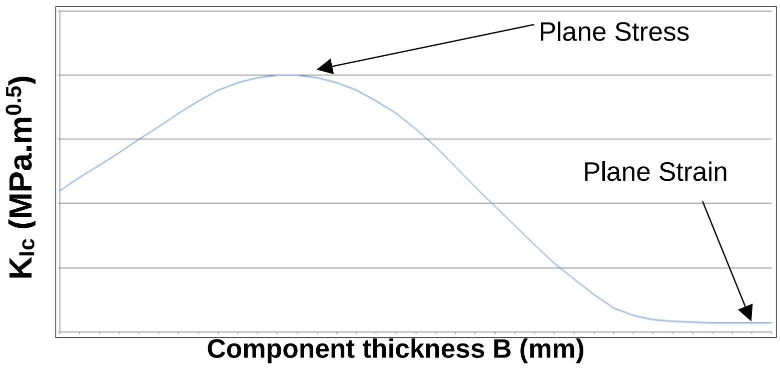

Figure 4-6 - K_{IC} as a function of thickness B

K_{IC} is considered a material property, but can vary with material thickness (see Figure 4-6), however, various studies have shown that when the material becomes sufficiently thick (in other words the tri-axial stress state becomes the dominant factor in the failure mechanism) the value becomes constant. This constant is referred to as plane strain fracture toughness (KI_C, the designation of plane strain fracture toughness).

The theory of linear elastic fracture mechanics (LEFM) was developed with brittle materials in mind and is therefore greatly reliant on the notion that the plasticity ahead of the crack tip is small in relation to the geometry of the part. In most metals there will be some form of plastic deformation and Irwin postulated that the plastic zone ahead of the crack tip could be expressed in terms of the materials fracture toughness and yield strength with the following equation[1]:

$$\boldsymbol{r_y = \frac{1}{2\pi}\left(\frac{K_c}{\sigma_y}\right)^2} \qquad \textbf{Equation 4-10}$$

The plastic zone described in Equation 4-10 considers the plastic zone ahead of the crack tip in terms of a linear stress distribution, where as in reality the plastic zone is larger than that which Equation 4-10 predicts. A second order derivative of Equation 4-10 can be derived to better describe the size of the plastic zone ahead of the crack, which results in a plastic zone twice the size of that predicted by Equation 4-10 [1].

$$\boldsymbol{r_p = \frac{1}{\pi}\left(\frac{K_c}{\sigma_y}\right)^2} \qquad \textbf{Equation 4-11}$$

Both these equations are applicable to plane stress conditions. When calculating the stress intensity factor considering the plastic zone the following equation is suggested[1]:

$$\boldsymbol{K_{(I,II,III)} = Y_{eff}\sigma\sqrt{\pi a_{eff}}} \qquad \textbf{Equation 4-12}$$

Where

$$\boldsymbol{a_{eff} = a + r_y} \qquad \textbf{Equation 4-13}$$

The form factor, Y_{eff} , is calculated using $\left[{a_{eff}}/{W}\right]$. Calculating the stress intensity factors using Equation 4-12 requires an iterative process since a_{eff} is now a function of the resultant stress intensity factor. It is advised that these equations be used with care and that if plasticity is dominant it is advised to rather employ the theories of elastic plastic fracture mechanics (EPFM)[32]. This study will however focus on the application of LEFM since it forms the basis of the TCD method.

4.2.2 Fracture toughness testing techniques

Numerous test methods have been developed over the years to address the need for the various failure conditions that may prevail. The ASTM in particular has developed a few. The ASTM E399 which describes plane strain fracture toughness[33] is severely stringent and requires limited plasticity and plane strain fracture. Other standards were developed to cater for plane stress fracture and plasticity effects. The ASTM E561 was developed for plane stress fracture toughness and allows for limited plasticity ahead of the crack tip[1, 32, 34, 35]. For EPFM the ASTM recommends the E1820 standard which is a combination of several methods and allows for the determination of the J value, CTOD and also K_{IC}[36]. For pipe applications, the ASTM have more specifically developed the ASTM E2472 which applies the crack tip opening angle (CTOA) method[37].

All of these methods have size requirements and in some cases the result may only be specific to the geometry used during the tests[32]. These tests are often expensive and ultimately the results may not to be qualified according to the standard due failure of prerequisite size requirements or crack front requirements[1, 38].

Alternative techniques using notches were proposed as it would greatly simplify the testing procedure. A number of these tests made use of round specimen or conventional fracture test coupons[38-45]

4.3 The theory of critical distance (TCD)

The concept that failure can be predicted using a critical distance as a material property was firstly proposed by Neuber and thereafter Peterson. When applying linear elastic calculations in the region of sharp notches, over conservative results were obtained in the prediction of fatigue life. Neuber attempted to address this by proposing that the stress distribution ahead of the geometrical discontinuity be averaged across a specific distance; a distance unique to an average stress acting across a distance typical to the material (this would be the basis for what is known as the line method).

Peterson had a similar idea except his idea was simpler: stating that failure would occur once a critical stress was reached at a distance typical to the material. These pioneers did not, however pursue the method much further due to the complex and tedious nature of the mathematics required. The method has been applied several times since then by various researchers on various materials but was only really developed in recent years, perhaps due to FEA software becoming commercially more available[8, 11, 46].

The TCD method is a modification of LEFM and likewise falls in the category of continuum mechanics. This suggests that this method is more applicable at predicting failure as a function of the average material's behaviour instead of a mechanistic approach which is better at explaining the behaviour at a microscopic level. The mechanistic approach is better suited to materials that have a completely homogeneous structure[8]. This approach would of course not be well suited to a welded component in which the weld has variable crystalline structures which may vary not only in size and shape but also in packing order.

There are variations of the TCD method, these being the point method (PM), line method (LM), area method (AM) and the volume method (VM). The finite fracture mechanics (FFM) approach is also another method, but unlike the aforementioned methods that are concerned with the stress line ahead of the notch the FFM is based on a stress intensity approach[8, 47].

Due to their simplistic methodology and reasonable accuracy the PM and LM are the most commonly used. According to Taylor[8] each of the two may perform better than the other in certain instances, but the variation is usually insignificant and therefore the point method seems to be favoured more than the line method.

The point method relates two theories of LEFM to one another; these being the fracture toughness of the material and also the variation of stress ahead of the crack tip by equating the formulae in Equation 4-14 and Equation 4-15 (simplified form of Westergaard's method which is applicable to short distances ahead of the crack) to form Equation 4-16, where L = 2r and at failure $\sigma_n = \sigma_f$ [8]. Note that r in this instance refers to the distance ahead of the crack tip.

$$\boldsymbol{\sigma_f = \frac{K_c}{\sqrt{\pi . a}}} \qquad \textbf{Equation 4-14}$$

$$\boldsymbol{\sigma_{(r)} = \sigma_n \sqrt{\frac{a}{2r}}} \qquad \textbf{Equation 4-15}$$

$$\boldsymbol{L = \frac{1}{\pi}\left(\frac{K_c}{\sigma_0}\right)^2} \qquad \textbf{Equation 4-16}$$

Equation 4-16 is the PM formula. For the purpose of this study, in view of the potential effects from size and ductile tearing, K_c will refer to the fracture toughness determined using the peak load which caused the onset of fracture and will be referred to as K_{Capp}.

The methodology essentially requires that notched specimens be tested to destruction either by three-point bending or in tension. The force at fracture is then used in a linear 2D (shell elements) FEA to generate the principal stress distribution (referred to as the stress line curve henceforth) ahead of the notch (preferably a notch sharp enough to behave in a crack-like manner). Originally the method only required one specimen since it was applied mostly to brittle materials and therefore the stress line curve and the UTS could be used to determine the critical parameters. For most other materials at least two curves are required of which at least one has to have a notch sharp enough to be representative of a notch as shown in Figure 4-7. Two material properties are determined when plotting these two curves, namely the critical distance L and the inherent material strength σ_0. Since σ_0 is determined considering only the linear elastic properties of the material and therefore neglecting any plasticity during the process leading up to fracture, it is only a notional value and does not have a physical relation to the material properties. It is therefore merely a parameter used in the TCD method.

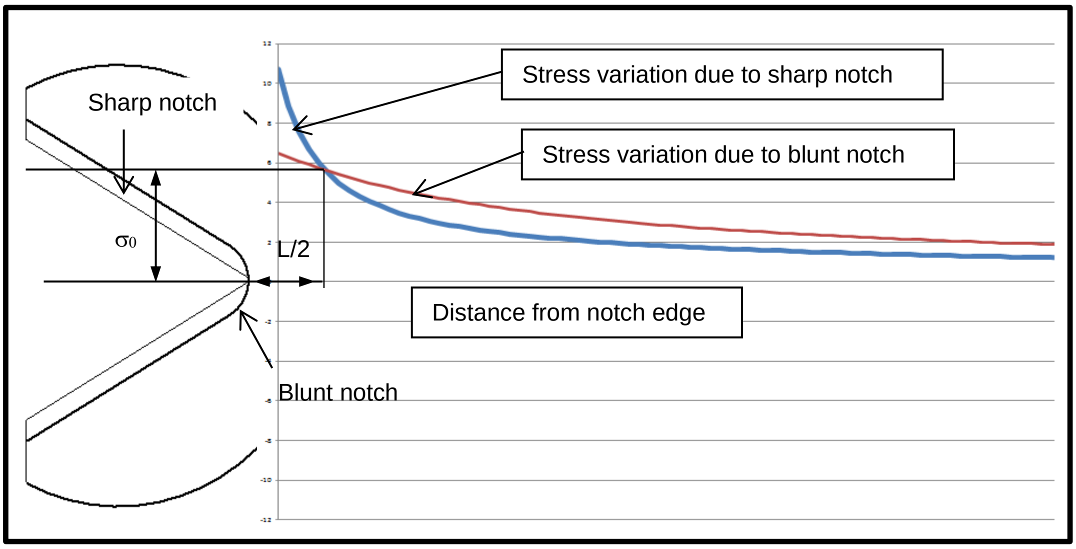

Figure 4-7 - Application of the point method (PM)

In their study, Louks et al. tried relating σ_0 (where σ_0 is the inherent material stress according to the TCD method as show in Figure 4-7) to the UTS of various materials in determining K_{IC}; however, large, but mostly conservative errors were noted[46]. However, other studies have applied the method on more ductile materials such as aluminium and steel and in these instances multiple samples with varying notch geometries were used to determine σ_0 and L[10, 11, 47]. It was noted in these studies that when using more ductile materials that σ_0 is higher than σ_u.

In their study, Susmel and Taylor varied the notch geometry and loading type of En3B steel which is a ductile material to determine the K_{IC} of the material. They first established the fracture toughness of the material as required by the ASTM E399 standard. By applying the TCD theory to samples of varying thickness (values far less than required by the standard) and various notch geometries subjected to either three-point bending or tensile loading they attained a remarkably similar result to that determined by the ASTM standard[11]. In a much more comprehensive study they applied the theory to various materials and also stated that in order to estimate K_{IC} the following rule should be applied:

$$\boldsymbol{K_t > \frac{\sigma_0}{\sigma_u}} \qquad \textbf{Equation 4-17}$$

They stipulated that the net section stress should be less than that of σ_u another possible indicator for successfully determining K_{IC} using the TCD method[10].In his book Taylor states that for metals the ratio $\frac{\sigma_0}{\sigma_u}$ commonly ranges between “2” to “4”, however, there are instances that could increase the range from “1” to “10” [8].

Predicting failure from notches is a complex matter and has been the subject of study for many years[48-50]. The reasons are similar to that of cracks, except for the extra variables surrounding the geometry that would define a notch coupled with scaling effects. The Fedderson diagram shown in Figure 4-8 shows how the variation in notch/crack length affects the allowable nominal stress on a structure. It can be seen that notches are not as severe as cracks, however, they do have angle as an added variable defined by β[49].

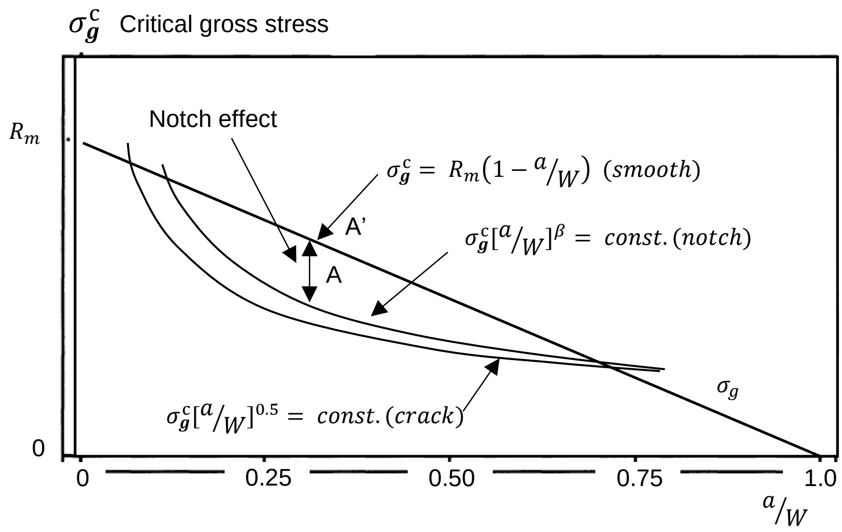

Figure 4-8 - Fedderson diagram[49]

In view of the complexities involved in predicting failure in notched structures, TCD may offer some solutions to this problem as well. The one technique involves using the critical values (σ_0 and L) obtained by means of testing as a reference point through which the stress line curve of the notch in question (obtained from an FEA or other appropriate analytical method) needs to pass. This is of course assuming the critical distance is indeed valid for all notch geometries.

Another method is to combine the theory of Creager and Paris (they developed formulae for elastic stress fields around a blunt crack tip) with the PM (or LM is also popular). This is a quicker method than the one mentioned above since it does not require FEA simulations once the critical values have been established. The Creager formula is as follows:

$$\boldsymbol{\sigma(r) = \frac{K}{\sqrt{2\pi x}}\left(1 + \frac{\rho}{2x}\right)}$$ **Equation 4-18[51, 52]**

Where $x = r + \frac{\rho}{2}$

r = the distance from the notch edge to the pint of interest

ρ = the notch radius

The formula requires however that $a \gg \rho$ (*a* being the notch depth).

Combining Equation 4-18 with Equation 4-16 the following equation is obtained:

$$\boldsymbol{K_{cm} = K_c \frac{(1+{}^{\rho}/_{L})^{\frac{3}{2}}}{\left(1+{}^{2\rho}/_{L}\right)}}$$ **Equation 4-19[8]**

In this case K_{cm} is the fracture toughness of a notch with a radius *ρ*.

Ciecero et al. undertook various studies utilising different methods of TCD and in some cases proposed methods to develop failure assessment diagrams FAD for notches[47, 53, 54]. They also applied the finite fracture mechanics method as a prediction tool using the following:

$$\boldsymbol{K_{cm} = K_{IC} \frac{1}{2.24}\sqrt{\frac{\rho}{L}}}$$ **(blunt solution) Equation 4-20 [55]**

$$\boldsymbol{K_{cm} = K_{IC} \sqrt{\frac{1}{1-\frac{\rho}{20.08L}}}}$$ **(sharp solution) Equation 4-21 [55]**

These formulas are more applicable to through thickness edge notches. The decision whether the notch is blunt or not is determined by the following:

$$\boldsymbol{2L < a^* = a_n \frac{F_2^2}{(F_1^2 K_t^2 - F_2^2)}}$$ **Equation 4-22 [55]**

Where F_1 and F_2 are constant related to the geometry of the sample, K_t is the notch stress concentration factor and a_n is the notch depth.

The graph in Figure 4-9 is typical of how the research on notch fracture toughness is depicted[8]. The fracture toughness in the instance of the experimental data was calculated using LEFM methods. The predictive curves were plotted by applying the various critical distances indicated in Equation 4-20.

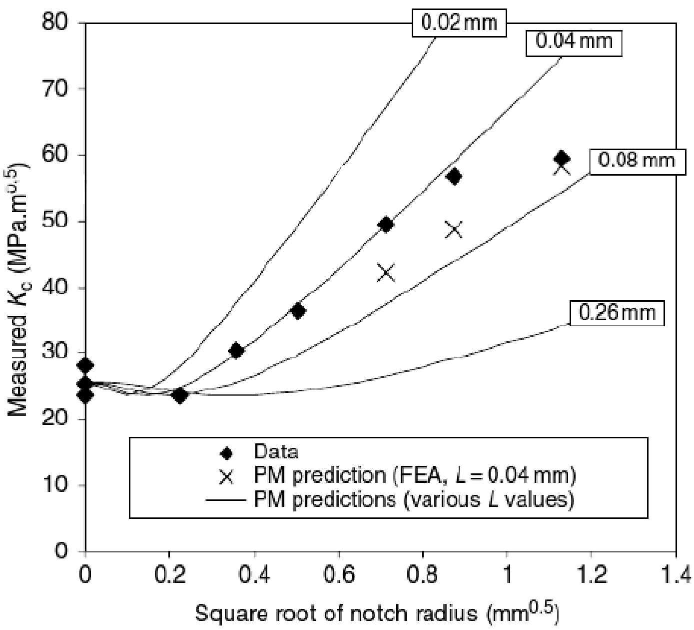

Figure 4-9 - Experimental data of Wilshaw et al. and predictions done by Taylor using TCD[8]

Research has shown that the critical distance can be applied with moderate success as a tool to predict the fracture toughness of a notched component[11, 51, 56].

4.4 Summary

Fracture mechanics has become a well-established method to predict failure and is implemented as a method for lean design strategies. The field is a complex field with many areas of speciality. Fracture mechanics consists mainly of two theories, these being LEFM and EPFM. The differentiation between the two can be related to plasticity effects. LEFM is very much constrained by its requirements in terms of plasticity ahead of the crack tip and is often more applicable to materials which behave in a more brittle manner. If the plasticized areas surrounding the crack tip are large in comparison to the geometry of the crack tip front and the geometry of the part, the EPFM methodologies would probably be more suitable.

When using either of these methods there are certain limiting criteria in terms of the material behaviour which a designer or analyst should consider. The stress surrounding the crack tip is often determined by means of the stress intensity factor K. When this parameter reaches a critical value, fracture may occur either by ductile tearing or unstable crack propagation. Fracture mechanics describes the event of unstable crack propagation as the critical point and in terms of stress intensity factors is denoted by K_C.

There are several standards that have been developed over the years to help determine these critical parameters. These standards are complex and often requires a few initial tests to first establish if the correct standard is being used or if the sample sizes are correct. The methodologies are stringent and require cracks to be grown into the test coupons. Controlling the crack front in order to conform to the requirement of the standard testing techniques are often very difficult. These tests are therefore expensive and numerous studies have been proposed that apply simpler techniques involving notched components to determine these critical material parameters. One of these techniques is the theory of critical distance. It is not a new technique, however, it has been reinvented and pioneered by Taylor. It proposes that the apparent fracture toughness can be determined by simply using test pieces with varying notch radii. Most of the work done in this field has been done using more brittle materials, thus its application to a more ductile material such as titanium could be of interest. For this study complexity is added in that titanium sheet is used, which implies that a plane strain condition will probably not be prevalent.

Chapter 5

Application of the Theory of Critical Distance Method toTi-6Al-4V sheet

5.1 Theory of critical distance experimental objectives

When commencing with testing of the theory of critical distance (TCD) a few questions needed to be answered as the technique is still relatively new and there is no international standard governing the methodology. Most of the research published deals with materials that are considered more brittle in behaviour, therefore plane strain conditions would prevail in most of these studies. The studies dealing with more ductile materials also dealt with sizes that would for the most part behave similarly to plane strain theory. For this research program, the initial challenges that had to be addressed included finding a suitable manufacturing method of the samples, establishing grinding techniques to remove surface case hardening effects due to the heat treatment process and developing a cost effective technique that would repeatedly give the desired notch angle and radius.

Since most literature deals with more brittle materials, situations arose where the stress distribution curves more or less converged at a specific position and for this research study it still had to be established if such a convergence point ($L/2$) could be attained and indeed, if so, which notch sizes would be more likely to yield such a convergence point. According to the literature; for more ductile materials this point is more like to happen at very small values[8], but in their study Susmel et al. used EN3B mild steel and found the critical point to be at a position of more or less $L/2$ = 3.7 mm[11].

In fracture testing geometrical features are always governed strictly by standard test methods[33, 34, 36] therefore it also needed to be established how the TCD technique compares to traditional LEFM methods in terms of results.

5.2 Material used for this study

The material used for this study was the same material used by Mashinini for his study on friction stir welding. Initially it was noted that the material was derived from two different batches, referred to in this study as “Batch A and B”. Considering that the material being used was not from the same batch, but from two different batches of material a slight variation in the results could occur, however this should not be significant.

5.3 Study 1 – Initial observations in the application of the theory of critical distance

The initial objective of this study was to evaluate how the TCD methodology could be applied to the titanium samples and how the material would react to variations in notch radius. The width and size of the notches were based on studies done by Susmel et al.[11] for which they used 25 mm wide samples and recommended a maximum notch angle of 60º (included). The notches were orientated so that they were longitudinal to the rolling direction of the sample.

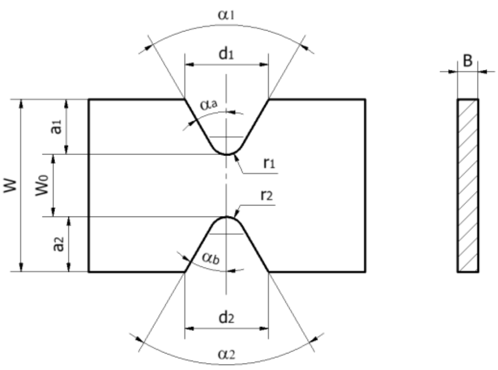

Figure 5-1 – Measurements of DENT sample

For this study the notches were cut using EDM wire cutting. This fabrication method was not used in subsequent studies because of cost and the fact that it is not capable of producing notches with radii sharper than 0.15 mm. Appendix A shows the measurements for all the notches for this thesis. The notch size measurements were made using a Mitutoyo shadow graph which has 10x magnification ability. Slight blurring of the edges influenced the measurement accuracy and was especially problematic for the sharper notches. The values in the Table A1 in Appendix A indicate the variation in the measured radii for the sharp notches. The radii were calculated by using the values of the measured notch depth (*a*), angle (α_1) and the notch opening (*d*) as shown in Figure 5-1.

The tensile testing was conducted using an Instron 8810 servo hydraulic testing machine. It is calibrated on a yearly basis by an independent company accredited for this purpose. The calibration of the 100kN load cell indicated an error within

0.1%, whilst the calibration of 25kN load cell indicated a maximum error of 0.5% (see Appendix J for the certificates). The samples were mounted in such a way as to ensure the centreline of the sample is coincident to that of the centreline of the applied force and an engineering square was used to make sure the centre lines were co-linear.

Table 5-1 indicates the results of the tensile tests. The notch depth "a" shown in this table is the average of the two measurements as shown in the table in Appendix A. The notch radii shown in the table in Appendix A - Notch geometry measurements were rounded to the values as indicated in Table 5-1.

Table 5-1 - Measured variables for Study 1 simulation

Initial Study 1						
Part Number	Group Number	W (mm)	B (mm)	a (mm)	r (mm)	Force (N)
WRCD01-01-01	25x3x1 (CL)	24,98	3,25	2,995	1	67549,32
WRCD01-01-02		24,96	3,25	2,97	1	67466,68
WRCD01-01-03		24,98	3,23	3,005	1	67149,89
WRCD01-01-04	25x3x0,1 (CL)	25,1	3,24	2,95	0,15	63041,54
WRCD01-01-05		25,12	3,24	2,92	0,15	65467,06
WRCD01-01-06		25,06	3,23	2,885	0,15	64501,7
WRCD01-01-07	25x3x1,8 (CL)	25,02	3,24	2,985	1,8	68190,49
WRCD01-01-08		25,04	3,24	2,9975	1,8	68130,42
WRCD01-01-09		24,95	3,24	2,975	1,8	67770,86

It should be noted that during the initial phase of this study, the sharp notches were meant to be 0.1 mm and the dimensions corresponding to this notch radius were meant to be executed by the wire EDM machine. The notches were modelled according to a 0.1 mm notch for the FEA studies, however, during the course of this study it became clear (subsequent notches were measured using a microscope) that the wire cutter cannot cut such a sharp radius and that the measurements from the shadow graph were indeed correct and the radius was remodelled to 0.15 mm and the results adjusted accordingly.

FEA simulations were conducted using the values shown in Table 5-1. These simulations were run utilising parabolic 2D elements and since the components were symmetric about two planes, quarter symmetry could be applied. For this thesis, the simulations were conducted using a linear elastic solver of Autodesk NASTRAN In CAD. The element size in the area of the notch was restricted to 0.002 mm (see Figure 5-2) since this would give sufficient data around the area of interest and it was small enough to ensure convergence of the results (see Figure 5-3). The convergence simulations were run utilising an elastic stiffness coefficient of 114.3 GPa and a Poisson's ratio of 0.34 on a 25 mm wide sample with a 3 mm deep notch. Quarter symmetry was used to model the part, to which a load of 30kN was applied (i.e. 60 kN on full specimen).

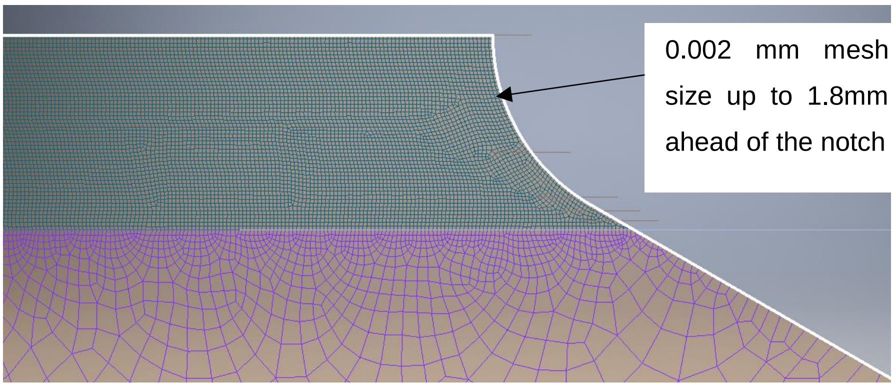

Figure 5-2 - 0.1 mm notch; 0.002 mm elements along a 1.8 mm path

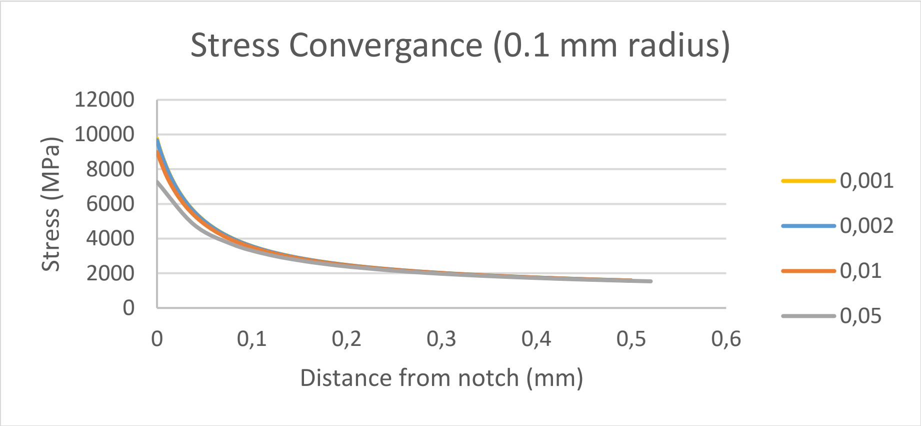

Figure 5-3 - Convergence check utilizing various element sizes for a 0.1 mm notch

The stress line plots in the graph shown in Figure 5-4 depict the average of the stress line plots for each respective radius. From this graph it is possible to find the intersecting points of the various curves. The 0.1 mm curve (25x3x0.1 CL) is intersected at two positions by the 1 mm and 1.8 mm stress line plots. These values are shown in Table 5-2 whilst the intersection between the 1.8 mm and 1 mm stress line plot is shown in Table 5-3.

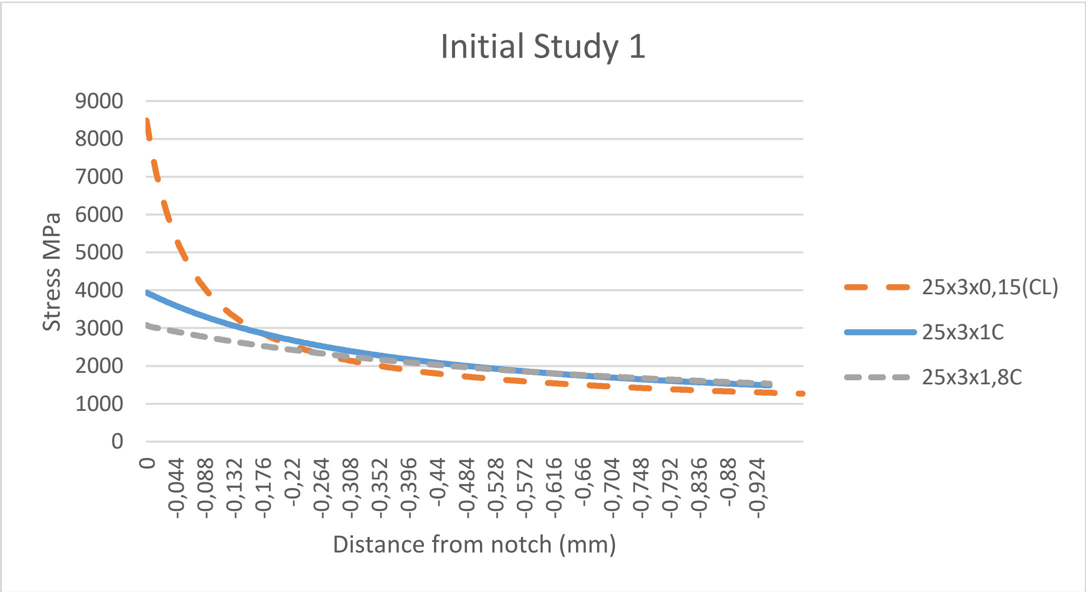

Figure 5-4 - Stress line plots for Study1

Table 5-2 - TCD results using the 0.15 mm stress line plot

Double edge notch tensile specimen Study 1									
		Kc							
		Root curve		0.15 (mm)					
		Intersecting curves		1 (mm)			1.8 (mm)		
Description	W (mm)	B (mm)	a (mm)	σ_0 (MPa)	L/2 (mm)	K_{Capp} (MPa.m^{0,5})	σ_0 (MPa)	L/2 (mm)	K_{Capp} (MPa.m^{0,5})
25x3 (CL)	25	3.24	3	2858	0.176	95	2343	0.258	94

Table 5-3 - TCD results using the 1 mm stress line plot

Double edge notch tensile specimen Study 1						
		Root curve		1 (mm)		
		Intersecting curves		1,8 (mm)		
Description	W (mm)	B (mm)	A (mm)	σ_0 (MPa)	L/2 (mm)	K_{Capp} (MPa.m^{0,5})
25x3 (CL)	25	3,24	3	1834	0,59	111,7E+0

The values of these intersecting points are used to calculate the apparent fracture toughness K_{Capp} using Equation 4-16.

These result indicate a large variation among the intersecting points in terms of the apparent fracture toughness and critical distance (*L*) when comparing the results of Table 5-2 to those of Table 5-3. The study provided insight for the application of the TCD method to titanium; however, questions pertaining to a convergence of the stress plot as well as the influence of size on the results still needed answers.

5.4 Study 2 - Effect of specimen width

One of the questions that the first study did not answer was whether sample size will have an effect on the results of the TCD method. For this study the notch depths were kept constant whilst varying the notch radii. By varying the size of the sample some insight could also be gained about the influence specimen size has on the critical distance.

Table 5-4 - Measured variables for Study 2 simulation

Initial Study 2						
Part Number	**Group Number**	**W (mm)**	**B (mm)**	**a (mm)**	**r (mm)**	**Force (N)**
WRCD01-01-20	25x3x1,8x2.9	24,94	2,84	2,77	1,8	59392,75
WRCD01-01-21		24,96	2,84	2,74	1,8	60425,42
WRCD01-01-22		24,98	2,84	2,8	1,8	61877,31
WRCD01-01-23	25x3x1,2x2.9	24,98	2,8	2,965	1,2	59087,15
WRCD01-01-24		24,98	2,82	3	1,2	58867,12
WRCD01-01-25		24,96	2,86	2,775	1,2	60973,7
WRCD01-01-26	25x3x0,1x2.9	24,98	2,86	2,97	0,1	49925,7
WRCD01-01-27		25,02	2,82	2,975	0,1	49330,78
WRCD01-01-28		24,98	2,88	2,855	0,1	51495,71
WRCD01-01-29	17x3x1,8x2.9	16,96	2,88	2,825	1,8	36953,47
WRCD01-01-30		16,94	2,92	2,8	1,8	37628,89
WRCD01-01-31		16,96	2,85	2,875	1,8	36277,17
WRCD01-01-32	17x3x1,2x2.9	16,8	2,85	2,815	1,2	36010,38
WRCD01-01-33		16,94	2,86	2,94	1,2	36225,63
WRCD01-01-34		16,96	2,88	2,935	1,2	36399,25
WRCD01-01-35	17x3x0,1x2.9	16,94	2,84	2,925	0,1	33233,14
WRCD01-01-36		16,96	2,84	2,915	0,1	33480,0
WRCD01-01-37		16,98	2,88	2,95	0,1	33624,9

Part Number	Group Number	W (mm)	B (mm)	a (mm)	r (mm)	Force (N)
WRCD01-01-38	9x3x1,8x2.9	8,96	2,84	2,695	1,8	12246,43
WRCD01-01-39		8,96	2,86	3,145	1,8	12294,96
WRCD01-01-40		8,98	2,88	2,655	1,8	12422,91
WRCD01-01-41	9x3x1,2x2.9	8,98	2,88	2,98	1,2	10526,38
WRCD01-01-42		8,9	2,84	2,865	1,2	10987,39
WRCD01-01-43		8,94	2,88	2,93	1,2	10705,83
WRCD01-01-44	9x3x0,1x2.9	8,98	2,82	2,965	0,1	11144,86
WRCD01-01-45		8,94	2,84	2,89	0,1	11419,89
WRCD01-01-46		9	2,8	2,935	0,1	11292,05

For all samples subsequent to study 1, the notches were created by using a shaping machine and mounting a turning tool in the shaping machine tool holder. The notches were cut perpendicular to the rolling direction for all samples. The turning tool allowed for interchangeability of standard carbide inserts. Some of the notch radii were not standard for that specific type of tip, so batches were customised for this study by the supplier, Iscar. The notch geometries were measured using a Mitutoyo shadow graph, however, since the samples were prepared in batches using the same tool tip, the notch radius was calculated for only one sample per batch, whilst for the rest a template was used to check for any drastic variation. All the notch depths were measured and these results can be seen in the Table A2 in Appendix A. The notch depth, angle and notch opening were measured and used to calculate the notch radius as done for Study 1

The same test methodology and simulation procedures used for Sudy1 were applied. The stress line plots of these tests are shown in Appendix B. whilst Table

5-5 and Table 5-6 show the values at the intersecting points of the respective curves.

Table 5-5 - TCD results using the 0.1mm stress line plots for various widths

Double edge notch tensile specimen Study 2									
		Root curve		0,1 (mm)					
		Intersecting curves		1,8 (mm)			1,2 (mm)		
Description	W (mm)	B (mm)	a (mm)	σ_0 (MPa)	L/2 (mm)	K_{Capp} (MPa.m^{0,5})	σ_0 (MPa)	L/2 (mm)	K_{Capp} (MPa.m^{0,5})
25x3 (2.9)	25	2,9	3	2533	0,170	83	2952	0,127	83
17x3 (2.9)	17	2,9	3	2172	0,224	82	2476	0,174	81
9x3 (2.9)	9	2,9	3	1493	0,278	62	1518	0,268	62

Table 5-6 - TCD results using the 1.2 mm stress line plots for various widths

Double edge notch tensile specimen Study 2						
		Root curve		1,2 (mm)		
		Intersecting curve		1,8 (mm)		
Description	W (mm)	B (mm)	a (mm)	σ_0 (MPa)	L/2 (mm)	K_{Capp} (MPa.m^{0,5})
25x3 (2.9)	25	2,9	3	1689	0,726	114
17x3 (2.9)	17	2,9	3	1649	0,598	101
9x3 (2.9)	9	2,9	3	1455	0,312	64

From the graphs shown in Appendix B it is also evident that for the 9 mm samples the stress at the notch tip has a drastic decrease for all three notch radii and it would appear as if the larger radii seem to have very similar stress concentrations. It is also apparent from the data in Table 5-5 and Table 5-6 that there is a definite decrease in the apparent fracture toughness between the results of the wider 25 mm and 17 mm samples compared to that of the 9 mm wide samples. When comparing the results of the larger radii one can see a decrease in fracture toughness as the width of the components decrease, that being 114.1 MPa.m$^{0.5}$ for the 25 mm wide samples and 101,1 MPa.m$^{0.5}$ for the 17 mm wide samples.

The reduction in the fracture toughness of the 9 mm samples can probably be attributed to plastic collapse across the net section of these samples. Applying Equation 4-11 the estimated plastic zone size would be more or less 2.4 mm, making the effective notch length 5.4 mm. This value suggests that the net section was fully plasticised.

5.5 Study 3 - Geometric limits

The results of study 2 clearly showed that size has an influence on the critical distance and the apparent fracture toughness values. It was therefore of interest to determine the geometrical limits that would yield a constant critical distance and apparent fracture toughness. The geometries in question were the notch depth, sample width and notch radius. Study 2 also did not yield a specific converging point that could be used to describe the critical distance *L.* Part of the objective of Study 3 was to ascertain whether such a point could be found by varying the notch radius and notch depth.

For this study, the values of σ_0 and L of the intersection between the stress lines curves of the 0.1 mm and 1 mm notches from Study 1 were used in FEA simulations to ascertain the geometrical limits for this study. It was therefore assumed that the stress line curves of all other notches would also pass through this point. This was a little presumptuous since sharper notches would result in higher stress concentrations and therefore stress line plots with steeper gradients close to the notch tip. If the sharp notch has a steep enough gradient and this curve is combined with curves of other sharp notches the stress line curves tend to intersect at the steep part of the gradient of the stress line plot of the sharp notch. This may not per se result in convergence at a specific spot, but since the stress plot for a sharp notch spans across a large stress range in a relatively short distance, perhaps a critical distance could be found.

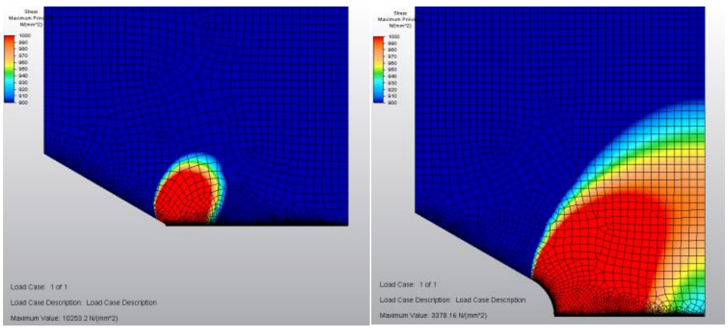

Figure 5-5 – Sharp notch and blunt notch stress distribution

When modelling with these parameters a few criteria were set. One of the limiting parameters of this study was to identify critical size notches that could possible yield a common intersection point for the various notch radii. The stress distribution in the region (not just in the plane perpendicular to the applied load) was taken note of. A sharp notch needed to yield a small local hot spot exceeding the UTS of the material around the notch tip as can be seen in Figure 5-5. If the area of stress that exceeded the UTS spanned across the remaining ligament length, the parameter was not considered to be a viable option for valid results, yet this still needed to be proven since all the simulation criteria assume linear behaviour, which it most definitely is not. Appendix C shows some images of the stress plots of the various simulations.

The effect of varying the notch angle from 0º to 60º at various notch depths and for various notch radii seem to be small, which confirmed the work of Susmel et al.[11] and the theory of Peterson[57].

From these predictions, it appears that for 25 mm samples with a sharp notch (0.1 mm radius), 1 mm deep net section yielding may occur. The study also suggests that the 1.8 mm radius will have net section yielding for most depths and that notches 6 mm and deeper will have either plastic collapse or large scale yielding if the notch exceeds 0.6 mm. The study also suggests that for 17 mm wide samples the optimum notch depth is 3.5 mm, since it will allow notches of radii up to 0.6 mm to be tested.

The study predicted that parts ranging in width between 9 and 13 mm would not be feasible as even the 0.1 mm notch showed large areas that exceeded yield. Although deemed unsuitable some of these notches were modelled to provide insight into the variation of toughness with regards to variable sample width.

Additionally, the study had to provide an idea of how the TCD predictions would compare to a cracked sample. In studies applying the TCD method various modes of testing were applied, these being tensile samples (with U and V notches and samples with holes), three-point bend samples and also compact tension (CT) samples[11, 47, 53, 58, 59]. As a result, this study also included three-point bend tests and it is also by means of three-point bending that cracked samples were tested. Figure 5-6 shows typical examples of specimens tested.

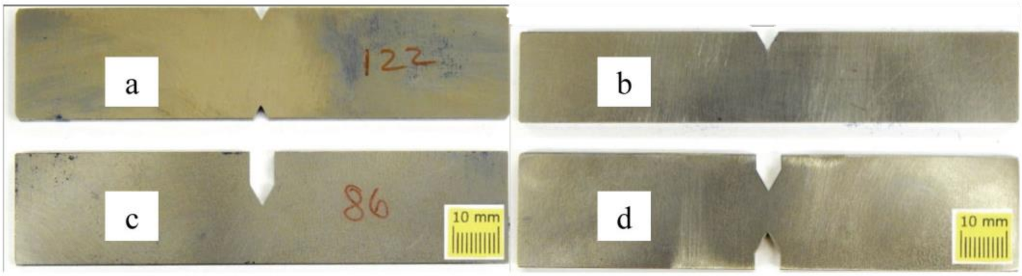

Figure 5-6 - Examples of various geometries investigated: (a) DENT, (b) TPB specimen for cracks, (c) TPB notched specimen, (d) DENT with deep notches

The study followed the same procedure as set out in the previous two studies, except extra notch radii were introduced and three-point bending tests were conducted. For the three-point bending tests, guides were used to ensure that the sample stayed vertical during the loading sequence. At selected notch depths only the 0.1 mm notch radius was employed, the reason for this being that the 0.1 mm notch is the most critical notch radius and therefore the K_{Capp} value would be of interest as a comparable value. The notch radii for this study were checked using a template consisting of transparent paper with the various notch radii printed on it. This was used as a medium to categorize the notch radii. This method proved to be effective since it immediately indicated that the radii thought to be 0.25 mm were actually 0.35 mm, and as a result the models were subsequently modelled according to this dimension.

Table 5-7 - Measured variables for Study 3 simulation

Study 3						
Part Number	Group Description	W (mm)	B (mm)	a (mm)	r (mm)	Force (N)
WRCD01-01-48	25x6x0,1	24.98	3.22	5.83	0.1	42085.62
WRCD01-01-49		25	3.24	5.9	0.1	42924.2
WRCD01-01-50		24.98	3.24	5.91	0.1	43150.82
WRCD01-01-51		25	3.22	5.815	0.1	42082.27
WRCD01-01-177		24.9	3.23	5.855	0.1	40202.89
WRCD01-01-178		25.06	3.23	6.08	0.1	39583.34
WRCD01-01-179		25.04	3.23	6.045	0.1	40361.7
WRCD01-01-180		25.05	3.23	6.035	0.1	39002
WRCD01-01-124		25	3.23	5.99	0.1	38808.2
WRCD01-01-125		25.02	3.23	6.02	0.1	37885.79
WRCD01-01-52	25x6x0,6	25	3.22	5.875	0.6	50010.66
WRCD01-01-53		25	3.22	5.855	0.6	50124.8
WRCD01-01-54		24.97	3.22	5.775	0.6	50749.77
WRCD01-01-55		25	3.22	5.84	0.6	48570.28
WRCD01-01-60	25x6x1,8	25	3.22	5.905	1.8	49450.96
WRCD01-01-61		24.96	3.25	5.83	1.8	50113.65
WRCD01-01-62		24.96	3.2	5.8	1.8	49869.6
WRCD01-01-63		24.97	3.23	5.775	1.8	50664.77
WRCD01-01-67	25x6x0,35	24.95	3.22	5.82	0.35	49379.84
WRCD01-01-68		25	3.22	5.94	0.35	48834.84
WRCD01-01-69		24.96	3.2	5.89	0.35	48870.65
WRCD01-01-70	25x3x0,35	25	3.2	2.93	0.35	66689.4
WRCD01-01-71		24.98	3.2	2.98	0.35	65021.09
WRCD01-01-72		24.96	3.22	2.955	0.35	66243.06
WRCD01-01-73	25x1x0,1	24.94	3.22	0.835	0.1	75623.02
WRCD01-01-74		24.98	3.2	0.9	0.1	75079.38
WRCD01-01-75	25x2x0,1	24.98	3.24	2.045	0.1	66305.61
WRCD01-01-76		25	3.24	1.975	0.1	65796.54

Part Number	Group Description	W (mm)	B (mm)	a (mm)	r (mm)	Force (N)
WRCD01-01-77	25x8x0,1	24.92	3.24	7.915	0.1	31718.3
WRCD01-01-78		24.94	3.21	8.025	0.1	32790.95
WRCD01-01-79		24.92	3.24	7.96	0.1	31291.01
WRCD01-01-80	25x8x0,35	25.02	3.24	8.03	0.35	34971.62
WRCD01-01-81		25	3.24	7.99	0.35	35010.17
WRCD01-01-82		24.98	3.24	7.99	0.35	35089.14
WRCD01-01-83	25x8x0,6	25.04	3.24	7.97	0.6	35327.15
WRCD01-01-84		24.94	3.24	7.95	0.6	35410.71
WRCD01-01-87	25x5x0,1	25.1	3.24	4.995	0.1	46347.32
WRCD01-01-88		25.05	3.24	5	0.1	46082.5
WRCD01-01-173		24.88	3.24	4.965	0.1	43322.36
WRCD01-01-174		25.04	3.22	4.775	0.1	44895.91
WRCD01-01-89	25x5x0,35	25.11	3.24	4.985	0.35	54677.98
WRCD01-01-90		25.09	3.24	4.905	0.35	55271.15
WRCD01-01-175		24.96	3.24	4.91	0.35	53925.99
WRCD01-01-176		24.92	3.24	4.795	0.35	54458.45
WRCD01-01-91	25x5x0,6	25.19	3.24	4.86	0.6	55473.54
WRCD01-01-92		25.18	3.24	4.94	0.6	54692.29
WRCD01-01-93	17x3,5x0,1	17.04	3.24	3.44	0.1	35101.38
WRCD01-01-94		17.08	3.24	3.385	0.1	35139.79
WRCD01-01-95	17x2,5x0,1	17.1	3.24	2.485	0.1	38103.04
WRCD01-01-96		17.09	3.24	2.45	0.1	41067.7
WRCD01-01-97	17x2,5x0,35	17.07	3.24	2.375	0.35	44565.82
WRCD01-01-98		17.1	3.24	2.395	0.35	44072.2
WRCD01-01-99	17x3,5x0,35	17.08	3.24	3.47	0.35	38147.65
WRCD01-01-100		17.05	3.24	3.415	0.35	38501.19
WRCD01-01-101	17x3,5x0,6	17.11	3.24	3.415	0.6	38873.74
WRCD01-01-103		17.09	3.24	3.425	0.6	38886.56

Part Number	Group Description	W (mm)	B (mm)	a (mm)	r (mm)	Force (N)
WRCD01-01-102	17x2,5x0,6	17.06	3.24	2.46	0.6	44995.59
WRCD01-01-104		17.06	3.24	2.42	0.6	44988.69
WRCD01-01-110	12x1x0,1	11.82	3.24	0.885	0.1	34867.79
WRCD01-01-111		11.98	3.24	0.99	0.1	35147.85
WRCD01-01-112	12x1x0,35	11.98	3.22	0.97	0.35	35527.97
WRCD01-01-113		11.96	3.24	0.955	0.35	35574.76
WRCD01-01-114	12x1x0,6	11.86	3.22	0.88	0.6	36041.5
WRCD01-01-115		12.02	3.2	0.945	0.6	36164.9
WRCD01-01-116	12x2x0,1	11.94	3.22	1.985	0.1	28520.39
WRCD01-01-117		12	3.2	1.975	0.1	29208.9
WRCD01-01-118	12x2x0,35	11.96	3.2	1.955	0.35	30144.41
WRCD01-01-119		12	3.2	1.92	0.35	30437.16
WRCD01-01-120	12x2x0,6	11.98	3.2	1.895	0.6	30761.97
WRCD01-01-121		12	3.22	1.88	0.6	30823.02
WRCD01-01-122	25x3x0,1 A	25	3.23	2.995	0.1	54433.82
WRCD01-01-123		25.01	3.23	3.035	0.1	55488.67
WRCD01-01-130	12x3x0,1	12.1	3.24	2.94	0.1	23590.59
WRCD01-01-131		12.05	3.23	2.905	0.1	23482
WRCD01-01-132	14x3x0,1	14.01	3.23	2.975	0.1	29154.71
WRCD01-01-133		14.01	3.22	2.965	0.1	29285.9
WRCD01-01-134	9x1.5x0,1	8.99	3.23	1.43	0.1	22535.31
WRCD01-01-135		8.76	3.24	1.445	0.1	22542.49
WRCD01-01-136	14x1x0,1	14.01	3.23	0.975	0.1	40890.5
WRCD01-01-137		14.05	3.23	0.915	0.1	41032.12
WRCD01-01-138	12x3,7x0,1	12.04	3.23	3.71	0.1	18524.01
WRCD01-01-139		12	3.23	3.69	0.1	18145.04

Part Number	Group Description	W (mm)	B (mm)	a (mm)	r (mm)	Force (N)
WRCD01-01-140	25x10x0,1	25	3.23	10.05	0.1	19553.8
WRCD01-01-141		24.99	3.23	10.04	0.1	19773.71

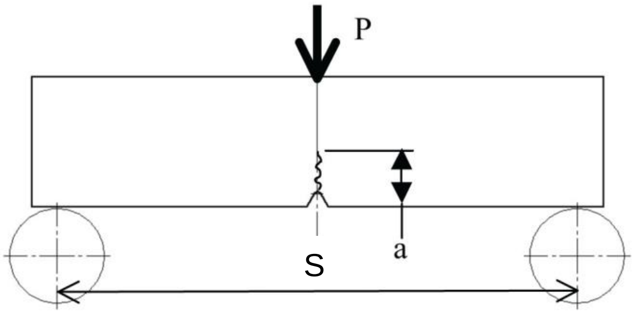

Figure 5-7 - Three-point bending set up

Table 5-8 - Three-point bend sample detail

Study 3 – Three-point bend tests							
Part Number	Group Number	W (mm)	B (mm)	a (mm)	r (mm)	Force (N)	S (mm)
WRCD01-01-85	25x12x0,1	24,98	3,24	11,88	0,1	-5533	85,00
WRCD01-01-86		24,98	3,24	11,96	0,1	-5537	85,00
WRCD01-01-105	25x12x0,6	24,89	3,24	12,07	0,6	-7831	85,00
WRCD01-01-106		25,01	3,24	11,96	0,6	-7960	85,00
WRCD01-01-142	9x3x0,1	8,96	3,23	3,63	0,1	-1382	75,28
WRCD01-01-143		8,96	3,23	3,47	0,1	-1464	75,28
WRCD01-01-144	12x4x0,1	12	3,23	3,92	0,1	-2824	75,28
WRCD01-01-145		12	3,23	3,99	0,1	-2748	75,28
WRCD01-01-146	12x5x0,1	12	3,23	4,91	0,1	-2300	75,28
WRCD01-01-147		11,98	3,23	4,9	0,1	-2295	75,28
WRCD01-01-148	17x5x0,1	16,98	3,23	5,08	0,1	-4680	75,28
WRCD01-01-149		17	3,23	5,01	0,1	-4718	75,28

Table 5-9 – Three-point bend specimen with cracks

Study 3 - Three point bend tests - cracked samples							
Part Number	**Group Number**	**W (mm)**	**B (mm)**	**a (mm)**	**r (mm)**	**Force (N)**	**S (mm)**
WRCD01-01-64	25x12x0,1 bend	24,98	3,24	0	0	No result	85
WRCD01-01-65		24,96	3,23	0	0	No result	85
WRCD01-01-66		25	3,24	12,16	0	-5007	85
WRCD01-01-126	20x10x0,1 bend	19,98	3,24	0	0	No result	85
WRCD01-01-127		19,96	3,22	9,94	0	-3344	85
WRCD01-01-128		19,98	3,24	0	0	No result	85

Table 5-10 - Results of Study 3 for 0.1 mm notches

Double edge notch tensile specimen Study 1									
		Kc							
		Root curve		**0.1(mm)**					
		Intersecting curve		**0.6(mm)**			**0.35(mm)**		
Description	W (mm)	B (mm)	a (mm)	σ_0 (MPa)	L/2 (mm)	K_{Capp} (MPa.m^{0,5})	σ_0 (MPa)	L/2 (mm)	K_{Capp} (MPa.m^{0,5})
25x3	25	3.24	3				4775	0.046	81
25x5	25	3.24	5	3937	0.078	87	5005	0.047	86
25x6	25	3.24	6	4006	0.077	88	5058	0.047	87
25x8	25	3.24	8	3321	0.111	88	4089	0.074	88
17x2,5	17	3.24	2.5	3309	0.090	79	3866	0.066	79
17x3,5	17	3.24	3.5	3277	0.102	83	3968	0.070	83
12x1	12	3.24	1	2393	0.112	63	2763	0.084	63
12x2	12	3.24	2	2704	0.121	75	3224	0.086	75

Table 5-11 - Results of Study 3 for 0.35 mm notches

Double edge notch tensile specimen Study 3									
		Root curve		0,35 (mm)					
		Intersecting curve		1,8 (mm)			0,6 (mm)		
Description	W (mm)	B (mm)	a (mm)	σ_0 (MPa)	L/2 (mm)	K_{Capp} (Mpa.m^{0,5})	σ_0 (MPa)	L/2 (mm)	K_{Capp} (Mpa.m^{0,5})
25x5	25	3,24	5				2589	0,280	109
25x6	25	3,24	6	2115	0,428	110	2885	0,230	110
25x8	25	3,24	8				2553	0,244	100
17x2,5	17	3,24	2,5				2765	0,168	90
17x3,5	17	3,24	3,5				2568	0,218	95
12x1	12	3,24	1				2038	0,186	70
12x2	12	3,24	2				2185	0,226	82

Table 5-12 - Results of Study 3 for 0.6mm notches

Double edge notch tensile specimen Study 3						
		Root curve		0,6 (mm)		
		Intersecting curve		1,8 (mm)		
Description	W	B	a	σ_0 (MPa)	L/2 (mm)	K_{Capp} (Mpa.m^{0,5})
25x6	25	3,24	6	1982	0,52194	114

Table 5-13 - Results of three-point bend tests

Single edge notch three-point bend specimen Study 3							
				Kc			
		Root curve		0,1			Crack
		Intersecting curve		0,6			
Description	W (mm)	B (mm)	a (mm)	σ_0 (MPa)	L/2 (mm)	K_C (MPa.m^{0,5})	K_C (MPa.m^{0,5})
25x12(bend)	25	3,24	12	5659	0,045	95	
25x 12.16	25	3,24	12,16				85
20x9,94	20	3,24	9,94				82

Table 5-10 to Table 5-13 show the results of Study 3. There were a few samples for which only one notch radius was tested. For these cases the stress line plot was used to plot the Kc value ahead of the notch as per Equation 5-1 below.

$$K_c = \sigma_0\sqrt{\pi L} \qquad \textbf{Equation 5-1}$$

This method was found to be quite useful not only in visualising where the various intersecting points were, but it also served as a method to visualise how the stress line plot is expressed in terms of a fracture toughness value.

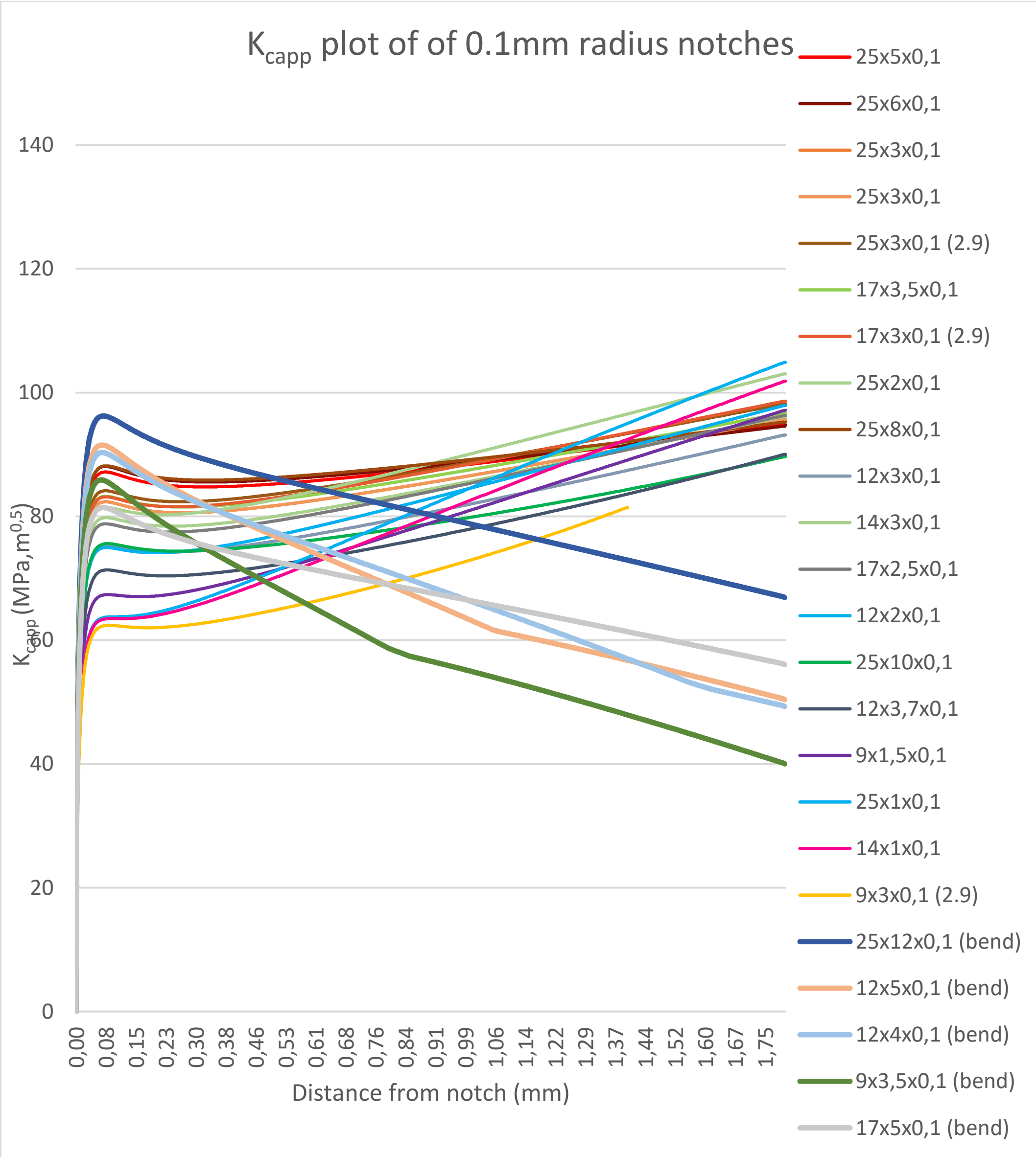

Figure 5-8 - Variation of K_{Capp} of the 0.1 mm notched samples

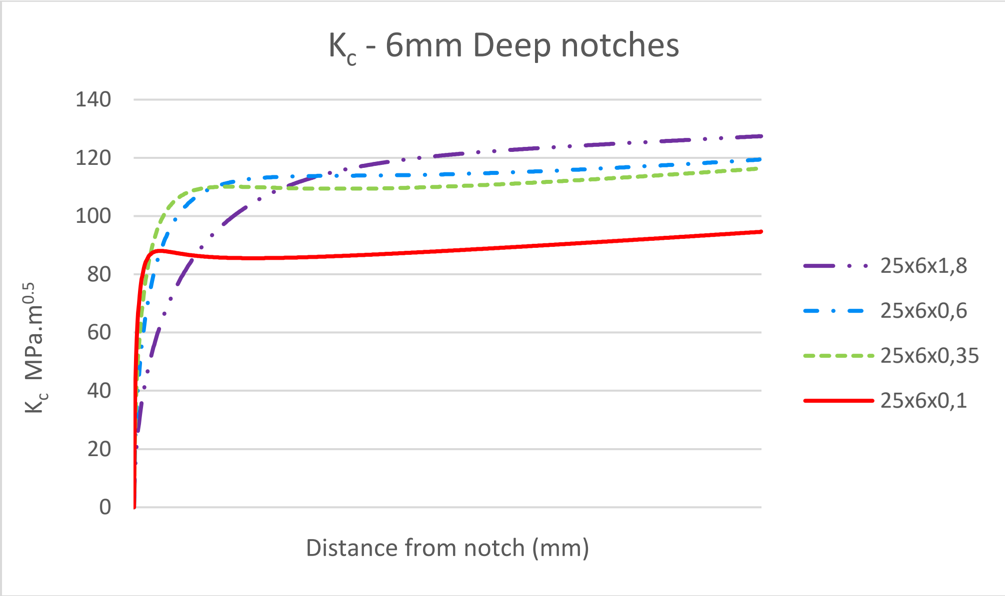

Figure 5-9 - Variation of K_{Capp} for 6 mm deep notches of varying radii

From the graph in Figure 5-8, it is clear that the fracture toughness value does not remain constant. It appears that the samples all have a very steep increase in the K_{Capp} value followed by an area of levelling off (apex of the initial part of the curve) after which there is a period of nearly more or less constant value followed by a gradual increase in the K_{Capp} value (for the DENT samples). In the instance of the SENB samples there will be a gradual decrease in the K_{Capp} values due to the stress gradient induced by bending. In terms of the tensile samples it is clear that the samples which yielded the lower K_{Capp} values (such as the 12 mm wide samples and notches 1 mm deep) all show a very steep rise in K_{Capp} shortly after the initial apex position. At the points where intersection occurs (*"L"* see Table 5-10 to Table 5-13 and Figure 5-9), it can be seen that for the tensile samples, these intersection points generally occur at positions leading up to the second gradual increase in K_{Capp}. For the sharper notches it appears that the intersecting points are in the region of the initial apex of the curve, with the 0.35 mm notches intersecting the 0.1 mm curves just prior to the apex (0.045 – 0.07 mm). This distance also seems to vary slightly and it appears that for the 8 mm deep notches, the intersection seems to shift further away from the notch. The apex of these 0.1 mm curves also show a dependence on the notch geometry. The notches that seem to have a more constant K_{Capp} beyond the initial apex, all seem to have the apex point at a position 0.07 to 0.076 mm ahead of the notch, whereas the notches with a very pronounced increase in K_c after the initial apex seem to be at positions 0.08 mm and further from the notch.

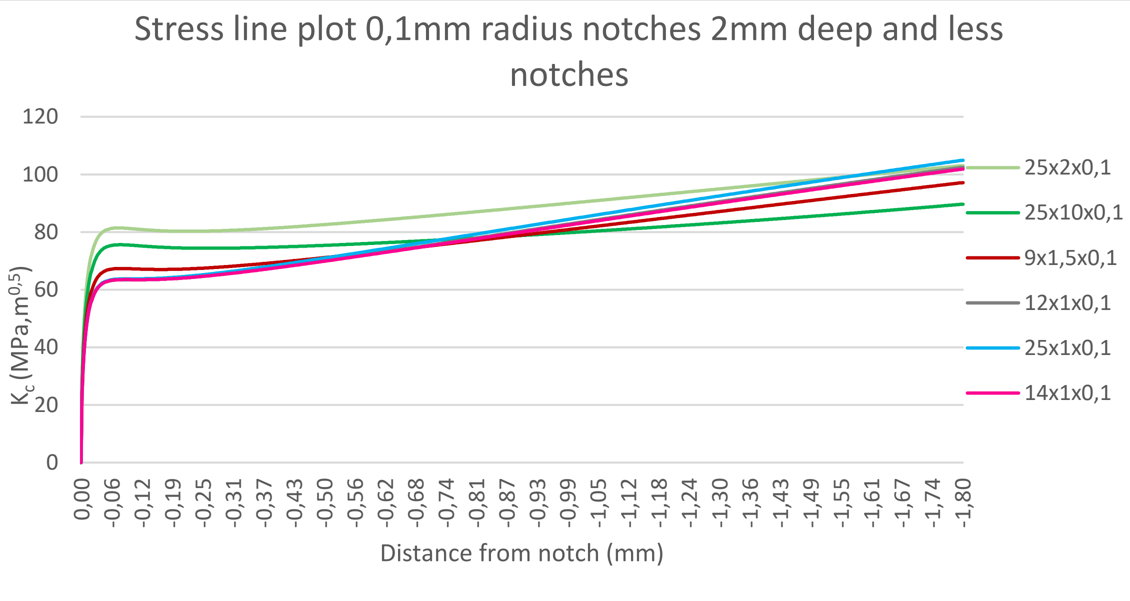

Figure 5-10 - K_{Capp} variation of shallow notches

All the 1 mm deep notches, irrespective of their width (25 x1, 14 x 1 and 12 x 1), seem to yield the same curve (Figure 5-10). The 0.1 mm radius three-point bend samples seem to have apex points coinciding at positions between 0.064 and 0.07 mm.

It is also evident from the data presented that there seems to be a definite decrease in the K_{Capp} value as the sample width decreases. It is most notable for the samples with width of 17 mm and less. It is also notable in the graph in Figure 5-11 that all the curves (barring the curve of the 12 x 3 x 0.1 plot) tend to converge at a position 1.5 mm away from the notch.

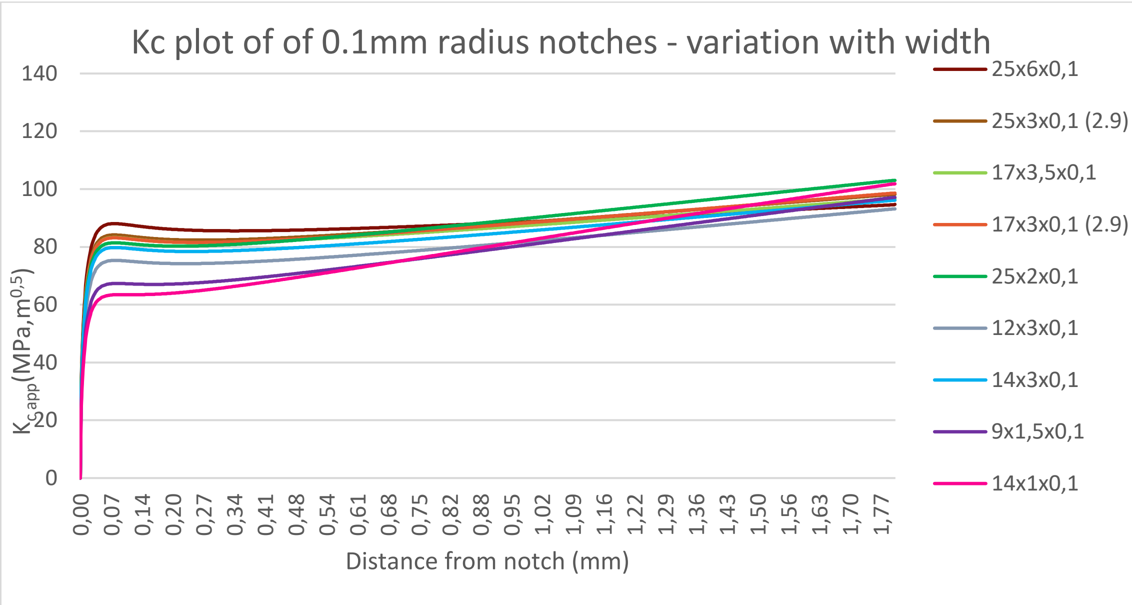

Figure 5-11 - Variation of K_{Capp} with varying sample width

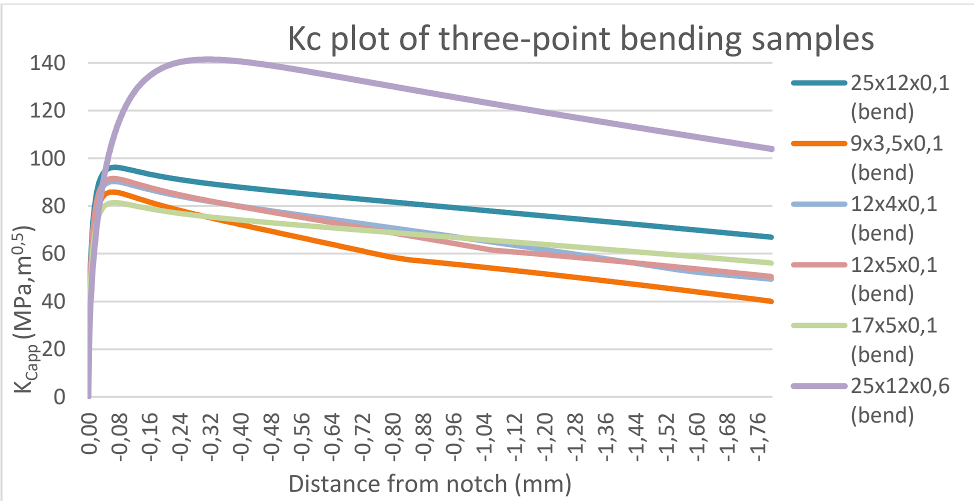

Figure 5-12 – K_{Capp} plots for three-point bend specimen

Figure 5-12 and Figure 5-13 show the K_{Capp} plots for the three-point bend specimen. The apparent fracture toughness values for this type of specimen seem to be both sensitive to specimen width as well as the ratio *a/W*. The fracture toughness of cracked three-point bend samples are shown in Table 5-13. It would appear that the cracked components seem to have a slightly lower apparent fracture toughness value than that of the notched component with similar geometry. This value is very similar to the fracture values obtained when compared to the values obtained the DENT samples using the TCD method. Attempts to grow cracks in DENT samples were made but these samples failed during the crack initiation sequence. The 0.1 mm radius three-point bend test specimen all seem to yield slightly higher values when compared to the values of the 0.1 mm radius, 25mm wide DENT specimens.

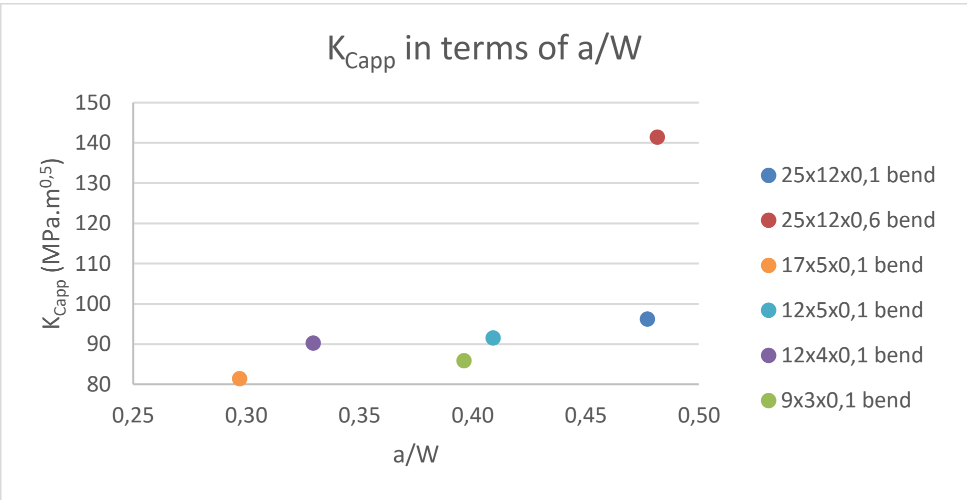

Figure 5-13 - K_{Capp} plots for three-point bend specimen for a/W

A notable variation is the apparent fracture toughness of the 0.6 mm radius specimens tested in bending as compared to the 25mm wide tension specimens (see Figure 5-9 and Figure 5-12). This can be ascribed to plasticity effects.

Figure 5-14 shows the variation of the nominal stress at fracture as a percentage of the UTS of the material. As expected there is a decrease in the nominal stress as the net section decreases. It is noticeable that for notches with radii 0.35 mm and larger, there is no significant change in the nominal fracture stress, whereas the sharper notches had a significant variation in the nominal stress at fracture.

Considering that the apparent fracture toughness of a cracked specimen was measured to be more or less 84 MP.m$^{0.5}$ (Table 5-13) it would appear that the 0.1 mm specimen has become more critical and when comparing the apparent fracture toughness calculated using the TCD method to the toughness value of the cracked sample it would appear that the 0.1 mm notch behaves in a crack like manner.

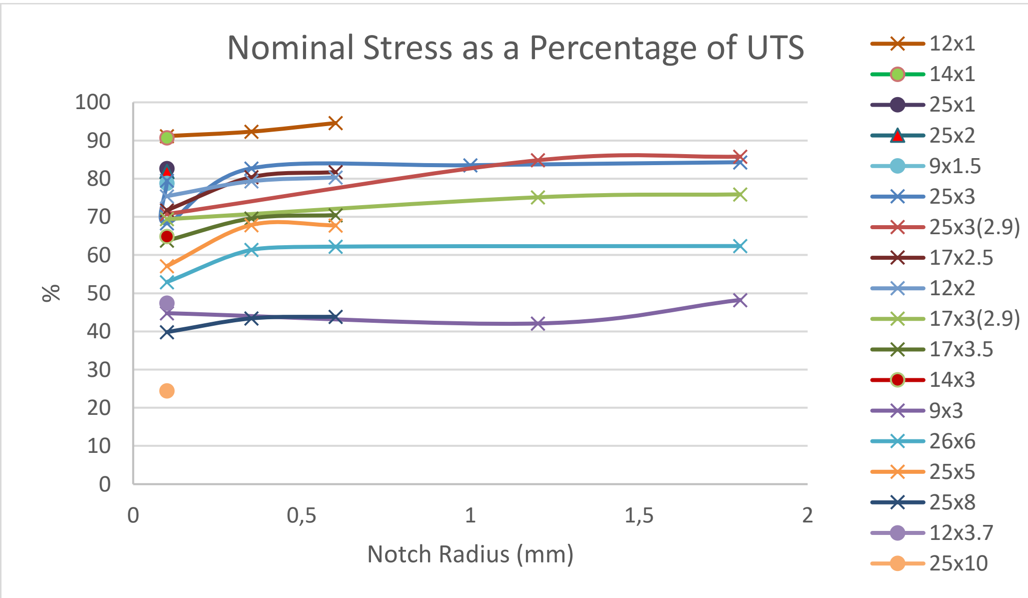

Figure 5-14 - Variation in nominal stress for various geometries

5.6 TCD as a predictive method

Figure 4-9 shows the application of the TCD method as a predictive tool. It compares the fracture toughness values of the material to the predicted values by applying various values of *"L"*. The measured values in the graph were calculated using traditional LEFM methods. To employ this method, it was of interest to compare the K_{Capp} values as calculated using traditional LEFM factors to the K_{Capp} values calculated using values obtained from the FEA studies. The graph in Figure 5-15 compares the K_{capp} values for the 25 mm wide DENT with 0.1 mm notch radius and the results of the SENB samples (varying width) calculated using the data obtained from FEA to those values calculated using the relevant LEFM equations. As the graph in Figure 5-15 indicates, there is slight discrepancy between K_{Capp} values calculated using LEFM methods when compared to the K_{Capp} values determined using FEA. The graph pertains to 25 mm DENT samples with 0.1mm radius notches.

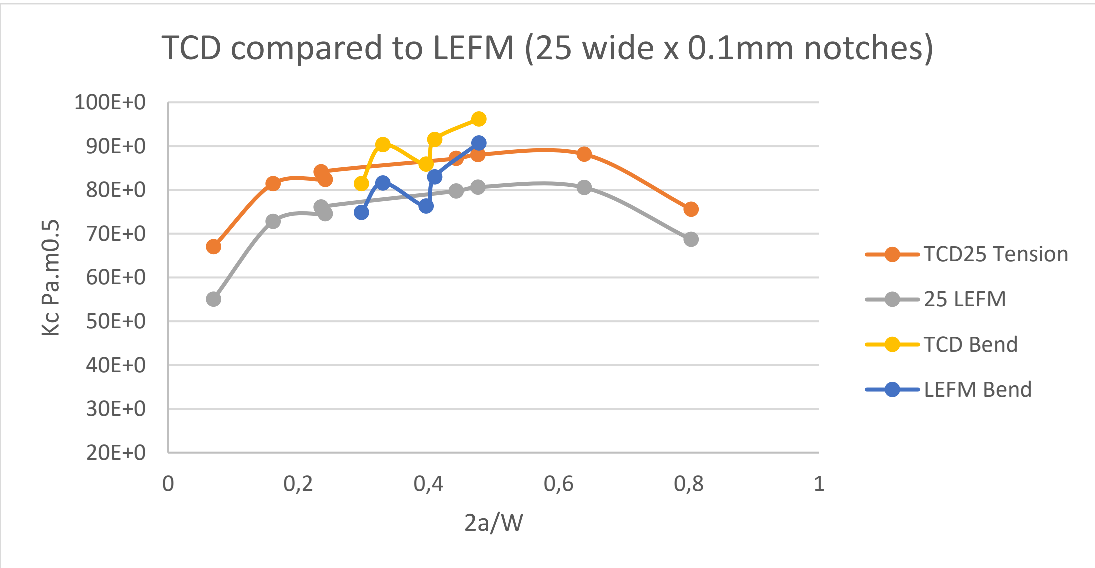

Figure 5-15 - Comparison of fracture toughness values using TCD and LEFM

The variation in the results can be attributed to the size of the plastic zone that develops ahead of the notch compared to the ligament length (the distance between the notch tips). This variation which can be explained using the Fedderson curve will be covered in a subsequent section.

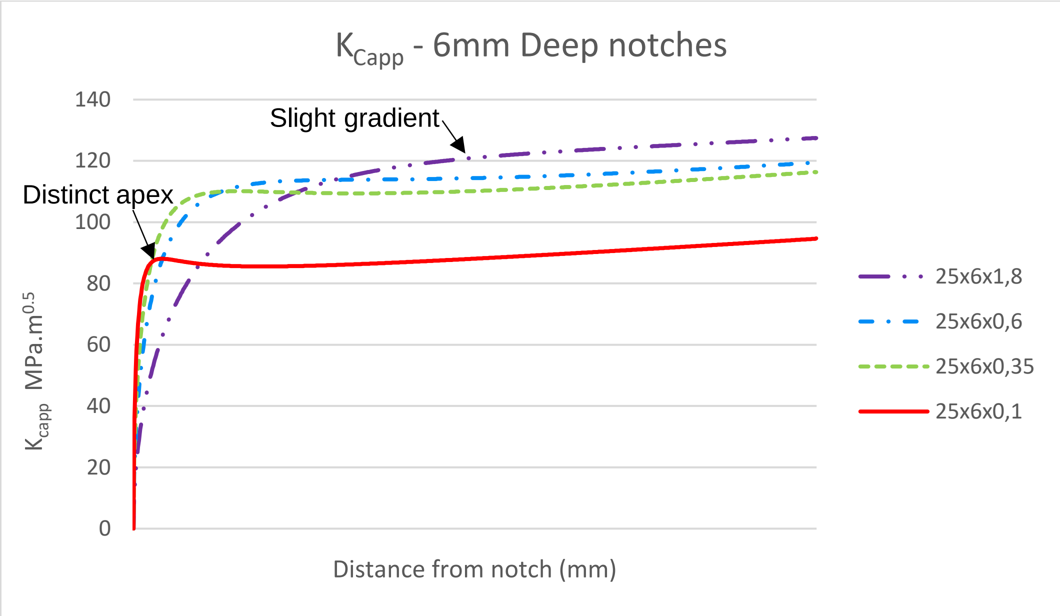

Figure 5-16 - Example of the application of the TCD method to determine K_{Capp} for the various notch types

In order to determine apparent fracture toughness of notches with radii other than 0.1 mm, the K_c value at the apex of each respective notch type was taken as the apparent fracture toughness of the notch. It is notable that for the more critical radii (0.1 and 0.35 mm) there seems to be a distinct apex to the curve (Figure 5-16) whilst for the larger notch sizes there was no distinct apex. In the absence of a distinct apex the fracture toughness was noted from the portion of the graph where the gradient was the least.

The graph in Figure 5-17 shows the application of various critical distances (*L*) using Equation 4-19. The results are indicated as Creager 0.07, 0.1 and 0.2. The fracture toughness used for calculating these graphs was 85 MPa.m$^{0.5}$, which was the average of the K_{Capp} values of the 3 mm, 5 mm and 6 mm deep notches. Since this value corresponds to the value of the 25 x 12 mm cracked sample it could be assumed the 0.1 mm notch started to act in a crack-like manner. It has to be considered, however that, the 0.1 mm notched bend specimen with similar dimensions yielded a K_{Capp} of 96MPa.m$^{0.5}$.

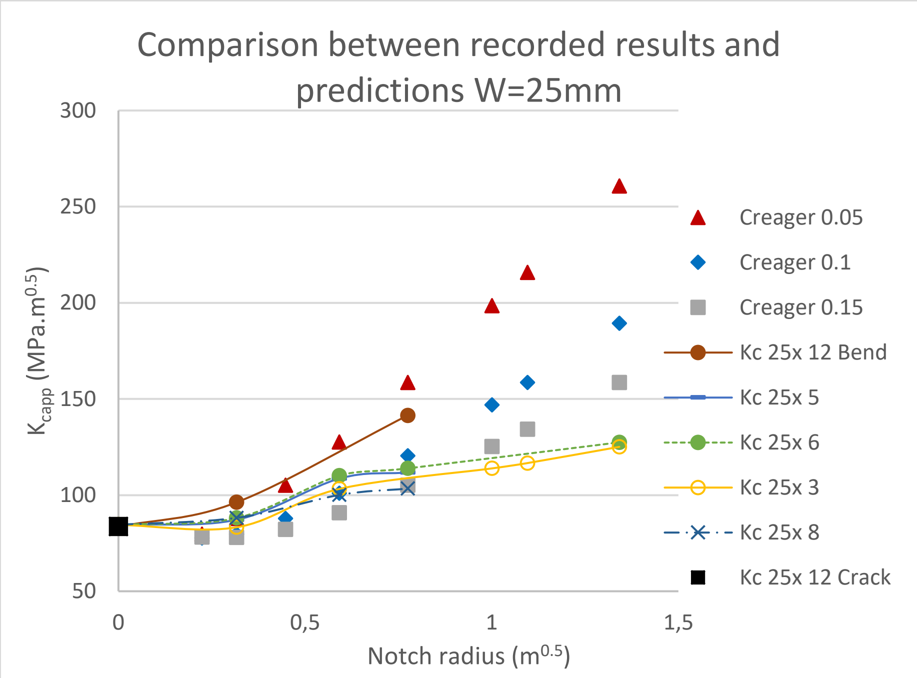

Figure 5-17 - Application of the Point Method to predict apparent fracture toughness (K_{Capp} = 85 MPa.m$^{0.5}$)

It appears that for the sharper notches (0.1, 0.35 and 0.6 mm) the critical distance *L* = 0.1 mm seems to fit the experimental data of the 25 x 3 tensile samples well, whereas for the 25 x 5 and 25 x 6 samples the experimental data seems to fit the predicted curve using *L* = 0.07 mm. This value is smaller than the predicted value of 0.092 as per Table 5-10. For the larger radii there is a significant deviation from the predicted data and this can be ascribed to the plastic zone size ahead of the notch becoming significant when compared to the ligament length. It is noteworthy that in the cases where the prediction matches the experimental data well, a distinct apex can usually be found in the K_c plot of the notch. For example, the 25 x 6 x 0.35 mm sample has a distinct apex in its K_c plot (Figure 5-16) and its data point seems to closely match the prediction of the curve using L = 0.07 mm. The K_c plot of the 0.6 mm notch in the graph of Figure 5-9 (25 x 6 x 0.6 mm samples) shows that it does not have a pronounced apex and in the graph of Figure 5-17 it is notable that the experimental results deviate from the predicted results at a radius of 0.6 mm.

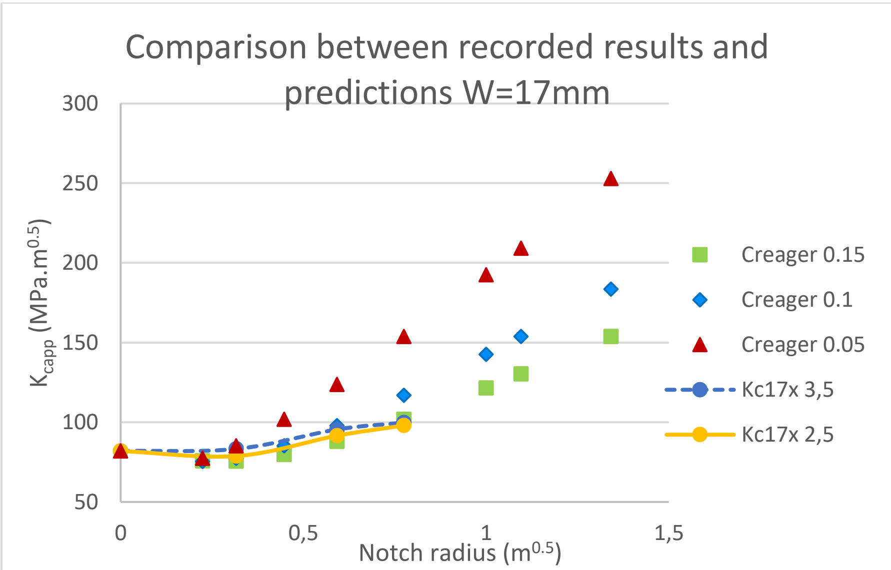

Figure 5-18 - Application of the Point Method to predict apparent fracture toughness (K_{Capp} = 82 MPa.m$^{0.5}$)

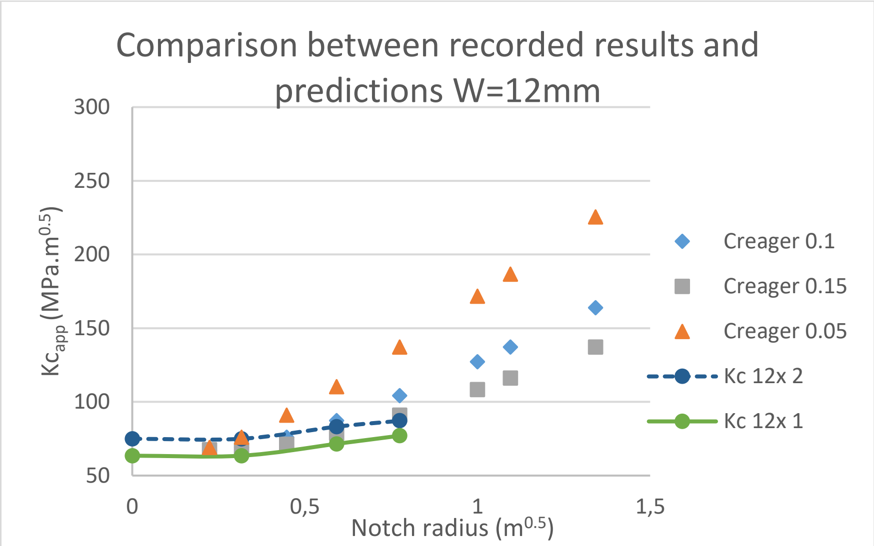

Figure 5-19 - Application of the Point Method to predict apparent fracture toughness (K_{Capp} = 73 MPa.m$^{0.5}$)

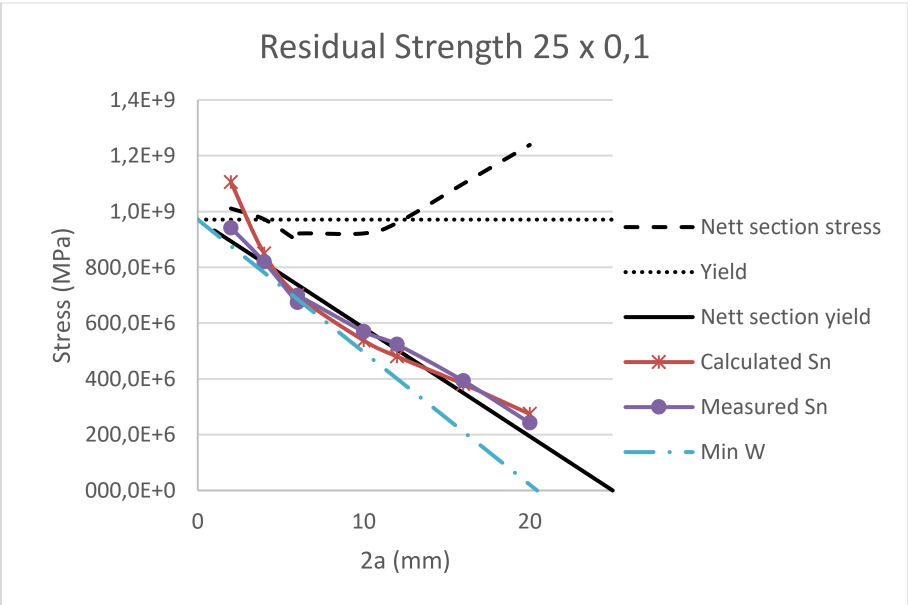

Figure 5-20 – Fedderson curve for W = 25 mm and r = 0.1 mm

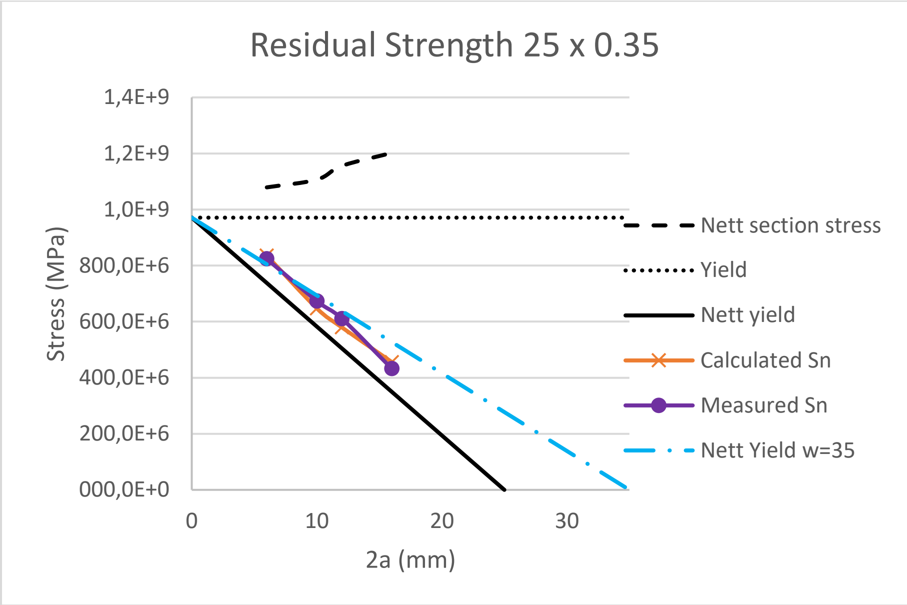

Figure 5-21 - Fedderson curve for W = 25 mm and r = 0.6 mm

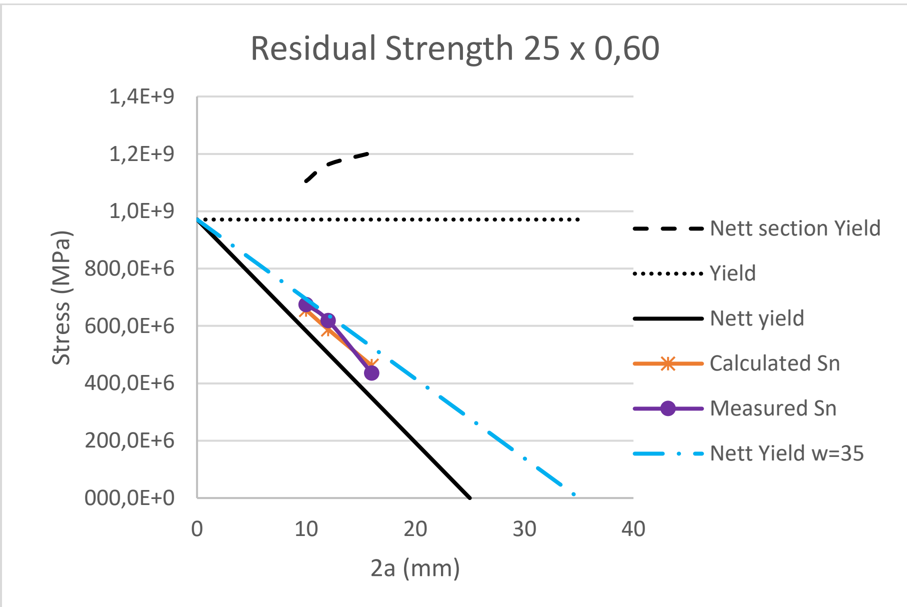

Figure 5-22 - Fedderson curve for W = 25 mm and r = 0.6 mm

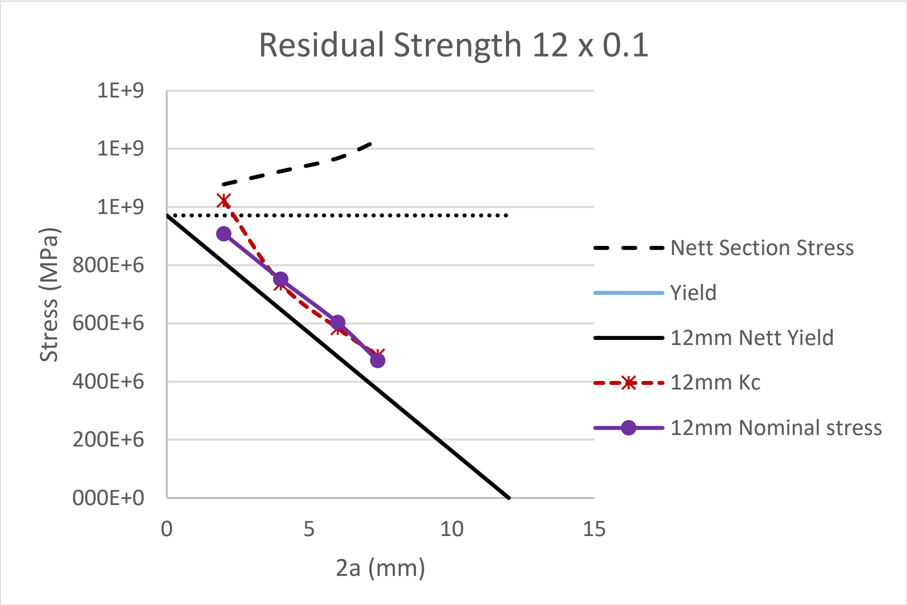

Figure 5-23 - Fedderson curve for W = 12 mm and r = 0.1 mm

Since it appears that net section yielding occurs when using larger notch radii, possible minimum widths for these radii could be predicted using the TCD method. If a critical distance of L= 0.07 mm is assumed (as it predicts the higher toughness value and would therefore require larger sample sizes) it is possible to determine the nominal stresses and plot these on a residual strength curve. For a 25 mm wide sample with a 0.35 mm notch the Kc value is 116.2 MPa.m$^{0.5}$, for a 0.6 mm sample it is 142 MPa.m$^{0.5}$ and for a 1 mm sample it is 175.8 MPa.m$^{0.5}$

The residual strength curves in Figure 5-20 to Figure 5-23 indicate the numerous aspects that could be considered when deciding on possible notch sizes to determine the critical parameters of the TCD method. These curves show the nett section yield line, the measured nominal stress curve and the calculated nominal stress line using the data from the FEA simulations. The graphs also show the yield stress of the material and the actual measured nett section stress.

It is clear from these graphs that other than the 0.1 mm graph, all the other samples exceeded the yield stress of the material in the nett section (the ligament length between the notches) and the measured nominal stress also exceeded the residual strength curve (nett section yield line).

It appears from this data that sample size and notch geometry used should at least allow failure such that the nominal stress does not exceed the nett section yield curve.

5.7 Conclusion

When starting this study little was known about the application of the TCD method to Ti-6Al-4V and in particular its application to thin sheet. It has been applied successfully in the past to mostly brittle materials and applications in which plane strain conditions are prevalent. This study has shown that the method still has limitations due to size effects.

In the study no specific critical length could be determined; however, using the data of the three-point bend (TPB) samples and the DENT samples it would appear that the critical distance is more in the region of 0.07 mm. The predictive curves also suggest that the larger 25 mm wide samples with sharp notches are better suited to determine the critical parameters. The best method is probably three-point bend testing; however, due to the distortion of the plate geometry during welding, three-point bending is not a suitable test method for welded specimen.

Chapter 6

TCD Applied to Friction Stir Welded Sheet

6.1 Introduction

The research completed up to this point was mainly focused on the influence sample size has on the fracture toughness and critical distance of the parent plate. In this chapter, the effect friction stir welding has on the critical distance and the fracture toughness of titanium will be investigated. Other than size effects of the sample, there are numerous material aspects that may contribute to the variation in fracture toughness and critical distance. In this study material aspects relating to the mechanical behaviour, metallurgical variation and residual stresses are investigated. Metallurgical aspects investigated in this study typically include the variation in microstructure of the material, variation in hardness and in terms of fracture, the fractured surface detail.

The methodology of each of the tests is explained and the subsequent results discussed. These results form part of the final discussion in which the fracture behaviour of the material tested is reflected on.

6.2 Friction stir welding set up

6.2.1 Material preparation for welding

Batch B was used for the welding experiment. The material was in the mill annealed state and since the mill anneal treatment is not a well-defined process it was decided to apply a secondary annealing process to the material. This secondary annealing process has the advantage of eliminating any unwanted residual stresses as well as removing excess oxygen if the annealing process is done in a vacuum environment (which is recommended when annealing). The plates were heated to 730 ºC in a vacuum furnace for two hours after which they were allowed to cool to room temperature in a 1 bar nitrogen environment within 20 minutes. The nitrogen reacted with the titanium at the annealing temperature and formed a nitride casing.

Figure 6-1 - Example of heat treated plate after grinding

Tensile samples were extracted from the annealed plate and machined according to the drawing in Figure G1 in Appendix G. The reason for the sub size samples is that the plates were only 120 mm wide. The standard size (according to the ASTM E8M) requires a longer specimen length. The samples were extracted so that the properties along and transverse to the rolling direction could be determined. The sample measurements were recorded as shown in Table G1 in Appendix G. The stresses were calculated according to the smallest measured area. These results are reflected in Table 6-1. It is clear that the material behaved in a very consistent manner both longitudinally along and transverse to the rolling direction. There is also very little difference in the stress values when comparing the two directions with the variation being in the region of 3%. If the value of TCD3_56 is discarded (it failed on the gauge line) the transverse direction performed slightly better with an average of 17% elongation compared to the 15% achieved by the longitudinal samples.

Table 6-1 - Parent plate tensile strength

Part #	Orientation		σ_y (MPa)	σ_u (MPa)	E (GPa)	% Elong.	% A
TCD3_55	Trans		966,4	1015,71	120,96	17,12	33,05
TCD3_56	Trans		966,01	1014,3	116,84	11,04	27,56
TCD3_57	Trans		966,31	1013,93	113,01	17,04	31,96
		Average	966,24	1015	116,94	15,07	30,86
TCD3_58	Long		995,12	1043,17	119,45	16,00	37,88
TCD3_59	Long		993,3	1042,75	122,01	15,20	38,54
TCD3_60	Long		988,42	1040	122,55	15,20	37,24
		Average	992,3	1041,86	121,33	15,47	37,88
		Average	977,4	1026	119,1	15,24	33,87

For friction stir welding purposes the hard nitride layer had to be removed by means of grinding. Literature suggests that the material distortion could be uneven during the annealing process. In an attempt to compensate for this uneven texture fixtures were made for the surface grinder that would clamp along the length on both sides of the plate. It was found, however, even with the added constraints of the fixtures; the removal of material was still uneven. Figure 6-1 shows an example of a plate after heat treatment and grinding. Since the material removal process was uneven, several measurements were taken along the length of the plate in order to establish the minimum thickness of the plate. This was important since it determined the weld tool geometry and plunge depth. The table in Appendix E shows the recorded measurements of the plates used for this experiment.

6.2.2 Platform and process related set up

The friction stir welding was carried out using an MTS I-Stir Process Development System as shown in Figure 6-2. The system is a closed loop controlled system and is fully automated to perform complex operational sequences.

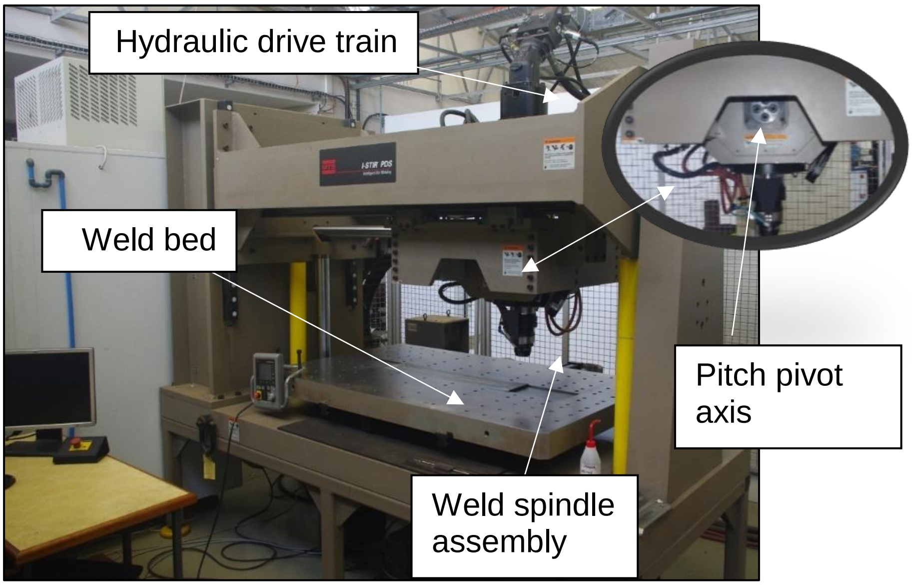

Figure 6-2 - The friction stir welding platform

The unit has 6 axes that can be controlled. There are the three translational axes (x, y, z), a pitch axis (rotation about the y-axis), a hydraulic drive which controls the spindle speed (or required torque) and the translational axis along the spindle axis which controls the retractable pin and forge force (Figure 6-3 and Table 6-2[7]).

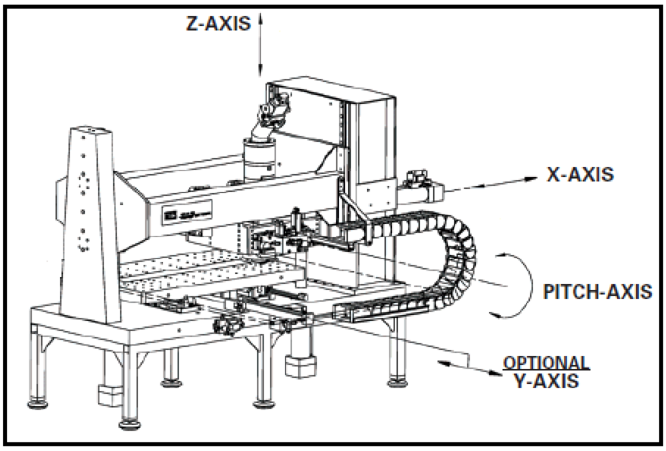

Figure 6-3 - Diagram of the controllable axes of the MTS unit

Table 6-2 - Perfomance specifications of the MTS I-Stir platform

Axis	Stroke	Speed	Force
X	1041 mm	0 to 2000 mm/min	0.88 to 667 kN
Y	1524 mm	0 to 2000 mm/min	0.88 to 36 kN
Z	610 mm	2.5 to 1400 mm/min	133 kN (tension) 22.24 kN (compression)
Tool rotation	Infinite; clockwise and counter-clockwise	200 to 2000 rpm 50 to 800 rpm (with gear reducer)	180 Nm 565Nm (with gear reducer 4:1)
Pitch adjustment	±15^{o}	0.1 to 300 ^{o}/min	0.88 to 66.7 kN
Adjustable pin	±15 mm	2.54 to 1270 mm/min	±89 kN

The unit is capable of high temperature welds since it has a cooling head adapter that can be added whenever required. During welding the weld tool position in relation to the work piece surface can be controlled either by means of position control or force control. Couplings connect the spindle and the weld head assembly and allows adjustment of the runout at the friction tool tip.

The friction stir welding parameters for this study were based on the study by Mashinini[7]. There were two parameter sets that yielded approximately the same performance in terms of fatigue and the one that was deemed the best was selected. The tool rotational speed for all the welds was 500 rpm whilst the feed rate was kept at 120 mm/min and the tilt angle at 1.5˚.

Two materials were used as backing plates (Figure 6-4). The main backing plate was made from EN10025 structural steel. It has a rectangular cut out into which the high temperature backing pate fits. This high temperature backing plate was made from Haynes 230 alloy (nickel-chromium-tungsten-molybdenum) and the reason for it only being an insert into the main backing plate is cost related. The reason for using this alloy is its resistance to oxidation and its ability to retain its strength at high temperatures.

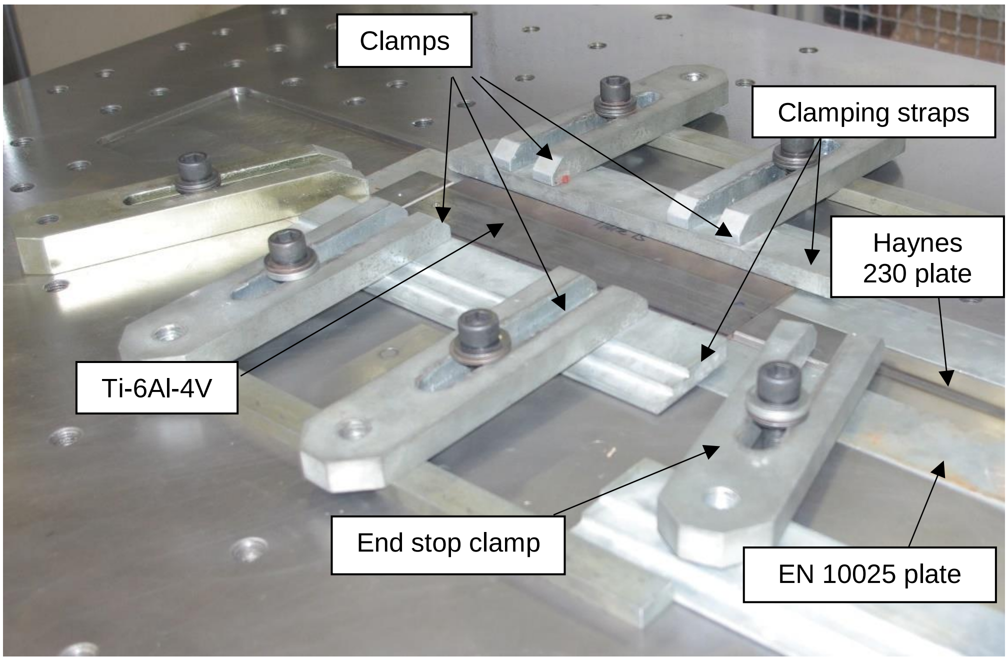

Figure 6-4 - FSW clamping set up

The plate was clamped in using a combination of clamping arms and clamping straps to secure it in place during welding. The end stop clamps were significant in that they helped reduce the risk of the plate slipping along the weld direction during a welding cycle. Side straps would normally be used when two plates are butt welded together to reduce the risk of the plates separating during the welding process. For this study, however, welding was performed on a single plate as a bead on weld and the end clamps also acted to stop any rotation of the plate during welding.

The tool used for this study was made from Lanthanated Tungsten (W-1%La_2O_3). The tool geometry used for all the welds is shown in Figure 6-5 and was achieved by means of turning machining using a CNC lathe. This tool geometry was developed by Mashinini in his study, and it proved to be the geometry that yielded the best performing welds in terms of weld defects and fatigue[7]. In this research study the tool tip length (indicated as 3.05 mm in the sketch) varied due to the variable thickness of the plate and as a result, the tip diameter also varied slightly.

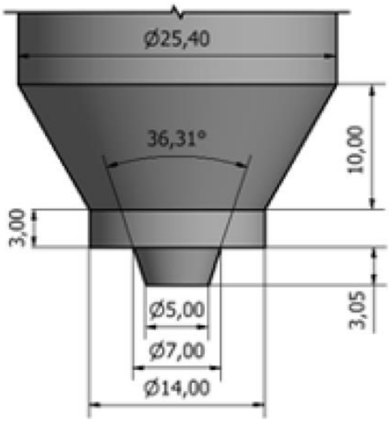

Figure 6-5 - Friction stir welding tool geometry[7]

The variation in tool tip length necessitated a variation in the plunge depth in order to maintain the 0.1 mm ligament length as best as possible. The tip length was determined by the smallest plate thickness measurement. The plunge depth during welding was controlled utilising the machine's position control function. Since the material thickness varied along the plate, the z displacement measurements were made at 10 mm intervals along the weld path. This plot was necessary regardless of the variation in material thickness since it ensured that the slight deflection in the machine bed during welding was also accounted for.

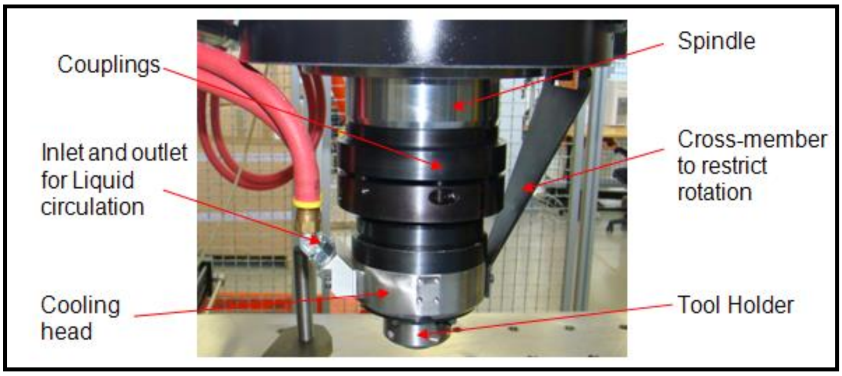

Figure 6-6 - Weld head set up[7]

Figure 6-6 shows the weld head assembly. The spindle and weld head assembly are connected by a coupling system which allows for adjustment for any eccentricity. To adjust the eccentricity, the run out close to the tool tip was measured using a dial indicator as shown in Figure 6-7. The couplings were adjusted until the runout was within 0.05 mm.

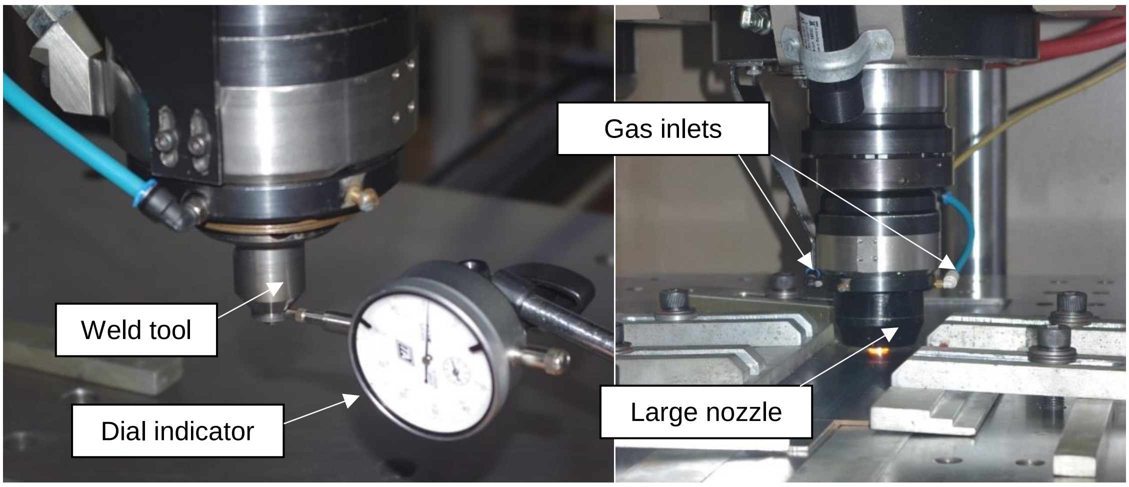

Figure 6-7 - Weld tool set up

In order to prevent the head from overheating, a cooling module was fitted to the assembly for high temperature welding.

After the tool concentricity was corrected the path plot as mentioned above was done. An abrasive pad was used to clean the surface of any unwanted dirt and a final cleaning of the surface was carried out using a paper towel doused with acetone. At this stage the large shielding gas nozzle was fitted so that its opening was approximately 10 mm above the tool shoulder. High purity Argon gas (baseline 5.0) was used as a shielding gas and the flow rate during welding was set to 35 l/min. The gas was opened as the plunging sequence started to ensure that the volume of air surrounding the weld is saturated with the Argon gas.

During plunging, 1000 revolutions per minute at a plunge feed rate of 10 mm/min was used after which a dwell time of 15 seconds was allowed. During the dwell time the spindle speed was ramped down to 500 rpm. The traverse speed was ramped up to the final speed over a period of 45 seconds after the dwell time. For the weld the spindle speed was set to 500 rpm and the feed rate to 120 mm/min.

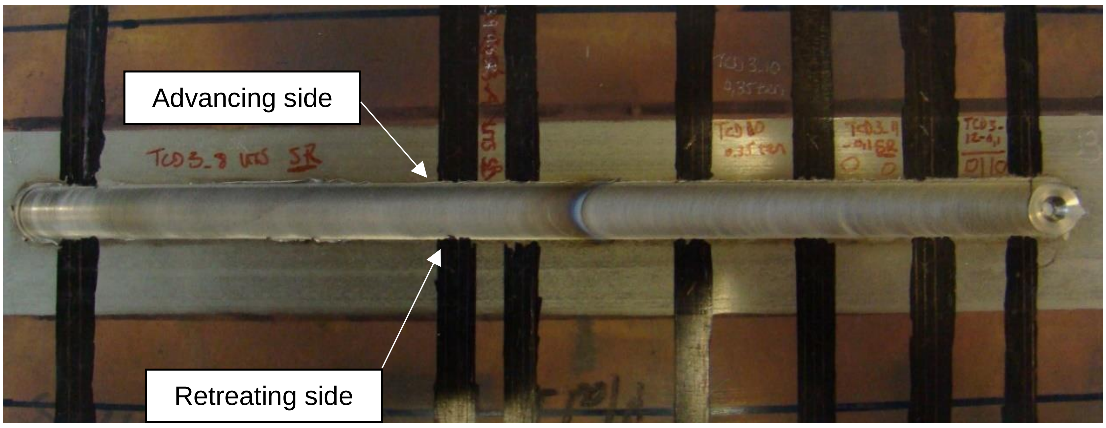

Figure 6-8 - Welded plate

Figure 6-8 show a typical welded plate. The discoloured area on the weld would indicate an area where oxidation occurred and this could be attributed to small droplets of water that would leak from the cooling head and drip onto the work piece from time to time.

6.3 Test sample extraction and orientation

For this experiment the mechanical properties of the welds longitudinal to the weld direction and transverse to the weld direction were to be determined for as welded condition as well as the stress relieved condition. Samples for residual stress measurements also had to be made from the welded plates. Appendix F shows the sample extraction across the welded plates. It can be seen from the drawings in Appendix F that the sample type was distributed in a random manner across the 11 welded plates. The samples were not only distributed in a random manner across the 11 welded plates, but their distribution within each plate was also taken into account, meaning that for a particular type of notch a sample would typically be removed at the start of the weld from one plate, the next sample would be removed more or less from the centre of another plate and the third sample would be removed from the end section of yet another plate.

There are two instances where samples were removed from a particular position in the welded plate. The first was for the tensile samples longitudinal to the weld and the reason for this distribution was to conserve material. The second was for samples used for metallurgical studies and these were removed from an area approximately midway along the welded plate.

The samples were removed from the plates using a band saw prior to any other processing. All fabrication processes were completed prior to stress relief heat treatment. This included sanding down the area ahead of the notch so that the “ratchet” marks of the weld process (left by the rotating tool) would be less prominent (Figure 6-9). By removing the ratchet marks, it was felt that the thickness of the material ahead of the notch could be measured more accurately which would allow for more accurate simulations.

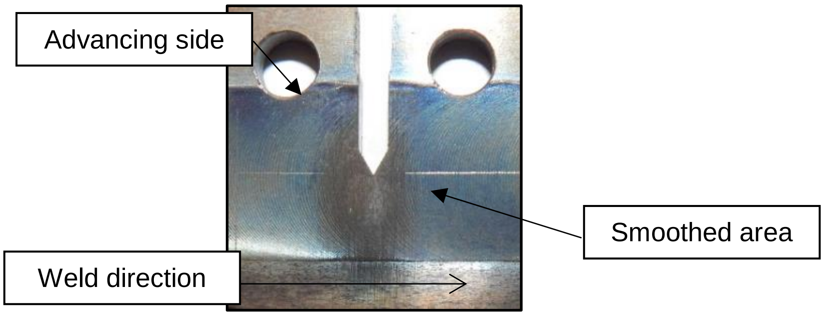

Figure 6-9 - CT sample with notch

Heat treatment was carried out at 590ºC which is the upper threshold for the formation of $TiAl_3$. Lower temperatures require longer times to relieve the stresses sufficiently and also result in the formation of $TiAl_3$. Since the heat treatment was carried out in a plain air furnace, excessively high temperatures would result in oxygen up take and the formation of a layer of titanium oxide. The literature suggests that for temperatures of 600ºC and less the build-up of oxide is minimal[14, 16]. If a vacuum furnace were to be used it would be optimal to use a temperature higher than the solvus range in which $TiAl_3$ is formed. Table 6-3 shows the stress relieving cycle applied to the samples.

Table 6-3 - Stress relief cycle

Cycle	Temp. (˚C)	Time (hours)	Comments
Heating	0-360	3	
Heating	360-590	1,5	
Heating	540-590	1	
Hold	590	1	
Cooling	590-380	1,5	vent open
Cooling	380- 20		crack open door - furnace cool

6.4 Mechanical properties of the welded plate

Sub-size (6 mm wide) tensile samples were made for the determination of the tensile strength of the welds longitudinally and transverse, the drawing of which can be found in Appendix G.

Figure 6-10 - Tensile samples of the welds

Figure 6-10 shows the tensile samples ready for testing. The ratchet marks left by the welding process were removed in the centre of the samples.

For the most part the tensile specimens were tested in accordance to the ASTM E8M-11; however, the extensometer used had a gauge length of 12.5 mm instead of the recommended 25 mm. The reason for the shorter gauge length extensometer is that it can measure directly across the weld zone, thus giving a better idea of how the material in the weld zone behaves. The results must be viewed in context because the extensometer was a single-sided type and any geometrical irregularities of the weld would have an influence on the measured data.

6.4.1 Weld tensile results

Table 6-4 shows the results of the tensile test samples. Some of the problems encountered with this test was that in some instances the failure would occur outside the gauge area and therefore valid elongation results could not be noted. Two specimens (specimens orientated longitudinal to the weld) did not fail because of slipping. This could be ascribed to the variation in thickness across the width of the specimen as a result of the welding process.

The results suggest that the material was strengthened by the stress relieving process but ductility was reduced. The results suggest an increase in the elastic modulus for the stress relieved material. It would be difficult to use the elastic modulus results conclusively in subsequent studies of this project since the measurement would typically include internal flaws and geometrical variations within the weld region.

Table 6-4 - Tensile test results of the weld

Part #	Orientation	Cond.	σ_u (MPa)	E (GPa)	% Elong.	Failure position
TCD3_15	Transverse	AW	981	106,3	9,76	Parent plate inside gauge area
TCD3_18	Transverse	AW	909	100,5	3,44	In weld zone
TCD3_37	Transverse	AW	996	102,2	10,56	Parent plate inside gauge area
		Average	962	103,0	7,92	
TCD3_4	Transverse	SR	1042	135,6	9,92	Parent plate inside gauge area
TCD3_9	Transverse	SR	1019	116,7	5,88	In weld zone
TCD3_23	Transverse	SR	1050	128,6	2,80	In weld zone
		Average	1037	127,0	6,20	
TCD3_17	Longitudinal	AW	999	105,1		Failed outside gauge area
TCD3_35	Longitudinal	AW	984	93,8		Failed outside gauge area
TCD3_40	Longitudinal	AW				Did not fail
		Average	991	99,5		
TCD3_8	Longitudinal	SR	1057	112,2		Failed outside gauge area
TCD3_44	Longitudinal	SR				Did not fail
TCD3_48	Longitudinal	SR	1099	114,2	9,12	Inside gauge clips area
		Average	1078	113,2	9,12	

Three failures occurred within the weld zone of the transverse tests. This could indicate that the flaws within the weld have become significant. These failures suggest a more brittle behaviour since all three showed a reduction in terms of elongation.

6.5 Microstructural analysis

6.5.1 Sample preparation for metallographic studies

Samples for metallographic studies were removed from the welded plates after all the tensile test specimen were removed. The samples were removed either by EDM wire cutting or by band saw. The samples were mounted utilising a combination of epoxy and bakelite. Epoxy was used since it allows for better edge retention during mechanical preparation processes and it adheres better to the mounted specimen. The weld was orientated as shown in Figure 6-11.

Figure 6-11 - Example of the cross section of a welded plate

After mounting the specimen, the samples were prepared using three stages of mechanical grinding and polishing only and one stage utilising a combination of mechanical polishing and chemical attack. The grinding process utilised a P360 grit sand paper and was limited to 40 seconds with the sample not being held in a specific position on the grinding paper for longer than 20 seconds. Grinding was followed by a polishing stage using a 9 µm diamond solution. The rotation speed was 200 rpm and the process for most samples lasted 4 minutes. The subsequent polishing stage utilised a 0.04 µm silica oxide solution (Struers OP-S Non Dry). This stage lasted typically 4 minutes and the rotation speed was limited to 100 rpm. For the final polishing stage, a mixture of the 0.04 µm silica oxide mixed with 2 ml H_2O_2 (30%) and 2 ml NaOH (10%)was used. This stage typically lasted 50 seconds and the polishing plate speed was set to 100 rpm.

Samples for microscopy were etched using Kroll's reagent. The mixture used consisted of 97 ml deionized water, 1 ml HF (40%) and 2 ml HNO_3 (30%) and this reagent was applied onto the sample using a dropper. The etching time was 20 seconds.

6.5.2 Microscopy and hardness testing

SEM work was undertaken on some of the fractured surfaces. The images were taken using magnifications of 40x, 1200x and 5000x. The images were taken in the middle of each sample in a region 0.2mm ahead of the notch.

Microscopy work was done using an Olympus DSX510 microscope. Images were taken of the parent plate after the duplex annealing process, a cross section of the weld of weld plate 12 and of the stress relieved sample TCD3-34. A stitched image of each of the afore-mentioned samples was generated using a magnification of 555x. Since the study focused mainly on the centre region of the weld in terms of fracture toughness, higher resolution images were restricted to this area of the weld. Images at magnifications of 2219x and 4995x were taken at the top, middle and bottom of the welds. Images of the same magnification were also taken of the parent plate approximately in the mid-section of the plate.

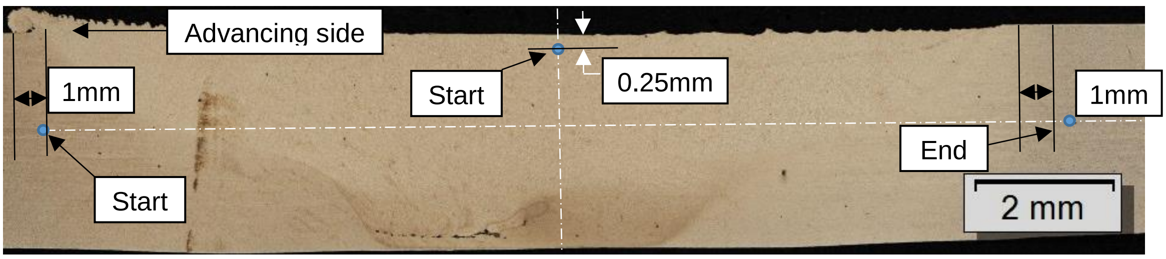

Figure 6-12 - Hardness measurement profile

Hardness measurements were taken using a Future Tech FM-700 micro-hardness testing machine. The calibration record would indicate that an error range of ±10 HV can be expected for the 300g indenter (See Appendix J). Measurements were recorded of the parent plate, welded samples and a stress relieved welded sample. Three welded samples were taken from three welded plates in which a variance in the forge force during welding was noted.

The hardness tests were performed using a 300 g indentation force. Paraffin was used as a lubricating medium to keep the indenter tip clean during measurement. Measurements were performed in the middle of the weld through the thickness of the weld, starting 0.25 mm below the top of the weld down to the bottom of the weld with a 0.25 mm step increment. Measurements were also performed across the weld at the mid-plane of the sample thickness. The measurements were started at 1 mm beyond the advancing side of the weld (therefore staring in the parent plate) and continued across the weld in 0.25 mm step increments to 1 mm beyond the retreating side of the weld. Figure 6-12 depicts the locations of the measurements.

6.5.3 Microscopy and fracture results

Figure 6-13 shows images of the microstructure of the parent plate at various magnifications. These images show the typical structure of mill annealed Ti-6Al-4V, this being an equiaxed microstructure.

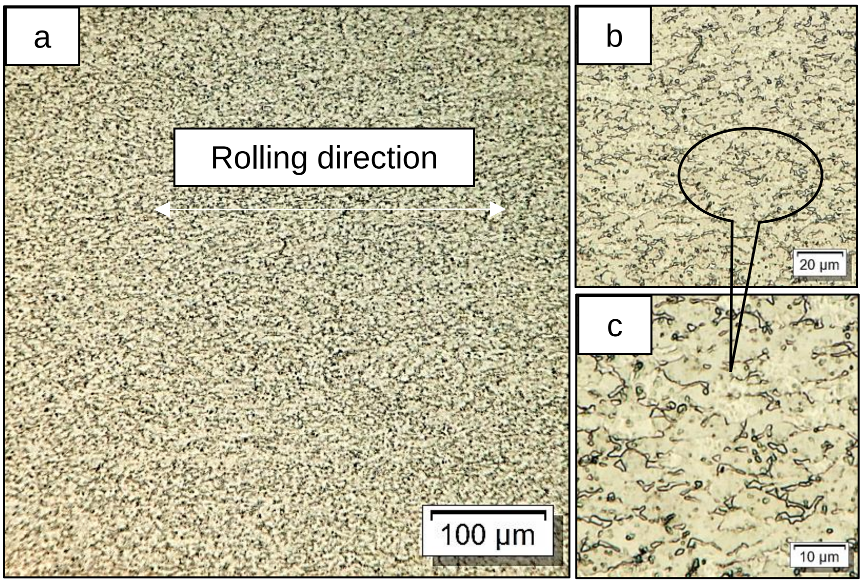

Figure 6-13 - Images of the microstructure of the parent plate (a) 555x (b) 2219x (c) 4995x

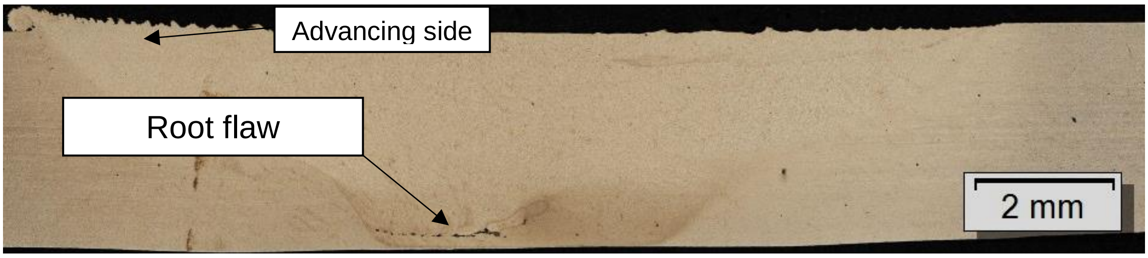

Figure 6-14 - Plate 12 weld cross section 555x

All the welds displayed a root flaw as shown in Figure 6-14 and Figure 6-18. This flaw could be ascribed to two possible causes. As mentioned in section 6.2.1 the material distorted during the heat treatment process. The uneven texture of the material could have caused a lack of contact between the tool shoulder and the weld surface which would cause variation in the heat input and down force. Another possibility could be the tool geometry used. A number of welds were made prior to the welds for this experiment and it was found that the tool wear and therefore some of the geometrical features of the tool depended significantly on the amount of wear during plunging. The final pilot hole used for this study allowed for less wear especially on the edges of the tool tip; however, a slight step was noticed on the tool tip after each weld.

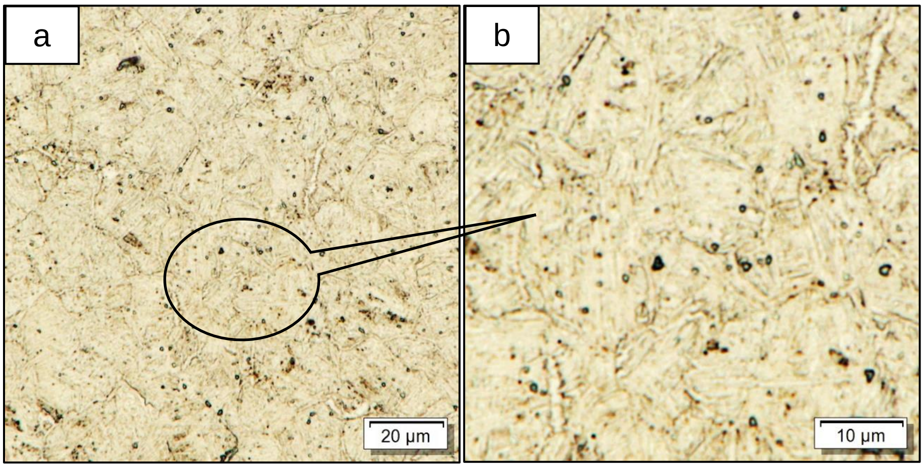

Figure 6-15 - Plate 12 weld - Down the centre of the weld at midpoint of the plate thickness (a) 2219x (b) 4995x

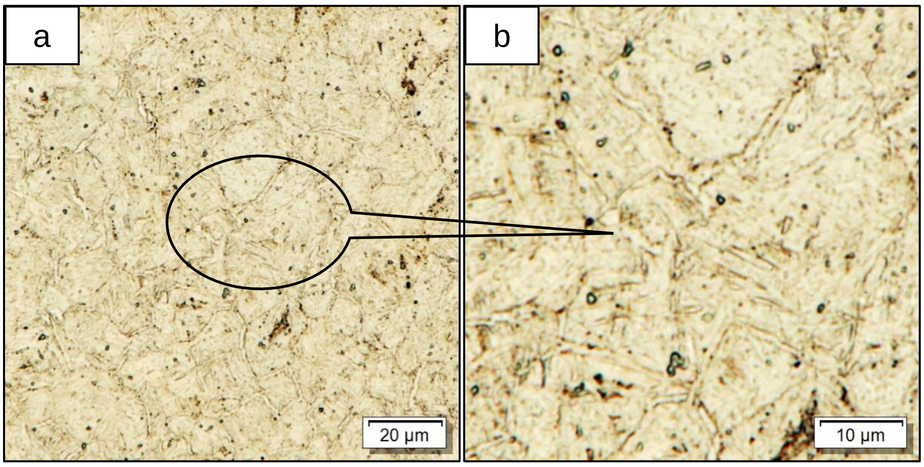

Figure 6-16 - Plate 12 weld - Microstructural images of the middle top region of the weld (a) 2219x (b) 4995x

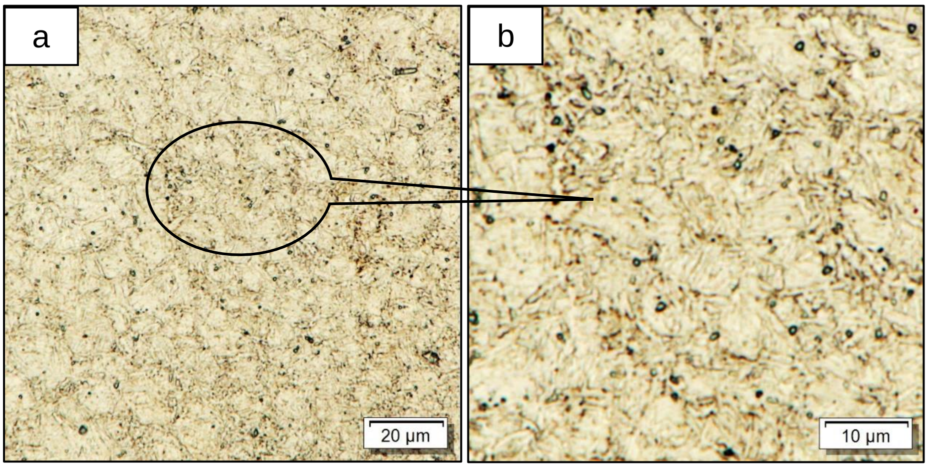

Figure 6-17 - Plate 12 weld - Microstructural images of the middle bottom region of the weld (a) 2219x (b) 4995x

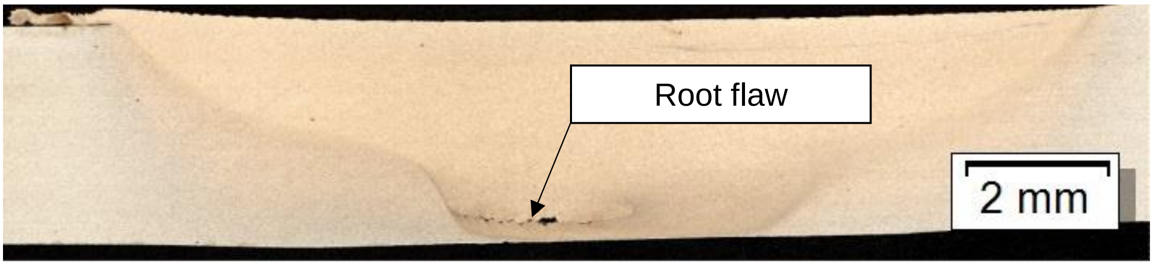

Figure 6-18 - TCD3-34 weld cross section 555x

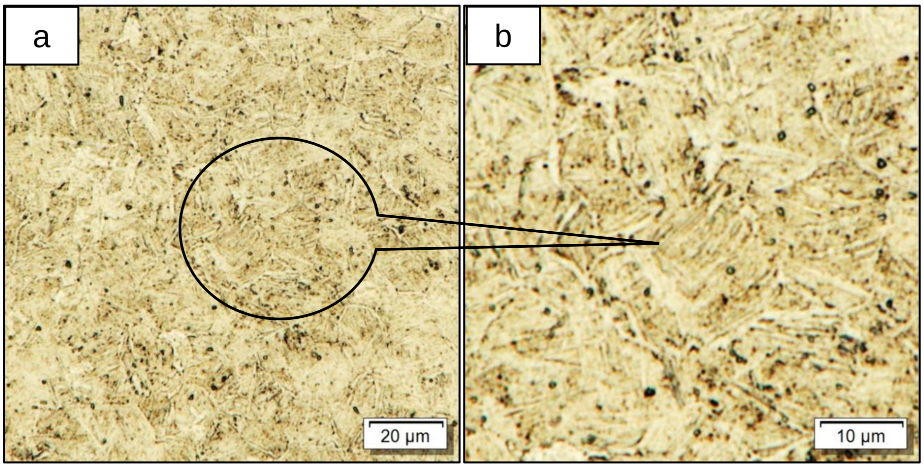

Figure 6-19 - TCD3-34 (weld 17) - Down the centre of of the weld at midpoint of the plate thickness (a) 2219x (b) 4995x

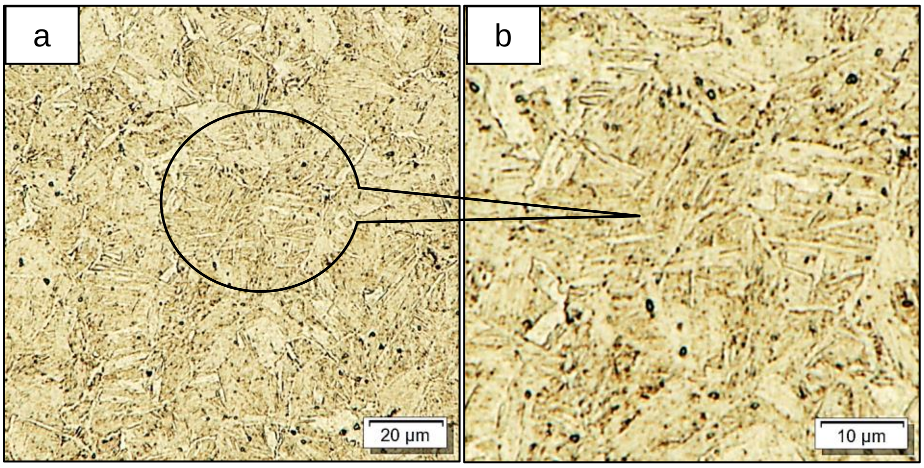

Figure 6-20 - TCD3-34 (weld 17) - Microstructural images of the middle top region of the weld (a) 2219x (b) 4995x

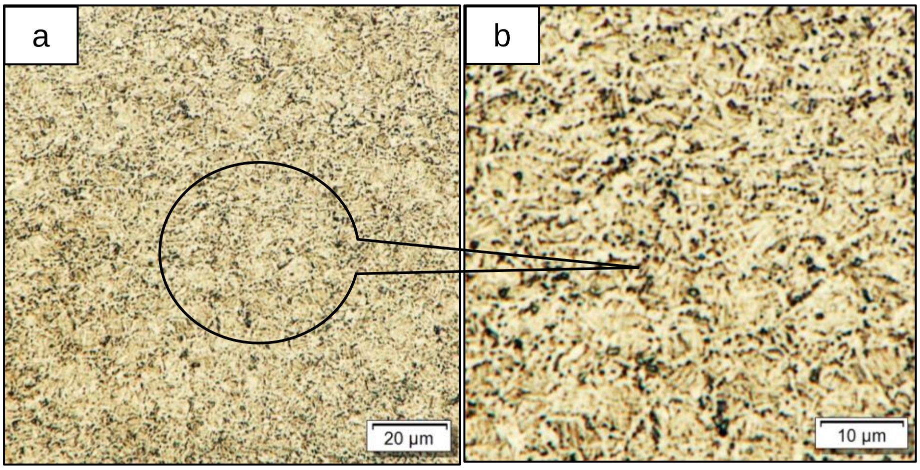

Figure 6-21 - TCD3-34 (weld 17) - Microstructural images of the middle bottom region of the weld (a) 2219x (b) 4995x

Figure 6-22 to Figure 6-27 show the fracture surfaces of the various samples. The numbers in the figures are reference of the sample number of the test specimen.

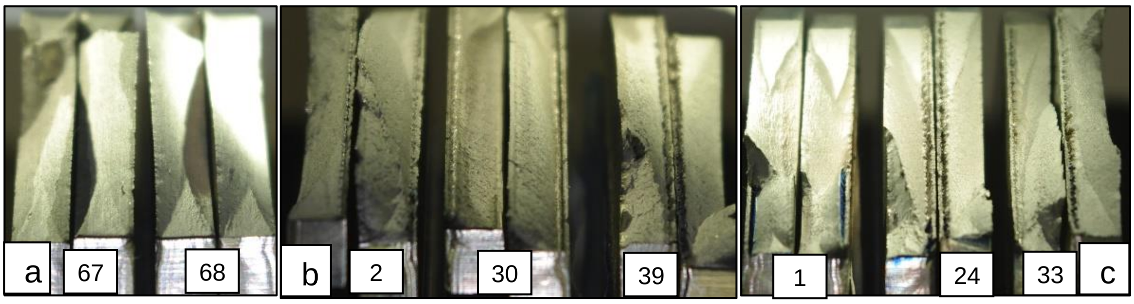

Figure 6-22 - Fracture surfaces of 0.1 mm notches (notches longitudinal to weld) (a) parent plate (b) as welded (c) stress relieved

For the 0.1 mm and 0.35 mm notches, a small flat region immediately ahead of the notch tip is present followed by a slanted shear face which constitutes most of the fracture surface. The fracture line across the width of the samples is mostly linear and perpendicular to the fracture load. The small flat fracture surface ahead of the notch tip indicates that a degree of plane strain fracture mode was involved during fracture.

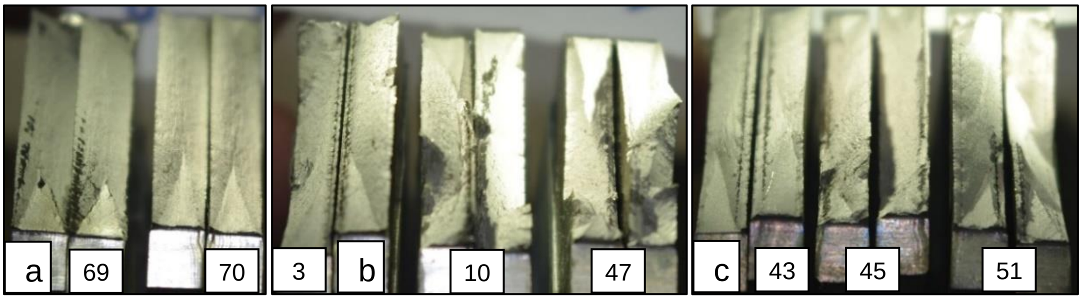

Figure 6-23 - Fracture surfaces of 0.35 mm notches (notches longitudinal to weld) (a) parent plate (b) as welded (c) stress relieved

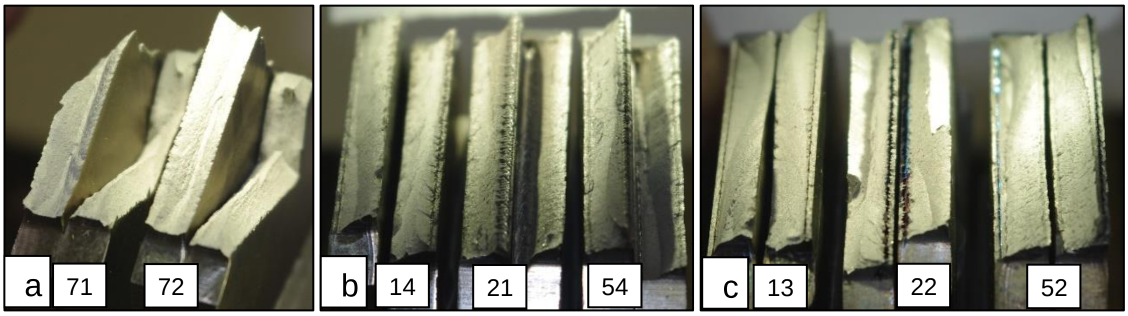

Figure 6-24- Fracture surfaces of 1 mm notches (notches longitudinal to weld) (a) parent plate (b) as welded (c) stress relieved

On the parent plate samples with the 1 mm radius notches, a small flat region (immediately ahead of the crack tip) flanked by the slanted shear lips can be observed. The fracture line across the sample width is also slanted in relation to the fracture load. The welded samples with the same size notch radius, however, all show a slanted shear face extending from the notch tips. The fracture line for these samples is perpendicular to the fracture load line. These failures suggest that plane stress was dominant across the entire width of the samples. All the samples with their notches longitudinal to the weld showed evidence of the presence of the root flaw.

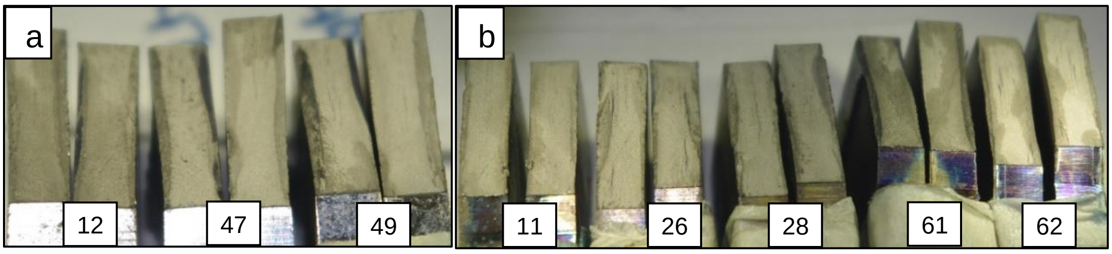

Figure 6-25- Fracture surfaces of 0.05 mm notches (notches transverse to weld) (a) as welded (b) stress relieved

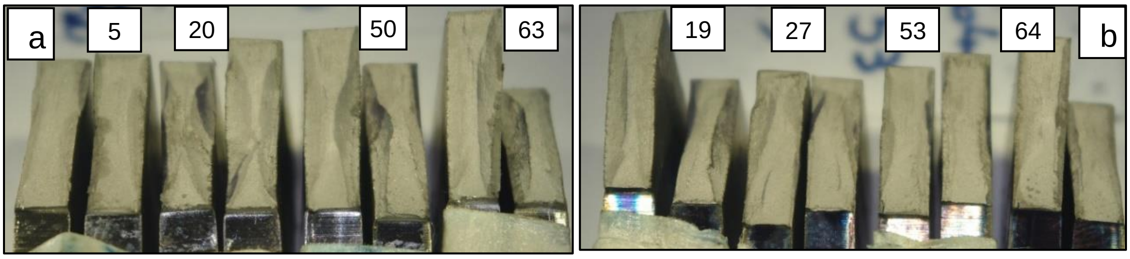

Figure 6-26- Fracture surfaces of 0.3 mm notches (notches transverse to weld) (a) as welded (b) stress relieved

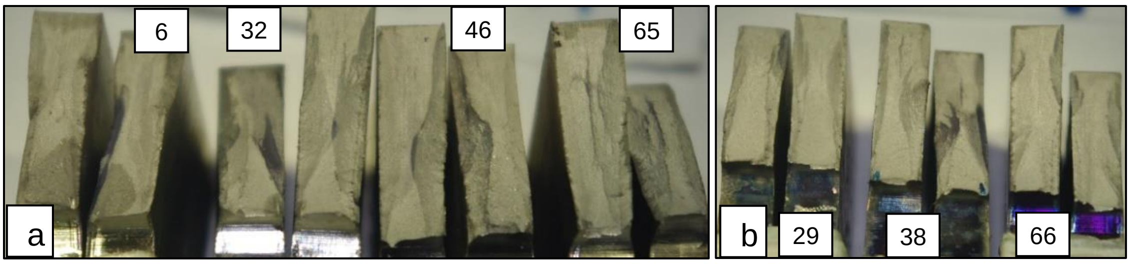

Figure 6-27 - Fracture surfaces of 1 mm notches (notches transverse to weld) (a) as welded (b) stress relieved

Figures 6-25 to 6-27 show the fracture surfaces of the samples with notches perpendicular to the weld. For these samples the shear lips appear to become more prominent as the notch radius increases. In the case of the 0.05 mm notches in the as welded condition, the shear lips seem to be slightly more prominent when compared to the 0.05 mm notch radius samples which had been stress relieved heat treated. The flat region ahead of the notch was present for all the radii of this loading type indicating that plane strain conditions were present during failure of these samples.

The graphs in Figures I-1 to I-8 in Appendix I show the fracture forces of the various samples. For a specific notch radius, the samples with the larger shear lips tend to have fractured at higher forces when compared to the forces of other samples with the same notch radius.

The images in Figures 6-28 to 6-31 were generated using a SEM facility. High resolution images of the fracture surfaces of the various notch radii were observed as well as lower resolution images. The images shown were chosen since they convey some pertinent detail.

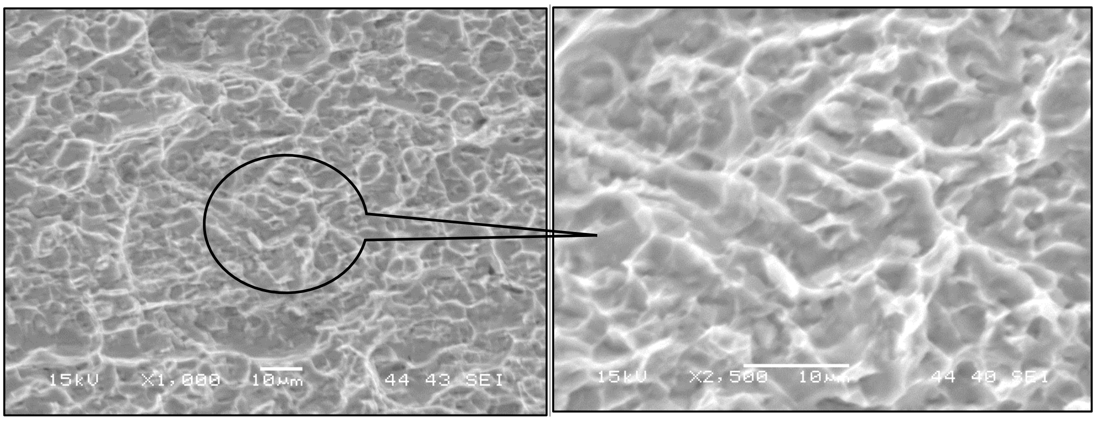

Figure 6-28 - SEM images of the fractured surface of TCD3-68 (parent plate)

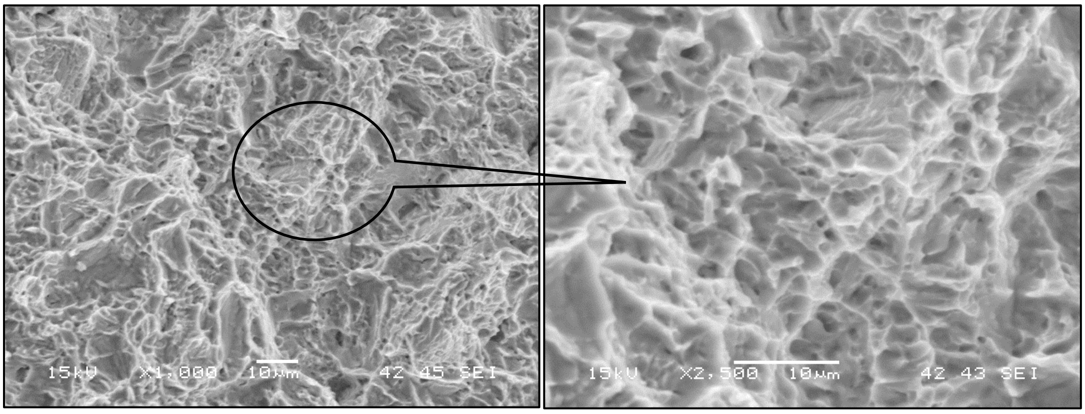

Figure 6-29 - SEM images of the fractured surface of TCD3-47 (as welded 0.05 mm notch transverse to notch)

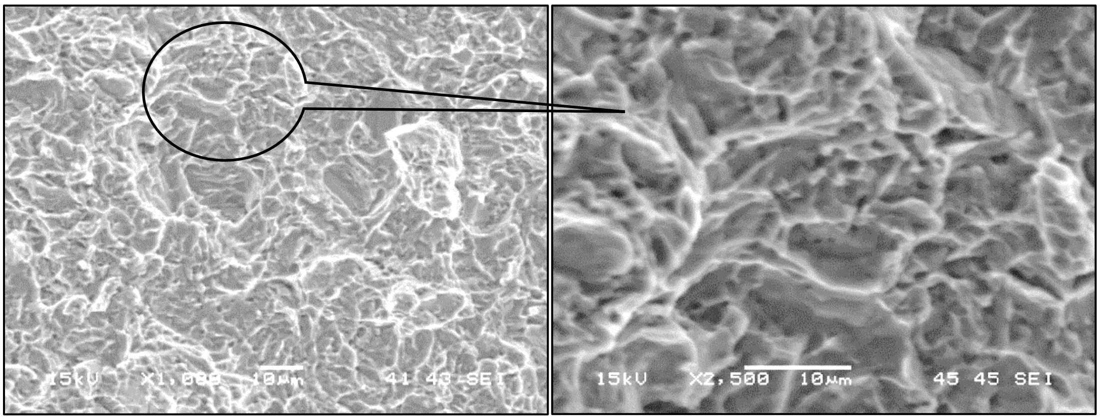

Figure 6-30 - SEM images of the fractured surface of TCD3-11 (stress relieved 0.05 mm notch transverse to notch)

The high resolution images shown in Figures 6-28 to 6-30 are that of the fracture surfaces of the parent plate (DENT with 0.1 mm notch radius) and of the as welded and stress relieved CT specimens with 0.05 mm radius notches.

In all three instances the fracture surfaces exhibit dimples which are typical of a ductile fracture. In the parent plate the dimples are more even in size, whereas for the welded specimen the dimple size tends to vary significantly exhibiting dimples within the larger dimples. There is not a significant difference between the as welded fracture surface (when magnified) when compared to the stress relieved fracture surface; however, the larger dimples of the heat treated specimen seem to have less features when compared to the as welded specimen.

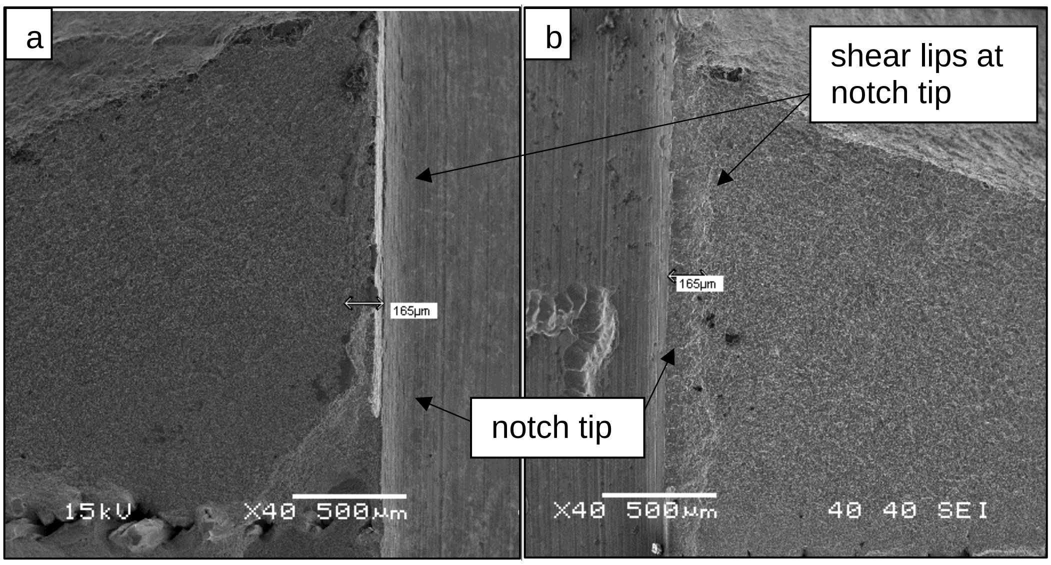

Figure 6-31 - Fracture surface of the 0.35 mm radius notches (a) TCD 3-51 (SR) (b) TCD3-3 (AW)

Figure 6-31 shows low magnification images of the 0.35 mm CT samples. It was noticed that in the instance of radii larger than 0.05 or 0.1 mm, shear lips form at the notch tip. For the 1 mm notches these shear lips were larger than those of the 0.35 mm notches.

6.5.4 Hardness results

Four samples were used for the hardness tests. Three of the samples were tested in the as welded condition and one represented a heat treated sample.

The three as welded samples represented the variation in forge force noted during the welding stage. Plate 13 was welded with a forge force of about 5kN, plate 21 about 4.5kN and plate 23 about 6.5kN. The forge force varied significantly during welding of the plate from which the stress relieved sample was obtained (it started at just over 6kN and ended at approximately 4kN), however, the region from where this sample was removed would have experienced a forge force of about 5kN.

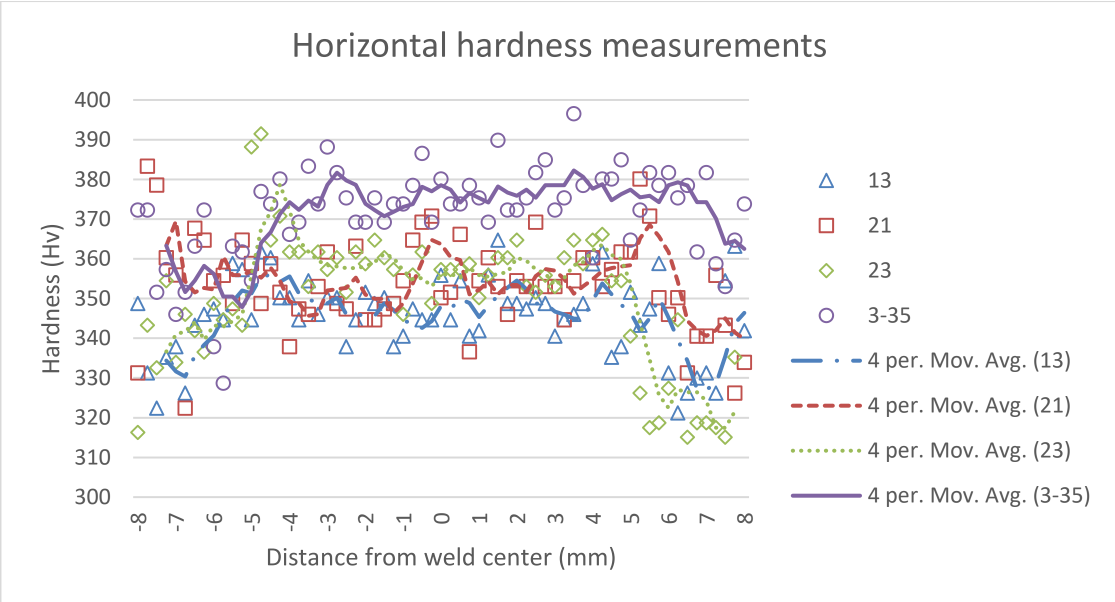

Figure 6-32 - Hardness variation at midplane across the weld

Figure 6-32 shows the hardness measurements. A large scatter in the hardness value was observed for all the specimens, however, some differences among the samples can be noted. All samples showed an increase in hardness when moving from the parent plate to the weld zone. The higher forge force produced a slightly harder weld zone. The stress relieved sample hardened significantly.

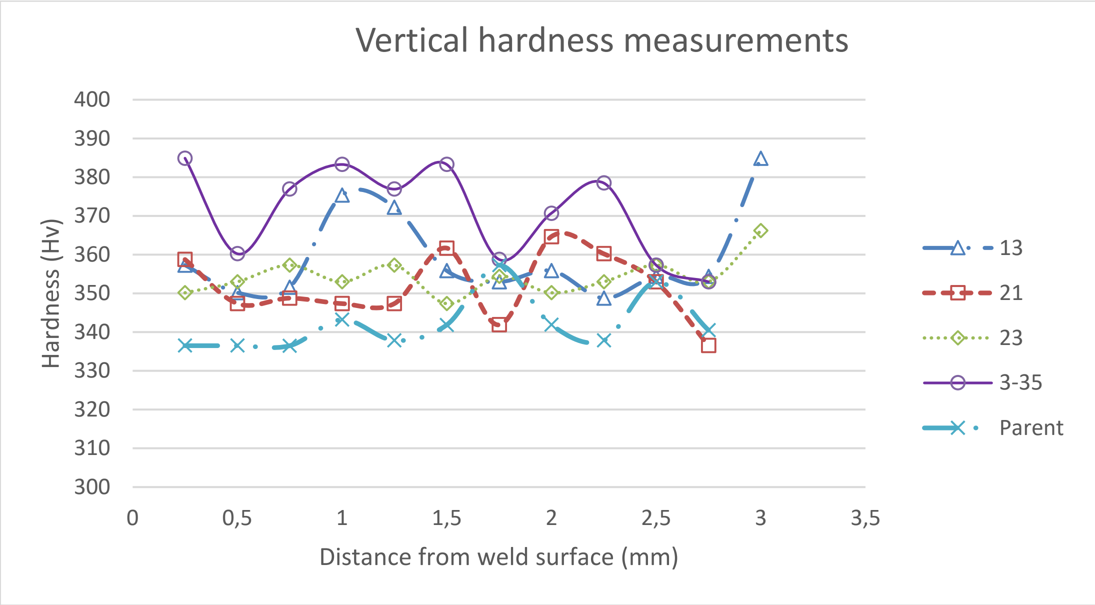

Figure 6-33 - Hardness variation at weld centres across the thickness

Figure 6-33 shows the hardness results in the region of interest for this study. This figure reaffirms the observations made above.

6.6 Residual stress analysis

6.6.1 Residual stress sample preparation

The residual stress samples followed a similar preparation process to that of the tensile and TCD specimens. The sample removal process has a significant effect on the residual stress within the sample coupon and research pertaining to this variation has been published [60].

As shown in the figures in Appendix F, 20 mm wide samples were removed from the welded plates for residual stress measurements. According to the “The Good Practice Guide No. 53”, any boundary adjacent to the hole should be a distance equal to six times the hole diameter away from the centre of the hole whilst the ASTM standard requires the distance to be 1.5 times the pitch circle diameter of the gauge grid[61]. The width is dependent on the hole diameter to be used during the drilling process. According to the ASTM 837 standard the sheet thickness would qualify as a “thick” sample if a 2.57 mm gauge diameter rosette is used. This implies that a 1mm diameter hole should be drilled and that the calculation method would be valid according to the ASTM 837 standard[61]. When drilling a 1 mm hole, a sample with a minimum width of 12 mm should be used.

With residual stresses one has to consider that when preparing the surface for strain gauge application, any mechanical processes used during this process will have an effect on the measured stress. The application of strain gauges requires a certain amount of surface preparation which does alter the stresses in close proximity to the surface. For this study the ratchet features were removed using a mechanical sanding device. After this initial sanding process some samples were heat treated according to the process stipulated in Table 6-3. Once the selected samples were heat treated both the heat treated samples and non-heat treated samples were sanded again using 180 grit sand paper. This final sanding process was used for two reasons. Firstly, the mechanical sanding process induced significant residual stresses. By hand sanding the parts, some of the stresses induced by the mechanical sander are removed. The second reason for manual sanding is that a gentle hand sanding process removes the oxide casing which formed during the stress relief heat treatment process. The stress induced due to the sanding can also be quantified, which helps when reflecting on the results obtained from the non-heat treated samples.

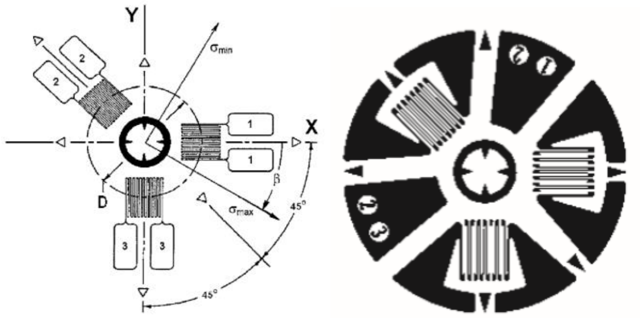

Figure 6-34 – Standard residual stress configuration

The gauges used for this experiment were Vishay Micro-Measurement gauges EA-06-031RE/SE rosette gauges (Figure 6-34 shows the gauge layout[62]). These gauges comply with the ASTM 873 standard in terms of size specifications which makes determining all other size-related issues less complicated.

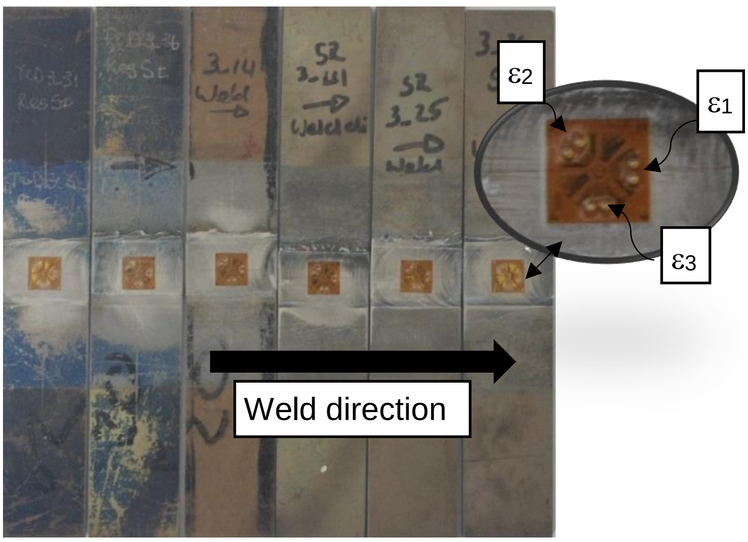

Figure 6-35 - Orientation of the residual stress gauges

Figure 6-35 shows the gauges as applied to the test pieces. All the gauges were orientated so that the measurement line of grid 1 (ε_1) is along the weld direction.

6.6.2 Residual stress testing

Residual stress measurements were performed using the high speed hole drilling technique. This method relies on the relaxation of stresses by means of material removal. These stresses are measured in terms of strain by using strain gauges made for this purpose. This technique is considered to be one of the better methods to determine stress in terms of material removal techniques. It utilises a flat end mill which has a conical shape that tapers slightly from a larger diameter at the end of the end mill to a smaller diameter further away from the end mill end. The shape is significant since it creates a hole with a flat bottom, without any fillets at the edges, whilst the taper prevents material removal from the side wall of the hole. This is significant in terms of the calculation since the formulas were derived by assuming the hole has a very flat surface without any edge fillets. The high speed drilling technique utilises a very high spindle speed with low torque to remove the material and therefore tends to induce very little stress during the cutting process.

There are a few methods which can be used for the calculation of the residual stress when using the hole drilling method[63]. The ASTM 837 adopted two methods which could be used to calculate the stress state in material. If the stresses are expected to be fairly uniform within the material, the uniform stress (stress averaging) method can be used. This method, however, tends to even out stresses that vary significantly across small distances, for example, stresses induced due to machining tends to vary significantly close to the surface of the machined surface and may be marginalised using this calculation technique. The uniform stress method essentially assume the stress stays constant throughout the entire depth of the hole created.

For of stresses varying drastically within the material the ASTM adopted another method to calculate the stress variation as a function of depth. This is essentially the method proposed by Schajer (the integral method)[64, 65].

The ASTM E837 also stipulates that when a component is considered to be a “thin” component, a through hole should be drilled; and if it is a “thick” component a blind hole should be drilled. This differentiation between thick and thin is also dependent on the hole size to be drilled[61]. The sample thickness for this project was approximately 3.1 mm. This thickness presented a slight problem in terms of the selection of an appropriate gauge size. The larger gauge would allow for a larger hole to be drilled and would therefore also allow for determining stress to a greater depth. However, the thickness was such that the maximum size gauge that could be used for this experiment was the smallest available on the market, that being the Micro-Measurements EA-06-031-120 gauge. Using this gauge meant that a hole size with a maximum diameter of 1 mm could be drilled, effectively limiting the determination of stress to a depth of 1 mm for the uniform calculation method or 0.5 mm for the non-uniform calculation method.

It is worth mentioning that the number “06” in the gauge number signifies that the gauge temperature compensation is set for steel parts; however, since the equipment was used in an environment where little temperature change occurs, the compensation factor should not be of any influence on the results.

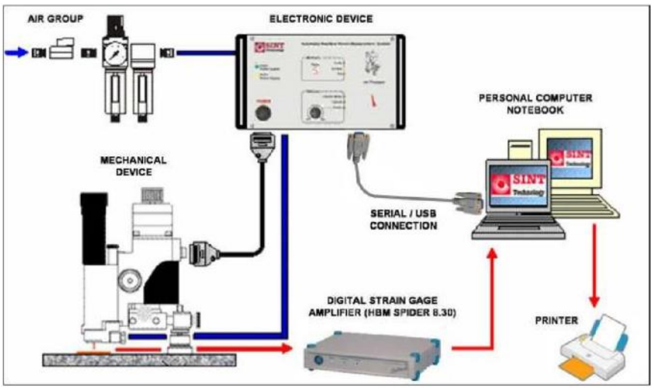

Figure 6-36 - SINT Restan 3000 system[66]

The equipment used for this experiment was the HBM SINT MTS3000 Restan automated drilling system. The hole drilling and data acquisition stages of this unit are automated. The unit is capable of drilling in 1 µm steps, whilst the drilling feed rate can be controlled between 0.03 and 1 mm/min[67]. The system is comprised of the drilling head, the instrument control unit, an HBM Spider 8-30 amplifier and a computer system with the control software. Figure 6-36 shows a diagram of the system layout as presented by SINT whilst Figure 6-37[66] shows some of the key features of the drilling head.

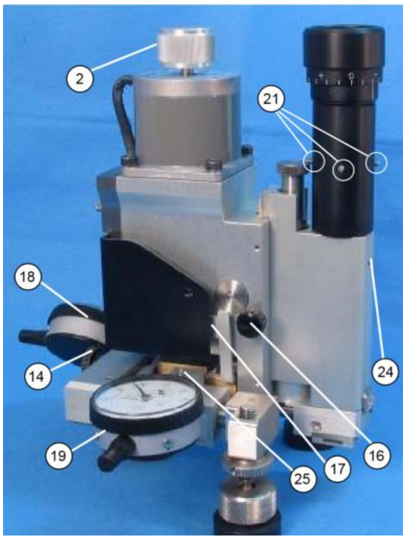

Figure 6-37 - Drilling machine assembly[66]

The control software allows for the setup of the necessary parameters for the drilling process. The drilling step increment for this study was set to 0.05mm, a value specified by the ASTM standard[61]. The software requires the gauge particulars, such as the gauge type and the gauge factors which are found on the gauge packaging (Appendix H). Material specifics, for instance, Young's modulus and Poisson's ratio are also required. A Young's modulus of 119.1GPa and a Poisson's ratio of 0.34 were used for this study. The drilling feed rate was set to 0.2 mm/min.

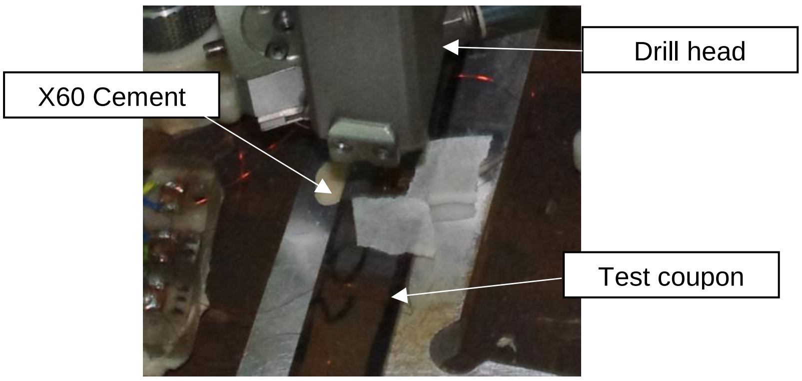

Figure 6-38 - Sample mounted for residual stress testing

The samples were secured to a level surface by means of HBM X60 cement. The cement was initially only used on the one side of the sample as shown in Figure 6-38; however, it was discovered that the drilled holes were much larger than the drill bit diameter. This is indicative of slight movement of the sample during the operation or that the bearings in the drill turbine allowed for too much radial eccentricity. To remedy the problem, the turbine was replaced and the sample was cemented in two positions. As a result of the cement being applied on both sides of the sample, a slight stress was induced on the sample due the setting of the cement. The strain measured in the axial direction along the weld was 11 µm/m.

Once the drilling procedure was completed the final hole size was measured. This measurement is significant since it helps determine the necessary calibration constants for the calculation methods and also allows for corrections if the hole is off centre.

6.6.3 Residual stress results

Using the high speed hole drilling method the relieved strains are recorded. Once the holes have been drilled decisions with regards to which stress calculation to use can be made. If the stress varies significantly with depth; the ASTM recommends using the calculation for non-uniform stress distribution. The SINT unit has a built in calculator to execute this calculation.

During the drilling process three holes were drilled which had hole diameters that were too large according to the ASTM standard. Baring one (TCD3-41), the results of the oversized holes were omitted from the graphs presented in the figures below.

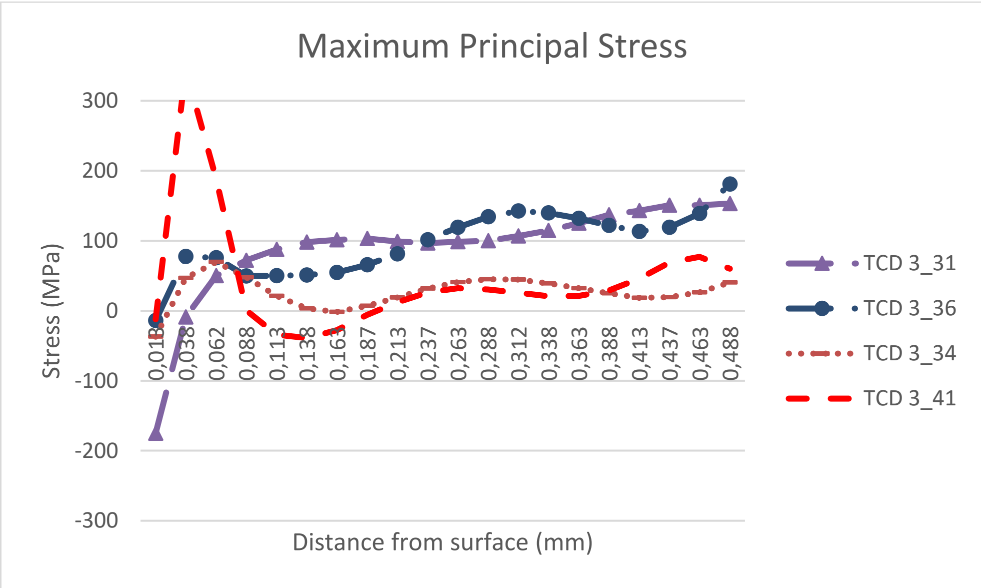

Figure 6-39 - Maximum principal stress

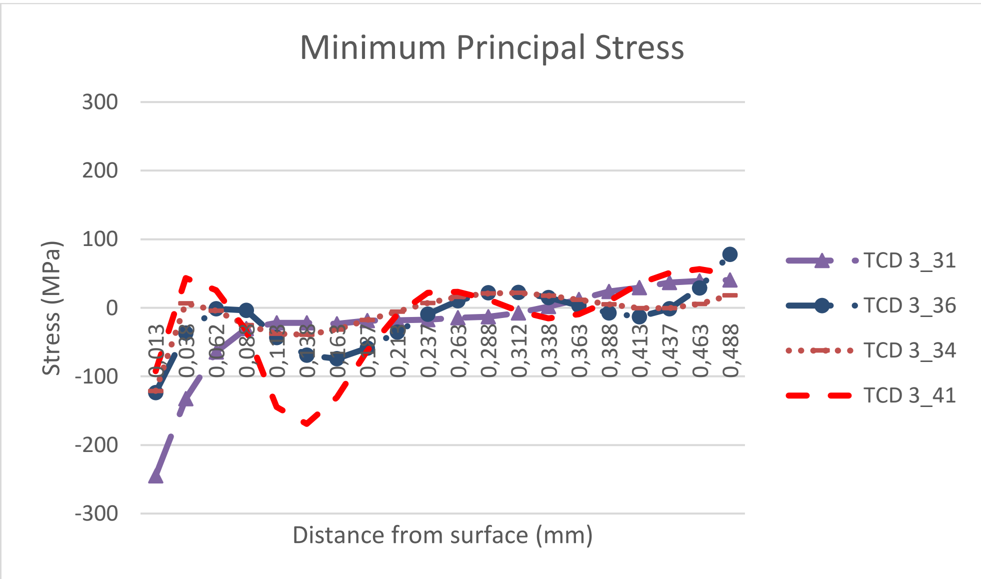

Figure 6-40 - Minimum principal stress

The graphs in Figures 6-39 and 6-40 show the maximum and minimum residual (principal) stress distributions within the welded components. The erratic results close to the surface of sample TCD3-41 can be attributed to the oversized hole that was drilled. TCD3-31 and TCD3-36 are the as welded samples whilst TCD3-41 and TCD3-34 are the stress relieved samples. It is evident from these results that most of the residual stresses have been removed. The stresses close to the surface of the stress relieved samples were probably induced by surface preparations for strain gauge application. These effects were more notable in the as welded samples since these samples still carried the stresses induced from not only manual mechanical (hand) surface preparation, but also the mechanical means of surface preparation.

The stresses in the as welded samples are significantly lower than that suggested by the literature (section 3.3.4); however, the residual stresses within the coupon change significantly when removing the coupon from the welded plate[60]

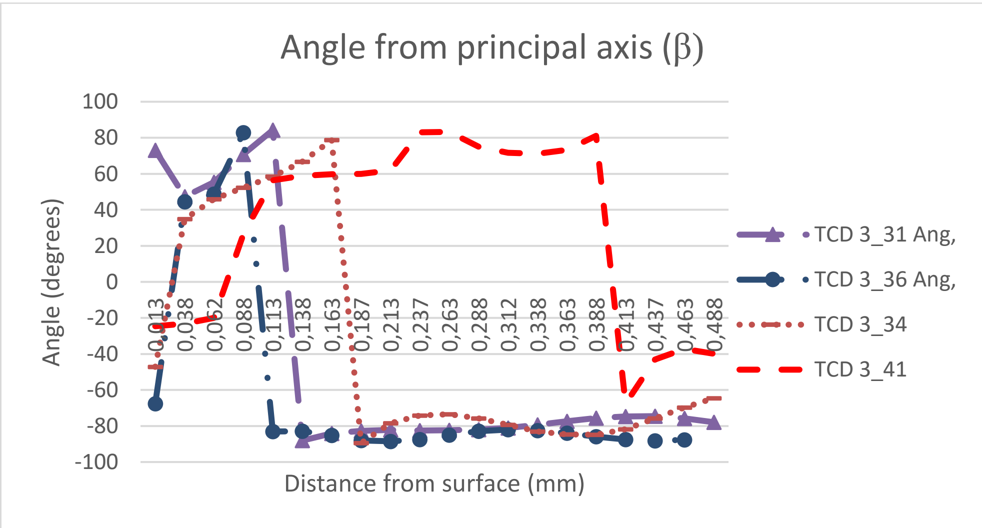

Figure 6-41 - Angle of maximum principle stress from principle axis

The angle (β) of the maximum principal stress in relation to the weld direction is shown in Figure 6-41. According to the gauge orientation as described in sections 6.6.1 and 6.6.2 the 0° angle corresponds to the weld direction. It appears from this graph that the maximum stress is orientated close to 90° to the weld direction.

6.7 Fracture studies

6.7.1 Sample preparation

All the notches were machined so that the notch tip coincided with the centreline of the weld. The DENT samples had 3 mm deep notches of radii 0.05, 0.1, 0.35 and 1 mm cut into them. The notches of the CT samples had radii of 0.05 mm, 0.3 mm and 1 mm. The reason for the slight variation in the notch radii, is that the tools used for the CT samples were slightly different to that used for the tensile samples. Since the notch depth for the CT samples was much deeper than that of the tension samples, coupled with the fact that the CT samples required a narrower tool due to their compact design, a different tool was needed to cut the notches within the CT samples. Appendix G shows the drawing template for the CT samples. These dimensions were based on the sizes given by the ASTM E1820 standard[36]. The notches in the CT samples were all cut from the advancing side of the weld as shown in Figure 6-9. The reason for cutting from this side, is that it was suspected that a root flaw existed on the advancing side of the weld and by machining from it the effect of this root flaw could be reduced.

Several questions arose because of the variance in specimen type and especially the variation in the sharper notch. In section 5.6 it was mentioned that the assumption that the 0.1 mm radius behaved in a crack like manner could be presumptuous. The reason for this statement was that the cracked sample in that study was less influenced by the effect of plasticity when compared to the 25 mm wide DENT with the 0.1 mm radius notch. Since the batch of material used for this study was different to the batch used in the studies leading up to this point, it was decided to determine the critical values for this batch as well. DENT samples, 25 mm wide, with notches 3 mm deep and radii of 0.05 mm, 0.1 mm, 0.35 mm and 1 mm were made. The samples containing the 0.05 mm radius notches were made with the same tool used for creating the notches in the CT samples. In order to determine the effect of variation in specimen type, a set of CT samples containing 0.05 mm radius notches was made from the parent plate. To determine how the material would behave with a crack in it, CT samples as well as 25 mm wide three-point bend test specimen were made.

Figure 6-42 shows the tensile samples ready for testing. Figure 6-43 shows examples of the CT samples with 1 mm radii

Figure 6-42 - DENT samples

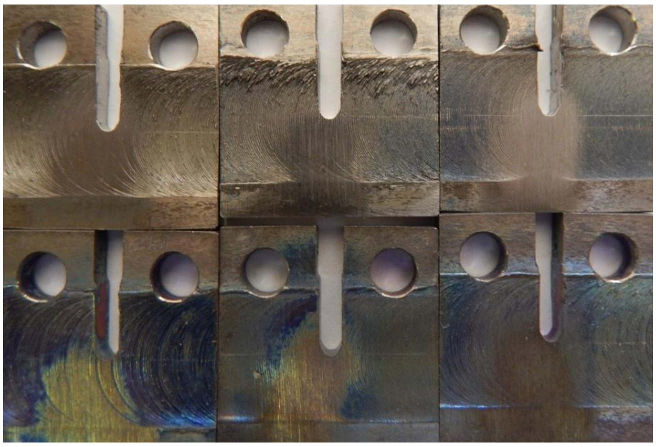

Figure 6-43 – 1 mm radius CT samples

6.7.2 Tensile testing

Prior to testing, numerous measurements were made which could be of significance to the performance of the material. Appendix G shows all the dimensional measurements taken for the respective samples. Also included in Appendix G are examples of the notch radius measurements made using a Zeiss stereo microscope.

Testing of the notched tensile samples was done utilizing the same technique as described in section 5.3. The test speed for these samples was kept at 2 mm/min. Care was exercised to keep the sample centreline collinear to the line in which the force acted.

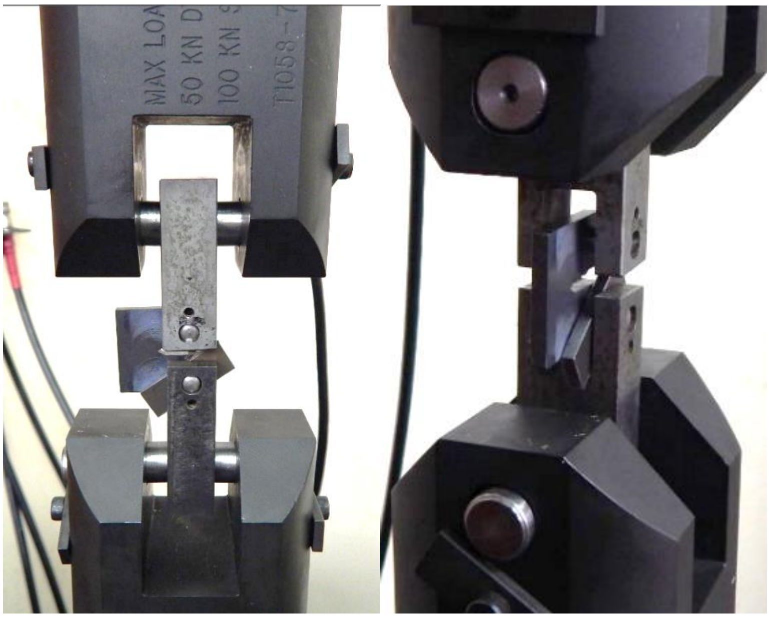

Figure 6-44 - CT sample in tensile coupling

Fixtures were made to accommodate the smaller CT samples. These samples were centralised within the CT type jaws with spacers, to ensure the sample was aligned with the line in which the force is applied. The test speed for these samples was set to 2kN/min which translates to 0.55MPa.m$^{0.5}$/s

6.7.3 Fracture testing results

Various fracture toughness studies were performed. DENT samples were used for notches longitudinal to the weld, whilst CT samples were used with notches perpendicular to the weld. DENT and CT samples were also made using parent plate. To confirm that the 0.05mm notches do perform in a crack like manner, CT samples using a 0.05 mm notch were made as well as three-point bend specimen in which cracks were grown. CT samples were also used for crack studies, but to grow the crack evenly in these proved to be challenging.

The force plots of the various tests are plotted on the graphs in Appendix I. The stress line plots for the various notch sizes are also shown. The various critical values obtained from these plots are shown in the tables in Appendix I. The K_{Capp} values in these tables are plotted in Figure 6-45.

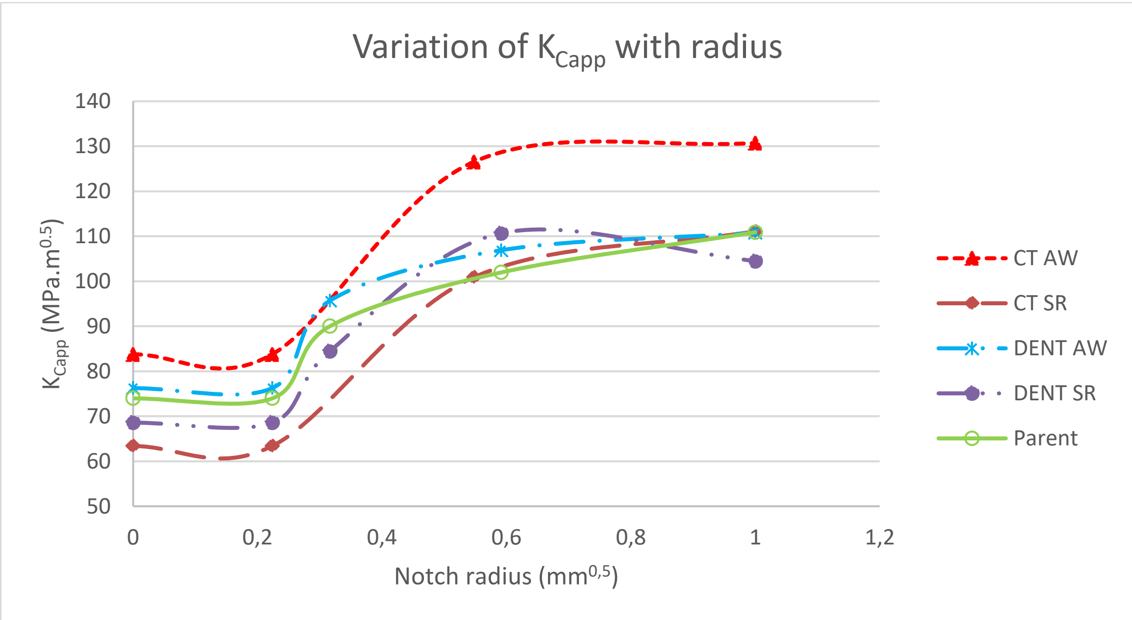

Figure 6-45 – K_{Capp} values of the parent plate and welded samples

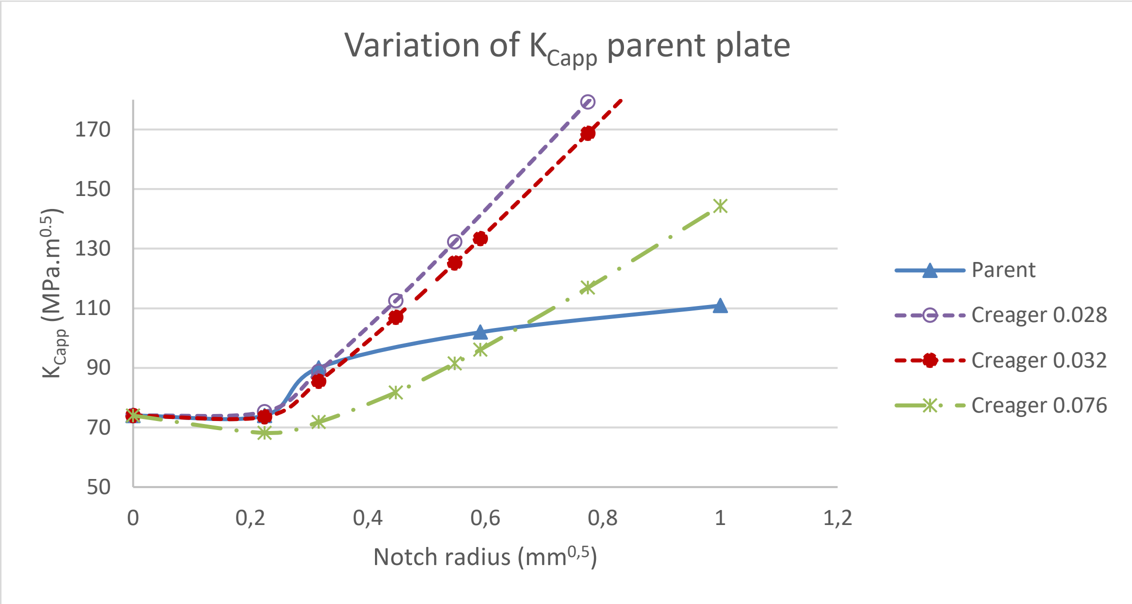

Figure 6-46 - K_{Capp} of the parent plate

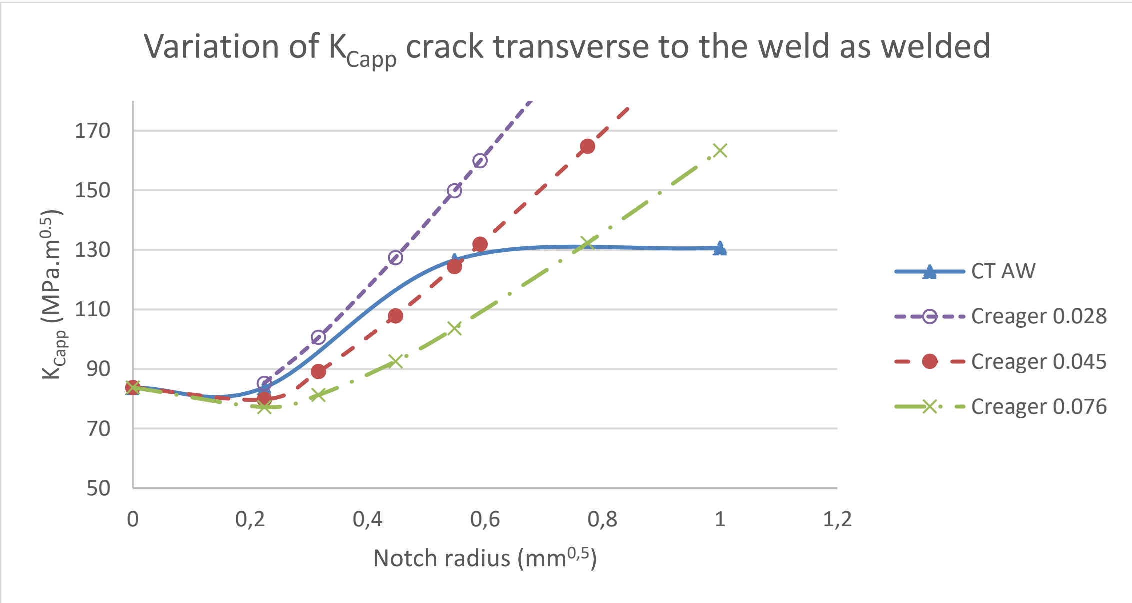

Figure 6-47 - K_{Capp} of the as welded material for a crack transverse to the weld

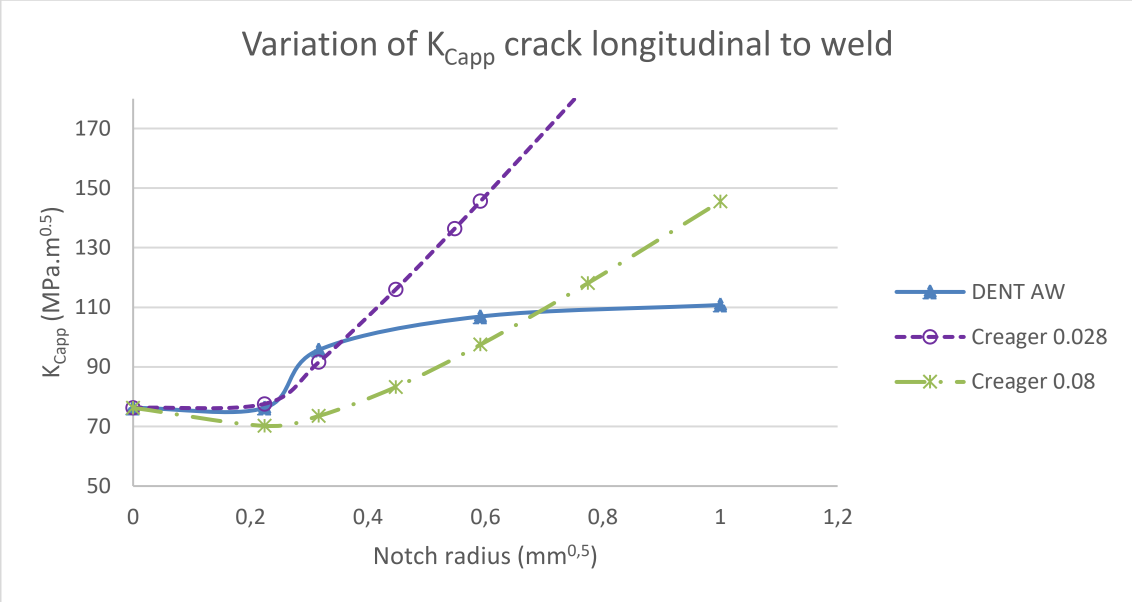

Figure 6-48 - K_{Capp} of the as welded material for a crack longitudinal to the weld

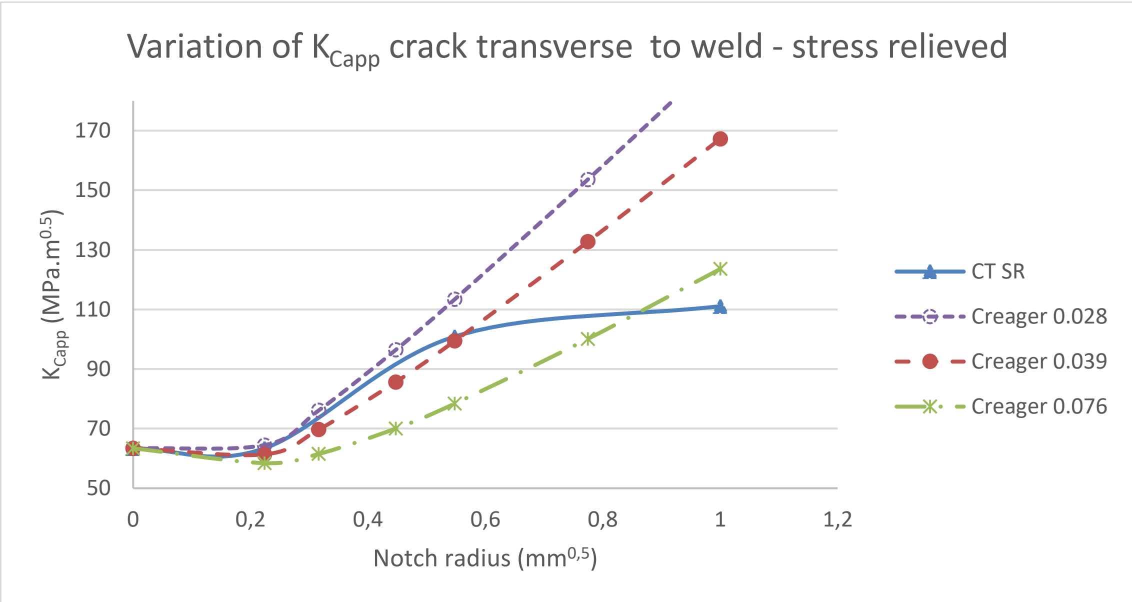

Figure 6-49 - K_{Capp} of the stress relieved welded material for a crack transverse to the weld

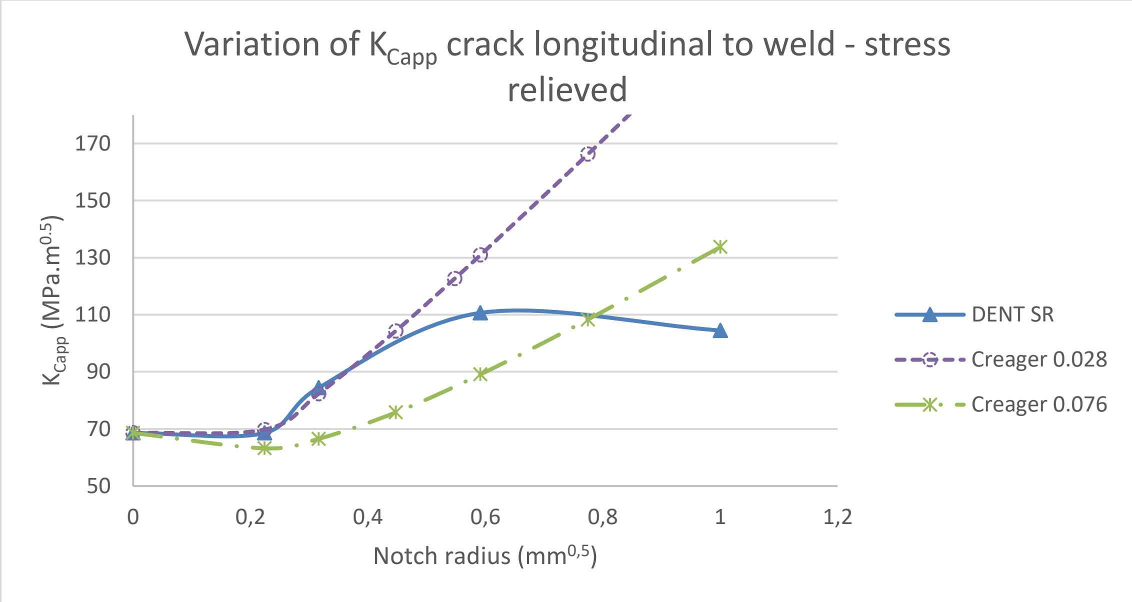

Figure 6-50 - K_{Capp} of the stress relieved welded material for a crack longitudinal to the weld

The graphs in Figures 6-46 to 6-50 show the plot of the K_{Capp} values as determined from test data. The predicted K_{Capp} curves were calculated using Equation 4-19. The critical distances were obtained from the intersection points of the two sharpest notches and also the peak value of the sharpest curve (these values are reflected in the tables in Appendix I). For each respective graph the K_{Capp} values obtained of the two sharpest notches were used for the prediction curves.

6.8 Discussion

In the final part of this study various tests were performed on friction stir welded Ti-6Al-4V. The material was heat treated prior to welding to minimize the effect of fabrication processes on the final result. The heat treatment, however, added some complexities such as geometrical distortion and a nitride casing, which required additional machining. The welding parameters, including the tool geometry used, was based on the work done by Mashinini. A critical parameter, pertaining to the friction stir welding process, emerged during this final part of the study, that being the size of the pilot hole. As a result of the variation in plate thickness and the variation in tool geometry all the welds had root flaws. In order to minimize the effect of the flaw and any variations as a result of the inconsistency of the material thickness, the samples (in terms of their orientation, notch type and heat treatment) were randomised to a degree among the various welded plates. To investigate the effect of residual stress on the fracture behaviours of the welded plate, some samples were subjected to a post-weld stress relief treatment.

In this study, the parent plate was again tested to serve as a bench mark for comparison to the results of the weld study. The three-point bending samples, which were used for crack studies, and the K_{Capp} results of the DENT specimens with 0.05 mm notches matched well. Since the DENT samples are more susceptible to the effect of plasticity on the results, CT samples with 0.05 mm were also tested. For all three (0.05 DENT, 0.05 CT and the three point bend with cracks) the results were similar. The cracked samples yielded a slightly lower K_{Capp} of 76 MPa.m$^{0.5}$ whilst the DENT and CT result was more or less 79 MPa.m$^{0.5}$. Based on these results it was decided that the results of the 0.05 mm notch could be considered crack like and could be used in simulation studies.

A few observations can be made from the fracture force graphs in Appendix I. The displacement measurements reflected are the measurements of the displacement between cross heads of the tensile machine. For most there seem to be a large variation in the measured forces for each respective notch size and geometry type. This variation could be the result of the root flaw present in the welded material and the fact that there was a slight variance in the forge force from one plate to the next. As a general observation it appears that the load line displacements are larger for the notches with larger radii; however, in the case of the DENT samples, numerous samples fractured between 1.5 mm and 2 mm displacements. Most of the CT samples fractured at displacements less than 1.5 mm. In all the samples, the fracture force reached a peak after which sudden fracture would occur for the DENT and some of the CT samples. A number of the CT samples, however, tore slowly after reaching the peak fracture force. It can also be seen on the graphs that some samples have a linear force displacement curve up to fracture whilst others (mostly the larger notch radii) the gradient decrease prior to fracture. Referring to the fracture images in Figures 6-22 to 6-27 it appears for the samples with smaller radii, those with the most prominent shear lips tended to have fractured at higher forces and yielded larger displacements, when compared to samples with small or no shear lips.

The residual stress results indicate the presence of a maximum principal stress in the region of 125 MPa, which is low in comparison to the yield strength of the material. The direction of this stress is perpendicular to the weld direction which could partly be the cause for the reduction of the fracture strength for notches longitudinal to the weld direction (DENT samples) when compared to the fracture strength of notches perpendicular to the weld direction (CT samples). It can be observed from the graph in Figure 6-45 that in the as welded condition the fracture toughness of the CT samples is higher by about 10 MPa.m$^{0.5}$ when compared to the DENT samples, however, when stress relieved the opposite is witnessed and the CT samples yield a fracture toughness value of approximately 5 MPa.m$^{0.5}$ less than the DENT samples.

Microscopy detail revealed that the parent plate had a typical equiaxed microstructure. The microstructure in the weld zone is more of a lamellar type structure which corresponds to literature published on this matter and presented in chapter 3. In terms of fracture toughness, the welded material performed slightly better than the parent plate material especially when the notch was perpendicular to the weld direction. This is in agreement with the literature (presented in chapter 2) that has shown that titanium lamellar microstructures tend to perform better than the equiaxed microstructures in terms of fracture toughness. The effect of residual stress also needs consideration, since it appears have an influence on the toughness as discussed earlier. The parent plate should have very low residual stress particularly as it was subjected to a duplex anneal process. The welded material, however, still performed marginally better than the parent plate considering the stress distribution in the welded plate.

Form the microstructures shown in Figures 6-15 to 6-21 little difference between the microstructure of the as welded material, when compared to the microstructure of a stress relieved sample, can be witnessed other than that it would appear more precipitates had formed on the grain boundaries of the stress relieved material. From the data in the graph of Figure 6-45 the welded material seemed to perform better in terms of fracture toughness than the parent plate.

The effect of the heat treatment on the fracture toughness was significant. For both notch directions (longitudinal and transverse) the fracture toughness was lower when compared to the as welded condition. The reduction in strength could possibly be attributed to the formation of $TiAl_3$ during the heat treatment process. This precipitate, however, can only be observed under a TEM. The SEM images of the fractured surfaces (Figures 6-28 to 6-30) of the parent plate, as welded material and heat treated material reveal that these samples have a fracture topography typical to that of a ductile fracture. The dimples observed on the fracture surface of the parent plate are more even in size, whilst the welded samples had a large variation in dimple size. The higher resolution images also reveal that the fracture topography of the stress relieved sample is slightly more featureless when compared to the as welded material, which could explain the lowered fracture toughness values.

The hardness results showed very large scatter. In both measurements taken (across the weld and through the thickness of the sample) there was a notable difference among the as welded material, stress relieved material and the parent material. During the welding process it was noted that the forge force varied at times from one plate to the other. Therefore, three samples of the as welded material, representing three different forge forces, were tested in order to establish the effect of the variation in forge force on the hardness. The samples from the plates welded at a lower forge force have a very similar hardness, whereas the higher forge showed an increase in the hardness of the material. The stress relieved sample yielded a notable increase in hardness when compared to the as welded material. This is consistent with what is presented in the literature in terms of precipitation hardening of titanium[16]. The fracture toughness results suggest an inversely proportional relationship to hardness.

The critical distance value for the DENT samples of welded material and parent plate material correspond well for the smaller more critical radii, this being a value of 0.028 mm. It appeared that the value could be valid for the CT samples as well, however, the 0.35 mm radius notch yielded a slightly lower value than the predicted curve. This was possibly due to the size of the plastic zone ahead of the notch becoming significant thereby lowering the measured K_{Capp} value. It is also notable from the graph in Figure 6-50 that there is a decrease in toughness for the larger 1 mm radius notches. For most of the samples with the larger 1 mm radius, the results indicate that when the plasticity ahead of the notch becomes dominant the fracture toughness variation reduces to a marginal amount (referring to the graphs in Figure 6-49 and Figure 6-50). It must also be considered that because of the material thickness, plane strain conditions do not dictate during fracture, therefore it is still unclear to what extent the plasticity ahead of the crack tip influences the fracture result when compared to the plane stress condition. This must be contextualised in terms of the size and shape of the shear lip formed on the fracture surface. The sharper notches tended to have a small area ahead of the notch with little or no shear lips, indicating a significant amount of plane strain immediately ahead of the notch, whilst the fracture surfaces of the larger notches consisted of only slanted type indicating that mostly plane stress conditions prevailed during fracture.

6.9 Conclusion

A fracture toughness study of friction stir welded titanium was performed and various analytical studies were undertaken in order to explain the variation in results. The fracture toughness of the parent plate was slightly lower when compared to the welded samples which were not heat treated. The stress relieving heat treatment possibly caused precipitation hardening of the material resulting in a reduced fracture toughness value. Residual stresses were significant enough to influence the fracture toughness value; however, since most of the stresses were probably removed during the removal of the samples from the welded plate, its influence was possibly reduced.

The critical distance for all the samples types seem to be similar when the notches are more critical. When using 0.05 mm and 0.1 mm notches it appears that the critical distance for the parent plate, as welded material and stress relieved samples tends to be 0.028 mm. The CT samples yielded a slightly larger value, however, the 0.35 mm notch may have already induced a large enough plastic zone ahead of the notch tip to influence the result to a degree. However, plane strain is not prevalent and the influence of plane stress conditions need to be considered as well.

Chapter 7

Discussion and Conclusion

At the time the idea of this project was conceived very little had been published on the fracture toughness of friction stir welded titanium let alone Ti-6Al-4V. Most of the studies completed on friction stir welded Ti-6Al-4V mostly revolved around the establishment of the process parameters and the determination of the subsequent mechanical properties such as tensile strength, hardness profile, residual stress distribution and fatigue performance. There were also a few studies involving crack growth rates. It can be argued that one of the reasons fracture toughness has not yet been widely published (on the topic friction stir welding of titanium) is that the testing techniques for fracture toughness are complex and costly.

The initial idea for this thesis stemmed from the lack of fracture toughness data available on friction stir welded Ti-6Al-4V. Initially the idea was to conduct a fracture toughness study involving the more traditional fracture mechanics approaches. However, deciding on which method be best suited for this study was not straight forward. The material is too thin to qualify for plane strain fracture toughness techniques and the plane stress fracture toughness method poses its own set of challenges. With this in mind the theory of critical distance and the advantages it proposes was hard to ignore and it was therefore decided to include the technique in this project.

The method is still in its infancy in terms of applicability and therefore it is a topic of interest. There is no standard governing the method of determining the critical parameters or exactly how to apply them, therefore several questions needed to be answered in terms of size effects.

This study set out to determine the fracture toughness of a friction stir welded Ti-6Al-4V plate by application of the TCD method. In order to do this some parameters had to be established. The TCD method proposes that a critical distance will be unique to a material and therefore suggests that when the fracture point of the notched material is reached the stress at this critical distance will be unique to the material regardless of the notch radius. The concept is a fairly simple one and the literature suggested using a sharp crack like notch and a blunt notch in order to determine the critical distance. A minimum of two notches are advised, but three or more would be preferential.

Since no study of this kind had been undertaken using Ti-6Al-4V sheet, no guidelines existed as to what specimen size or notch size to use. The initial study, therefore, was a very basic study and the test piece sizes were largely based on those that other studies had used when testing a more ductile material. From this study no conclusive critical distance was obtained. This result therefore sparked several questions, one of those being the influence that sample size has on the critical distance and if narrower samples will allow for the determination of these critical parameters. The results of study one show that the sharper notch determines the fracture toughness of the material, but no conclusive intersection point was reached from the results of the three notch sizes that were tested.

In study two a definite decrease in the apparent fracture toughness was observed for the samples narrower than 17 mm. There was still no clear evidence of a specific critical point. Since the study indicated a variation in the measured fracture toughness it made sense that a further study be undertaken that investigated not only the of changes in the width of the sample has on the critical distance and fracture toughness, but also the notch size. The notches in study two also did not indicate a convergence point and therefore sharper notches needed to be utilised. The question whether the sharper 0.1mm notches are crack like also needed to be answered.

A more in-depth study was conducted ascertain if sharper notches will yield the common convergence point and how varying the notch depth and sample width would influence the apparent fracture toughness and the critical distance. In some literature three-point bend test specimens were used, therefore some samples were tested using the three-point bend testing technique as well. The apparent fracture toughness of a cracked samples was also established by means of this method.

The study clearly shows that the critical distance varies as the sample width decreases. The 17 mm and 25 mm samples yielded very similar fracture toughness results; however, there was a distinct difference in the critical distances. Sharper notches (0.35 mm and 0.6 mm) were used with the 0.1 mm notches and again a distinct critical distance was not attained when using DENT samples. The three-point bend sample with the 0.6 mm notch however yielded a very similar critical distance to that of the 0.35 mm DENT sample. For these results it appears that the critical distance is in the order of 0.09 mm or smaller. When reflecting on the Fedderson curves, it appears that it is best to use samples that fracture below the nett section yield curve or at least that the nett section stress at fracture should be less than the materials yield strength. It can therefore be concluded, that for optimal results similar rules to that stipulated in the plane stress fracture toughness standard (ASTM E561) and the EPFM standard test technique (ASTM 1820), in terms of the allowable size of the plastic zone ahead of the notch, should apply.

The final phase of tests determined if there were any variations in the critical distance after the material had been welded. Studies on heat treated welded material could also aid in explaining any variations in the critical distance and fracture toughness of the material.

The fracture testing utilised two different types of samples, these being DENT samples for notches longitudinal to the weld and CT samples for notches perpendicular to the weld. The use of the CT notches was necessary as it saves material. It is unfortunate that two different types of fracture samples were used, since the plasticity effects ahead of the notch were significant in both instances (for the samples containing notches with the larger radii), however the influance of plasticity on the results were different for the DENT samples when compared to the CT samples.

Microscopy work revealed that the material had transformed from an equiaxed microstructure (parent plate) to a more lamellar microstructure once welded. Hardly any change in micro structural evidence was witnessed between the as welded material and the stress relieved samples other than possible precipitates at the grain boundaries. Hardness tests revealed that the stress relieved samples had hardened indicating the possible formation of $TiAl_3$.

The residual stress results were lower than found in other literature; however, this was expected since removal of the test coupons from the welded plate would reduce the residual stresses in the test coupons significantly. The direction of the residual stresses was surprising. It is the author's experience that when dealing with welded components, albeit applied to the more traditional fusion welding techniques, that the direction of the maximum principal stress often coincides with the direction of the weld. In this case the direction of the maximum principal residual stress was perpendicular to the direction of the weld. However, by stress relieving the material it appeared that the fracture toughness was influenced significantly. The stress relieved samples had a significantly lower fracture toughness, which could be as a result of the formation of $TiAl_3$. It was also noticeable that the fracture toughness of the as welded material was higher for the cracks perpendicular to the weld direction, whereas in the stress relieved condition the fracture toughness was higher for the notches longitudinal to the weld direction.

Reflecting on the results of study 3 in conjunction with the Fedderson curves, it made sense to make use of sharper notches in conjunction with the blunt notches. Additionally, the results of study 3 indicated that there may have been a size effect causing the fracture toughness of the 0.1 mm notched DENT samples to be slightly lower than it should be. This was evident when comparing the result of the three-point bend test specimen with a 0.1 mm radius notch to that of the 25 mm wide DENT samples with the same notch radius. The results of study 3 also showed that the critical distance varied significantly as the plasticity effects ahead of the notch became more dominant.

It made sense, therefore, that the final study test two sharp notches which would fracture when the nett section stress was below the yield stress of the material. The results from the notches made in the DENT samples also needed to be comparable to that of the CT samples. It was decided therefore that notches with a 0.05mm radius also be applied to the DENT samples. In order to ensure that the 0.05mm samples behaved like a crack, three-point bend test pieces as well as CT samples were used to grow cracks. In both instances, especially in the instance of the CT samples, growing the cracks straight proved very difficult. For the parent plate, the fracture toughness results of the sharper 0.05 mm notches in DENT and CT samples were compared to the fracture toughness of cracked samples using TPB samples. The apparent fracture toughness of all these samples compared well and it is therefore assumed firstly, that the 0.05 mm notch does act crack like and secondly that the results of the CT samples and the DENT samples using this notch size are comparable.

In terms of the fracture testing of the weld specimen, it is evident that there is a large variation in the fracture force, especially for the stress relieved specimen. The weld zone in all the welded plates contained root flaw; however, the welded samples show an increase in the apparent fracture toughness when compared to the parent plate. Unfortunately, it is difficult to compare the results of the larger notches since the plasticity effects vary between the two different fracture sample types used, these being the DENT and CT types. When using notches which result in fracture whilst the nett section stress is less than the material's yield stress, a very small value (0.028 mm) for the critical distance is obtained. This value increases as the notch radius increases. This can again be explained by the size of the plasticity ahead of the notch in relation to the remaining ligament length. When using the critical distance value in conjunction with Creager's formula for crack tip radius it appears that the results and the predictive curve fit well in the instances when the critical value was obtained whilst the nett section stress at failure was less than the yield strength of the material. From a TCD methodology standpoint, it appears that in order to obtain constant results (for applications Ti-6Al-4V sheet) it is best to use samples that comply with the ASTM E561 requirements in terms of sample size.

The study unfortunately did not clearly differentiate how the plasticity ahead of the crack tip affects the critical distance compared to the effect the variation in plane stress conditions has on the fracture toughness. This could perhaps be the focus of a future study.

In terms of FSW it would perhaps also be of use to investigate the relationship between tool wear and the minimum size pilot hole required to deliver defect free welds. It could also be of interest to investigate the effect variation of welding parameters have on the fracture behaviour of the welded material.

Bibliography

1. Anderson TL. Fracture mechanics: fundamentals and applications. 3rd ed: CRC press; 2005.
2. I V. Titanium centre works towards 20 000 t/y plant as it seeks to create new industry [Online. Mining Weekly [Internet]. 2011 Jun 6 2012 June 8. Available from: http://www.miningweekly.com/article/titanium-centre-works-towards-20-000-ty-plant-as-it-seeks-to-create-new-industry-2011-06-06.
3. Solutions SS. Rosoboronexport controls titanium in Russia2006 June 23. Availablefrom:https://web.archive.org/web/20121111061856/http://www.sevanco.net/news/full_story.php?id=1122.
4. Damm O dPW. Progress Made by the South African Light Metals Development Network Materials Science Forum. 2009;Volumes 618-619:147-54
5. Ding RJ, Schneider J, Walker B, editors. Advances in Solid State Joining of High Temperature Alloys. The Twenty-first International Offshore and Polar Engineering Conference; 2011: International Society of Offshore and Polar Engineers.
6. Mashinini PM. Process window for friction stir welding of 3 mm titanium (Ti-6Al-4V) 2011.
7. Mashinini MP. Dynamic properties of 3 mm Ti-6Al-4V laser beam and friction stir welded sheets [PhD Thesis]: Nelson Mandela Metropolitan University; 2015.
8. Taylor D. The Theory of Critical Distances: A New Perspective in Fracture Mechanics: Elsevier Science; 2010.
9. Susmel L, Taylor D. The Theory of Critical Distances to estimate the static strength of notched samples of Al6082 loaded in combined tension and torsion. Part I: Material cracking behaviour. Engineering Fracture Mechanics. 2010;77(3):452-69.

10. Susmel L, Taylor D. The Theory of Critical Distances as an alternative experimental strategy for the determination of KIc and ΔKth. Engineering Fracture Mechanics. 2010;77(9):1492-501.
11. Susmel L, Taylor D. On the use of the Theory of Critical Distances to predict static failures in ductile metallic materials containing different geometrical features. Engineering Fracture Mechanics. 2008;75(15):4410-21.
12. Leyens C, Peters M. Titanium and titanium alloys: Fundamentals and applications: Wiley; 2006.
13. Donachie MJ. Titanium: A technical guide, 2nd edition: ASM International; 2000.
14. Welsch G, Boyer R, Collings EW. Materials properties handbook: Titanium alloys: ASM International; 2007.
15. Lampman S. Wrought Titanium and titanium alloys. In: Committee AIH, editor. Properties and Selection: Nonferrous Alloys and Special- Purpose Materials. 10 ed: ASM International; 1990.
16. Lütjering G, Williams JC. Titanium: Springer Berlin Heidelberg; 2007.
17. Sieniawski J, Ziaja W, Kubiak K, Motyka M. Microstructure and mechanical properties of high strength two-phase titanium alloys. Titanium Alloys-Advances in Properties Control. 2013:69-80.
18. Nandan R, DebRoy T, Bhadeshia H. Recent advances in friction-stir welding–process, weldment structure and properties. Progress in Materials Science. 2008;53(6):980-1023.
19. O'Brien A, Guzman C. Welding processes Part 2. In: Welding Handbook Committee on friction stir welding, editor. AWS Welding Handbook. 3. 9th ed. Miami: American Welding Society; 2007.
20. Lohwasser D, Chen Z. Friction stir welding: From basics to applications: Elsevier; 2009.
21. Mahoney M, Mishra R. Friction stir welding and processing. ASM International,. 2007.

22. Steuwer A, Hattingh D, James M, Singh U, Buslaps T. Residual stresses, microstructure and tensile properties in Ti–6Al–4V friction stir welds. Science and Technology of Welding and Joining. 2012;17(7):525-33.
23. Zhou L, Liu HJ, Liu QW. Effect of rotation speed on microstructure and mechanical properties of Ti–6Al–4V friction stir welded joints. Materials & Design. 2010;31(5):2631-6.
24. Pasta S, Reynolds AP. Residual stress effects on fatigue crack growth in a Ti-6Al-4V friction stir weld. Fatigue & Fracture of Engineering Materials & Structures. 2008;31(7):569-80.
25. Liu HJ, Zhou L, Liu QW. Microstructural characteristics and mechanical properties of friction stir welded joints of Ti–6Al–4V titanium alloy. Materials & Design. 2010;31(3):1650-5.
26. Zhang Y, Sato YS, Kokawa H, Park SHC, Hirano S. Microstructural characteristics and mechanical properties of Ti–6Al–4V friction stir welds. Materials Science and Engineering: A. 2008;485(1-2):448-55.
27. Pilchak AL, Juhas MC, Williams JC. Microstructural Changes Due to Friction Stir Processing of Investment-Cast Ti-6Al-4V. Metallurgical and Materials Transactions A. 2007;38(2):401-8.
28. Pasta S, Reynolds A. Evaluation of residual stresses during fatigue test in an FSW joint. Strain. 2008;44(2):147-52.
29. Edwards P, Petersen M, Ramulu M, Boyer R, editors. Mechanical Performance of Heat Treated Ti-6Al-4V Friction Stir Welds. Key Engineering Materials; 2010: Trans Tech Publ.
30. Edwards P, Ramulu M. Fracture toughness and fatigue crack growth in Ti-6Al-4V friction stir welds. Fatigue & Fracture of Engineering Materials & Structures. 2015;38(8):970-82.
31. Sanders DG, Edwards P, Cantrell AM, Gangwar K, Ramulu M. Friction Stir-Welded Titanium Alloy Ti-6Al-4V: Microstructure, Mechanical and Fracture Properties. Jom. 2015;67(5):1054-63.
32. Janssen M, Zuidema J, Wanhill R. Fracture Mechanics London: Spon Press; 2004 [Available from: http://public.eblib.com/choice/publicfullrecord.aspx?p=200785.

33. ASTM. E399 - 12$^{\varepsilon 3}$. Standard Test Method for Linear-Elastic Plane-Strain Fracture Toughness K_{Ic} of Metallic Materials
West Conshohocken: ASTM International; 2013. p. 33.

34. ASTM. E561-10$^{\varepsilon 2}$. Standard Test Method for KR Curve Determination. West Conshohocken: ASTM International; 2013. p. 16.

35. Zhu X-K, Leis B. Revisit of ASTM Round-Robin Test Data for Determining R Curves of Thin-Sheet Materials. Fatigue and Fracture Mechanics: 37th Volume: ASTM International; 2011.

36. ASTM. E1820-11$^{\varepsilon 2}$. Standard test method for measurement of fracture toughness. West Conshohocken: ASTM International; 2011. p. 58.

37. Zhu X-K, Joyce JA. Review of fracture toughness (G, K, J, CTOD, CTOA) testing and standardization. Engineering Fracture Mechanics. 2012;85:1-46.

38. Wilson CL, JD Fracture Toughness Testing with Notched Round Bars. ASTM International. 2000;Fatigue and Fracture Mechanics 30th Volume:69-82.

39. Mourad A-HI, El-Domiaty A. Notch Radius and Specimen Size Effects on Fracture Toughness of Low Alloy Steel. Procedia Engineering. 2011;10(0):1348-53.

40. Ule B, Leskovšek V, Tuma B. Estimation of plain strain fracture toughness of AISI M2 steel from precracked round-bar specimens. Engineering Fracture Mechanics. 2000;65(5):559-72.

41. Lee B-W, Jang J-i, Kwon D. Evaluation of fracture toughness using small notched specimens. Materials Science and Engineering: A. 2002;334(1–2):207-14.

42. Baratta F, Barker L. Comparisons of fracture toughness measurements by the short rod and ASTM standard method of test for plane-strain fracture toughness of metallic materials (E 399-78). Journal of Testing and Evaluation. 1980;8(3):97-102.

43. Sarchamy D, Burns MG. Estimation of fracture toughness values for titanium alloy using small centre notched round specimens. Small Specimen Test Techniques: ASTM International; 1998.

44. Vanian GG, Hellier AK, Zarrabi K, Prusty BG. Fracture Toughness Determination for Aluminium Alloy 2011-T6 using Tensile Notched Round Bar (NRB) Test Pieces. Int J Fract. 2013;181(1):147-54.
45. Qiu H, Enoki M, Kawaguchi Y, Kishi T. A model for the static fracture toughness of ductile structural steel. Engineering fracture mechanics. 2002;70(5):599-609.
46. Louks R, Askes H, Susmel L. Static assessment of brittle/ductile notched materials: an engineering approach based on the Theory of Critical Distances. Fracture and Structural Integrity. 2014(30):23-30.
47. Madrazo V, Cicero S, Carrascal IA. On the Point Method and the Line Method notch effect predictions in Al7075-T651. Engineering Fracture Mechanics. 2012;79(0):363-79.
48. Pluvinage G. Notch effects in fatigue and fracture: Springer; 2001.
49. Pluvinage G. Fatigue and fracture emanating from notch; the use of the notch stress intensity factor. Nuclear Engineering and Design. 1998;185(2–3):173-84.
50. Náhlík L, Huta P, Stegnerová K. Critical applied stresses for a crack initiation from a sharp V-notch. Frattura ed Integritá Strutturale. 2014(30):55.
51. Taylor D, Kasiri S. A comparison of critical distance methods for fracture prediction. International Journal of Mechanical Sciences. 2008;50(6):1075-81.
52. Creager M, Paris P. Elastic field equations for blunt cracks with reference to stress corrosion cracking. International Journal of Fracture Mechanics. 1967;3(4):247-52.
53. Cicero S, Madrazo V, Carrascal I, Cicero R. Assessment of notched structural components using failure assessment diagrams and the theory of critical distances. Engineering Fracture Mechanics. 2011;78(16):2809-25.
54. Cicero S, García T, Madrazo V. On the Line Method apparent fracture toughness evaluations: Experimental overview, validation and some

consequences on fracture assessments. Theoretical and Applied Fracture Mechanics. 2015;78:15-9.

55. Cicero S, Madrazo V, Carrascal I. Analysis of notch effect in PMMA using the Theory of Critical Distances. Engineering Fracture Mechanics. 2012;86:56-72.

56. Cornetti P, Pugno N, Carpinteri A, Taylor D. Finite fracture mechanics: A coupled stress and energy failure criterion. Engineering Fracture Mechanics. 2006;73(14):2021-33.

57. Pilkey WD, Pilkey DF. Peterson's Stress Concentration Factors: Wiley; 2008.

58. Cicero S, Gutiérrez-Solana F, Horn AJ. Experimental analysis of differences in mechanical behaviour of cracked and notched specimens in a ferritic–pearlitic steel: Considerations about the notch effect on structural integrity. Engineering Failure Analysis. 2009;16(7):2450-66.

59. da Silva BL, Ferreira JLA, Araújo JA. Influence of notch geometry on the estimation of the stress intensity factor threshold by considering the Theory of Critical Distances. International Journal of Fatigue. 2012;42:258-70.

60. Kumar N, Mishra RS, Baumann JA. Residual stresses in friction stir welding. Oxford: Butterworth-Heinemann; 2014.

61. ASTM. Standard test method for determining residual stresses by the hole-drilling strain gage method. E837-08$^{\varepsilon 2}$. West Conshohocken: ASTM International; 2013. p. 17.

62. Group VP. Measurment of residual stresses by the hole-drilling strain-gage method. 2010 01 Nov 2010. Report No.: Contract No.: 11053.

63. Lu J. Handbook of measurement of residual stresses: Fairmont Press; 1996.

64. Schajer G. Measurement of non-uniform residual stresses using the hole-drilling method. Part I—Stress calculation procedures. Journal of Engineering Materials and Technology. 1988;110(4):338-43.

65. Schajer G. Measurement of non-uniform residual stresses using the hole-drilling method. part II—practical application of the integral method. Journal of Engineering Materials and Technology. 1988;110(4):344-9.

66. SINT. RESTAN system for measuring residual stress by the hole-drilling method - operating and maintenance manual. SINT Technology.

67. SINT. MTS3000 - Restan Automatic sytem for residual stresses measurment by hole-drilling. SINT Technology.

Appendices

Appendix A - Notch geometry measurements

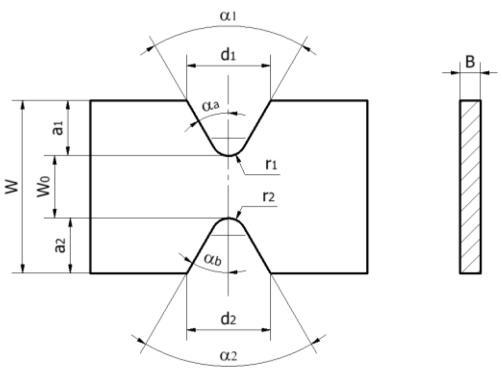

Figure A 1

Table A 1 - Study 1 sample dimensions

Part Number	r (mm)	W (mm)	a (mm)	B (mm)	W_0 (mm)	α°	α_b°	α_2°	α_a°	α_1°	a_1 (mm)	a_2 (mm)	d_1 (mm)	d_2 (mm)	r_1 (mm)	r_2 (mm)
WRCD01-01-01	0.97	24.98	3.00	3.25	18.99	59.50	30.00	59.50	29.50	59.50	3	2.99	4.55	4.55	0.97	0.98
WRCD01-01-02	1.00	24.96	2.97	3.25	19.02	59.33	29.83	59.67	29.17	59.00	2.93	3.01	4.48	4.61	1.00	1.00
WRCD01-01-03	0.96	24.98	3.01	3.23	18.97	59.83	29.92	60.00	29.83	59.67	2.99	3.02	4.56	4.58	0.98	0.95

Part Number	r (mm)	W (mm)	a (mm)	B (mm)	W_0 (mm)	α°	α_b°	α_2°	α_a°	α_1°	a_1 (mm)	a_2 (mm)	d_1 (mm)	d_2 (mm)	r_1 (mm)	r_2 (mm)
WRCD01-01-04	0.14	25.1	2.95	3.24	19.2	59.88	29.92	59.92	29.83	59.83	2.92	2.98	3.56	3.55	0.17	0.10
WRCD01-01-05	0.12	25.12	2.92	3.24	19.28	59.88	29.83	59.83	-30.00	59.92	2.94	2.9	3.54	3.46	0.13	0.11
WRCD01-01-06	0.16	25.06	2.89	3.23	19.29	59.88	29.83	59.83	-30.00	59.92	2.85	2.92	3.46	3.55	0.15	0.17
WRCD01-01-07	1.78	25.02	2.99	3.24	19.05	59.63	30.25	59.75	30.00	59.52	2.98	2.99	5.49	5.47	1.80	1.76
WRCD01-01-08	1.78	25.04	3.00	3.24	19.045	59.21	29.00	58.75	30.00	59.67	3.01	2.99	5.51	5.45	1.78	1.78
WRCD01-01-09	1.79	24.95	2.98	3.24	19	60.00	30.00	59.75	30.25	60.25	2.99	2.96	5.52	5.48	1.78	1.80

Table A 2 - Study 2 sample dimensions

Part Number	r (mm)	W (mm)	a (mm)	B (mm)	W_0 (mm)	α°	α_b°	α_2°	α_a°	α_1°	a_1 (mm)	a_2 (mm)	d_1 (mm)	d_2 (mm)	r_1 (mm)	r_2 (mm)
WRCD01-01-26	0.14	24.98	2.97	2.86	19.04	58.71	29.33	59.25	29	58.167	2.99	2.95	3.5	3.51	0.15	0.13
WRCD01-01-27		25.02	2.98	2.82	19.07						3.05	2.9				
WRCD01-01-28		24.98	2.86	2.88	19.27						2.9	2.81				
WRCD01-01-23	1.18	24.98	2.97	2.8	19.05	60.00	30	60	30	60	2.99	2.94	4.84	4.72	1.20	1.15
WRCD01-01-24	1.19	24.98	3.00	2.82	18.98	60.09	30.08	59.85	29.83	60.333	2.98	3.02	4.85	4.84	1.21	1.18
WRCD01-01-25		24.96	2.78	2.86	19.41						2.76	2.79				
WRCD01-01-20	1.77	24.94	2.77	2.84	19.4	59.92	30.25	59.833	30	60	2.74	2.8	5.2	5.28	1.76	1.78
WRCD01-01-21	1.77	24.96	2.74	2.84	19.48	60.71	30	60	30.58	61.417	2.78	2.7	5.3	5.18	1.76	1.79
WRCD01-01-22		24.98	2.80	2.84	19.38						2.8	2.8				

Part Number	r (mm)	W (mm)	a (mm)	B (mm)	W_0 (mm)	$\alpha°$	$\alpha_b°$	$\alpha_2°$	$\alpha_a°$	$\alpha_1°$	a_1 (mm)	a_2 (mm)	d_1 (mm)	d_2 (mm)	r_1 (mm)	r_2 (mm)
WRCD01-01-35	0.16	16.94	2.93	2.84	11.09	58.46	29	58.25	29.42	58.67	2.99	2.86	3.53	3.4	0.15	0.18
WRCD01-01-36	0.19	16.96	2.92	2.84	11.13	58.50	29.17	58.67	29.17	58.33	2.97	2.86	3.53	3.45	0.18	0.20
WRCD01-01-37		16.98	2.95	2.88	11.08	58.67			29.17	58.67	2.93	2.97	3.41			
WRCD01-01-32	1.19	16.8	2.82	2.85	11.17	59.83	29.67	59.67	30	60	2.78	2.85	4.58	4.65	1.19	1.19
WRCD01-01-33		16.94	2.94	2.86	11.06						2.92	2.96				
WRCD01-01-34		16.96	2.94	2.88	11.09						2.93	2.94				
WRCD01-01-29	1.79	16.96	2.83	2.88	11.31	60.58	30.42	60.5	30.83	60.67	2.8	2.85	5.31	5.4	1.77	1.81
WRCD01-01-30		16.94	2.80	2.92	11.34						2.84	2.76				
WRCD01-01-31		16.96	2.88	2.85	11.21						2.9	2.85				
						□	□	□	□	□						
WRCD01-01-44	0.16	8.98	2.97	2.82	3.05	58.54	29.5	58.5	29	58.58	2.99	2.94	3.56	3.47	0.18	0.15
WRCD01-01-45		8.94	2.89	2.84	3.16						2.87	2.91				
WRCD01-01-46		9	2.94	2.8	3.13						2.91	2.96				
WRCD01-01-41	1.19	8.98	2.98	2.88	3.02	60.67	30.8333	60.42	30.67	60.92	2.97	2.99	4.83	4.86	1.17	1.20
WRCD01-01-42		8.9	2.87	2.84	3.17						2.94	2.79				
WRCD01-01-43		8.94	2.93	2.88	3.08						2.95	2.91				

Part Number	r (mm)	W (mm)	a (mm)	B (mm)	W_0 (mm)	$\alpha°$	$\alpha_b°$	$\alpha_2°$	$\alpha_a°$	$\alpha_1°$	a_1 (mm)	a_2 (mm)	d_1 (mm)	d_2 (mm)	r_1 (mm)	r_2 (mm)
WRCD01-01-38	1.79	8.96	2.70	2.84	3.57	60.75	30.8333	60.667	31.1667	60.833	2.81	2.58	5.36	5.05	1.80	1.77
WRCD01-01-39		8.96	2.65	2.86	3.67						2.54	2.75	0	0		
WRCD01-01-40		8.98	2.66	2.88	3.67						2.79	2.52	0	0		

Table A 3 - Study 3 sample dimensions

Part Number	r (mm)	W (mm)	a (mm)	B (mm)	W_0 (mm)	$\alpha°$	a_1 (mm)	a_2 (mm)
WRCD01-01-70	0.37	25	2.93	3.2	19.14	59.00	2.95	2.91
WRCD01-01-71	0.38	24.98	2.98	3.2	19.02	59.25	2.95	3.01
WRCD01-01-72	0.35	24.96	2.96	3.22	19.05	60	2.95	2.96
WRCD01-01-122	0.10	25	3.00	3.23	19.01	60	2.97	3.02
WRCD01-01-123	0.10	25.01	3.04	3.23	18.94	60	3.05	3.02
WRCD01-01-73	0.10	24.94	0.84	3.22	23.27	60	0.96	0.71
WRCD01-01-74	0.10	24.98	0.90	3.2	23.18	60	1	0.8
WRCD01-01-75	0.10	24.98	2.05	3.24	20.89	60	2.04	2.05
WRCD01-01-76	0.10	25.00	1.98	3.24	21.05	60	1.98	1.97
WRCD01-01-87	0.10	25.1	5.00	3.24	15.11	60	4.94	5.05
WRCD01-01-88	0.10	25.05	5.00	3.24	15.05	60	4.95	5.05
WRCD01-01-173	0.10	24.88	4.97	3.24	14.95		4.93	5
WRCD01-01-174	0.10	25.04	4.78	3.22	15.49		4.76	4.79

Part Number	r (mm)	W (mm)	a (mm)	B (mm)	W_0 (mm)	α°	a_1 (mm)	a_2 (mm)
WRCD01-01-89	0.35	25.11	4.99	3.24	15.14	60	5.01	4.96
WRCD01-01-90	0.35	25.09	4.91	3.24	15.28	60	4.96	4.85
WRCD01-01-175	0.35	24.96	4.91	3.24	15.14		4.84	4.98
WRCD01-01-176	0.35	24.92	4.80	3.24	15.33		4.71	4.88
z								
WRCD01-01-91	0.60	25.19	4.86	3.24	15.47	60	4.85	4.87
WRCD01-01-92	0.60	25.18	4.94	3.24	15.3	60	4.98	4.9
WRCD01-01-48	0.10	24.98	5.83	3.22	13.32	60	5.79	5.87
WRCD01-01-49	0.10	25	5.90	3.24	13.2	60	5.97	5.83
WRCD01-01-50	0.10	24.98	5.91	3.24	13.16	60	6.01	5.81
WRCD01-01-51	0.10	25	5.82	3.22	13.37	60	5.79	5.84
WRCD01-01-124	0.10	25	5.99	3.23	13.02	60	6.03	5.95
WRCD01-01-125	0.10	25.02	6.02	3.23	12.98	60	5.97	6.07
WRCD01-01-177	0.10	24.90	5.86	3.23	13.19		5.81	5.9
WRCD01-01-178	0.10	25.06	6.08	3.23	12.9		6.02	6.14
WRCD01-01-179	0.10	25.04	6.05	3.23	12.95		6.09	6
WRCD01-01-180	0.10	25.05	6.04	3.23	12.98		6.09	5.98
WRCD01-01-67	0.35	24.95	5.82	3.22	13.31	60	5.69	5.95
WRCD01-01-68	0.35	25	5.94	3.22	13.12	60	5.93	5.95
WRCD01-01-69	0.35	24.96	5.89	3.2	13.18	60	6.02	5.76

Part Number	r (mm)	W (mm)	a (mm)	B (mm)	W_0 (mm)	$\alpha°$	a_1 (mm)	a_2 (mm)
WRCD01-01-52	0.60	25	5.88	3.22	13.25	60	5.86	5.89
WRCD01-01-53	0.60	25	5.86	3.22	13.29	60	5.9	5.81
WRCD01-01-54	0.60	24.97	5.78	3.22	13.42	60	5.71	5.84
WRCD01-01-55	0.60	25	5.84	3.22	13.32	60	5.82	5.86
WRCD01-01-60	1.80	25	5.91	3.22	13.19	60	5.84	5.97
WRCD01-01-61	1.80	24.96	5.83	3.25	13.3	60	5.81	5.85
WRCD01-01-62	1.80	24.96	5.80	3.2	13.36	60	5.68	5.92
WRCD01-01-63	1.80	24.97	5.78	3.23	13.42	60	5.96	5.59
WRCD01-01-77	0.10	24.92	7.92	3.24	9.09	60	7.91	7.92
WRCD01-01-78	0.10	24.94	8.03	3.21	8.89	60	8.03	8.02
WRCD01-01-79	0.10	24.92	7.96	3.24	9	60	7.94	7.98
WRCD01-01-80	0.35	25.02	8.03	3.24	8.96	60	8.01	8.05
WRCD01-01-81	0.35	25	7.99	3.24	9.02	60	7.97	8.01
WRCD01-01-82	0.35	24.98	7.99	3.24	9	60	7.97	8.01
WRCD01-01-83	0.60	25.04	7.97	3.24	9.1	60	8.05	7.89
WRCD01-01-84	0.60	24.94	7.95	3.24	9.04	60	7.88	8.02
WRCD01-01-140	0.10	25	10.05	3.23	4.91	60	10.11	9.98
WRCD01-01-141	0.10	24.99	10.04	3.23	4.92	60	10.07	10

Part Number	r (mm)	W (mm)	a (mm)	B (mm)	W_0 (mm)	$\alpha°$	a_1 (mm)	a_2 (mm)
WRCD01-01-95	0.10	17.1	2.49	3.24	12.13	60.00	2.52	2.45
WRCD01-01-96	0.10	17.09	2.45	3.24	12.19	60.00	2.52	2.38
WRCD01-01-97	0.35	17.07	2.38	3.24	12.32	60.00	2.29	2.46
WRCD01-01-98	0.35	17.1	2.40	3.24	12.31	60.00	2.51	2.28
WRCD01-01-102	0.60	17.06	2.46	3.24	12.14	60.00	2.41	2.51
WRCD01-01-104	0.60	17.06	2.42	3.24	12.22	60.00	2.45	2.39
WRCD01-01-93	0.10	17.04	3.44	3.24	10.16	60.00	3.51	3.37
WRCD01-01-94	0.10	17.08	3.39	3.24	10.31	60.00	3.42	3.35
WRCD01-01-99	0.35	17.08	3.47	3.24	10.14	60.00	3.51	3.43
WRCD01-01-100	0.35	17.05	3.42	3.24	10.22	60.00	3.46	3.37
WRCD01-01-101	0.60	17.11	3.42	3.24	10.28	60.00	3.46	3.37
WRCD01-01-103	0.60	17.09	3.43	3.24	10.24	60.00	3.46	3.39
WRCD01-01-136	0.10	14.01	0.98	3.23	12.06	60.00	0.98	0.97
WRCD01-01-137	0.10	14.05	0.92	3.23	12.22	60.00	0.96	0.87
WRCD01-01-132	0.10	14.01	2.98	3.23	8.06	60.00	2.92	3.03
WRCD01-01-133	0.10	14.01	2.97	3.22	8.08	60.00	2.99	2.94

Part Number	r (mm)	W (mm)	a (mm)	B (mm)	W_0 (mm)	$\alpha°$	a_1 (mm)	a_2 (mm)
WRCD01-01-110	0.10	11.82	0.89	3.24	10.05	60.00	0.8	0.97
WRCD01-01-111	0.10	11.98	0.99	3.24	10	60.00	1.01	0.97
WRCD01-01-112	0.35	11.98	0.97	3.22	10.04	60.00	1.01	0.93
WRCD01-01-113	0.35	11.96	0.96	3.24	10.05	60.00	0.91	1
WRCD01-01-114	0.60	11.86	0.88	3.22	10.1	60.00	0.93	0.83
WRCD01-01-115	0.60	12.02	0.95	3.2	10.13	60.00	0.93	0.96
WRCD01-01-116	0.10	11.94	1.99	3.22	7.97	60.00	1.93	2.04
WRCD01-01-117	0.10	12	1.98	3.2	8.05	60.00	1.97	1.98
WRCD01-01-118	0.35	11.96	1.96	3.2	8.05	60.00	2.04	1.87
WRCD01-01-119	0.35	12	1.92	3.2	8.16	60.00	1.95	1.89
WRCD01-01-120	0.60	11.98	1.90	3.2	8.19	60.00	1.89	1.9
WRCD01-01-121	0.60	12	1.88	3.22	8.24	60.00	1.85	1.91
WRCD01-01-130	0.10	12.1	2.94	3.24	6.22	60.00	2.86	3.02
WRCD01-01-131	0.10	12.05	2.91	3.23	6.24	60.00	2.91	2.9
WRCD01-01-138	0.10	12.04	3.71	3.23	4.62	60.00	3.77	3.65
WRCD01-01-139	0.10	12	3.69	3.23	4.62	60.00	3.71	3.67
WRCD01-01-134	0.10	8.99	1.43	3.23	6.13	60.00	1.41	1.45
WRCD01-01-135	0.10	8.76	1.45	3.24	5.87	60.00	1.5	1.39

Appendix B – Stress line plots for study 2

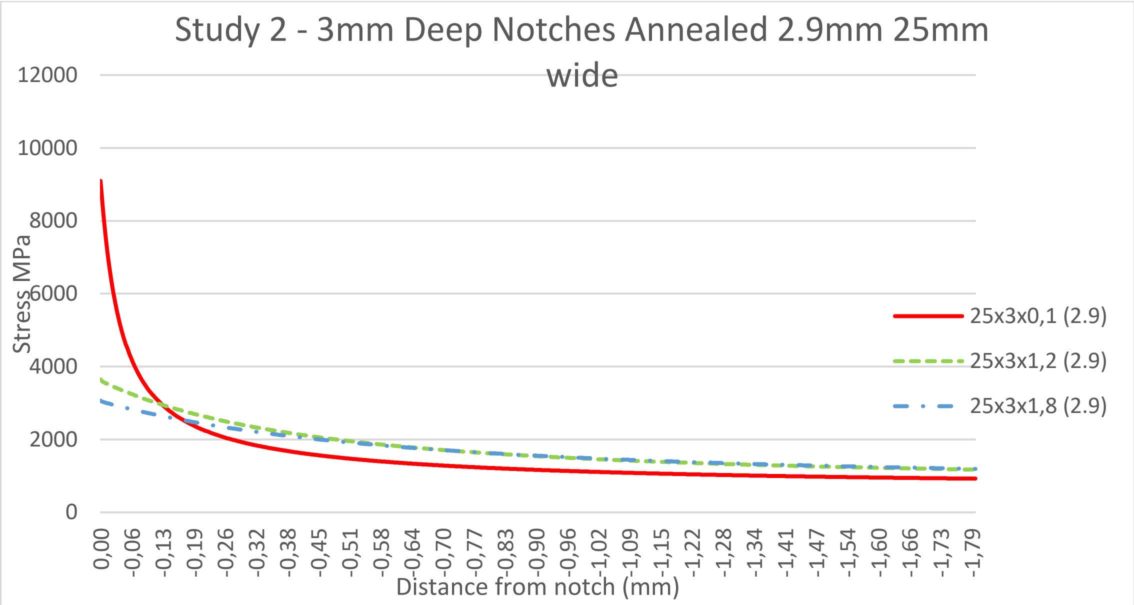

Figure B 1 - – Study 2 - Stress line plots for 25 mm wide samples

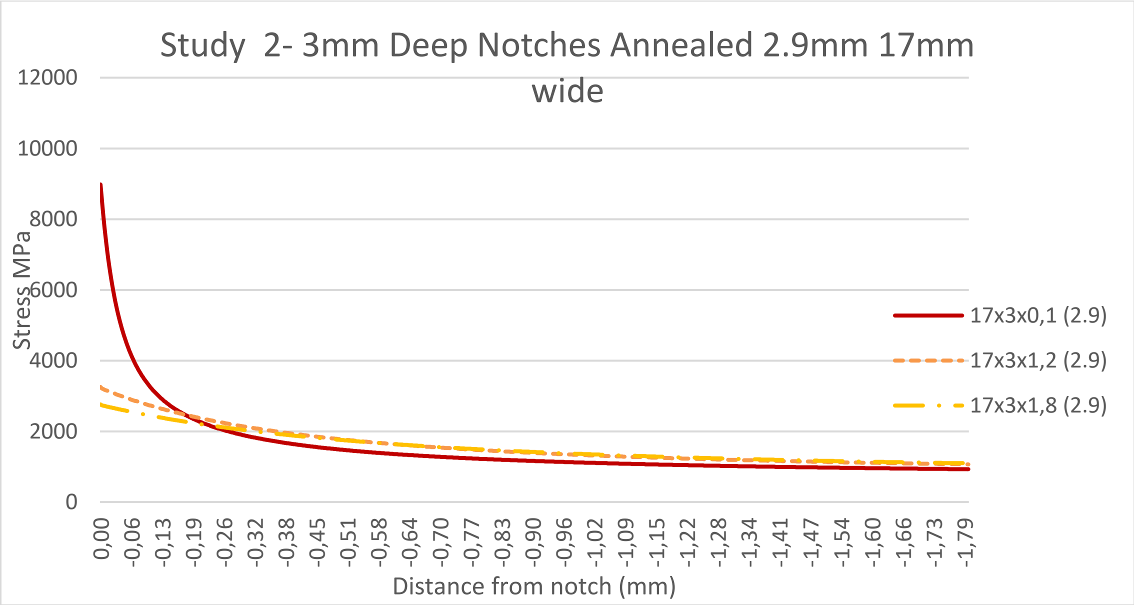

Figure B 2 - Study 2 – Stress line plots for 17 mm wide samples

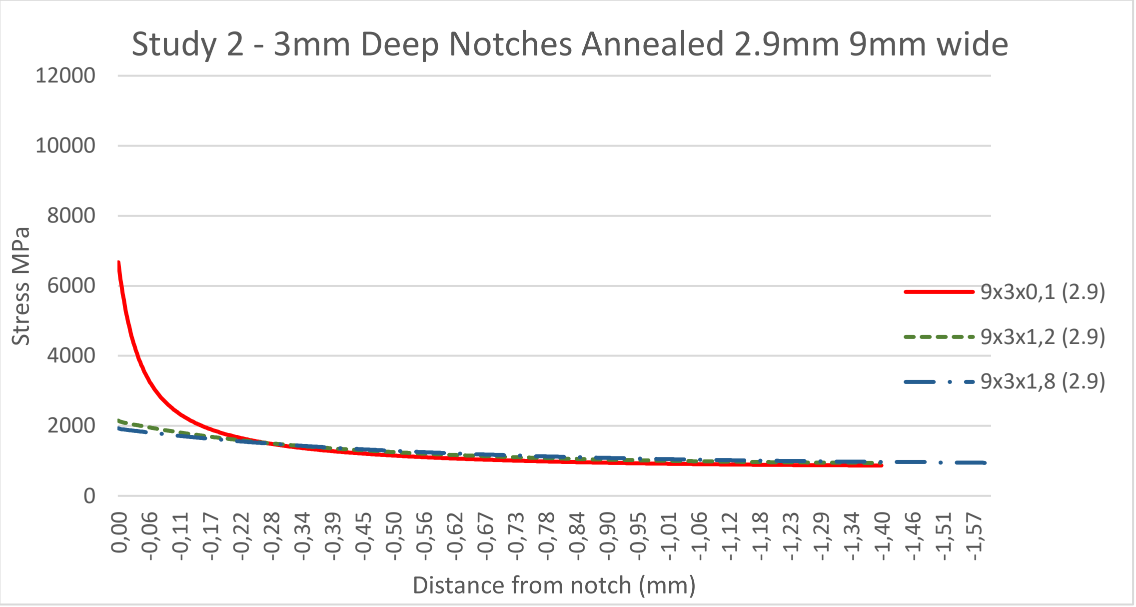

Figure B 3 - Study 2 - Stress line plots for 9 mm wide samples

Appendix C – Stress plots for study 3

Effect of angle on stress surrounding a notch

25 mm wide samples

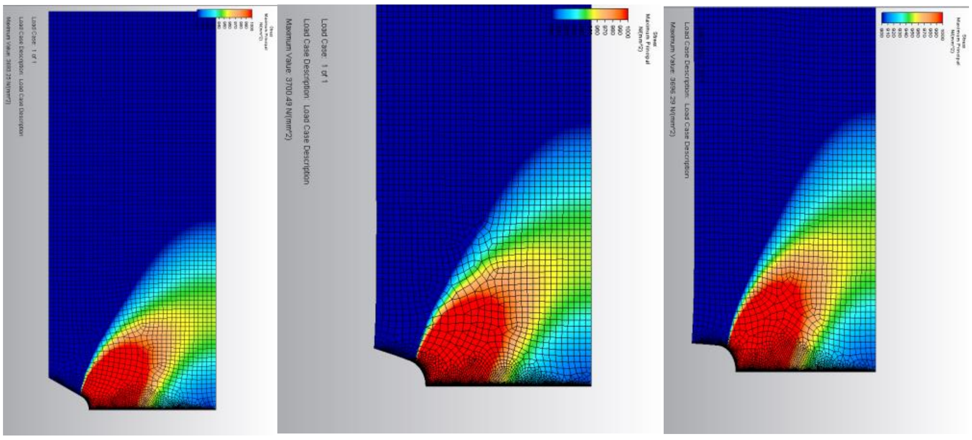

Figure C 1 - 3 mm deep 1.8 mm radius 60º, 30º and 0º

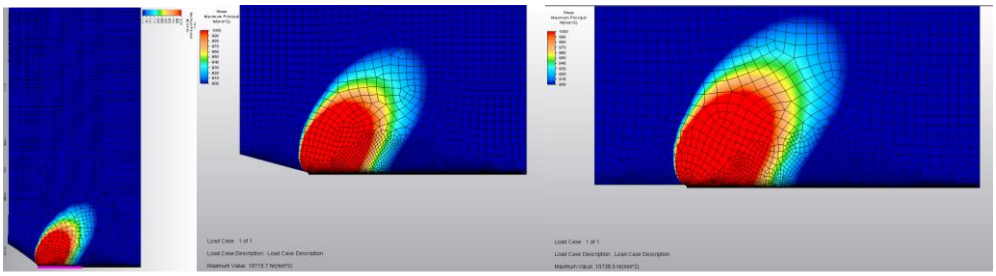

Figure C 2 - 3 mm deep 0.1 mm radius 60º, 30º and 0º

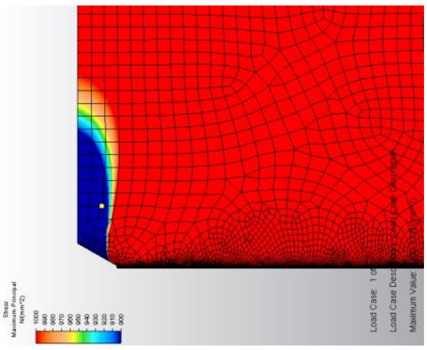

Figure C 3 - 1 mm deep angle 60º 0.1 mm radius

Effect of radius on stress surrounding a notch

25 mm wide samples

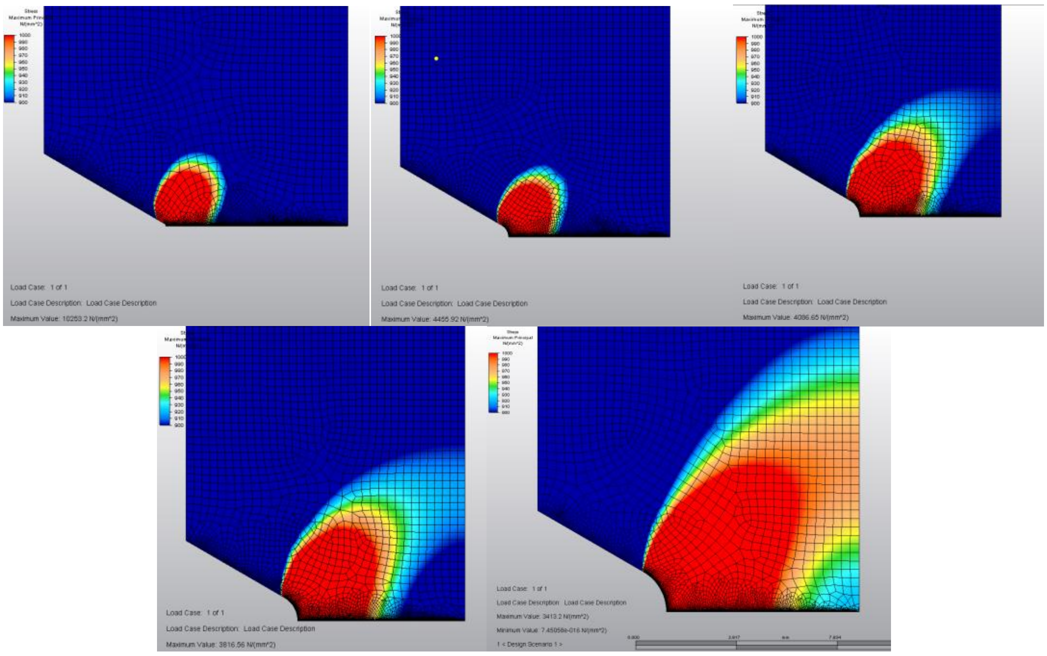

Figure C 4 - 5 mm deep 60º angle 0.1, 0.6, 1, 1.2 and 1.8 mm radii

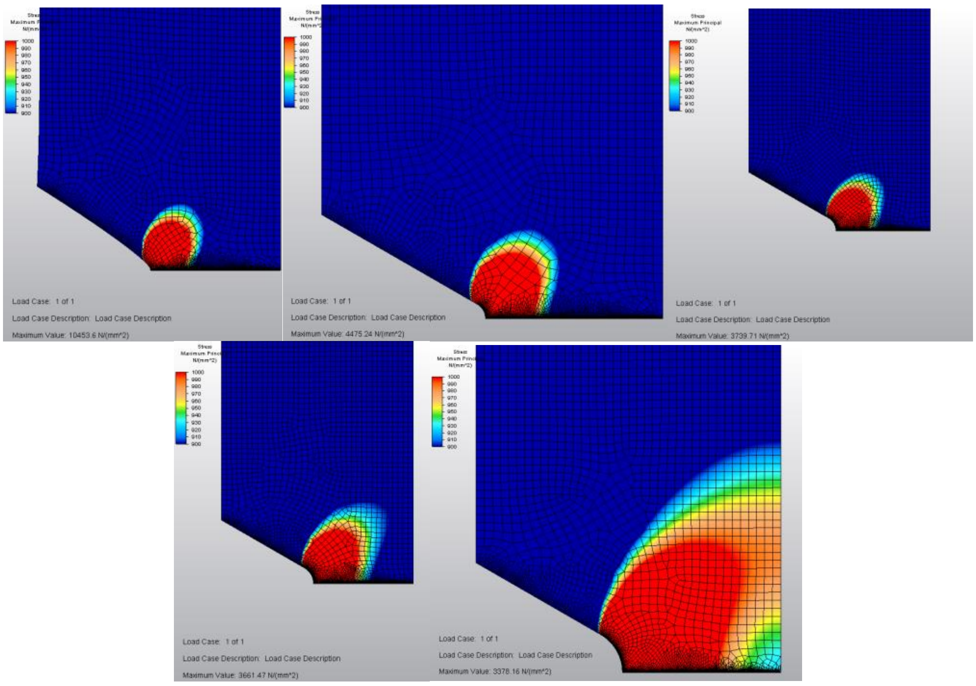

Figure C 5 - 6 mm deep 60º angle 0.1, 0.6, 1, 1.2 and 1.8 mm radii

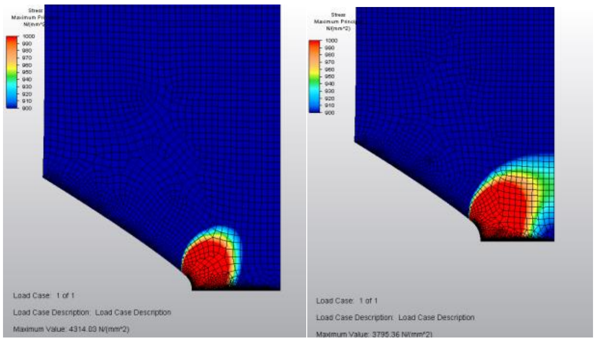

Figure C 6 - 6 mm deep 60º angle 0.6 and 1 mm radii

Effect of radius on stress surrounding a notch

17 mm wide samples

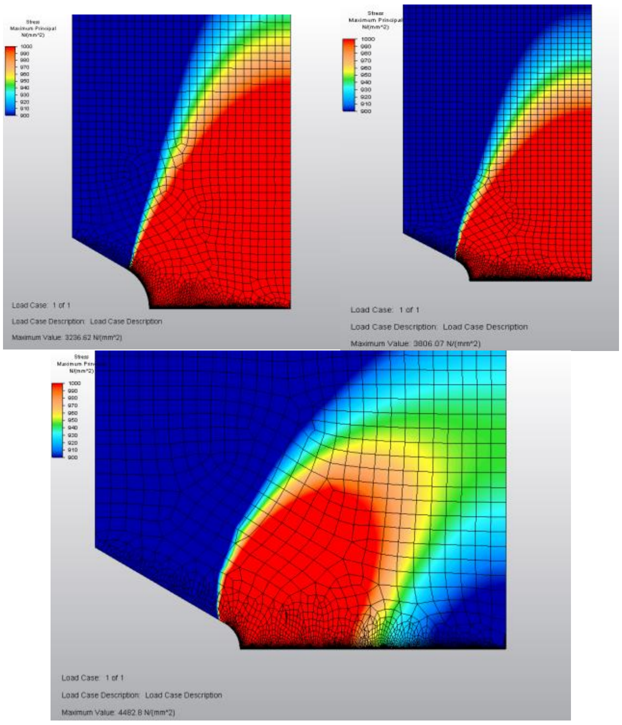

Figure C 7 - 3 mm deep and 60º angle 1.8, 1.2 and 1 mm radii

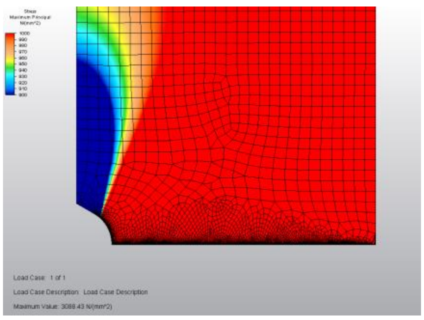

Figure C 8 - 1 mm deep and 60º angle 1 mm radius

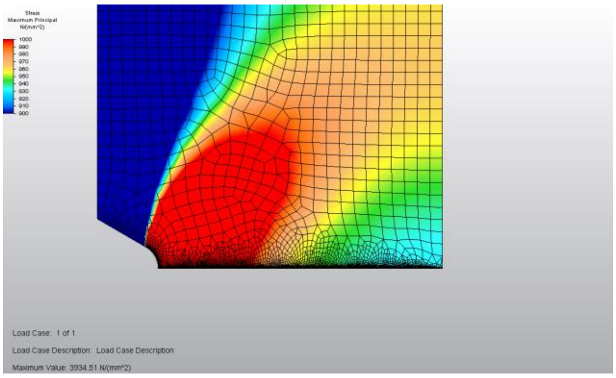

Figure C 9 - 1.5 mm deep and 60º angle 0.6 mm radius

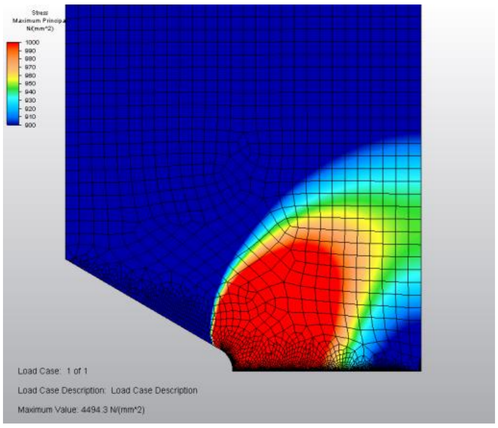

Figure C 10 - 4 mm deep and 60º angle 0.6 mm radius

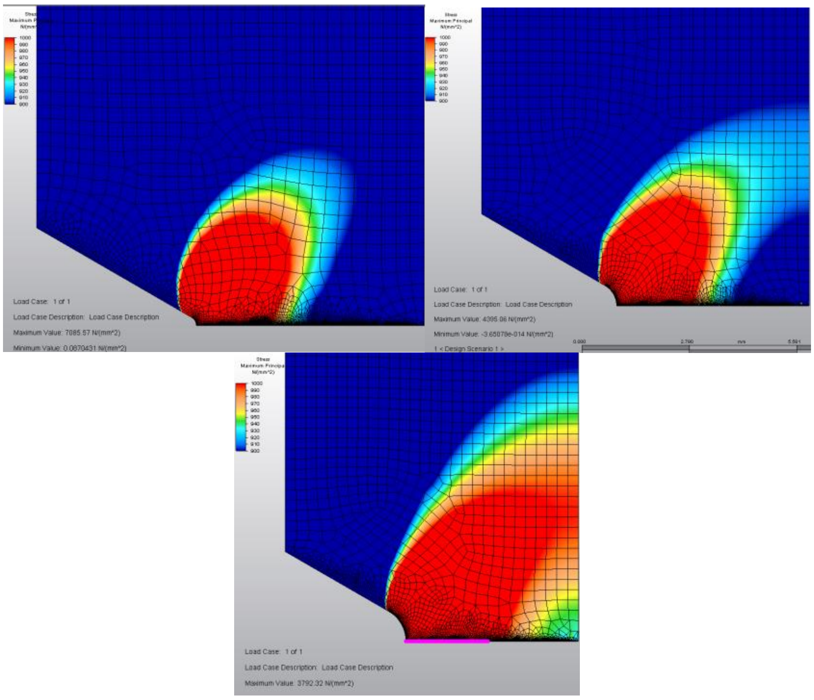

Figure C 11 - - 3.5 mm deep and 60º angle 0.2, 0.6 and 1 mm radii

Appendix D – Stress line plots for study 3

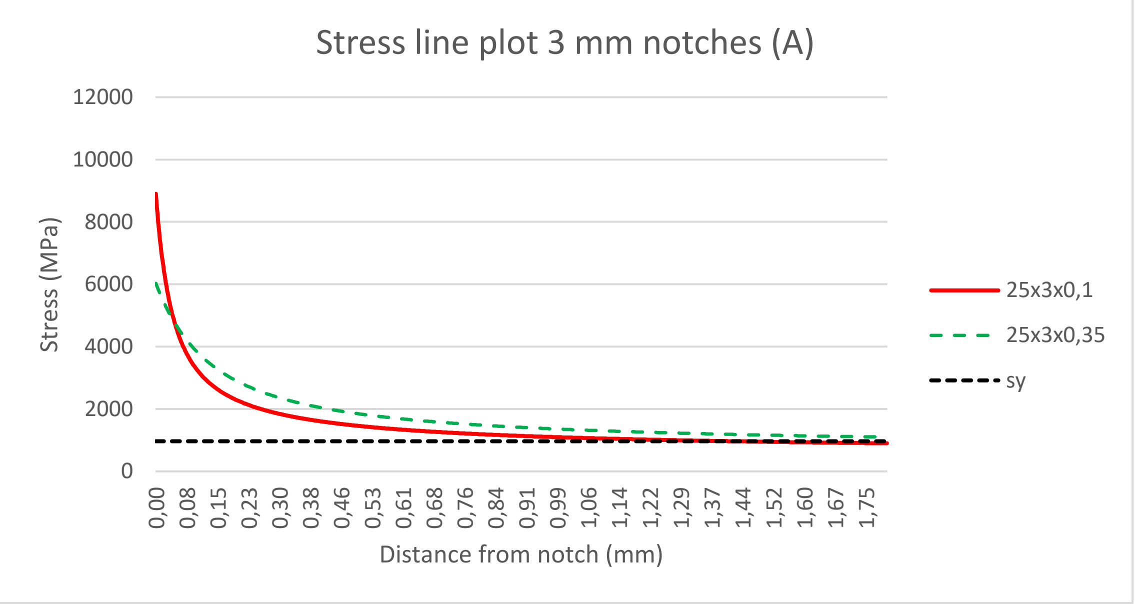

Figure D 1 - Stress line plots for 25 mm x 3 mm

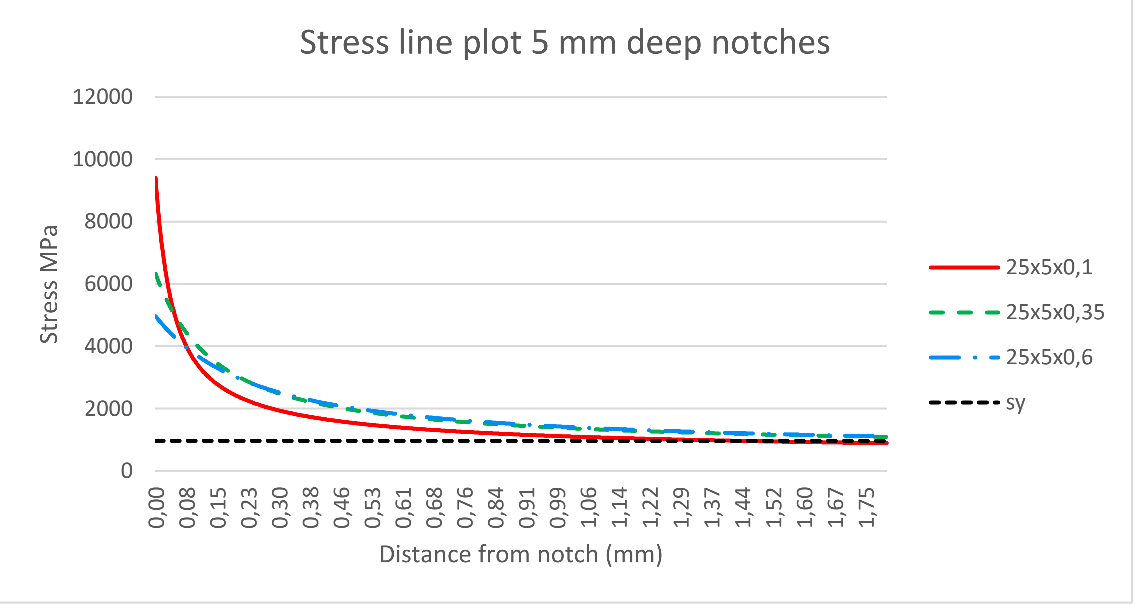

Figure D 2 - Stress line plots for 25 mm x 5 mm

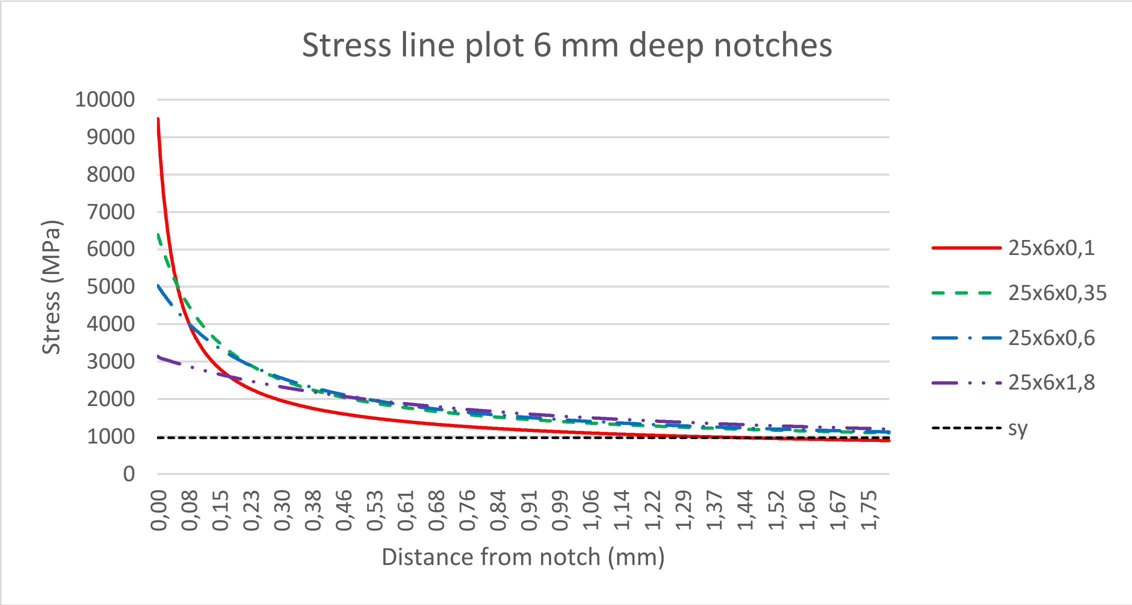

Figure D 3 - Stress line plots for 25 mm x 6 mm

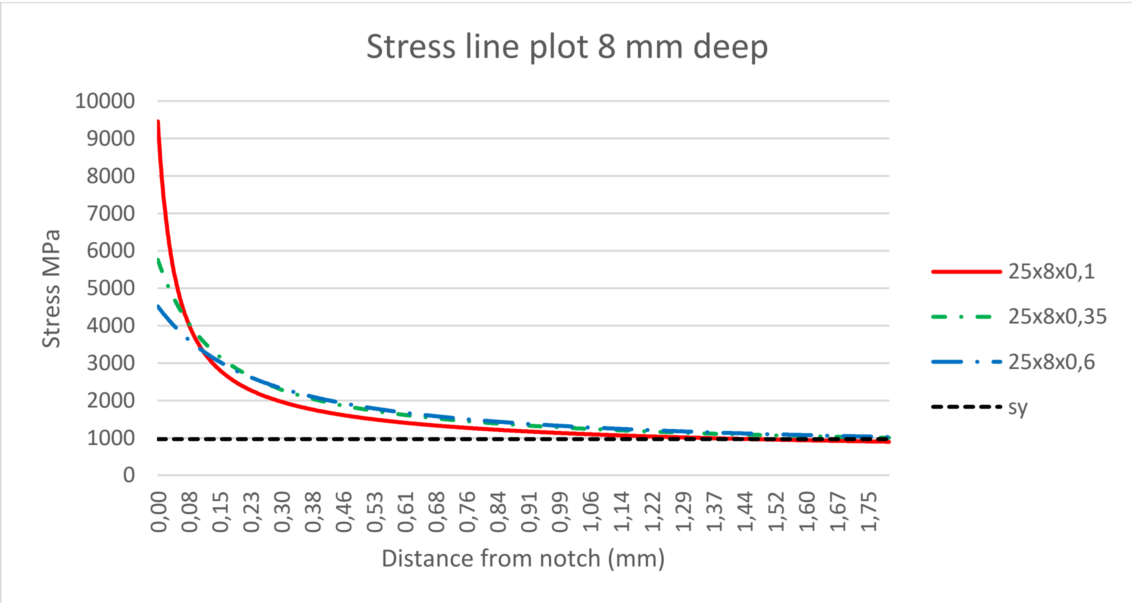

Figure D 4 - Stress line plots for 25 mm x 8 mm

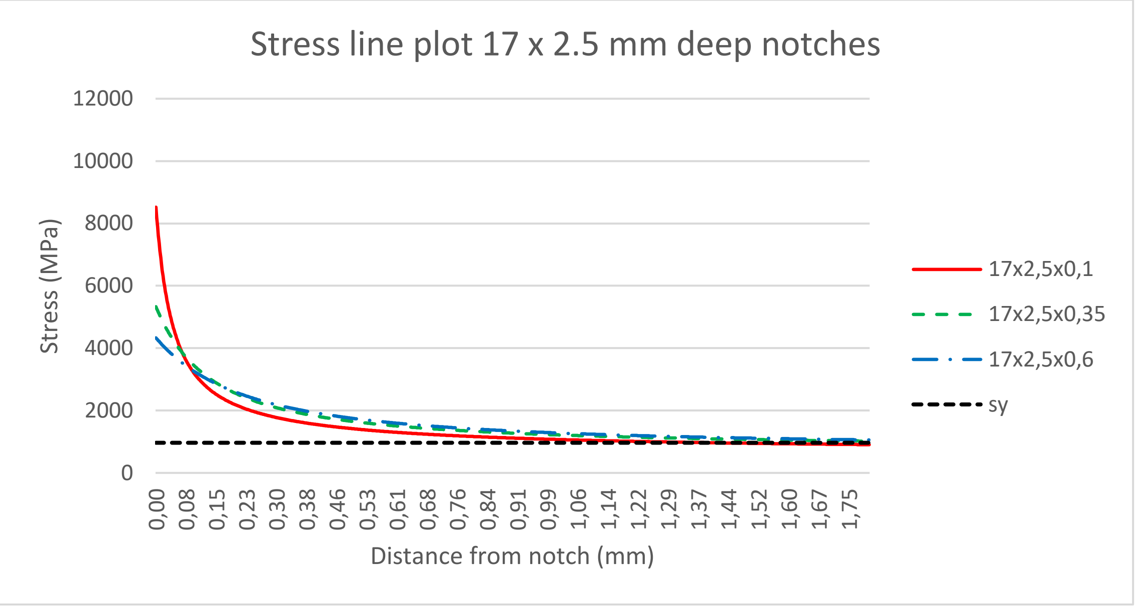

Figure D 5 - Stress line plots for 17 mm x 2.5 mm

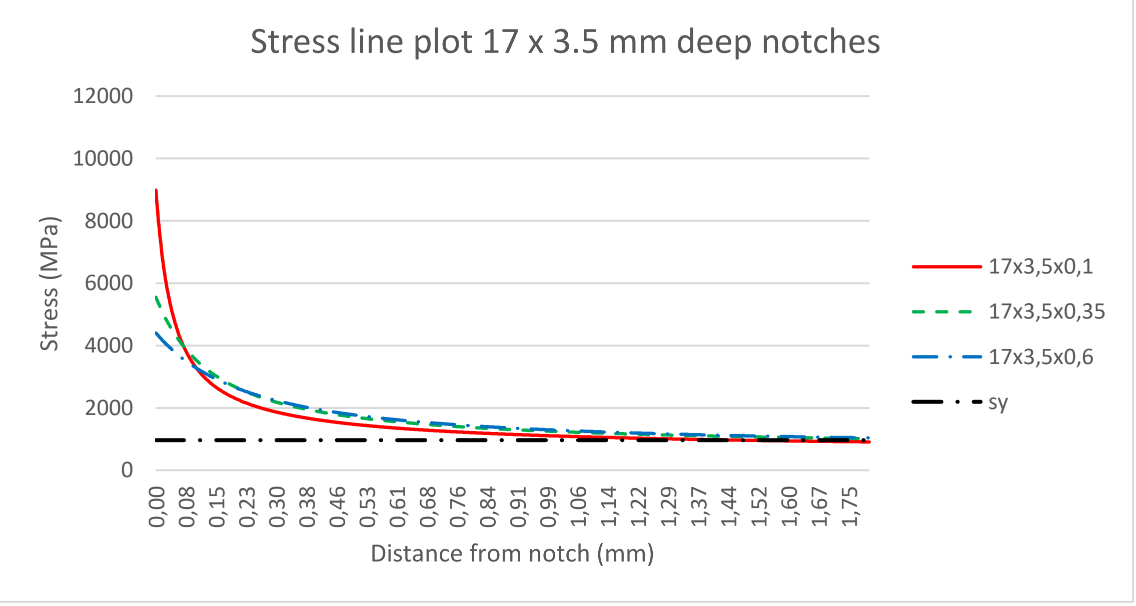

Figure D 6 - Stress line plots for 17 mm x 3.5mm

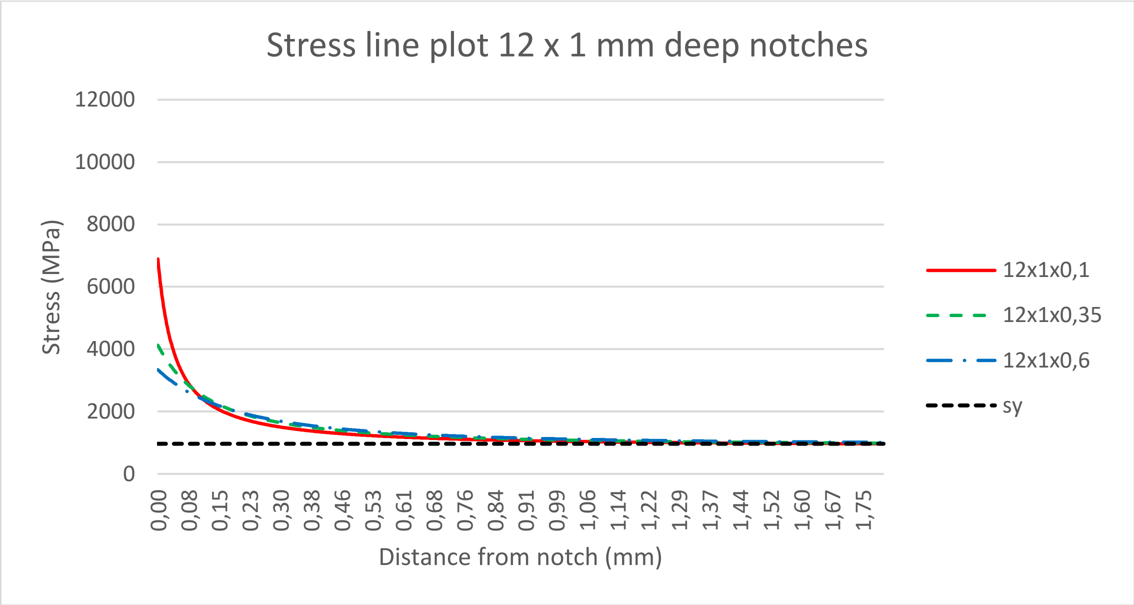

Figure D 7 - Stress line plots for 12 mm x 1 mm

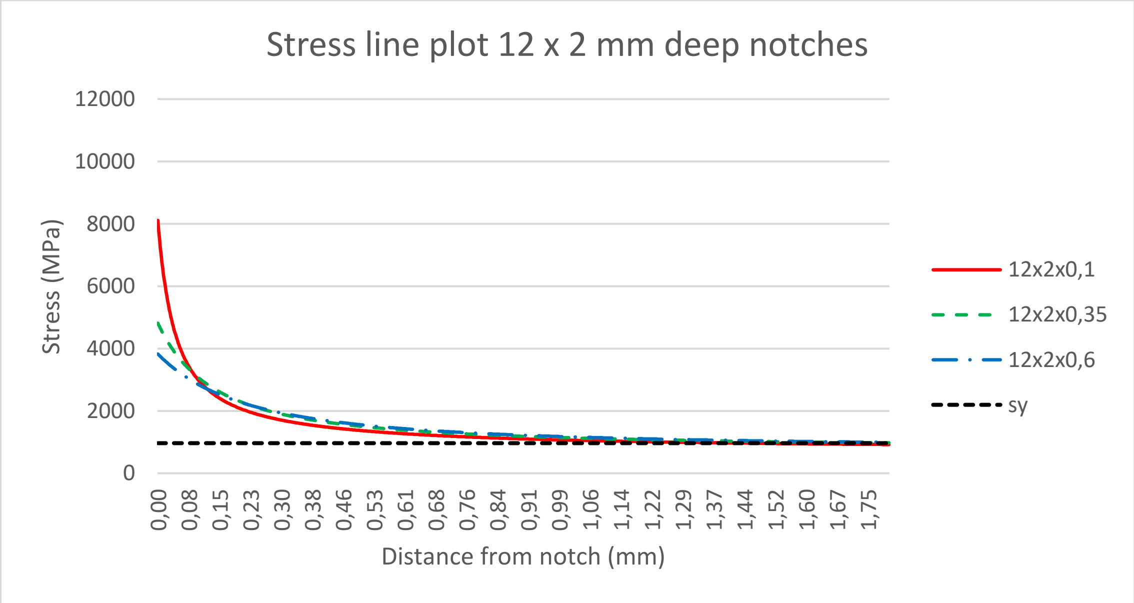

Figure D 8 - Stress line plots for 12 mm x 2 mm

Appendix E – Post grinding material thickness

Table E 1 - Post grinding material thickness

	Distance from plate end					
Plate no.	20 (mm)	50 (mm)	125 (mm)	200 (mm)	275 (mm)	
	Measured thickness (mm)					
12	3,08	3,09	3,1	3,13	3,09	pin length 2.96 mm plunge 2.98 mm
13	3,1	3,13	3,12	3,13	3,12	pin length 2.96 mm plunge 2.98 mm
14	3,09	3,08	3,1	3,08	3,08	pin length 2.96 mm plunge 2.98 mm
15	3,08	3,08	3,09	3,09	3,09	pin length 2.96 mm plunge 2.98 mm
16	3,12	3,13	3,14	3,15	3,13	pin length 3 mm plunge 3.02 mm
19	3,12	3,15	3,17	3,16	3,15	pin length 3 mm plunge 3.02 mm
20	3,1	3,11	3,12	3,12	3,1	pin length 2.96 mm plunge 2.98 mm
21	3,12	3,1	3,1	3,1	3,1	pin length 2.96 mm plunge 2.98 mm
22	3,11	3,11	3,1	3,1	3,1	pin length 2.96 mm plunge 2.98 mm
23	3,15	3,15	3,16	3,14	3,14	pin length 3 mm plunge 3.02 mm
24	3,06	3,08	3,08	3,09	3,08	pin length 2.9 mm plunge 2.92 mm

Appendix F – Sample distribution

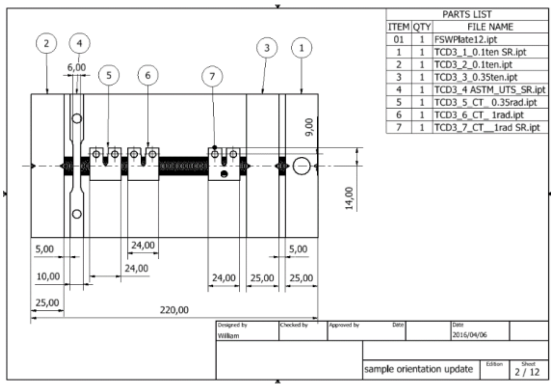

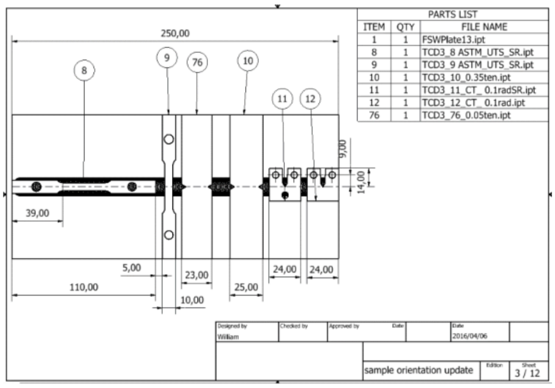

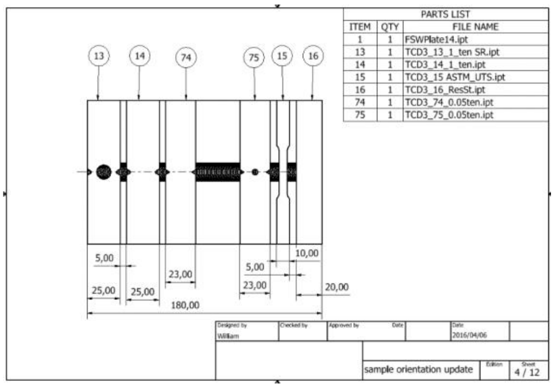

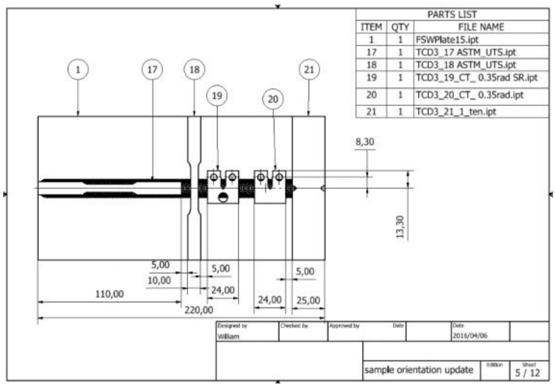

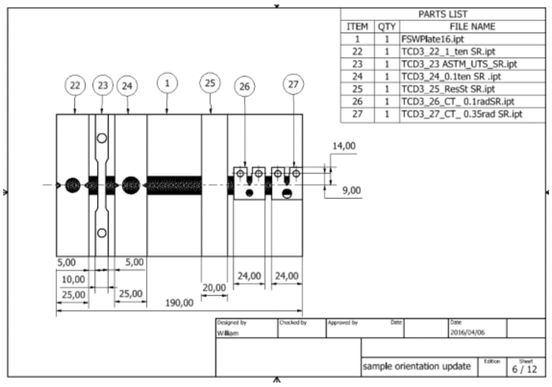

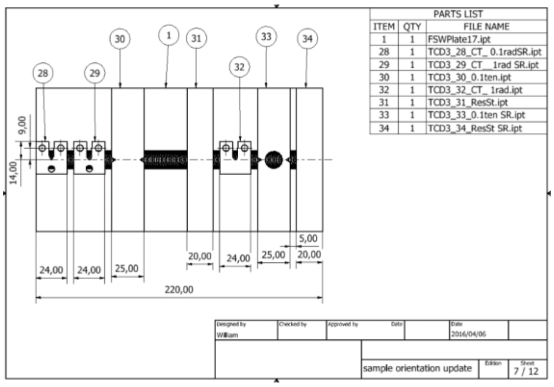

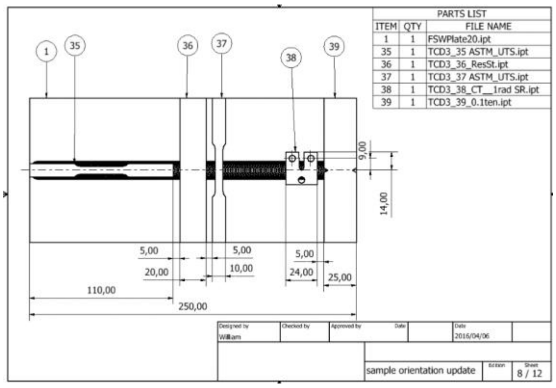

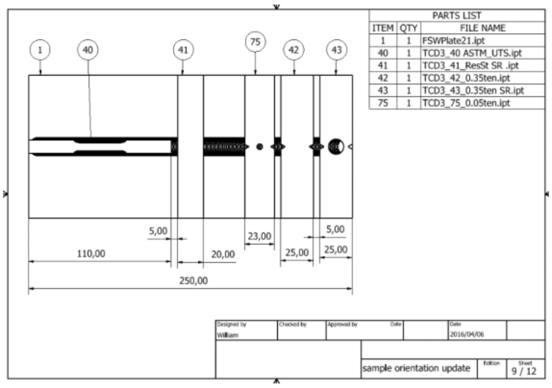

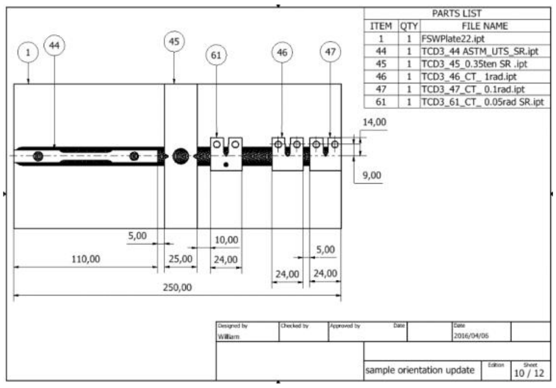
PARTS LIST
ITEM QTY FILE NAME
1 1 FSWPlate22.ipt
44 1 TCD3_44 ASTM_UTS_SR.ipt
45 1 TCD3_45_0.35ten SR .ipt
46 1 TCD3_46_CT_ 1rad.ipt
47 1 TCD3_47_CT_ 0.1rad.ipt
61 1 TCD3_61_CT_ 0.05rad SR.ipt
14,00
9,00
5,00
10,00
5,00
110,00
25,00
24,00
24,00
24,00
250,00
Designed by
William
Checked by
Approved by
Date
Date
2016/04/06
sample orientation update
Edition
Sheet
10 / 12

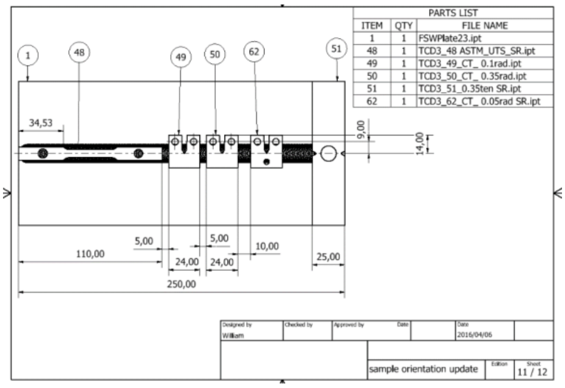
PARTS LIST
ITEM QTY FILE NAME
1 1 FSWPlate23.ipt
48 1 TCD3_48 ASTM_UTS_SR.ipt
49 1 TCD3_49_CT_ 0.1rad.ipt
50 1 TCD3_50_CT_ 0.35rad.ipt
51 1 TCD3_51_0.35ten SR.ipt
62 1 TCD3_62_CT_ 0.05rad SR.ipt
34,53
9,00
14,00
5,00
5,00
10,00
110,00
24,00
24,00
25,00
250,00
Designed by
William
Checked by
Approved by
Date
Date
2016/04/06
sample orientation update
Edition
Sheet
11 / 12

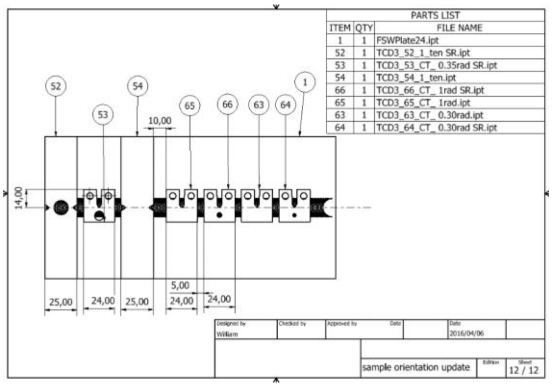
PARTS LIST
ITEM QTY FILE NAME
1 1 FSWPlate24.ipt
52 1 TCD3_52_1_ten SR.ipt
53 1 TCD3_53_CT_ 0.35rad SR.ipt
54 1 TCD3_54_1_ten.ipt
66 1 TCD3_66_CT_ 1rad SR.ipt
65 1 TCD3_65_CT_ 1rad.ipt
63 1 TCD3_63_CT_ 0.30rad.ipt
64 1 TCD3_64_CT_ 0.30rad SR.ipt
10,00
14,00
5,00
25,00
24,00
25,00
24,00
24,00
Designed by
William
Checked by
Approved by
Date
Date
2016/04/06
sample orientation update
Edition
Sheet
12 / 12

T

Appendix G – Weld study sample dimensions

Tensile Samples

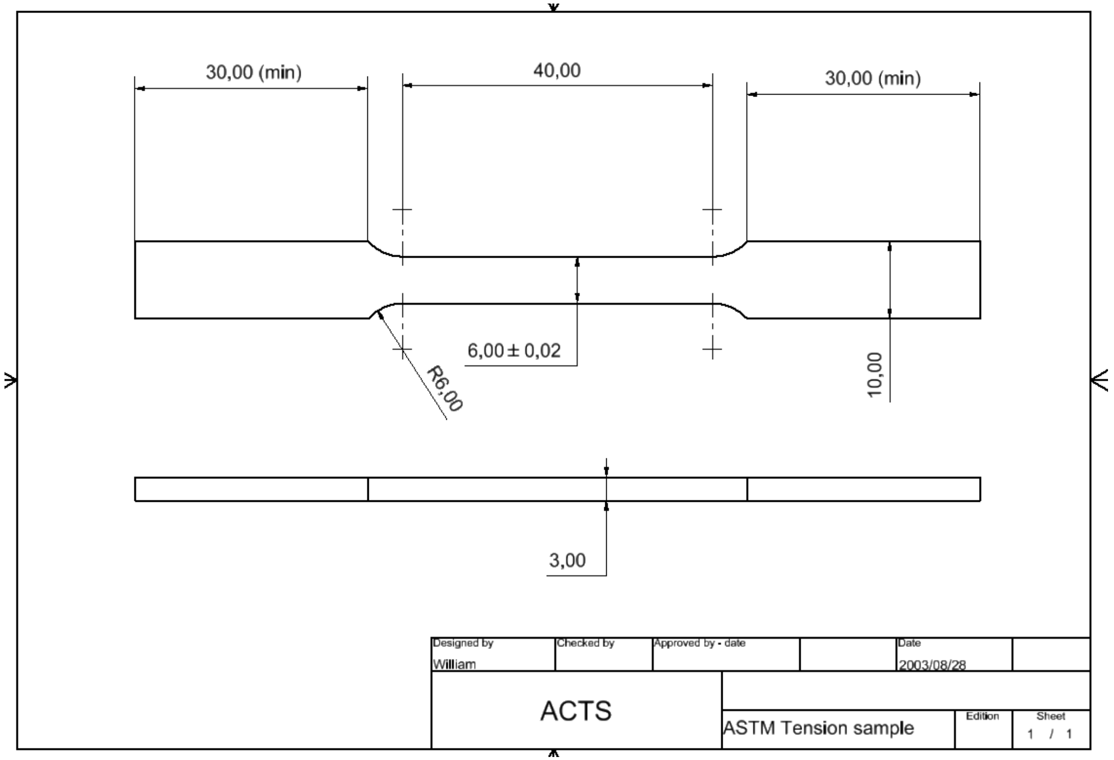

Figure G 1 - Sub-size tension sample drawing

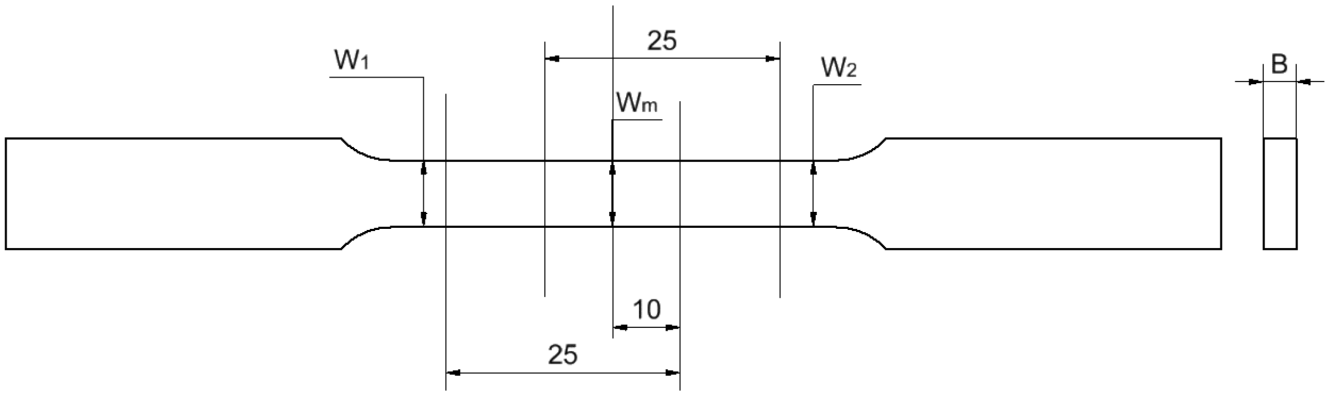

Figure G 2 - Measurements of tension specimens

Table G 1 – Batch B tensile measurements

Part #	Orientation	B	W1	Wm	W2	Force
TCD3_55	Trans	3,16	6,01	6,05	6,06	19,418
TCD3_56	Trans	3,16	6,02	6,04	6	19,359
TCD3_57	Trans	3,16	5,98	5,98	5,97	19,283
TCD3_58	Long	3,16	6	6,02	6,02	19,844
TCD3_59	Long	3,16	5,99	6	6,01	19,203
TCD3_60	Long	3,16	5,97	5,98	5,97	19,613

Transverse

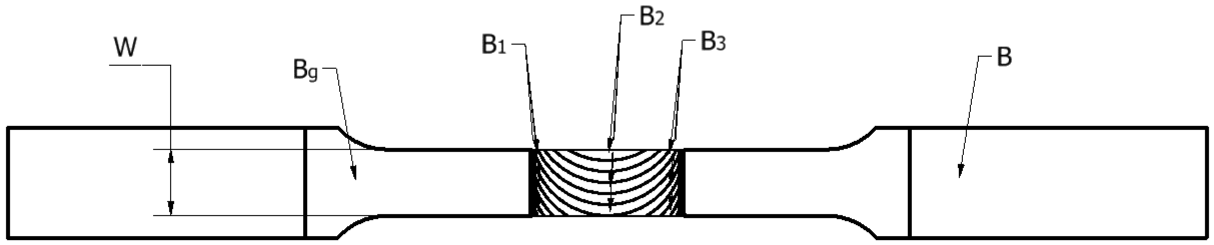

Figure G 3 - Transverse tension specimen diagram

Table G 2 - Transeverse tension specimens measurements

Part #	condition	B	B_g	B1			B2			B3			W	B_{fail}	
														Smallest section	
TCD3_15	AW	3,16	3,11	3,13	3,13	3,13	3,07	3,06	3,05	3,25	3,26	3,26	6,05	3,11	B_g
TCD3_18	AW	3,18	3,12	3,1	3,11	3,12	3,14	3,136	3,12	3,31	3,3	3,3	6	3,132	B_2
TCD3_37	AW	3,17	3,134	3,1	3,12	3,15	3,11	3,13	3,14	3,32	3,36	3,33	5,97	3,134	B_g
TCD3_4	SR	3,17	3,11	3,08	3,09	3,09	3,1	3,1	3,11	3,19	3,23	3,26	5,97	3,11	B_g
TCD3_9	SR	3,17	3,14	3,1	3,1	3,1	3,1	3,12	3,12	3,27	3,3	3,29	6,09	3,113333	B_2
TCD3_23	SR	3,2	3,164	3,18	3,18	3,18	3,08	3,08	3,08	3,21	3,23	3,25	5,98	3,08	B_2

Longitudinal

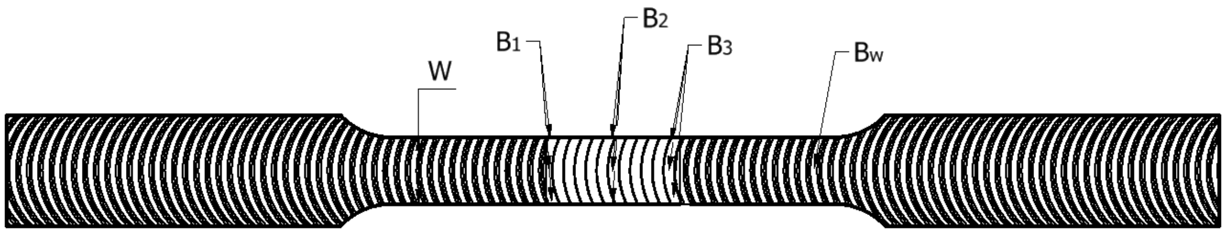

Figure G 4 - Longitudinal tension specimen diagram

Table G 3 - Longitudinal tension specimens measurements

Part #	Condition	B	B_w	B_1			B_2			B_3				B_{fail}	
				1	2	3	1	2	3	1	2	3	W	Smallest section	
TCD3_17	AW		3,22	3,12	3,15	3,2	3,12	3,15	3,18	3,12	3,14	3,18	6,04	3,22	B_w
TCD3_35	AW		3,2	3,06	3,09	3,14	3,14	3,08	3,05	3,06	3,1	3,15	6	3,2	B_w
TCD3_40	AW		3,09	2,96	3	3,04	3,03	2,98	2,95	3,03	3	2,97	6		
TCD3_8	SR		3,19	3,14	3,13	3,11	3,12	3,1	3,08	3,15	3,12	3,1	6,02	3,19	B_w
TCD3_44	SR		3,11	3,1	3,09	3,06	3,08	3,07	3,04	3,07	3,05	3,04	6		
TCD3_48	SR		3,26	3,22	3,21	3,2	3,2	3,19	3,17	3,19	3,19	3,18	6,01	3,187	B_2

TCD Drawings and measured dimensions

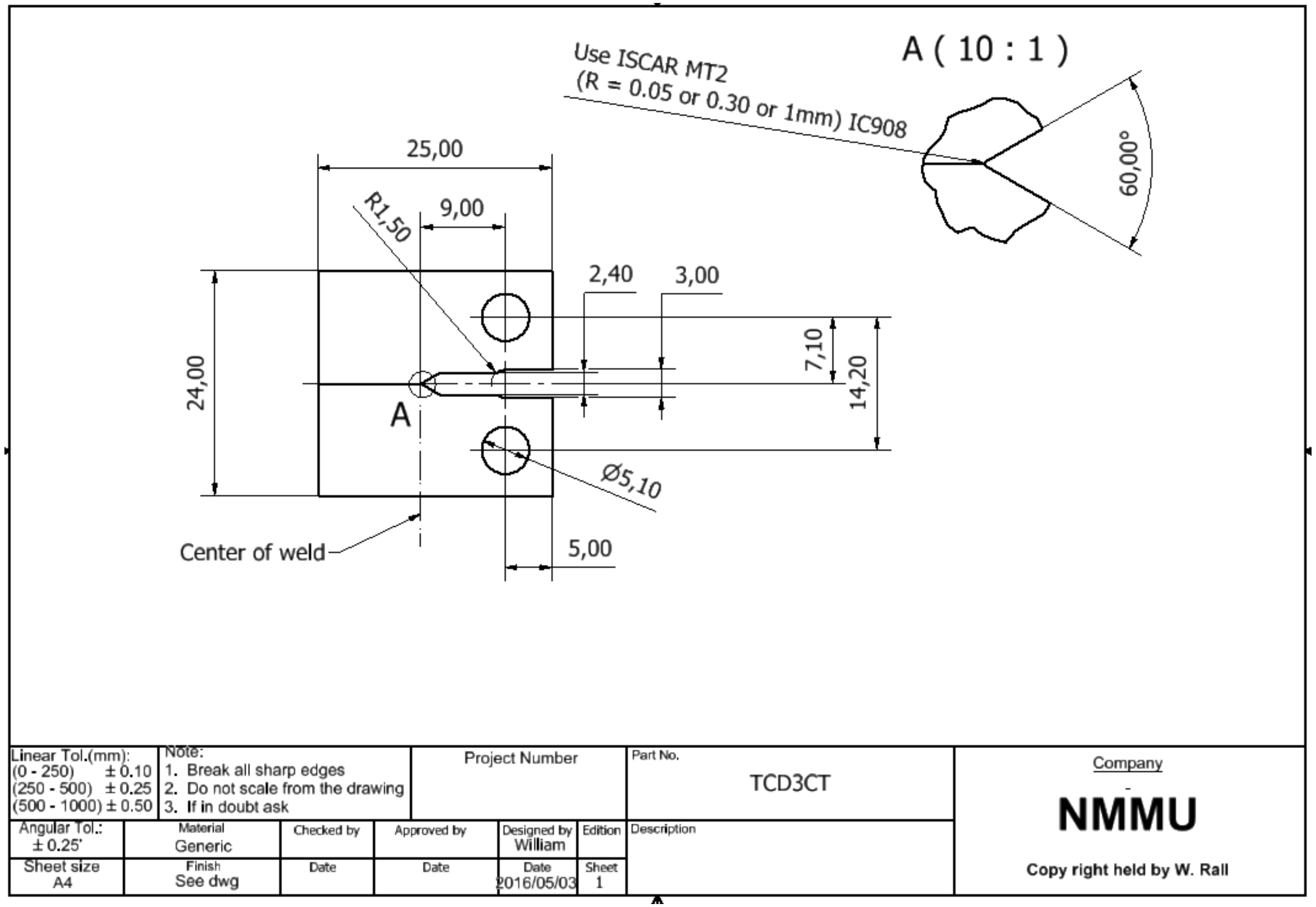

Figure G 5 - CT specimen drawing

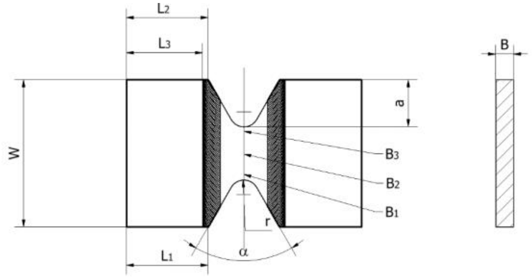

Figure G 6 - Welded DENT specimen diagram

Table G 4 - Welded DENT specimens measurements

Part #	Condition	r (mm)	W (mm)	L1 (mm)	L2 (mm)	L3 (mm)	a1 (mm)	a2 (mm)	B1 (mm)	B2 (mm)	B3 (mm)	a (mm)	B (mm)	Offset (mm)	Centre offset (mm)	Test Speed (mm/min)
TCD3_1	SR	0.1	25.06	57.8	57.88	52.06	2.91	2.94	3.09	3.101	3.084	2.925	3.092	-0.08	0.61	2
TCD3_2	AW	0.1	25	57.47	57.18	52.11	3	3	3.108	3.106	3.126	3	3.113	0.29	-0.14	2
TCD3_24	SR	0.1	25	57.76	57.8	52.35	3.03	2.92	3.052	3.064	3.094	2.975	3.070	-0.04	0.24	2
TCD3_30	AW	0.1	25.02	57.17	57.13	52.18	3	2.87	3.086	3.108	3.11	2.935	3.101	0.04	-0.26	2
TCD3_33	SR	0.1	25.01	57.8	57.62	52.17	2.91	2.97	3.116	3.133	3.094	2.94	3.114	0.18	0.24	2
TCD3_39	AW	0.1	25.05	57.84	57.84	52.24	2.96	2.97	3.085	3.091	3.075	2.965	3.084	0	0.39	2
TCD3_3	AW	0.35	25.05	57.68	56.61	52.35	2.91	2.98	3.093	3.129	3.131	2.945	3.118	1.07	-0.806	2
TCD3_10	AW	0.35	25.04	57.3	57.6	51.9	2.93	3.01	3.113	3.117	3.132	2.97	3.121	-0.3	0.634	2
TCD3_42	AW	0.35	24.92	57.67	57.69	52.42	3.02	2.89	3.001	2.993	2.989	2.955	2.994	-0.02	0.204	2
TCD3_43	SR	0.35	25.01	57.53	56.81	52.06	2.98	2.91	3.062	3.021	3.003	2.945	3.029	0.72	-0.316	2
TCD3_45	SR	0.35	24.99	57.19	57.07	51.85	2.88	2.94	3.005	3.029	3.028	2.91	3.021	0.12	0.154	2
TCD3_51	SR	0.35	24.99	57.21	57.08	51.92	2.98	2.94	3.207	3.195	3.185	2.96	3.196	0.13	0.094	2

Part #	Condition	r (mm)	W (mm)	L1 (mm)	L2 (mm)	L3 (mm)	a1 (mm)	a2 (mm)	B1 (mm)	B2 (mm)	B3 (mm)	a (mm)	B (mm)	Offset (mm)	Centre offset (mm)	Test Speed (mm/min)
TCD3_13	SR	1	24.76	56.52	56.6	52.3	2.97	2.98	3.05	3.03	3.06	2.975	3.047	-0.08	-0.391	2
TCD3_14	AW	1	24.99	56.74	56.94	52.23	2.97	2.96	3.041	3.039	3.045	2.965	3.042	-0.2	0.019	2
TCD3_21	AW	1	24.98	57.24	57.24	52.33	2.98	3.02	3.123	3.113	3.127	3	3.121	0	0.219	2
TCD3_22	SR	1	24.74	57.44	57.6	52.3	2.84	2.73	3.123	3.131	3.14	2.785	3.131	-0.16	0.609	2
TCD3_52	SR	1	25.01	56.25	56.94	51.84	2.87	3.01	3.146	3.126	3.121	2.94	3.131	-0.69	0.409	2
TCD3_54	AW	1	25.03	56.79	56.86	51.7	2.9	2.92	3.08	3.093	3.098	2.91	3.090	-0.07	0.469	2

TCD3_73	SR	0.05	22.24				3.13	2.97	3.044	3.027	3.07	3.05	3.047	0	-4.691	2
TCD3_74	AW	0.05	22.29				3.36	3.18	3.095	3.047	3.054	3.27	3.065	0	-4.691	2
TCD3_75	SR	0.05	22.43				3.06	3.12	3.038	3.04	3.054	3.09	3.044	0	-4.691	2
TCD3_76	AW	0.05	22.53				3.47	3.27	3.15	3.12	3.114	3.37	3.128	0	-4.691	2

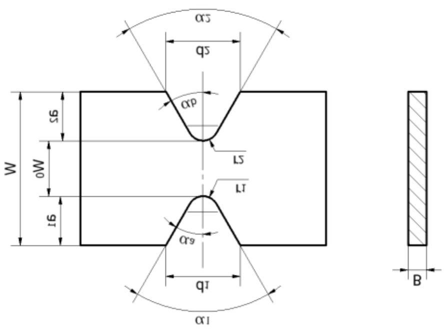

Figure G 7 - Parent plate DENT specimen diagram

Table G 5 - Parent plate DENT specimens measurements

Part Number	r (mm)	W (mm)	a (mm)	B (mm)	W (mm)	α (°)	Condition	a1 (mm)	a2 (mm)
TCD3_67	0.10	25.11	3.48	3.18	18.16	60.00	parent	3.32	3.63
TCD3_68	0.10	25.08	3.44	3.19	18.2	60.00	parent	3.32	3.56
TCD3_69	0.35	24.96	2.87	3.18	19.23	60.00	parent	2.88	2.85
TCD3_70	0.35	25.06	2.92	3.19	19.22	60.00	parent	2.9	2.94
						60.00			
TCD3_71	1.00	25.11	2.86	3.17	19.39	60.00	parent	2.91	2.81
TCD3_72	1.00	24.96	2.78	3.18	19.4	60.00	parent	2.78	2.78
TCD3_83	0.05	25.14	3.38	3.20	18.38	60.00	parent	3.49	3.27
TCD3_84	0.05	25.14	3.32	3.20	18.5	60.00	parent	3.24	3.4

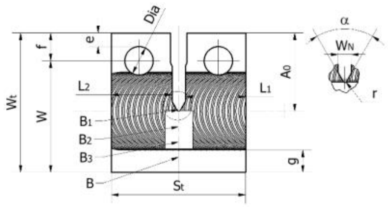

Figure G 8 - Welded CT specimen diagram

Table G 6 - Welded CT specimens measurments

Part #	Condition	r (mm)	W_N (mm)	W_t (mm)	A_0 (mm)	e (mm)	Dia. (mm)	g (mm)	B_1 (mm)	B_2 (mm)	B_3 (mm)	B (mm)	B_{av} (mm)	S_t (mm)	F (mm)	W (mm)	Test Speed (mm/min)
TCD3_11	SR	0.05	2.36	25.13	14	2.5	5.09	3.78	3.097	3.082	3.084	3.09	3.088	23.94	5.045	20.085	0.5
TCD3_12	AW	0.05	2.39	25.06	14.19	2.38	5.06	3.31	3.092	3.097	3.103	3.08	3.093	24.04	4.91	20.15	0.5
TCD3_26	SR	0.05	2.39	25.02	14.17	2.56	5.09	3.71	3.034	3.05	3.122	3.12	3.082	23.99	5.105	19.915	0.5
TCD3_28	SR	0.05	2.38	25.05	13.85	2.49	5.1	4.41	3.124	3.111	3.116	3.06	3.103	24.07	5.04	20.01	0.5
TCD3_47	AW	0.05	2.36	25.05	14.05	2.49	5.1	4.03	3.01	3.003	3.027	3.085	3.031	24.04	5.04	20.01	0.5
TCD3_49	AW	0.05	2.38	25.11	14.07	2.5	5.1	3.74	3.2	3.187	3.202	3.13	3.18	24.01	5.05	20.06	0.5
TCD3_61	SR	0.05	2.41	24.95	14.59	2.29	5.15	3.97	3.027	3.024	3.041	3.124	3.054	23.92	4.865	20.085	0.5
TCD3_62	SR	0.05	2.39	24.84	14.47	2.42	5.07	4	3.196	3.183	3.158	3.165	3.176	24.12	4.955	19.885	0.5
TCD3_5	AW	0.3	2.39	25.13	13.88	2.46	5.1	4.52	3.11	3.105	3.1	3.08	3.099	24.02	5.01	20.12	0.5
TCD3_19	SR	0.3	2.41	25.07	14.13	2.46	5.1	3.86	3.12	3.102	3.088	3.09	3.1	23.98	5.01	20.06	0.5
TCD3_20	AW	0.3	2.4	24.91	13.65	2.44	5.09	4.14	3.108	3.085	3.087	3.1	3.095	24.04	4.985	19.925	0.5
TCD3_27	SR	0.3	2.43	25.02	14.28	2.45	5.1	3.78	3.017	3.025	3.111	3.12	3.068	24.04	5	20.02	0.5
TCD3_50	AW	0.3	2.41	25.07	13.77	2.53	5.1	4.11	3.165	3.163	3.174	3.12	3.156	24.09	5.08	19.99	0.5
TCD3_53	SR	0.3	2.42	25.07	13.73	2.5	5.1	4.5	3.091	3.092	3.094	3.06	3.084	24.01	5.05	20.02	0.5
TCD3_63	AW	0.3	2.45	25.07	14.23	2.39	5.09	3.96	3.104	3.094	3.141	3.095	3.1085	24.03	4.935	20.135	0.5
TCD3_64	SR	0.3	2.45	25.06	14.23	2.48	5.11	3.89	3.083	3.071	3.077	3.099	3.0825	23.95	5.035	20.025	0.5

Part #	Condition	r (mm)	W_N (mm)	W_t (mm)	A_0 (mm)	e (mm)	Dia. (mm)	g (mm)	B_1 (mm)	B_2 (mm)	B_3 (mm)	B (mm)	Bav (mm)	S_t (mm)	F (mm)	W (mm)	Test Speed (mm/min)
TCD3_6	AW	1	2.45	25.08	14.26	2.4	5.1	3.55	3.095	3.083	3.08	3.08	3.085	24.03	4.95	20.13	0.5
TCD3_7	SR	1	2.41	25.1	14.05	2.3	5.11	3.84	3.137	3.093	3.062	3.07	3.091	24.06	4.855	20.245	0.5
TCD3_29	SR	1	2.4	25.04	14.13	2.5	5.1	3.81	3.125	3.116	3.114	3.06	3.103	23.98	5.05	19.99	0.5
TCD3_32	AW	1	2.39	25.07	14.36	2.45	5.1	3.56	3.087	3.047	3.048	3.06	3.061	24.03	5	20.07	0.5
TCD3_38	SR	1	2.45	24.99	14.01	2.45	5.09	3.92	3.125	3.095	3.088	3.07	3.095	23.99	4.995	19.995	0.5
TCD3_46	AW	1	2.43	25.05	14.17	2.36	5.11	3.82	3.015	3.007	3.051	3.09	3.041	24.01	4.915	20.135	0.5
TCD3_65	AW	1	2.46	25.03	14.68	2.43	5.18	3.9	3.091	3.085	3.091	3.092	3.09	23.89	5.02	20.01	0.5
TCD3_66	SR	1	2.46	25.06	14.13	2.4	5.09	4	3.086	3.084	3.112	3.097	3.095	24.07	4.945	20.115	0.5
TCD3_77	parent	0.05	2.39	25.13	14.59	2.31	5.17	n/a	n/a	n/a	n/a	3.21	3.21	24.04	4.895	20.235	0.5
TCD3_78	parent	0.05	2.44	25.13	14.66	2.53	5.13	n/a	n/a	n/a	n/a	3.2	3.2	23.96	5.095	20.035	0.5
TCD3_79	parent	crack	2.41	25.12	13.24	2.33	5.18	n/a	n/a	n/a	n/a	3.19	3.19	24.04	4.92	20.2	0.5
TCD3_80	parent	crack	2.41	25.1	13.24	2.4	5.14	n/a	n/a	n/a	n/a	3.2	3.2	24.14	4.97	20.13	0.5

Notch measurements

DENT samples

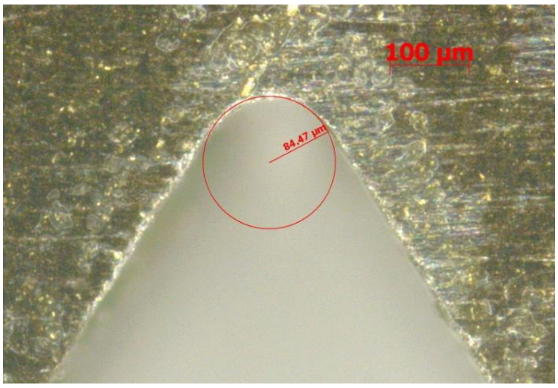

Figure G 9 - 0.1 mm notch measurement

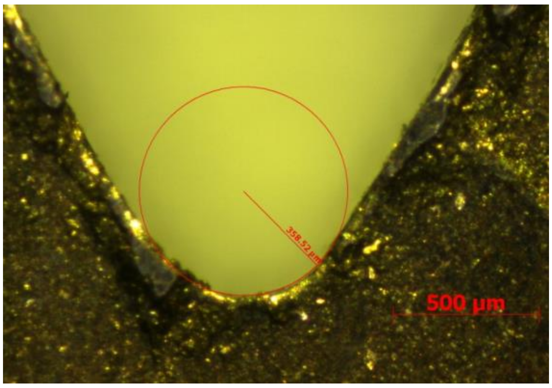

Figure G 10 - 0.35 mm (TCD3-45) - notch measurement

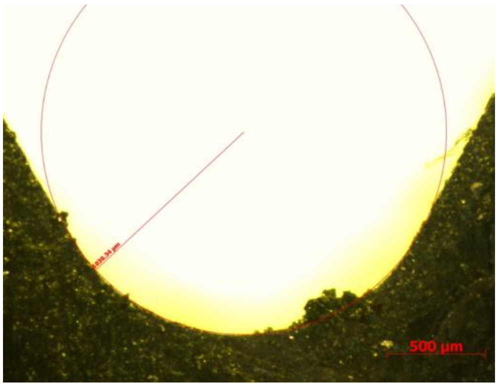

Figure G 11 - 1 mm (TCD3-21) - notch measurement

CT Samples

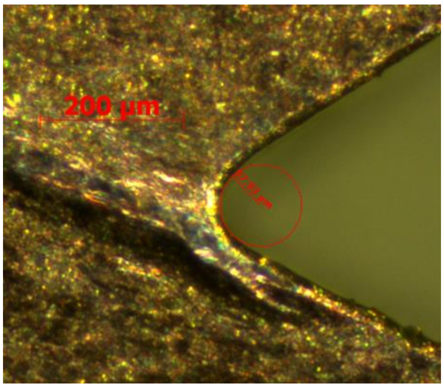

Figure G 12 - 0.05 mm (TCD3-47) - notch measurement

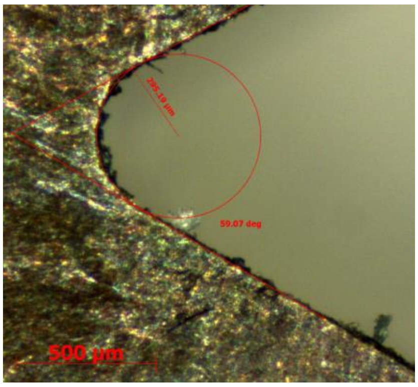

Figure G 13 - 0.3 mm (TCD3-5) - notch measurement

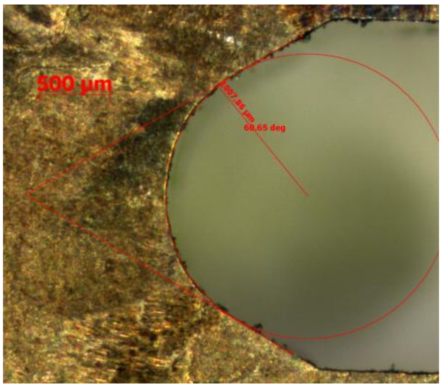

Figure G 14 - 1 mm (TCD3-36) - notch measurement

Appendix H – Strain gauge detail

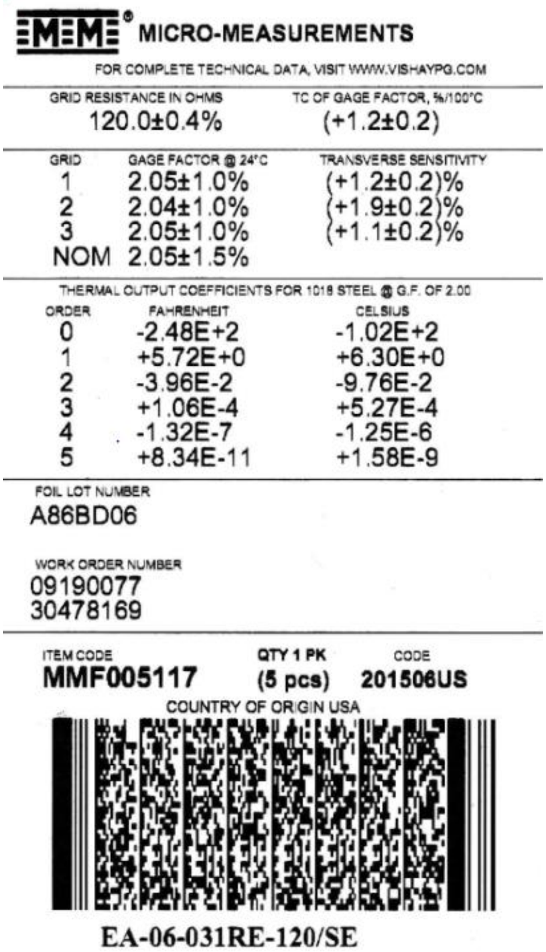

Figure H 1 - Strain gauge detail

Appendix I – Weld study results

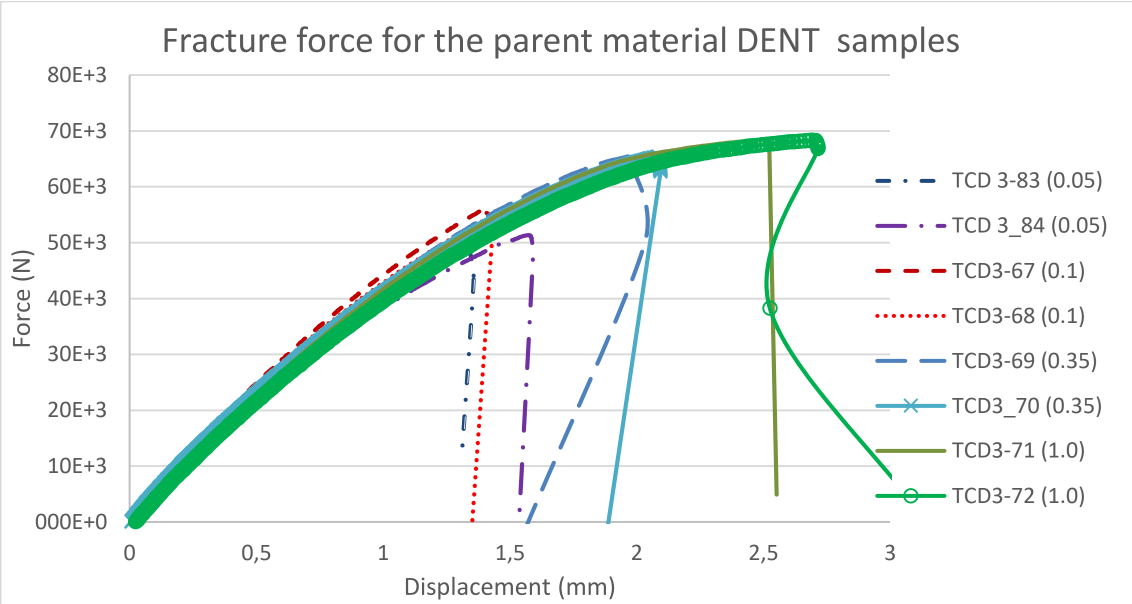

Figure I 1 - Fracture force for DENT parent plate samples

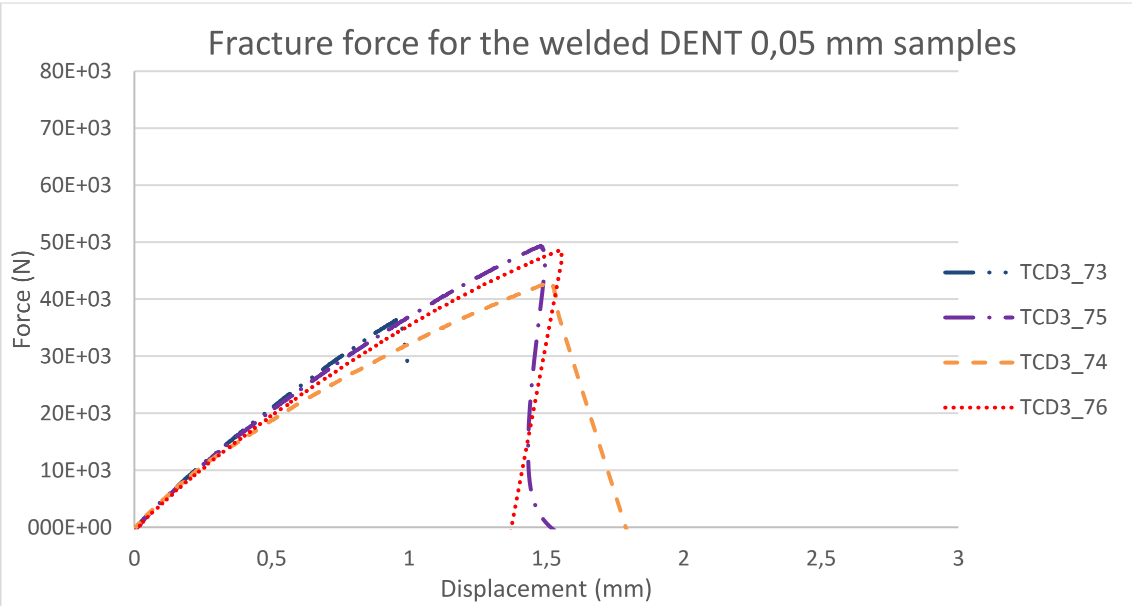

Figure I 2 - Fracture force for DENT 0.05 mm welded samples

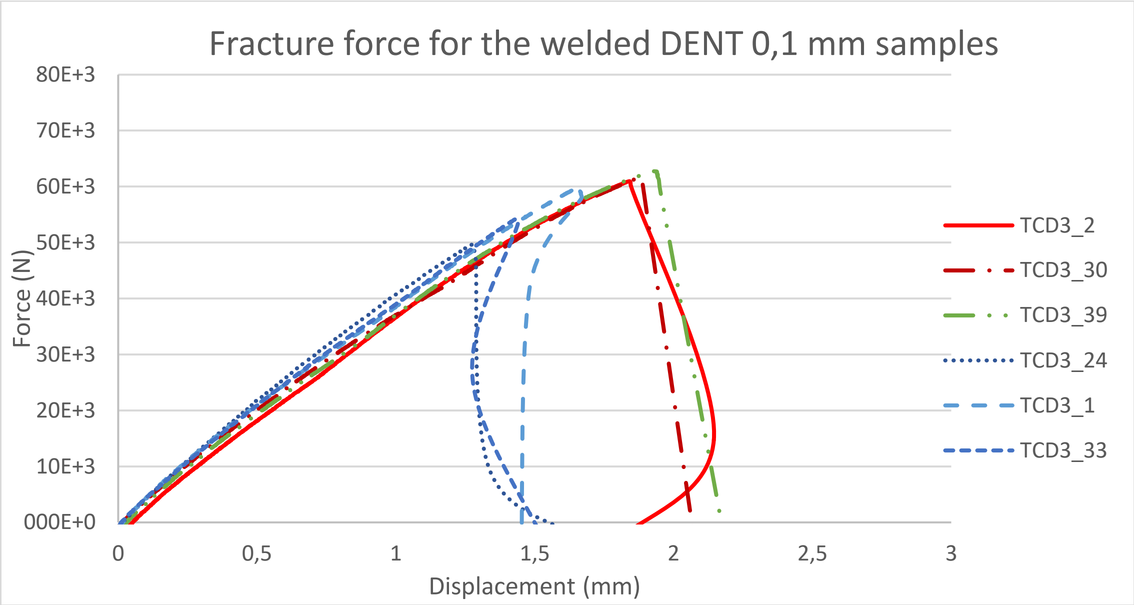

Figure I 3 - Fracture force for DENT 0.1 mm welded samples

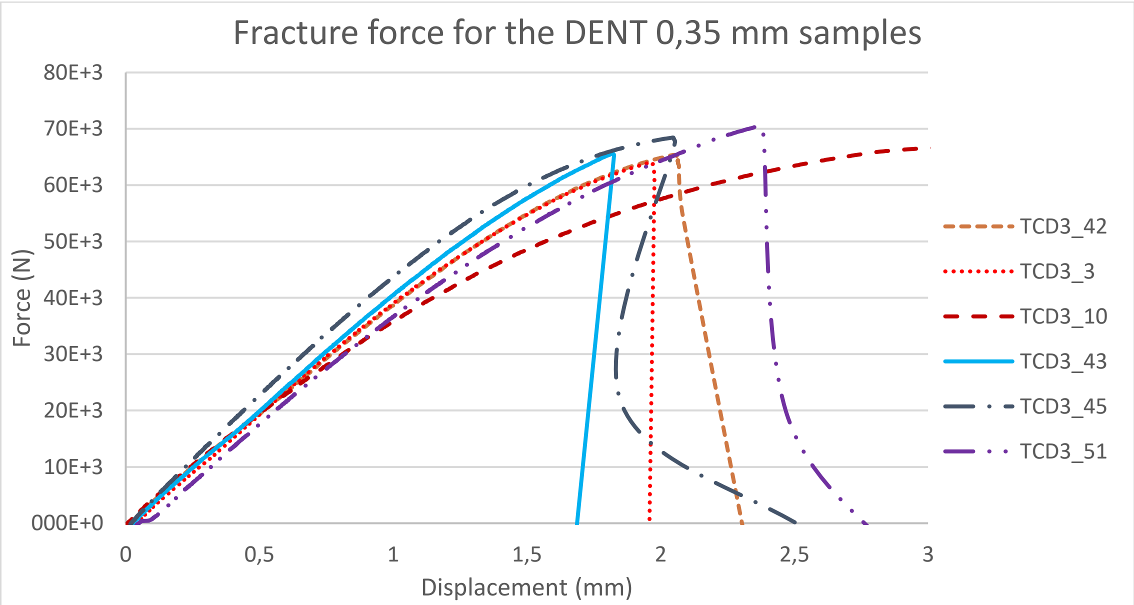

Figure I 4 - Fracture force for DENT 0.35 mm welded samples

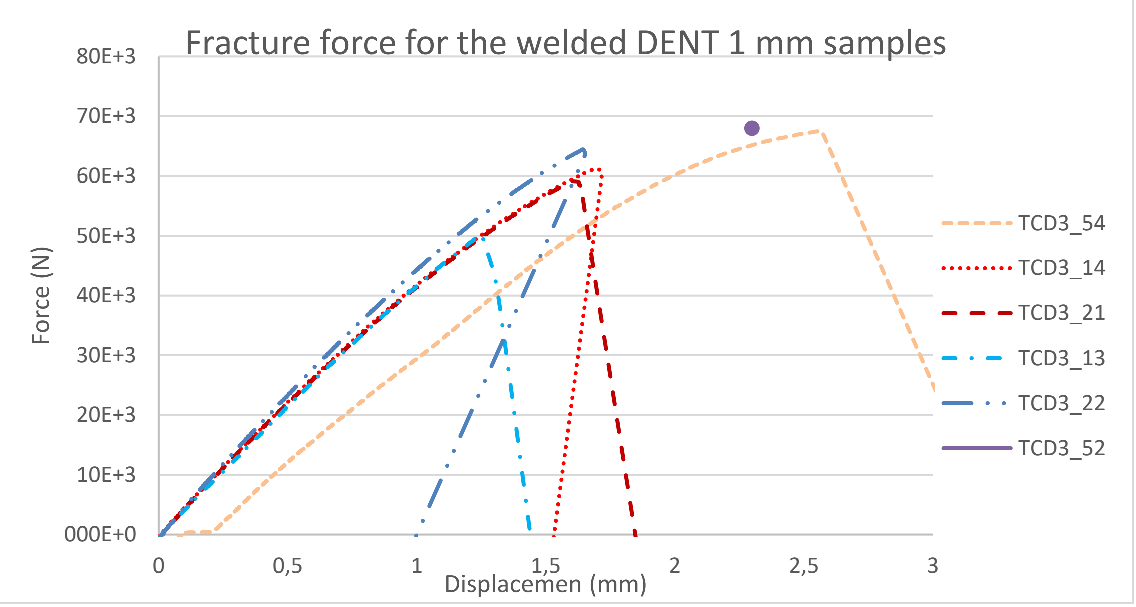

Figure I 5 - Fracture force for DENT 1 mm welded samples

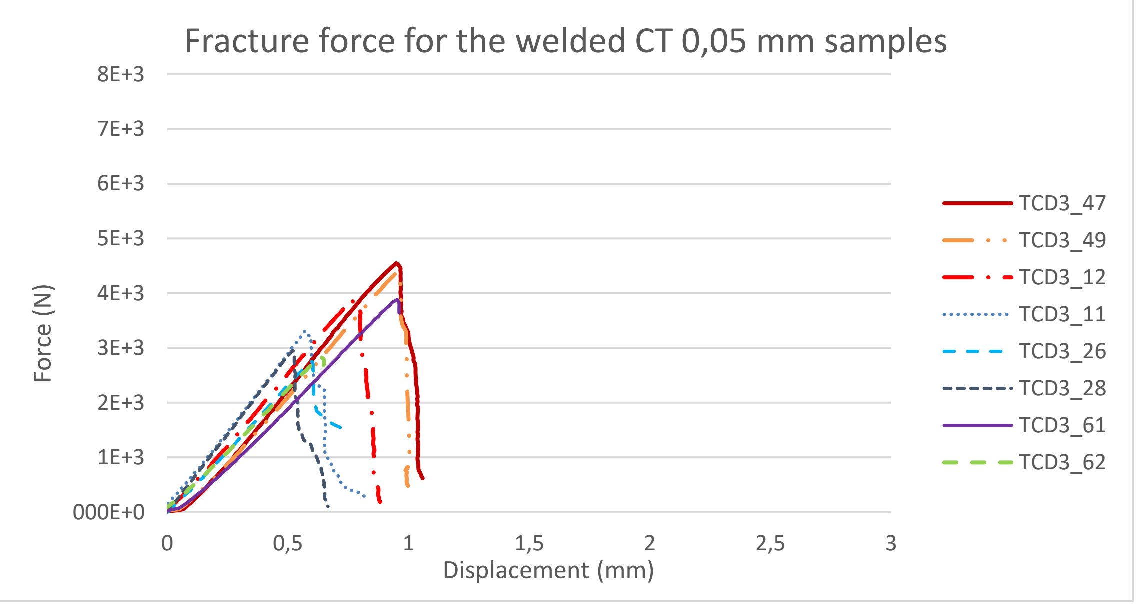

Figure I 6 - Fracture force for CT 0.05 mm welded samples

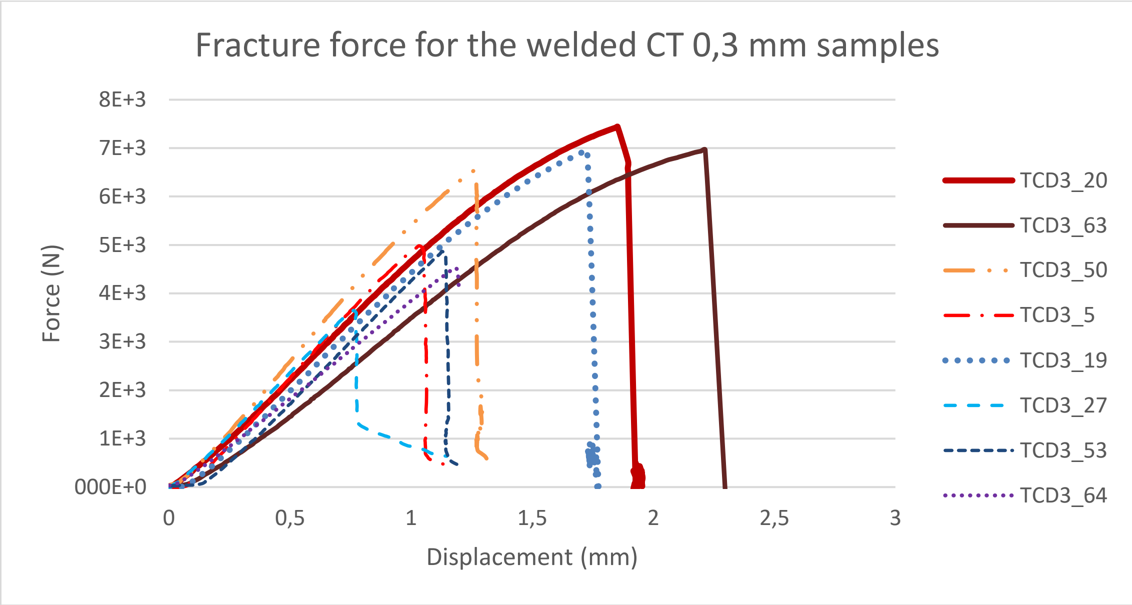

Figure I 7 - Fracture force for CT 0.3 mm welded samples

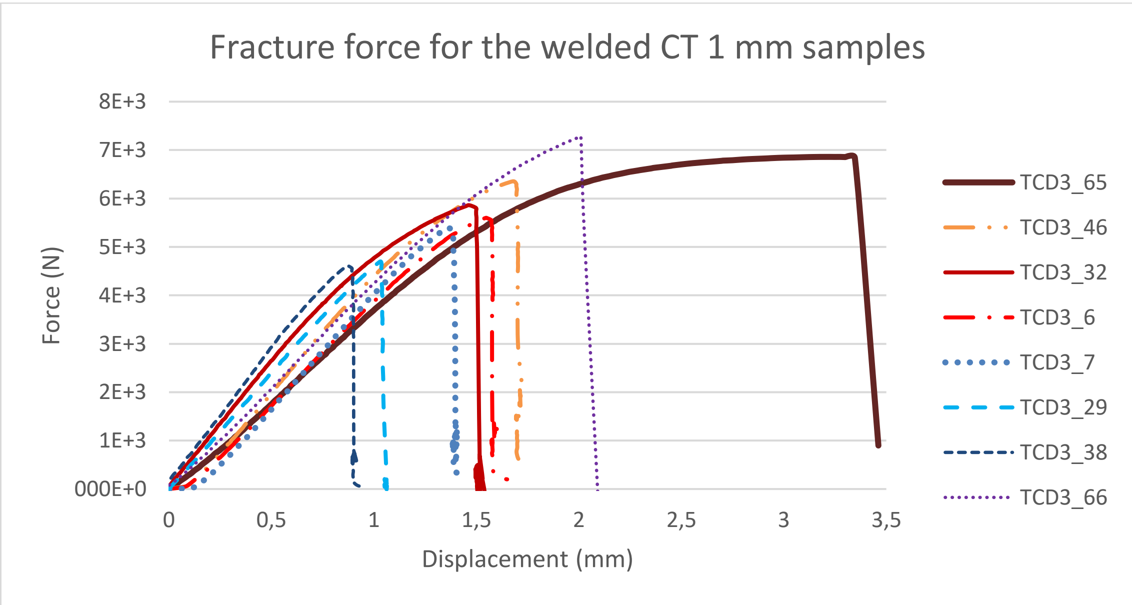

Figure I 8 - Fracture force for CT 1 mm welded samples

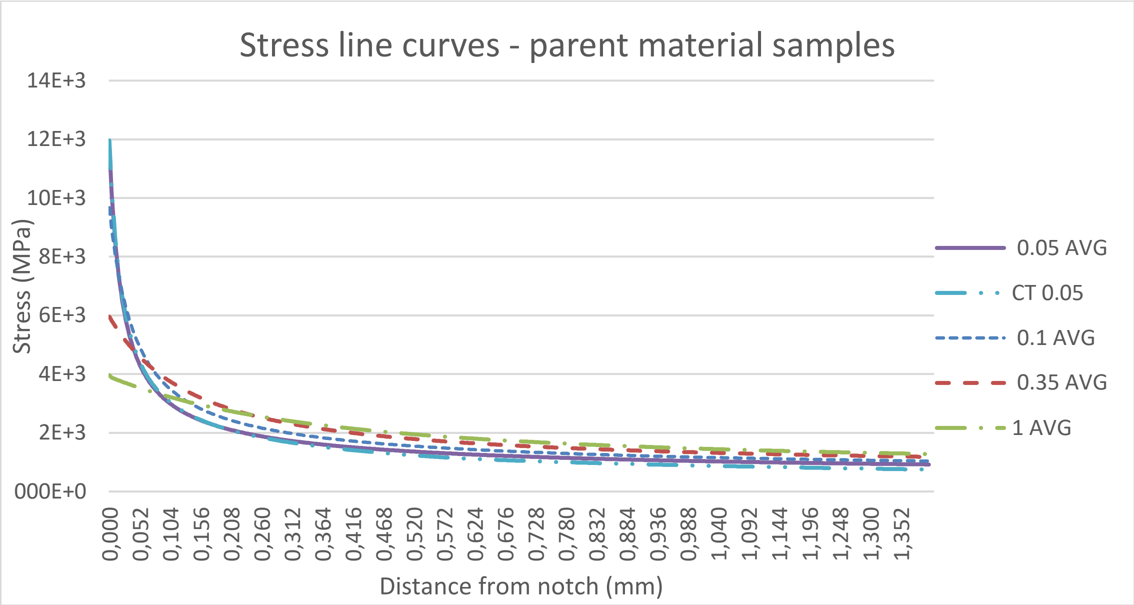

Figure I 9 - Batch B stress line curves

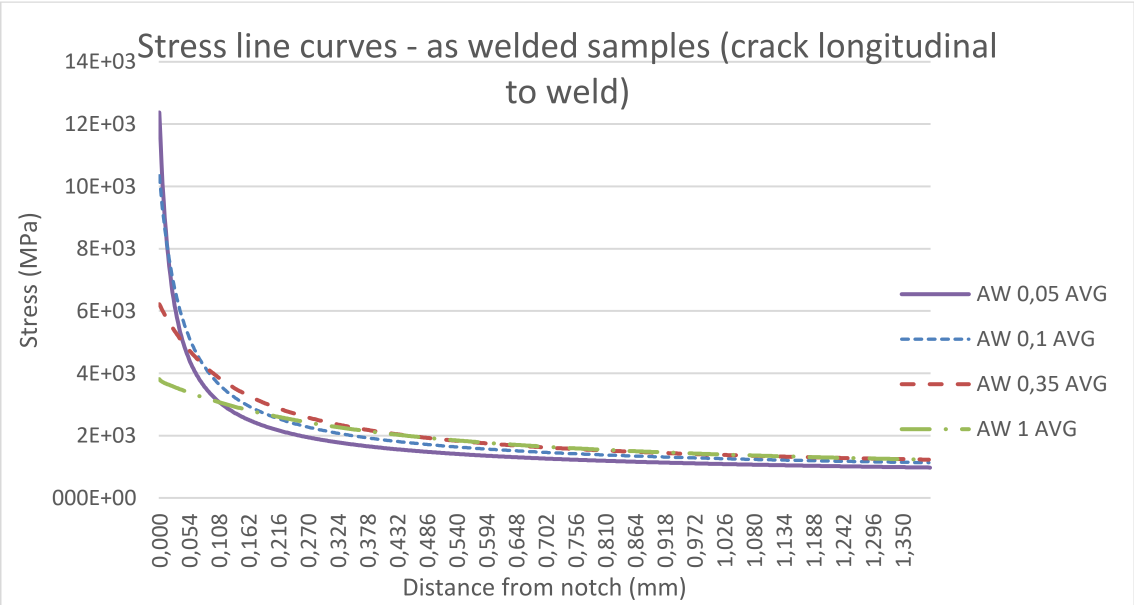

Figure I 10 - DENT weld stress line curves

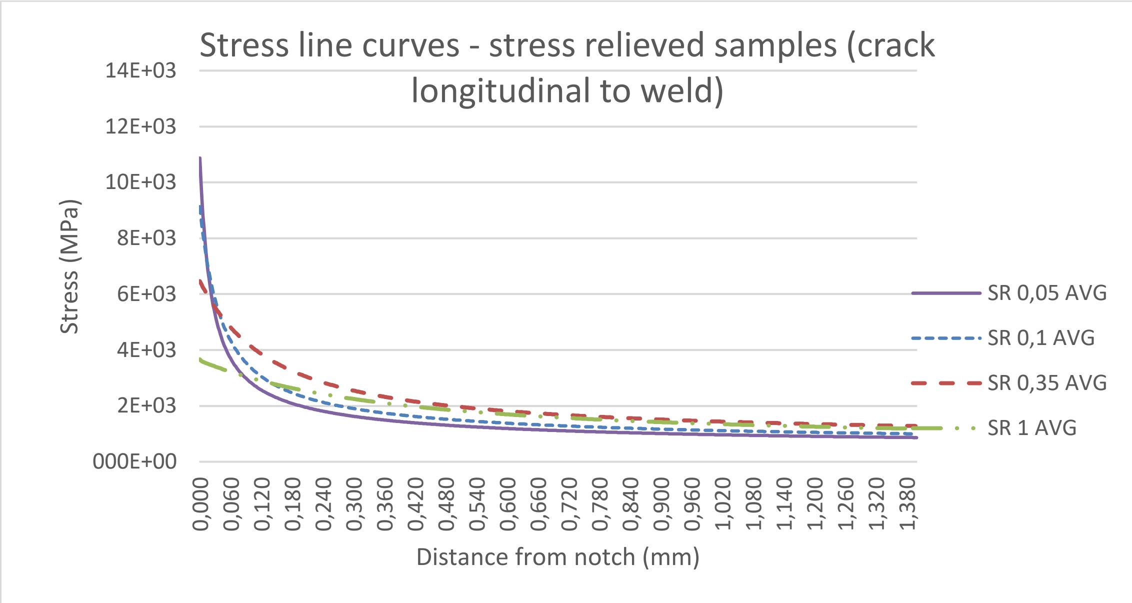

Figure I 11 - DENT stress relieved stress line curves

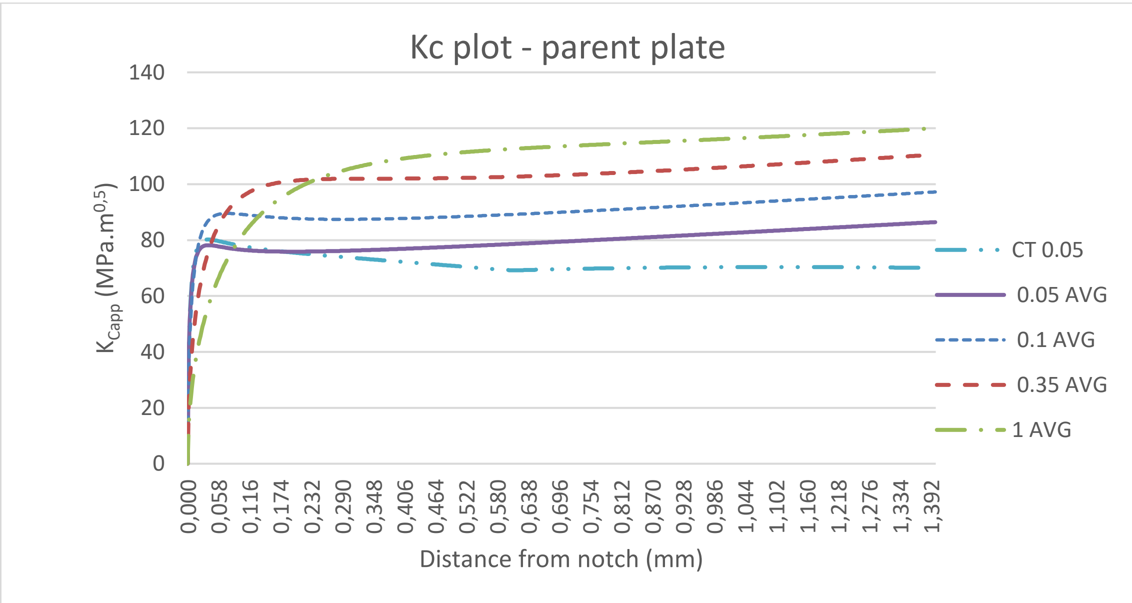

Figure I 12 - K_{Capp} plot parent plate

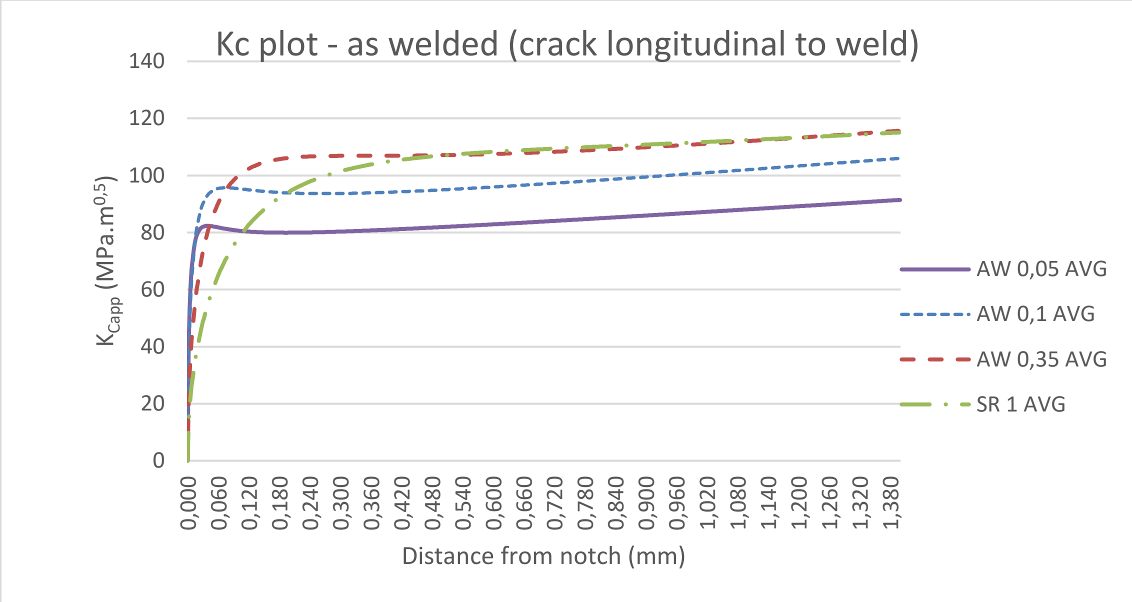

Figure I 13 - K_{Capp} plot DENT welded plate

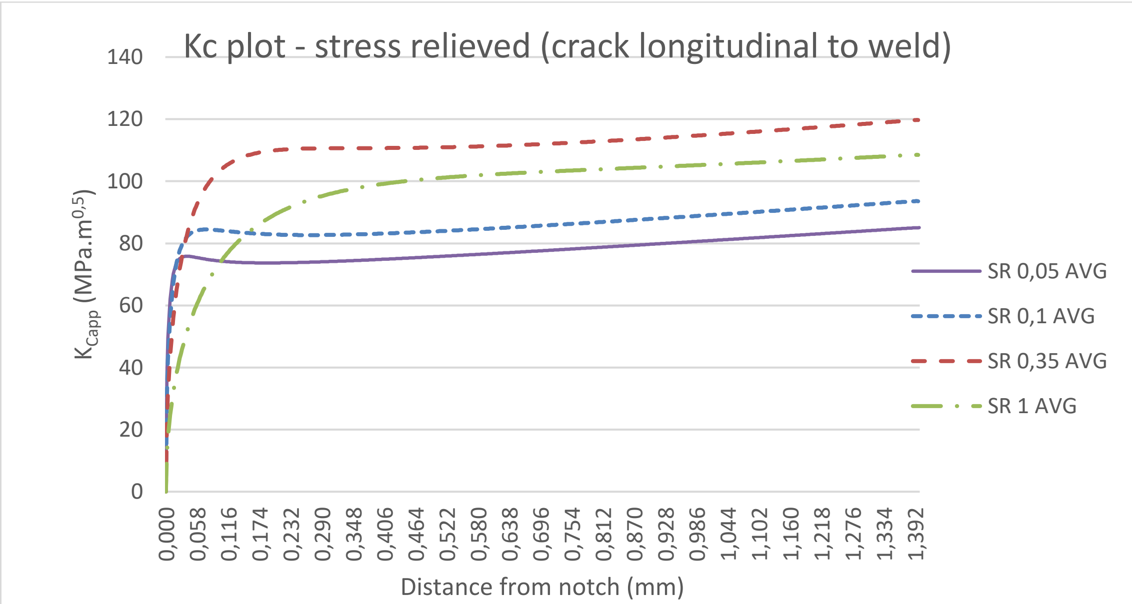

Figure I 14 - K_{Capp} plot DENT stress relieved plate

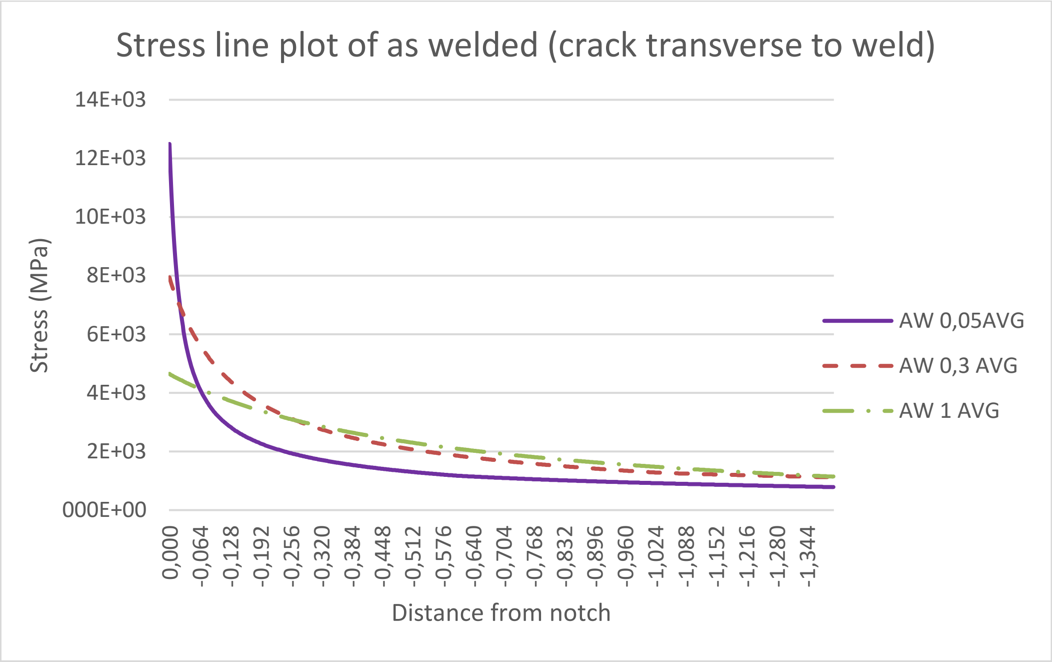

Figure I 15 - CT weld stress line curves

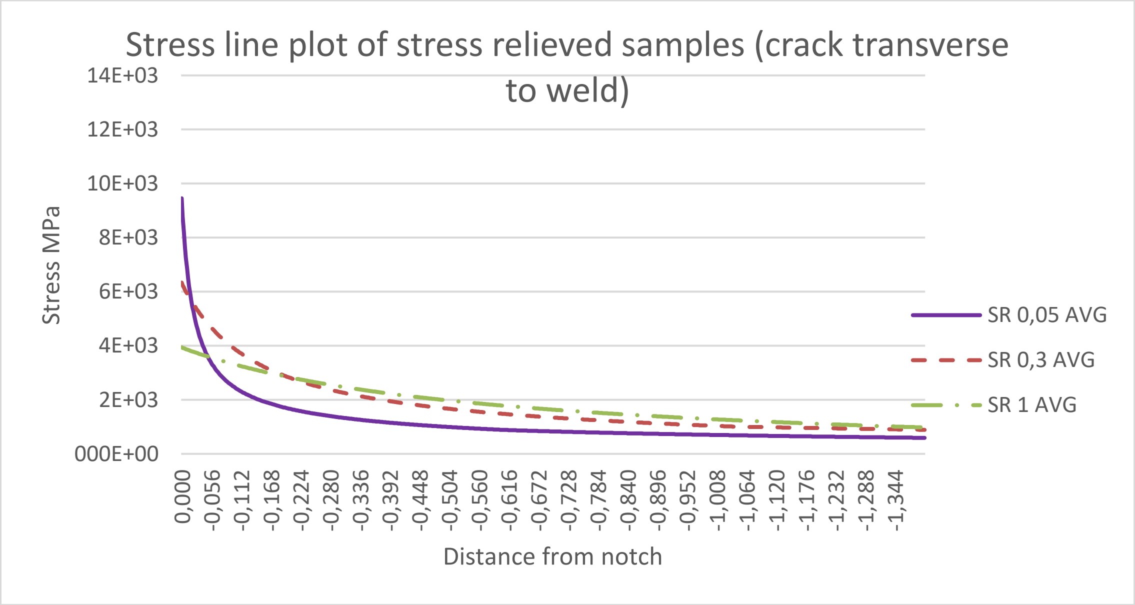

Figure I 16 - CT stress relieved stress line curves

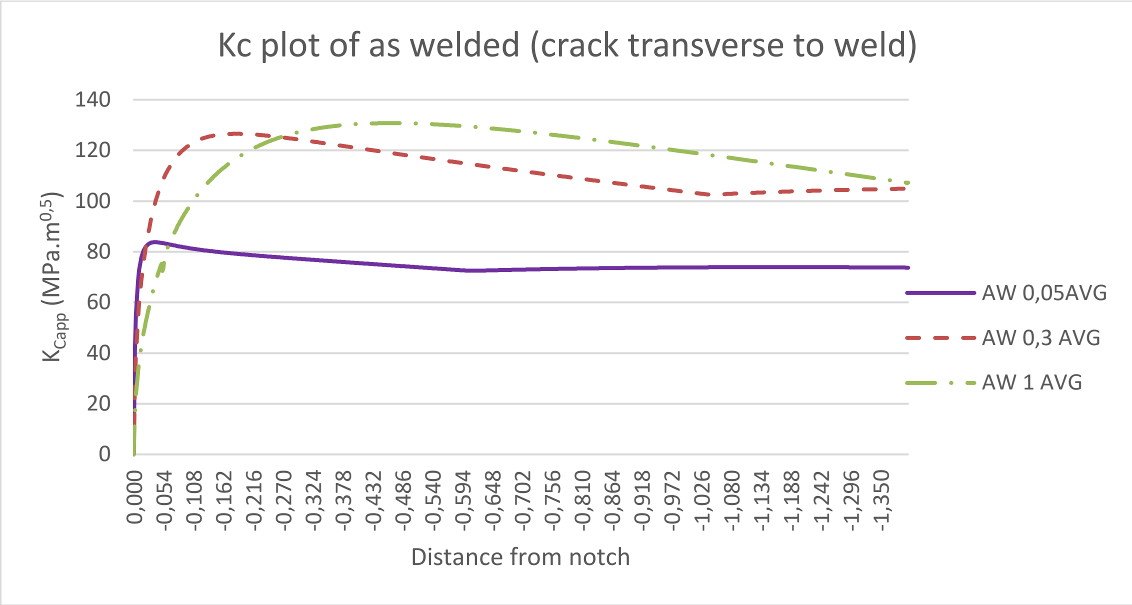

Figure I 17 - K_{Capp} plot CT welded plate

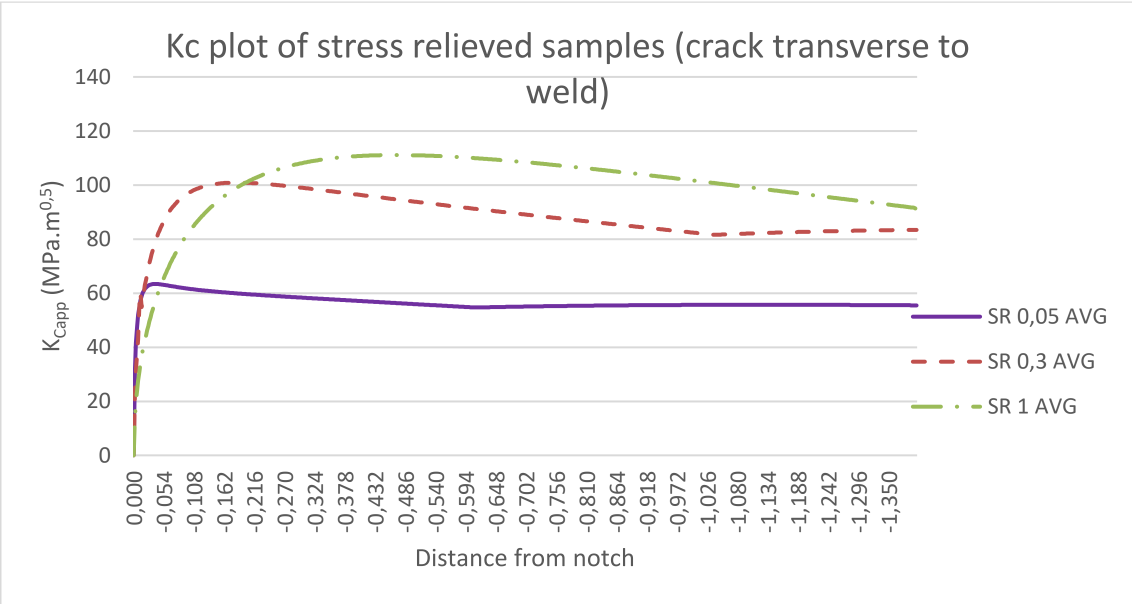

Figure I 18 - K_{Capp} plot CT stress relieved plate

Table I 1 - K_{Capp} for CT samples

Critical values for samples with notch perpendicular to weld (intersection points)									
Root radius	0.05 mm						0.3 mm		
Comparative radius	1 mm			0.3 mm			1 mm		
Condition	σ_0 (MPa)	L/2 (mm)	K_{Capp} (MPa.m$^{0.5}$)	σ_0 (MPa)	L/2 (mm)	K_{Capp} (MPa.m$^{0.5}$)	σ_0 (MPa)	L/2 (mm)	K_{Capp} (MPa.m$^{0.5}$)
AW	4130	0.064	83	6968	0.022	82	3063	0.265	125
SR	3603	0.049	63	5566	0.019	61	2843	0.200	101

Table I 2 - K_{Capp} for CT samples (peak)

Critical values for samples with notch perpendicular to weld at peaks (values at peaks)									
Root radius	0.05 (mm)			0.3 (mm)			1 (mm)		
Condition	σ_0 (MPa)	L/2 (mm)	K_{Capp} (MPa.m$^{0.5}$)	σ_0 (MPa)	L/2 (mm)	K_{Capp} (MPa.m$^{0.5}$)	σ_0 (MPa)	L/2 (mm)	K_{Capp} (MPa.m$^{0.5}$)
AW	5418	0.038	84	3702	0.186	127	2416	0.466	131
SR	4105	0.038	63	2967	0.184	101	2049	0.468	111

Table I 3 - K_{Capp} for DENT samples

Critical values for samples with notch longitudinal to weld (intersection points)									
Root radius	0.1 (mm)						0.35 (mm)		
Comparative radius	1 (mm)			0.35 (mm)			1 (mm)		
Condition	σ_0 (MPa)	L/2 (mm)	K_{Capp} (MPa.m$^{0.5}$)	σ_0 (MPa)	L/2 (mm)	K_{Capp} (MPa.m$^{0.5}$)	σ_0 (MPa)	L/2 (mm)	K_{Capp} (MPa.m$^{0.5}$)
AW	2676	0.196	94	4267	0.08	96	1957	0.472	107
SR	2794	0.142	83	5301	0.038	82	No intersection		

Table I 4 - K_{Capp} for DENT samples (0.05 mm)

Critical values for samples with notch longitudinal to weld (intersection points)									
Root radius	0.05 (mm)								
Comparative radius	0.1 (mm)			0.35 (mm)			1 (mm)		
Condition	σ_0 (MPa)	L/2 (mm)	K_{Capp} (MPa.m$^{0.5}$)	σ_0 (MPa)	L/2 (mm)	K_{Capp} (MPa.m$^{0.5}$)	σ_0 (MPa)	L/2 (mm)	K_{Capp} (MPa.m$^{0.5}$)
AW	8139	0.014	76	5010	0.043	82	3061	0.110	80
SR	7169	0.014	69	5606	0.026	75	3060	0.086	75

Table I 5 - K_{Capp} for DENT samples (peak values)

Critical values for samples with notch longitudinal to weld at peaks (values at peaks)									
Root radius	0.1 (mm)			0.35 (mm)			1 (mm)		
Condition	σ_0 (MPa)	L/2 (mm)	K_{Capp} (MPa.m$^{0.5}$)	σ_0 (MPa)	L/2 (mm)	K_{Capp} (MPa.m$^{0.5}$)	σ_0 (MPa)	L/2 (mm)	K_{Capp} (MPa.m$^{0.5}$)
AW	4438	0.074	96	2289	0.344	107	1478	0.894	111
SR	3917	0.074	84	2373	0.346	111	1423	0.894	104

Table I 6 - K_{Capp} for DENT samples (peak values of 0.05 mm)

Critical values for samples with notch longitudinal to weld at peaks (values at peaks)			
Root radius	0.05 (mm)		
Condition	σ_0 (MPa)	L/2 (mm)	K_{Capp} (MPa.m$^{0.5}$)
AW	5330	0.04	82
SR	4682	0.038	76

Table I 7 - K_{Capp} for DENT parent plate samples

Parent plate (intersection points)									
Root radius	0.1 (mm)						0.35 (mm)		
Comparative radius	1 (mm)			0.35 (mm)			1 (mm)		
Condition	σ_0 (MPa)	L/2 (mm)	K_{Capp} (MPa.m$^{0.5}$)	σ_0 (MPa)	L/2 (mm)	K_{Capp} (MPa.m$^{0.5}$)	σ_0 (MPa)	L/2 (mm)	K_{Capp} (MPa.m$^{0.5}$)
	3053	0.134	89	4239	0.071	90	2609	0.242	102

Table I 8 - K_{Capp} for DENT parent plate samples (0.05 mm)

Parent plate (intersection points)									
Root radius	0.05 (mm)								
Comparative radius	0.35 (mm)			0.1 (mm)			1 (mm)		
Condition	σ_0 (MPa)	L/2 (mm)	K_{Capp} (MPa.m$^{0.5}$)	σ_0 (MPa)	L/2 (mm)	K_{Capp} (MPa.m$^{0.5}$)	σ_0 (MPa)	L/2 (mm)	K_{Capp} (MPa.m$^{0.5}$)
	4810	0.042	78	7380	0.016	74	3306	0.086	77

Table I 9 - K_{Capp} for TPB parent plate samples

Parent plate – Three-point bend tests							
Part Number	Group Number	W (mm)	B (mm)	a (mm)	S (mm)	Force (N)	K_{Capp} (MPa.m$^{0.5}$)
WRCD01-01-85	TPB	25.14	3,19	13.37	100	-3390	79
WRCD01-01-86		25.14	3,19	13.24	100	-3683	84

Appendix J – Calibration certificates

CME

Metrology cc

Riley Street, Beaconvale, Cape Town
Tel + 27 21 9311101 Fax +27 21 9311126

sanas Calibration Laboratory
Accredited Lab No 819

Calibration Certificate

Certificate No: T4875.5 Page No: 1 of 2

Calibration details

Calibration of: Universal Tester
Mainframe Serial No: 6068
Manufacturer: Instron
Location: On Site - Lab
Loadcell Serial No: 43298
Capacity: 100 kN
Resolution: 0.01 kN
Test speed: Manual
Procedure No: FP1
Method: Tension
Calibration date: 31-May-2016
Date of Issue: 17-Jun-2016
Calibration frequency: 12 months

Customer details

Calibration for: Nelson Mandela
Address: Metropolitan University
Mech. Engineering Dept.
Port Elizabeth

Contact person: Mervin Knoeson
Order No: N/A
Job No: T4785
Date received: N/A
Condition of UUT: Good
Repair/Maintenance: General

Calibrated by: T.Thomson

Traceability

Loadcell: 100kN Serial No: 137113

Results

Client's Instrument kN	Before Adjustment	True Load kN Run 1	Run 1A	Run 2	Run 3	Average Load kN	Average error %	Uncertainty ± %
0.00		0.00	0.00	0.00	0.00	0.00	n/a	n/a
10.00		9.99	9.99	9.99	9.99	9.99	-0.100	0.500
20.00		19.98	19.98	19.98	19.98	19.98	-0.100	0.500
30.00		29.98	29.98	29.98	29.98	29.98	-0.067	0.500
40.00		39.97	39.97	39.97	39.97	39.97	-0.075	0.500
50.00		49.96	49.96	49.96	49.96	49.96	-0.080	0.500
60.00		59.95	59.95	59.96	59.96	59.96	-0.075	0.500
70.00		69.94	69.94	69.95	69.94	69.94	-0.082	0.500
80.00		79.92	79.91	79.94	79.93	79.93	-0.094	0.500
90.00		89.91	89.91	89.93	89.92	89.92	-0.092	0.500
100.00		99.90	99.90	99.91	99.90	99.90	-0.097	0.500
Temperature Recorded		22.2°C	22.3°C	22.4°C	22.6°C	n/a	n/a	
Client's instrument resolution %							0.01	
Other factors %							0.02	

Remarks: Equipment not adjusted.Force component only.
Calibration and Measurement Capability is 0,5 %

Technical Signatory: T.Thomson Checked by: K.Myburgh

The reported expanded uncertainty is based on a standard uncertainty multiplied by a coverage factor of K=2 providing a level of confidence of approximately 95%. The uncertainties of measurement have been estimated in accordance with the principles defined in Guide to Uncertainty of Measurement (Gum).These results relate only to the item tested or calibrated. All measuring equipment used is traceable to National Measuring Standards.

CME Metrology cc

Riley Street, Beaconvale, Cape Town
Tel + 27 21 9311101 Fax +27 21 9311126

sanas
Accredited Lab No 819

Calibration Certificate

Certificate No: T4875.5 Page No : 2 of 2

Graph

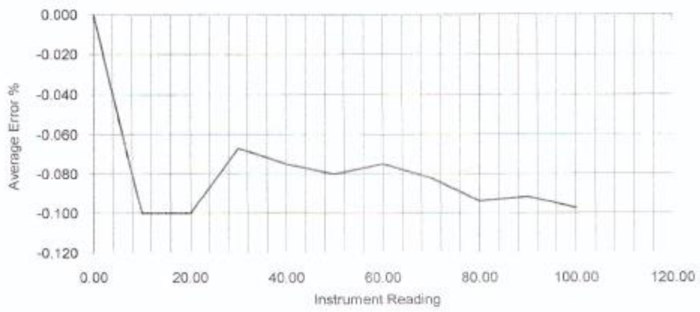

Machine Service Report					
Machine Condition	Good	Poor	***Loadcell and Extension***	Good	Poor
Crosshead & Leadscrews :	x		Linearity :	x	
Speed & Drive Control :	x		Repeatability :	x	
Control Buttons :	x		Zero Drift :	x	
Limit Switches :	N/A		Extension Readings :	x	
Loading surfaces :	x		Machine working conditio	x	
Remarks: None.					

Technical Signatory: T.Thomson Checked by: K.Myburgh

CME

Metrology cc

sanas
Calibration Laboratory

Riley Street, Beaconvale, Cape Town
Tel + 27 21 9311101 Fax +27 21 9311126

Accredited Lab No 819

Calibration Certificate

Certificate No: T4875.6

Page No : 1 of 2

Calibration details

Calibration of: Universal Tester
Mainframe Serial No: 6068
Manufacturer: Instron
Location: On Site - Lab
Loadcell Serial No: 05556
Capacity: 25 kN
Resolution: 0.01 kN
Test speed: Manual
Procedure No: FP1
Method: Tension
Calibration date: 31-May-2016
Date of Issue: 17-Jun-2016
Calibration frequency: 12 months

Traceability

Loadcell: 100kN Serial No: 137113

Customer details

Calibration for: Nelson Mandela
Address: Metropolitan University
Mech. Engineering Dept.
Port Elizabeth

Contact person: Mervin Knoeson
Order No: N/A
Job No: T4785
Date received: N/A
Condition of UUT: Good
Repair/Maintenance: General

Calibrated by: T.Thomson

Results

Client's Instrument kN	Before Adjustment	True Load kN Run 1	Run 1A	Run 2	Run 3	Average Load kN	Average error %	Uncertainty ± %
0.00		0.00	0.00	0.00	0.00	0.00	n/a	n/a
2.50		2.50	2.51	2.50	2.50	2.50	0.100	0.500
5.00		5.02	5.02	5.02	5.02	5.02	0.400	0.500
7.50		7.53	7.54	7.53	7.53	7.53	0.433	0.500
10.00		10.05	10.05	10.05	10.04	10.05	0.475	0.500
12.50		12.56	12.56	12.56	12.56	12.56	0.480	0.500
15.00		15.07	15.07	15.07	15.07	15.07	0.467	0.500
17.50		17.58	17.58	17.58	17.58	17.58	0.457	0.500
20.00		20.09	20.09	20.09	20.09	20.09	0.450	0.500
22.50		22.59	22.60	22.60	22.60	22.60	0.433	0.500
25.00		25.10	25.11	25.11	25.11	25.11	0.430	0.500
Temperature Recorded		22.8°C	23.0°C	23.2°C	23.3°C	n/a	n/a	
Client's instrument resolution %							0.04	
Other factors %							0.08	

Remarks: Equipment not adjusted.Force component only.
Calibration and Measurement Capability is 0.5 %

Technical Signatory: T.Thomson

Checked by: K.Myburgh

The reported expanded uncertainty is based on a standard uncertainty multiplied by a coverage factor of K=2 providing a level of confidence of approximately 95%. The uncertainties of measurement have been estimated in accordance with the principles defined in Guide to Uncertainty of Measurement (Gum).These results relate only to the item tested or calibrated. All measuring equipment used is traceable to National Measuring Standards.

CME

Metrology cc

Riley Street, Beaconvale, Cape Town
Tel + 27 21 9311101 Fax +27 21 9311126

sanas

Accredited Lab No 819

Calibration Certificate

Certificate No: T4875.6 Page No : 2 of 2

Graph

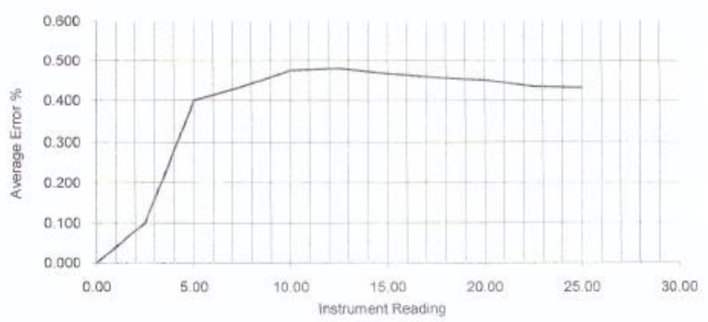

Machine Service Report					
Machine Condition	Good	Poor	***Loadcell and Extension***	Good	Poor
Crosshead & Leadscrews :	x		Linearity :	x	
Speed & Drive Control :	x		Repeatability :	x	
Control Buttons :	x		Zero Drift :	x	
Limit Switches :	x		Extension Readings :	x	
Loading surfaces :	x		Machine working conditic	x	
Remarks: None.					

Technical Signatory: T.Thomson Checked by: K.Myburgh

R.W.K. AGENCIES cc

TESTING & MEASURING EQUIPMENT FOR HARDNESS, THICKNESS,
COATING THICKNESS, SURFACE ROUGHNESS & VIBRATION
Whatever we sell, whatever we do must be good for us AND good for YOU.

P.O. Box 1952
Randburg, 2125
Reg. No: 2010/076274/23

Tel: 0861 100 079
Fax: 086 274 4305
rwk@rwkagencies.co.za

CERTIFICATE OF CALIBRATION

IN COMPLIANCE WITH: SANS/ISO 6507 ERROR + REPEATABILITY

COMPANY: NMMU.

NAME & MODEL OF MACHINE: FutureTech FM-700

SERIAL NO: AR 2115

TEST RESULTS

TYPE OF TEST	HV0.3	HV0.3	HV0.5	HV0.5	
TEST BLOCK HARDNESS	187.5	733.1	733.5	183.4	
TEST BLOCK SERIAL NO	078805	076182	076182	078805	
TEST No. 1.	183	754	749	189	
TEST No. 2.	192	759	747	188	
TEST No. 3.	184	747	745	186	
TEST No. 4.	185	760	745	185	
TEST No. 5.	182	758	747	186	
MEAN HARDNESS	185.2	755.6	746.6	186.8	
PERMITTED ERROR	±9.4	±73.2	±51.3	±9.2	
ACTUAL ERROR	−2.3	+22.5	+13.1	+3.4	
REQUIRED REPEATABILITY	≤22.0	≤59.0	≤59.0	≤22.0	
ACTUAL REPEATABILITY	10.0	13.0	4.0	4.0	

TESTED BY:

NAME: ANDRE JOOSTE SIGNATURE: [signature]

TEST DATE: 19 APRIL 2012 EXPIRY DATE: 18 APRIL 2013

RECEIVED BY: Glynne Erasmus 19April2012 DATE:

Appendix K – Conferences, seminars and publications